Optimization of a 4D-PTV metrology for the characterization of a turbulent flow at very small scales

Tarek Chaabo

CENTRALE LILLE

THÈSE

Présenté en vue
d'obtenir le grade de

Docteur
En

Spécialité : Mécanique

Par
Tarek Chaabo

Titre de thèse :
OPTIMIZATION D'UNE MÉTROLOGY 4D-PTV POUR LA CARACTÉRISATION D'UN ÉCOULEMENT TURBULENT à TRÈS PETITES ÉCHELLES.

Soutenue le 06 décembre 2022 devant le jury d'examen

Président :	Serge Simoens, DR CNRS Lyon.
Rapporteur :	Henda Djeridi, Professeur Université de Grenoble.
Rapporteur :	Lionel Thomas, Professeur Université de Poitiers.
Examinateur :	Marie Couliou, PhD, Ingénieure de recherche à l'Onera.
Directeur de thèse :	Jean-Marc Foucaut, Professor Centrale Lille.
Co-Directeur de thèse :	Jean Philippe Laval, DR CNRS Lille.
Co-Directeur de thèse :	Christophe Cuvier, Maitre de conférence, Centrale Lille.

Thèse préparée au Laboratoire de Mécanique des Fluides de Lille - Kampé de Fériet
Ecole doctorale ENGSYS 632

Centrale Lille
Cité Scientifique – CS20048 – 59651 Villeneuve d'Ascq Cedex – France
Tél. + 33 (0)3 20 33 53 53 – https://centralelille.fr

CENTRALE LILLE

PhD THESIS

Submitted to obtain the degree of

Doctor
In
Mechanical Engineering

by

Tarek Chaabo

Thesis title:
OPTIMIZATION OF a 4D-PTV METROLOGY FOR THE CHARACTERIZATION OF a TURBULENT FLOW AT VERY SMALL SCALES.

Oral defense at Central Lille on the 6th of December 2022 in front of the examination board:

President of jury:	Serge Simoens, DR CNRS Lyon.
Reviewer:	Henda Djeridi, Professor Université de Grenoble.
Reviewer:	Lionel Thomas, Associate professor Université de Poitiers.
Examiner:	Marie Couliou, PhD, Research engineer at Onera.
Supervisor:	Jean-Marc Foucaut, Professor Centrale Lille.
Supervisor:	Jean Philippe Laval, DR CNRS Lille.
Supervisor:	Christophe Cuvier, Assistant professor Centrale Lille.

Thesis prepared at the LMFL laboratory
Ecole doctorale ENGSYS 632

Centrale Lille
Cité Scientifique – CS20048 – 59651 Villeneuve d'Ascq Cedex – France
Tél. + 33 (0)3 20 33 53 53 – https://centralelille.fr

Résumé

La méthode « Particle Tracking Velocimetry – PTV » est une des approches classiques pour étudier la complexité de la dynamique des échelles dissipative dans un écoulement turbulent. La richesse des mécanismes qui existent dans ces écoulements rend quasiment impossible la prise en compte de l'ensemble de ces phénomènes. Dans le but de caractériser ces phénomènes, le présent travail est basé sur une technique de suivi de particules appelée « Shake-The Box » pour mesurer les champs de vitesse tridimensionnels en fonction du temps à une résolution pouvant avoisiner l'échelle dissipative. Le dispositif expérimental d'un écoulement Von Karman Géant « GVK » et le traitement de la technique « Shake the Box » ont été optimisés et poussés à leurs limites afin d'améliorer la résolution spatiale et la précision des trajectoires lagrangiennes mesurées. L'approche utilisée dans cette thèse est basée non seulement sur des données expérimentales mais aussi sur des images synthétiques PIV basées sur une simulation numérique directe des équations de Navier Stokes.

Résumé des optimisations expérimentale :

L'expérience GVK présente de nombreux défis pratiques, notamment pour effectuer des mesures optiques à l'intérieur pour extraire des informations sur la turbulence. Le but du projet était d'étudier finement la turbulence générée par ce GVK à des nombres de Reynolds très élevés. La turbulence étant un phénomène 3D, la méthode "Shake the Box" (STB) a été choisie car elle fournit des informations sur les 3 composantes de la vitesse dans un volume en fonction du temps. Pour cette raison, une expérience mimétique qui reproduit l'accès optique dont nous disposons pour GVK a été utilisée dans le but d'affiner tous les obstacles expérimentaux possibles auxquels nous pourrions être confrontés sur l'expérience principale GVK. Tout d'abord, nous avons testé deux configurations possibles pour le placement des caméras autour de l'expérience quasi-cylindrique afin d'examiner les performances optiques. Les points d'accès optiques ont été conçus à 22,5°, 45° et 67,5° de l'illumination du volume laser. Les premiers tests ont été effectués en utilisant les fenêtres à 45° et 67° avec des particules de sphères creuses Lavision 10µm pour l'ensemencement. L'énergie laser nécessaire pour les caméras à 67.5° était importante dans cette expérience et le bruit de fond enregistré était élevé. Les images des particules étaient fluctuantes en taille et des clusters étaient observés partout sur les images. Pour cette raison, nous avons pensé qu'il valait la peine d'investir dans des particules de meilleure qualité.

La deuxième configuration a été testée en changeant la position des caméras à ±22,5° et ±45° de l'illumination du volume. De plus, nous avons utilisé différentes particules pour l'ensemencement provenant de Spherotech (PP-50-100) avec un diamètre moyen plus petit (5,09µm) et plus monodispersé (c'est-à-dire une fonction de densité de probabilité plus étroite). Ces nouvelles particules, à notre connaissance, n'étaient pas utilisées pour la PIV auparavant et elles ont montré une grande capacité à améliorer les mesures. De plus, et en raison des niveaux de bruit élevés observés auparavant liés aux petites impuretés de moins de 1-3 µm présentes dans l'eau, nous avons décidé d'utiliser un

système de filtration de l'eau installé dans la salle d'expérience pour réduire toute contamination de l'eau par la poussière ou les fibres plastiques des conteneurs utilisés pour le transport de l'eau. La qualité de l'eau est d'une grande importance et des précautions doivent être prises en compte lors de l'ouverture du couvercle de l'expérience.

La différence d'intensité visible sur les différentes caméras en raison de leur position dans les angles de diffusion avant est un paramètre expérimental qui ne pouvait pas être modifié. Ce phénomène est problématique car il diminue la qualité des résultats de la STB. Ce phénomène peut être atténué en fermant davantage l'ouverture des caméras qui reçoivent moins de lumière, mais cela augmente la taille de l'image des particules, ce qui peut également détériorer les résultats STB. La perspective offre quelques propositions/solutions à ce problème.

Sur la base de la qualité des images ainsi que des résultats STB de la deuxième configuration proposée comme solution de mesure optique dans le chapitre III, il a été décidé d'utiliser cette solution dans la campagne GVK. Pendant les mesures, nous avons observé des effets d'astigmatisme sur les 4 caméras, mais plus particulièrement sur les caméras aux angles de ±22,5°. Ceci pourrait être dû à des contraintes mécaniques appliquées sur les vitres d'accès de GVK, endommageant ainsi ses propriétés optiques. Pour cette raison, nous nous sommes retrouvés avec une solution "non désirée" consistant à augmenter le nombre de diaphragmes des caméras afin d'obtenir un meilleur compromis sur la taille des images de particules dans le volume complet. Cette modification augmente considérablement la taille des images de particules, ce qui rend plus difficile l'identification et le suivi des particules par STB, comme le montre le chapitre IV.

Malgré tous ces obstacles, une grande base de données STB dans GVK pour étudier sa turbulence a été générée au cours de ce doctorat. Pour les quatre fréquences de turbines étudiées (0.004, 0.01, 0.025 et 0.1 Hz) et les deux configurations contra et anti de GVK, 40 runs ont été enregistrés pour chacun de ces 8 cas avec une résolution spatiale STB d'environ $0.6\ mm$. Pour chaque cas, un total d'environ 30 échelles de temps intégrales est disponible pour la configuration 0.004Hz et environ 50 à 60 pour les autres.

Résumé des résultats de post traitement :

Les qualités des tracks ont été exploitées pour les données expérimentales et synthétiques. Nous commençons par une comparaison entre les résultats du STB pour la 1ère configuration et la 2ème configuration testée sur un réservoir d'eau similaire de GVK (SWT). Ensuite, nous avons testé l'algorithme STB sur des données synthétiques pour comprendre l'effet des différents paramètres ainsi que pour essayer de pousser la méthode à ses limites. Enfin, nous avons mené l'expérience GVK en nous basant sur les conclusions obtenues sur les tests SWT et synthétiques.

Tout d'abord, les particules achetées pour la deuxième configuration, ainsi que le changement de configuration des caméras, ont eu un impact massif sur la quantité et la qualité des tracks STB. Pour une concentration donnée de particules par pixel de 0,05ppp, nous avons pu suivre 80 000 particules de plus que lors de la première expérience réalisée sur SWT. De plus, la qualité globale des tracks et le niveau de bruit étaient bien meilleurs, même si la comparaison de différents essais peut être trompeuse dans le sens où les caractéristiques de l'écoulement peuvent affecter les résultats du STB et où la reproductibilité de l'expérience était faible. Pour cette raison, nous avons décidé d'étudier en profondeur l'effet de différents paramètres "expérimentaux" ainsi que les paramètres de traitement de la STB au moyen d'images synthétiques de PIV créées en utilisant des

traceurs lagrangiens intégrés à partir d'un DNS. Cette expérience synthétique simule en grande partie ce que nous avions testé auparavant sur SWT. Les résultats de la STB ont été comparés à la référence DNS avec une algorithme innovant basée non seulement sur les particules mais aussi sur les informations des tracks. Ces tests ont montré que :

1. La taille des particules est le facteur le plus important à régler autour de 2,4 pixels.
2. La différence d'intensité entre les images des caméras pose un problème au système de suivi et réduit considérablement la longueur des tracks. Cette différence d'intensité entre les caméras doit être aussi faible que possible.
3. Le STB a une très forte limitation de la densité des particules de l'image pour une taille moyenne donnée de l'image des particules. Par exemple, il est montré que 0.05ppp semblait un peu trop pour la valeur de la taille des particules que nous avions d'environ 3.8 pixels en moyenne.

De plus, ces tests ont montré que, même pour de très bonnes cartes « Optical Transfer Functions - OTF » et de disparité, les tracks sont fragmentées, la longueur des tracks est parfois surestimée, et les 15 à 20 premiers pas de temps présentent des valeurs d'erreur plus élevées que le reste des pas de temps. Ces résultats suggèrent que le premier morceau d'une track devrait être éliminé du post-traitement si l'on veut réduire le bruit dans les données.

Toutes les informations collectées ont été appliquées à l'expérience GVK, les résultats STB ont montré une légère diminution de la qualité par rapport à nos tests sur SWT en raison des problèmes expérimentaux rencontrés que nous avons décrits précédemment. Notamment l'augmentation de la taille des particules pour limiter le problème d'astigmatisme ainsi que l'augmentation du rapport d'intensité entre les images des différentes caméras. Nous avons également montré que l'utilisation d'un filtre médian est utile pour supprimer les tracks fantômes, mais qu'il affecte drastiquement la longueur des tracks même. Ce paramètre doit être utilisé avec précaution et avec des tests prolongés avant de décider du meilleur ensemble de paramètres pour chaque exécution.

Enfin, nous avons fait une comparaison entre la version Trackfit de Lavision et la version Trackfit créée au sein de laboratoire LMFL. Les différents paramètres du logiciel pouvaient être contrôlés par l'utilisateur pour maximiser la qualité des traces ainsi que le spectre spatial des vitesses contrairement à la boîte noire Trackfit de Lavision. Pour cette raison, Trackfit de Cheminet et al 2021 conduit à de meilleurs résultats en termes de résolutions temporelles et spatiales et il est essentiel d'aller plus loin dans l'analyse de la turbulence car nous sommes capables de contrôler les propriétés du filtre.

To my mother Nada and all my family.

Acknowledgments

First of all, I would like to acknowledge the support of EXPLOIT ANR who funded this project, and the direction of the LMFL who allowed me to use their premises. These four years of thesis were marked by moments of inspiration and other moments of doubts. I am grateful for my supervisors who helped through moments of doubts and inspired this thesis work. Thank you, Jean Marc, for always being there when I needed a support. Your sense of analysis, experience, and your ability to listen guided me and made progress throughout my thesis. Thank you, Jean Philippe, for the endless support and for always being there when I could not see the light at the end of the tunnel. This thesis will not be possible without you. Thank you, Christophe, I think I won't be exaggerating if I said that you and Jean Marc together are one of the best teams who does PIV in Europe. I learned a lot of your work ethics and I am proud to be your first supervised PhD student. I want to say thank you as well to one of the nicest people that I have worked with, Adam Cheminet, you may not be an official supervisor of mine, but this thesis won't be possible without you too. Also, thanks to Yasar who left the team a year ago.

Special thanks to all the CEA Saclay team. I had an absolute pleasure to know, Bérengère Dubrulle one of the greatest theoretical physicists alive. Also, to know François, Cécile, Damien, and Hugues. You made me feel at home when I was on a mission in Saclay.

I can't not to mention my colleagues, my brothers Hussein, Rakesh, Nathaniel, Florian, Sarp, Paul, Argyris, Felipe and many others. Likewise, my friends outside work: Theodore, Ayman, Mohammad, Mahdi, Narimane Nicolas, Frederique and many others. You helped me to find a good balance between work and other aspects of life.

Finally, the last piece of the puzzle that complete this picture is my close family. This thesis is specially dedicated to my mother Nada who always dreamt about me becoming a doctor. I won't be standing in this position without your constant support. I love you and wish you good health. Thanks to my father Jamal who was like a friend that I could talk to him about anything. Thank you to all my sisters and brother: Omar, Ghina (my lovely little sister), Rania and Bassma. Also, I would like to take this opportunity to thank my "new" brothers, my brothers in law: Ahmad, Tarek and Imad.

List of figures

List of tables

Contents

Chapter I Introduction

Contents

I.1 Why turbulence flows are interesting to study?

Naturally, flows can be in two different states: laminar and turbulent. Laminar flow is when fluid particles move in the same direction. This is the case of very viscous fluids like oil or flows in microscopic pipes. On the other hand, turbulence is chaotic and undergoes irregular fluctuations. Turbulent flows can be found in flowing rivers, the atmospheric and oceanic flows, pipelines transportation, flow around vehicles, and many other practical engineering applications. They are also essential for the formation of rain drops, so a one might say it is vital for all life forms on earth.

Despite the fact that turbulence occurs regularly in nature and in a variety of scientific fields, we still don't have a complete understanding of the associated physics. This does not mean that nothing has been done in the last four decades. On the contrary, our understanding of turbulence phenomenology has improved dramatically. New experimental techniques have been developed that allow us to measure aspects of turbulence that were previously thought to be impossible to observe. New experimental facilities were built, allowing us to better reproduce turbulence on realistic large-scale problems.

Turbulent flows have multiple characteristic: **The first characteristic** is that it is unpredictable, it is chaotic and therefore very sensitive to the initial conditions. It is very difficult to predict the exact state of turbulent flows over a long time, but one can expect to predict its statistics though. Flows can be modeled by the famous Navier-Stokes equations that describe most of the fluid flows, but they are notoriously difficult to solve. Actually, there is a 1M$ award for the one who is able to solve these equations. **The second characteristic** of turbulent flow is that it is very dissipative compared to laminar flows. It takes in energy at the largest scales from big eddies, then this energy is transferred to the smallest scales where it is dissipated as heat.

I.2 Turbulence basic information

An important physical equation of any flow is the Navier Stokes equations named after French physicist Claude-Louis Navier and English physicist George Gabriel Stokes. The Navier–Stokes equations mathematically express conservation of momentum and conservation of mass for Newtonian fluids. For low Mach numbers, the incompressible Navier-Stokes equations are:

$$\begin{cases} \partial_t \boldsymbol{u} + (\boldsymbol{u}.\nabla)\boldsymbol{u} = -\frac{1}{\rho}\boldsymbol{\nabla} p + \nu \Delta \boldsymbol{u} \\ \nabla.\boldsymbol{u} = 0 \end{cases} \qquad \textit{(I-1)}$$

where ρ is the constant density of the fluid, p is the pressure and $\boldsymbol{u}$ is the velocity vector, representing the three components of the velocity field and ν is the kinematic viscosity (m^2/s). A Poisson equation for the pressure can be obtained by taking the divergence of the momentum equation and using the continuity equation:

$$\Delta p = -\rho \, div\big((\boldsymbol{u}.\boldsymbol{\nabla})\boldsymbol{u}\big) \qquad \textit{(I-2)}$$

Solving the Poisson's equation leads to choosing a numerical method to invert a Laplacian. As the momentum and Poisson's equation cannot be solved implicitly, an iterative method is usually used to solve alternatively each of the two equations up to convergence.

I.2.1 Different regimes of a fluid flow

Osborne Reynolds studied fluid flow regimes in 1883 (Reynolds, 1883). He observed that the inertial effects, or entrainment by the fluid around an object, are dominant over the dissipative viscous effects, and that the fluid can at least absorb the fluctuations and instabilities that may appear in the velocity field. He created a dimensionless number, which bears his name today, and used it to describe different regimes of a flow. Mathematically speaking, the NS equations were rewrote using dimensionless (noted *) variables. The dimensionless NS equations becomes:

$$\partial_{t^*}\,\boldsymbol{u}^* + (\boldsymbol{u}^*.\nabla^*)\boldsymbol{u}^* = -\boldsymbol{\nabla}^* p^* + \frac{\nu}{LU}\Delta^*\boldsymbol{u}^* \qquad (I\text{-}3)$$

Where L and U are respectively some characteristic length and velocity of the problem. In this form, the equation displays a dimensionless number used to predict the behavior of a fluid in a system. This number is the so-called Reynolds number:

$$Re = \frac{inertial\ forces}{viscous\ forces} = \frac{LU}{\nu} \qquad (I\text{-}4)$$

If the Reynolds is low, the flow is *"Laminar"*. By increasing the forcing, the inertial forces will become more and more important, instabilities will appear, until the flow becomes completely chaotic leading to the name *"turbulence"*, originating from the Latin *"turba"* meaning disorder. Such flow is commonly seen in ocean currents, the flow in boat wakes and around aircraft-wing tips.

I.2.2 The Richardson's cascade

Richardson predicted qualitatively that turbulence is actually a cascade of energy transfer from large structures to smaller ones (Richardson and Lynch, 1922) until the energy can be dissipated by viscosity. He described his observations in his famous poem:

> *Big whorls have little whorls*
> *that feed on their velocity, and little whorls*
> *have smaller whorls and so on to viscosity - in the molecular sense*

In other words, there is a hierarchy of different vortices with different scales that extend from large to small scales.

The nonlinear term of Navier-Stokes equations conserves the kinetic energy, and the viscous term on the right hand side of equation (I-1) is responsible to dissipate it into heat.

Figure I.1 depicts this hierarchy, in which energy from the large-scale flow is injected at a rate of ϵ into eddies at the integral scale L. These large eddies break up into smaller eddies, which break up even more until the turbulent energy is dissipated as heat by molecular viscosity. Statistics are flow dependent above the integral scale. However, statistics are supposed to be universal in the inertial and dissipation ranges, regardless of how turbulence is generated.

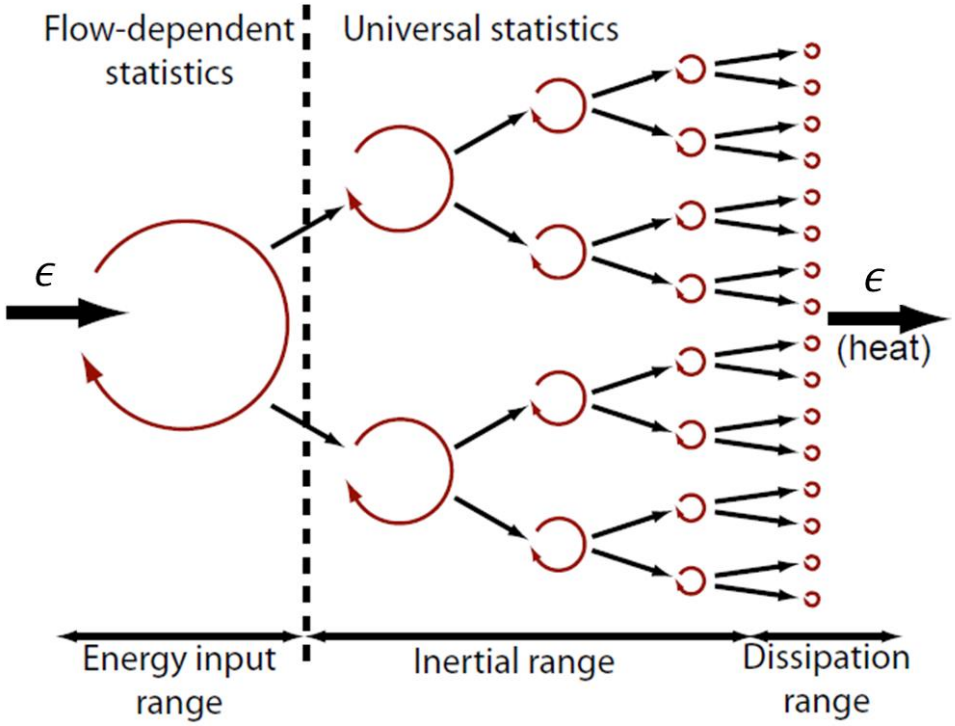

Figure I.1 The Richardson cascade (Extracted from (George, 2013))

I.2.3 Kolmogorov scaling

In 1941, Kolmogorov, 1941 found quantitative expressions for the intensity of fluid motions at scale ℓ and for the dissipation scale ℓ_d. Furthermore, at scales much smaller than ℓ_I (the injection scale) the flow can be considered homogeneous. Turbulence is thus characterized by three parameters: the injection scale ℓ_I, the injection velocity u_I and the viscosity of the fluid ν. These parameters have dimensions $[\ell_I] = L$, $[u_I] = LT^{-1}$ and $[\nu] = LT^{-2}$.

The first hypothesis of Kolmogorov is that dissipation is independent of the viscosity, thus the only combination of u_I and ℓ_I with a correct dimension is u_I^3/ℓ_I. This gives the following expression of the dissipation rate:

$$\epsilon \sim \frac{u_I^3}{\ell_I} \qquad (I\text{-}5)$$

The second and third hypothesis are that $\delta u(\ell)$ $\left(\delta u(\ell) = u(x+\ell) - u(x)\right)$ does not depend on ν for $\ell_d < \ell < \ell_I$, and $\delta u(\ell)$ is function only of the dissipation rate and ℓ

$$\delta u(\ell) \sim (\epsilon \ell)^{1/3} \tag{I-6}$$

Using equations (I-5), (I-6) can be written as:

$$\delta u(\ell) \sim u_I \left(\frac{\ell}{\ell_I}\right)^{1/3} \tag{I-7}$$

Then we can compute the Reynolds number associated with motions at scale ℓ as:

$$Re_\ell \sim \frac{\delta u(\ell)\ell}{\nu} = \frac{\epsilon^{1/3}\ell^{4/3}}{\nu} \tag{I-8}$$

Viscous dissipation will take place at scales ℓ_d such that $Re_{\ell_d} \approx 1$. This scale is what will be called this point forward the Kolmogorov scale η:

$$\eta \sim \left(\frac{\nu^3}{\epsilon}\right)^{1/4}, \quad t_\eta = \left(\frac{\nu}{\epsilon}\right)^{1/2}, \quad u_\eta = (\nu\epsilon)^{1/4} \tag{I-9}$$

where t_η and u_η are respectively the time and velocities associated to Kolmogorov scale. A last hypothesis that we wish to recall for the understanding of the cascade in the sense of Kolmogorov, is when the Reynolds is sufficiently large, there is an intermediate range of scales between the large scales and the dissipative scales for which the dynamics is driven only by the rate of energy injection/dissipation ϵ and independent of the viscous effects driven by ν . This range is called the inertial range (George, 2013)

Finally, let us note that the link between the injection rate of kinetic energy at large scales and the rate of dissipation by small scales implies the possibility of defining the Kolmogorov scales from large scales:

$$\eta \sim \frac{\ell_I}{Re_L^{3/4}}, \quad t_\eta = \frac{\ell_I}{u_I . Re_L^{1/2}}, \quad u_\eta = \frac{u_I}{Re_L^{1/4}} \tag{I-10}$$

Where $\ell_I, \ell_I/u_I$ and u_I are related to large scales and the Re_L represents here the Reynold's number associated to the biggest turbulent structures of the flow.

I.3 Turbulence and singularities

Starting from Kolmogorov theory we will follow the path opened by George Batchelor to discover possible pitfalls of Kolmogorov, 1941 to see how they are linked to intermittency. This will lead us to a modern description of small scales structures.

Intermittency in a nutshell is the variation in time and space of the dissipation rate ϵ. When it is the cascade rate that fluctuates at inertial scales, one talks about "inertial intermittency". Connection between possible singularities of NSE and local interscale energy transfer and dissipation are explained to understand why dissipation contributes to intermittency.

I.3.1 Kolmogorov theory in a nutshell (1941)

Kolmogorov theory is based on symmetries of NS equations. Then, using the hypothesis of homogeneity, one can derive the Karman-Howarth equations as follow:

$$\frac{1}{2}\partial_t\langle(\delta u_\ell)^2\rangle + \epsilon = -\frac{1}{4}\nabla_\ell\langle(\delta u_\ell)^3\rangle + \nu\Delta_\ell\langle(\delta u_\ell)^2\rangle \qquad \textit{(I-11)}$$

- $\delta u(\ell) = u(x+\ell) - u(x)$ is the increment of velocity at scale ℓ.
- ϵ is the quantity of energy injected in the system.
- $\nu\Delta_\ell\langle(\delta u_\ell)^2\rangle$ is the diffusion due to viscosity.
- $\frac{1}{4}\nabla_\ell\langle(\delta u_\ell)^3\rangle$ is energy transfer (flux) that describe how energy flow from large eddies to small eddies.

This equation was derived by Karman-Howarth using only homogeneity assumption. Then Kolmogorov introduced the famous 4/3 law by taking the equation (I-11) and adding the assumption of self-similarity and stationarity. He described that it exists an inertial range where the viscosity effects are negligible. This leads to:

$$\frac{4}{3}\epsilon\ell \propto \langle(\delta u_\ell)^3\rangle \qquad \textit{(I-12)}$$

Self-similarity means that the divergence term is equal to ϵ in the inertial range so the second order moment should be scaled as the third order moment. Using a self-similarity hypothesis and the equation (I-12) one obtains:

$$\langle(\delta u_\ell)^2\rangle \propto (\epsilon\ell)^{2/3} \qquad \textit{(I-13)}$$

Then by simple Fourier transform one can obtain the famous Kolmogorov spectrum:

$$E(k) = C\epsilon^{2/3}k^{-5/3} \qquad \textit{(I-14)}$$

where C is the Kolmogorov constant.

When Batchelor and Townsend, 1949 learned about the theory of K41, they were impressed by it. They investigated the limitations of this theory and its behavior at small scales in the Kolmogorov picture (in other words they investigated how the spectrum is terminated at high frequencies). In their paper, they concluded that "*there appear to be isolated regions in which the large wave numbers, i.e. small scales, are activated separated by regions of comparative quiescence. This spatial inhomogeneity becomes*

more marked with increase in the order of velocity derivative, i.e at small scales.". This inhomogeneity they talked about is what today we call intermittency.

I.3.2 Oppositions to Kolmogorov theory - Batchelor & Landau (1953)

Early experimental evidence aided the K41's theory initial success (Batchelor, 1953). However, as previously stated, the experiments later revealed some flaws in the theory, particularly in relation to small-scale intermittency.

Batchelor objection:

As he was looking at higher and higher frequency of a turbulent flow using hot wire measurements, he saw that velocity is very intermittent meaning that it cannot be self-similar.

Landeau objection:

Landeau observed that the energy dissipation is highly inhomogeneous, so turbulence cannot be self-similar. These objections were confirmed by looking at the velocity structure function later in 1990s.

According to Kolmogorov, if the structure function is self-similar then it should scale as:

$$S_p(\ell) = (\delta u)^P > \sim \ell^{P/3} \qquad \textit{(I-15)}$$

But recent observations identify a potential problem in this hypothesis by recording deviation from self-similarity. In the Figure I.2, we present structure functions at small scales. Indeed, they follow a power law, but the exponent of the plots of the left figure deviates from the $P/3$ law (see right figure). This was also observed in DNS and it indicates that the K41 is not always valid.

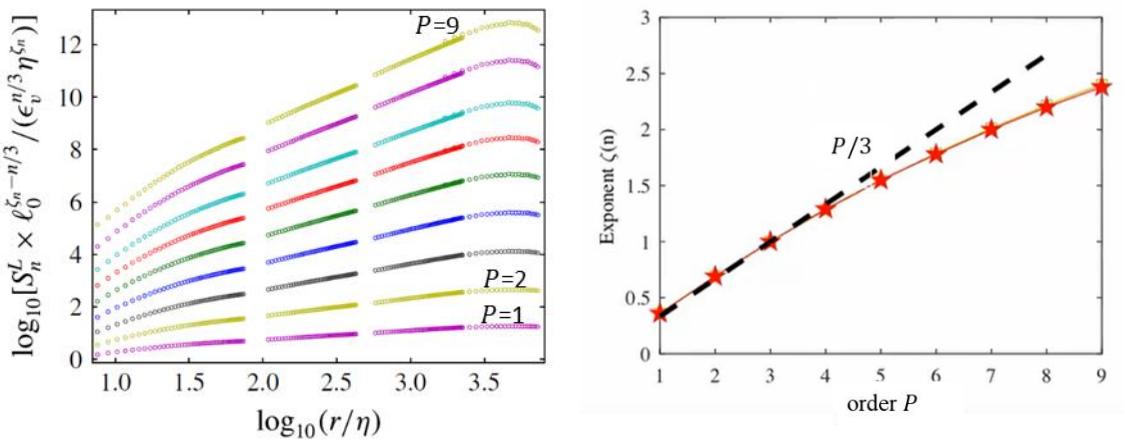

Figure I.2 (Left) Structure functions at different scales. (Right) The corresponding exponent of the plots (Figures extracted from (Saw et al., 2018)).

I.3.3 Kolmogorov refinement of previous hypothesis (1962)

At this point, it is established that the Kolmogorov theory fails at small scales. For this reason, Kolmogorov himself corrected his model (Kolmogorov, 1962a) by assuming that dissipation is not homogeneous as it was stated in equation (I-11). Instead, the dissipation is local to each scale ϵ_ℓ. In that way the velocity structure functions become:

$$S_p(\ell) \sim \langle \epsilon_\ell^{p/3} \rangle \, \ell^{p/3} \tag{I-16}$$

And he introduced a correction term that depends on the statistical properties of ϵ:

$$S_p(\ell) \sim \ell^{\tau(p/3)+p/3} \tag{I-17}$$

Additionally, Kolmogorov made a second assumption that the local dissipation has a log normal distribution:

$$\overline{\ln(\epsilon_\ell)} = \ln \epsilon + \mu_{k62} \ln(\ln(\ell/L) + A \tag{I-18}$$

where μ_{K62} is a constant. This was a very strong assumption made by Kolmogorov, but his prediction was very good and validated by DNS. But still, the main failure of Kolmogorov model was that the local dissipation was not derived directly from Navier Stokes equations (NSE).

I.3.4 Parisi and Frisch (1995)

The first attempt to derive the local dissipation from NSE was in 1995 by Parisi and Frisch, 1995 where they indirectly derive the local dissipation from NSE using the multifractal model. They observed that there is a fundamental symmetry in NSE $\left((t, \boldsymbol{x}, \boldsymbol{u}) \; to \; (\lambda^{1-h} \, t, \lambda \boldsymbol{x}, \lambda^h \, \boldsymbol{u})\right)$, for arbitrary λ and Holder exponent h. They introduced the function $C(h)$ which is a codimension of the places where the velocity increment scales like ℓ^h. Then they postulate that the exponent of the velocity structure function should be as follow:

$$\xi(n) = min_h\left(nh + C(h)\right) \tag{I-19}$$

By this method, all the properties of the intermittency should be encoded in the function $C(h)$ the multifractal spectrum. An example of this spectrum is shown in the Figure I.3 (right) where the minimum is close to a value of h of 1/3.

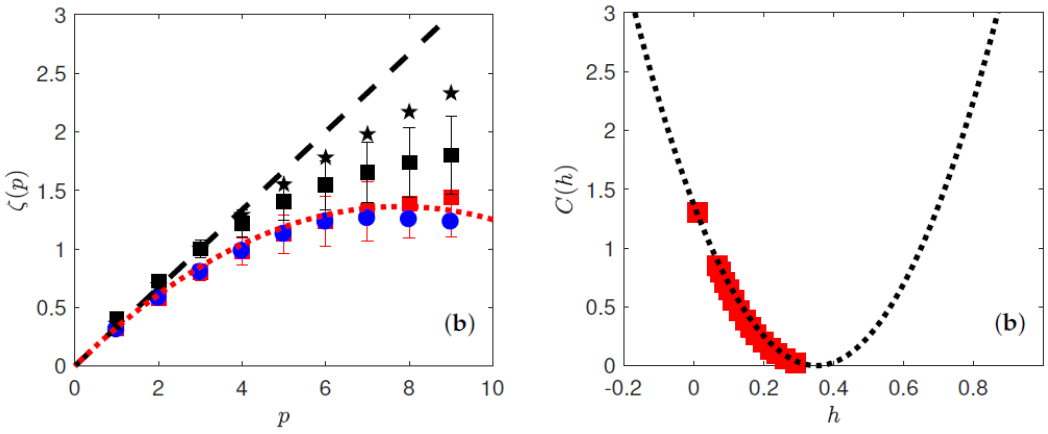

Figure I.3 (Left) Scaling exponents $\zeta(p)$ of the wavelet structure functions as a function of the order. (Right) Multifractal spectrum C(h) for Von Karman swirling flow. The spectrum is obtained from the scaling exponents $\zeta(p)$ shown in the figure to the left. The dotted line is a parabolic fit $C(h) = \frac{(h-a)^2}{2b}$ (Figures extracted from (Geneste et al., 2019)).

I.3.5 Modern view of this problem

The work of (Duchon and Robert, 1999) generalizes the Karman-Howarth equation to anisotropic, nonhomogeneous flows and they proposed a local energy budget considering a possible non-regularity of the velocity field:

$$\frac{1}{2}\partial_t \boldsymbol{u}^2 + \mathrm{div}\left(u\left(\frac{1}{2}\boldsymbol{u}^2 + p\right)\right) = D(\boldsymbol{u}) - \nu(\nabla \boldsymbol{u})^2 \qquad \textit{(I-20)}$$

Compared to the classical NSE, there is a new term called the Duchon-Robert term $D(\boldsymbol{u})$. This term comes from the possibility of having singularities in the flow. In practical, they introduced a smoothing of the velocity field at scale ℓ and they obtained the smoothed NSE with the Duchon Robert term $D(\boldsymbol{u})$:

$$D(\boldsymbol{u}) = \lim_{\ell \to 0} \frac{1}{4} \int_{r \leq \ell} \nabla \varphi_\ell \, (r) \; \delta \boldsymbol{u}_r |\delta \boldsymbol{u}_r|^2 dr^3 \qquad \textit{(I-21)}$$

where φ_ℓ is a smoothing function convoluted with the velocity field $\boldsymbol{u}$ to obtain the smoothed velocity field. This term provides a new criterion to look for possible singularities.

The work by Duchon and Robert supports the idea that a singularity would generate additional dissipation due to the lack of regularity of the velocity field. This technique allows a spatial localization of the singularity. Kuzzay 2015b showed that such technique allows detection of possible singularities using Stereoscopic PIV velocity measurements.

I.4 EXPLOIT project

In the cascade picture of turbulence, energy dissipation is due to viscous effects that become significant at scales which are small enough. However, very little is known about the dynamics and statistics of the corresponding dissipative structures. Further, the connection between structures and turbulent scales dynamic has largely focused on rotation-dominated flows and relied upon data from numerical simulations only. This is mainly because experimental studies of the dissipation have long faced technical barriers since direct estimate of the viscous dissipation $\epsilon = \nu\overline{(\partial_j u_i')^2}$ requires resolutions down to the Kolmogorov scale. Local probes such as hot wires can achieve this resolution but require a complex array arrangement to allow for estimation of velocity gradient. Particle Image Velocimetry (PIV) allows for a simple computation of velocity gradients, but the Kolmogorov resolution is only achieved for Reynolds of the order of 10^4 (Delafosse et al., 2011) and not all the terms can be obtained for planar PIV measurements (Foucaut et al., 2021). Additionally, in the past, most detection of the smallest turbulent structures have been done using techniques based either on the vorticity monitoring in numerical simulations, or on statistical analysis of 1D velocity signal. The vorticity monitoring requires an access to the 3 components of the velocity at the dissipative scale. Due to the inherent limitations, this has been achieved in the fully turbulent regime mainly in numerical simulations with special geometries, such as fully periodic flow with high degree of symmetry. Therefore, the experiment requires using 3D-PIV with precision down to dissipative scale and even below the Kolmogorov scale if possible.

The originality of the EXPLOIT project is to make a high-resolution PIV measurement on a big Von Karman flow experiment. This big experiment allows us to reach high Reynolds number without decreasing too much the Kolmogorov scale. The data will be used to detect the dissipation structures down to the Kolmogorov scale and beyond and to study the dissipation, not only from the point of view of the viscous contribution, but also to locate quasi-singularities and estimate their contribution to the dissipation.

I.4.1 Von Karman flow

The flow between two counter-rotating impellers enclosed by a cylinder is often used for studying fundamental aspects of turbulence specially to study the turbulence characteristics on different scales. This flow is generated in the so called Von Kármán tank (Kármán, 1921). In the central region of this tank, quasi-isotropic, homogeneous turbulence with relatively large Reynolds is created. Such conditions are similar to homogeneous isotropic turbulence, which the configuration of many DNS studies (Faller et al., 2021), and thus are suitable for fundamental turbulence research. The impellers can rotate in a variety of modes, linked to different forcing mechanisms. This flow allows us to achieve high Re_λ[1]. The Von Karman flow encounters successive cascades of bifurcations towards a turbulent flow (Ravelet, 2005). As seen on the Figure I.4, bifurcation occurs when the average velocity field changes to a state with just one rotating cell imposing its direction. The flow is said to split (bifurcated) when symmetry is broken.

[1] The Taylor microscale is the intermediate length scale at which fluid viscosity significantly affects the dynamics of turbulent eddies in the flow. $Re_\lambda = \overline{u}'\lambda/\nu$. λ is the Taylor microscale.

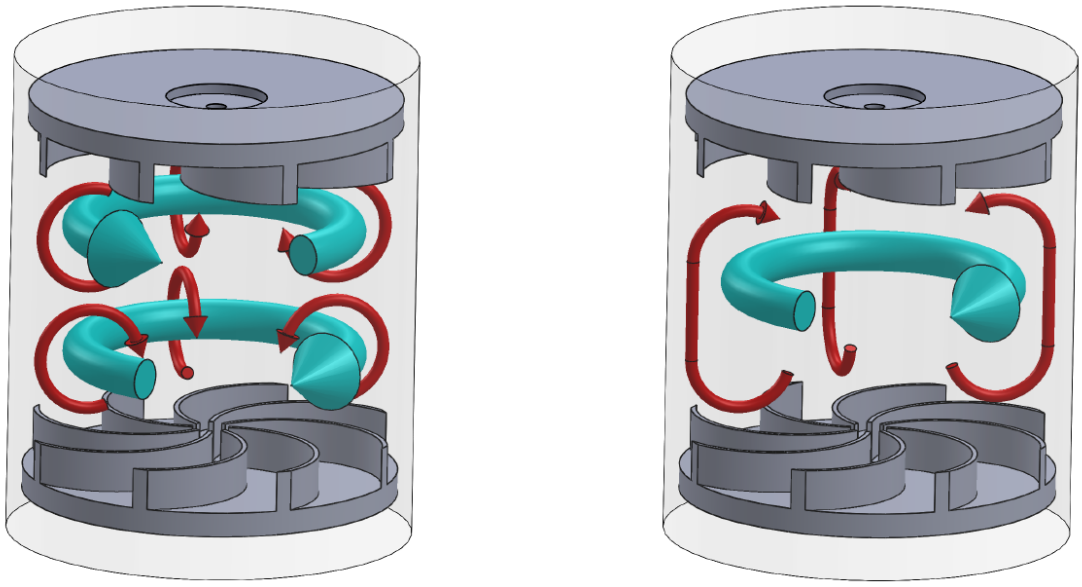

Figure I.4 Schematic of the average flow in von Karman experiment. (a) "Anti" direction, symmetrical flow. (b) "Anti" direction, bifurcated flow (bottom impeller imposing its direction). The blue arrows correspond to the toroidal components and the red arrows to the poloidal components (Figure extracted from (Debue, 2019)).

We distinguish between the positive direction of rotation, called "Contra", when the convex side of the impellers pushes the fluid, and the negative direction, called "Anti", when it is the concave side of the impellers which pushes the fluid. The Figure I.5 depicts the impeller geometry of the experiment we are doing in this thesis.

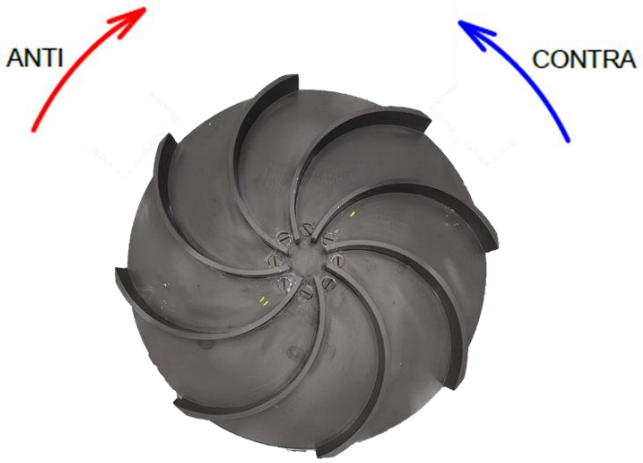

Figure I.5 The geometry of an impeller that show the two cases of forcing depending on the rotation direction.

I.4.2 Advantages of using Von Kármán flow

First, the Von Karman flow have been widely studied, both experimentally and numerically, therefore we have a good knowledge of its physical properties. On the other hand, we seek to measure a small region at the center of the Von Karman experiment. This will allow us to consider that the flow is almost isotropic and homogeneous. In

decaying homogeneous isotropic turbulence, the variables K (kinetic energy) and ϵ are functions of time alone and are quite simply related to each other ($dK/dt = -\epsilon$). Kuzzay et al., 2015a showed that most of the dissipation happens at the center of the cylinder.

Finally, this setup is well suited for multi-scale turbulence analysis due to the simplicity with which the Reynolds number can be varied by manipulating either the impeller rotation frequency or the fluid viscosity.

I.4.3 Small experiment VK2 (previous work)

The study of Von Karman flows in Saclay started with a smaller experiment. The VK2 set-up, displayed on Figure I.6, is constituted of a vertical Plexiglas cylinder. Its radius is 10 cm, and its height is 47 cm, its thickness is 1 cm, and it can be filled with glycerol, water, or a mixing of both. This cylindrical tank is placed inside another outer tank of 1 cm thickness, filled with the same fluid as the cylindrical tank. The addition of this outer tank aims at decreasing aberrations which occur at the interface air-Plexiglass when using optical measurement systems. This setup was used during the thesis of Debue, 2019.

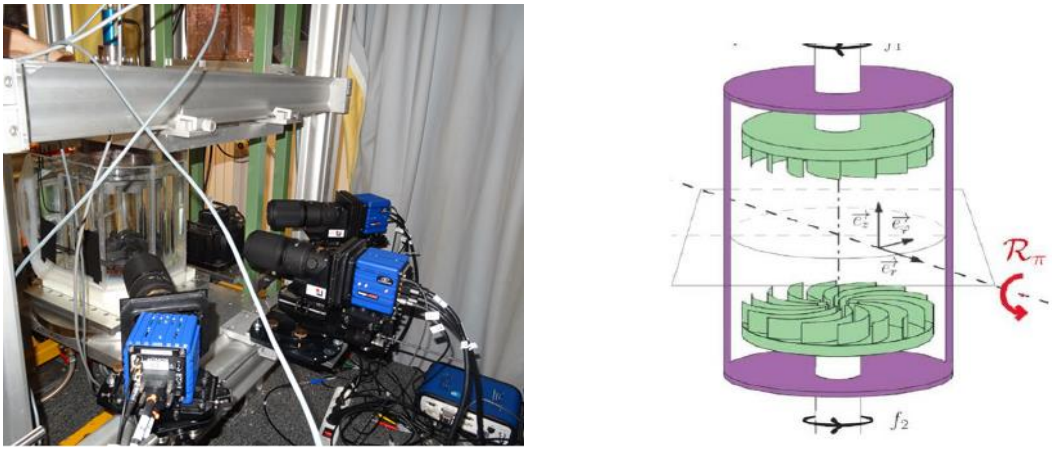

Figure I.6 (Left) Photograph of the VK2 setup. (Right) Perspective view of the considered von Karman flow

In his thesis work, Tomographic-PIV was used to measure the 3D components of the flow field at the center of the Von Karman flow.

In the Table I-1 we present the Reynolds achieved; these values shown here are calculated based on the cylinder radius R, the impeller revolution per second F and the fluid kinematic viscosity ν as follows:

$$Re = \frac{\omega R^2}{\nu} = \frac{2\pi R^2 F}{\nu} \qquad (I\text{-}22)$$

Also, we included the associated Kolmogorov length scale and the ratio of this scale to the Tomo-PIV resolution (Δ_x^{tomo}). The resolution achieved using TomoPIV was still not enough to resolve one Kolmogorov scale.

Table I-1:Kolmogorov scale in the von Kármán flow for ***R=10 cm (VK2 set-up)*** *at different Reynolds numbers and the associated spatial resolution in the Kolmogorov scale (Δ_x^{tomo} =2mm, i.e. size of interrogation volume for an image density of 0.05 ppp). The Taylor-scale Reynolds number is useful to compare the level of turbulence in a von Kármán flow and in a direct numerical simulation (DNS) of homogeneous isotropic turbulence.*

Re	Re_λ	η	$\frac{\eta}{\Delta_x^{tomo}}$
6.3×10^3	110	$0.39\ mm$	0.19
3.1×10^4	240	$0.11\ mm$	0.05
6.3×10^4	340	$0.07\ mm$	0.03
3.1×10^5	780	$0.021\ mm$	0.01
1.6×10^6	1700	$0.0064\ mm$	0.003

I.4.4 Bigger experiment – GVK

The aim of the EXPLOIT project is to build a bigger experiment for multiple reasons. As mentioned before in a previous work of Debue, 2019 on the VK2 setup (Figure I.6), he showed that there is very intense events of inter-scale transfer even in the beginning of the dissipative range (Dubrulle, 2019). This suggests that the Kolmogorov scale is not the smallest scale in a turbulent flow. In order to confirm these results, measurements in the far dissipative range should be done. This could be achieved by improving the spatial resolution of PIV system. However, due to PIV limitations, spatial resolution cannot be increased linearly by increasing the number of particles. This leads us the main goal of designing the "Grand von Karman" set up (GVK) in order to increase the size of the Kolmogorov scales for the equivalent Reynolds numbers. This way the GVK will mainly act as a magnifying lens to look more in depth to rare dissipative events.
In other words, the resolution of the optical system should be smaller than the Kolmogorov scale. For the VK2, the Tomo-PIV resolution Δ_x^{tomo} was about $2mm$ almost 5 times the estimated Kolmogorov scale for Re of 6.3×10^3 ($\eta = 0.39\ mm$). This is clearly not enough to investigate what happens at the Kolmogorov scale and beyond.
Increasing the cylinder radius by a factor of 5 compared to the VK2 set-up is enough to obtain a resolution smaller than the Kolmogorov scale, but one could be tempted to increase it even more. Nevertheless, we chose to limit to a factor 5 for practical issues. As the spatial resolution of Tomo-PIV was shown to be limited and practically difficult to improve, we decided to use particle tracking technique. In theory, the resolution defined by the mean particle spacing could be 3 times better since we don't use cross correlation methods in a volume (particles are tracked individually) and cross correlation need between 10 to 20 particles inside the volume (Adrian, 1997). In this thesis 4D velocity tracks (3 velocity components as function of time measured in the volume) are obtained by PTV in a real turbulent flow in order to provide more insight into the possible singularities that might occur in the solutions to the 3D incompressible Navier-Stokes equations.

In Table I-2, we show the difference in expected spatial resolution capabilities between Tomo-PIV and 4D-PTV applied to the GVK. The table show that we are able to solve one Kolmogorov length scale using Tomo-PIV at the lowest Reynolds. On the other hand, 4D-PTV can solve up to 0.7η for a Reynold number of the order of 6.3×10^4. We should keep in mind that the resolution for both Tomo-PIV and 4D-PTV are for images with the same number of particles per pixels. Tomo-PIV uses typical correlation methods with windows that include 10 to 20 particles. On the other hand, 4D-PTV track individually every particle in the volume. This is the reason why the Tomo-PIV resolution is estimated to be 3 times less Debue, 2019 than the PTV resolution.

Table I-2:Kolmogorov scale in the von Kármán flow for ***R=50 cm (GVK set-up)*** *at different Reynolds numbers and the highest achieved spatial resolution for both Tomo PIV and PTV ($\Delta_x^{tomo} = 2mm$ and $\Delta_x^{PTV} = 0.5mm$ for an image density of 0.05 ppp and for same field of view). The Taylor-scale Reynolds number is useful to compare the level of turbulence in a von Kármán flow and in a direct numerical simulation (DNS) of homogeneous isotropic turbulence.*

Re	Re_λ	η	$\frac{\eta}{\Delta_x^{tomo}}$	$\frac{\eta}{\Delta_x^{PTV}}$
6.3×10^3	493	$2\ mm$	1	4
3.1×10^4	1200	$0.59\ mm$	0.295	1.2
6.3×10^4	1500	$0.35\ mm$	0.175	0.7
3.1×10^5	3500	$0.1\ mm$	0.05	0.2
1.6×10^6	7700	$0.031\ mm$	0.0155	0.06

Chapter II Optical metrology for turbulence measurement

Contents

II.1 The evolution of turbulence measurement techniques

Leonardo da Vinci was probably the first who did a visualization of turbulent flows Figure II.1 (top). The fact that the patterns were stable and repeatable struck Leonardo as evidence that the flow was not chaotic but subject to physical laws, and he attempted to frame such principles in notes. The ability to store pictures or even movies of flows using photographic recording techniques was a major breakthrough in qualitative flow visualization in the late 19th and early 20th centuries. Figure II.1 (bottom) shows Prandtl in front of his water channel in 1904, manually controlling the flow with a paddle wheel. The box camera above the channel was most likely used to capture single frame time-lapse photographs. Prandtl discovered a number of fundamental characteristics of unsteady flow phenomena. However, only photographic recording of the flow field visible through the tracers was possible at the time. There was no way to get quantitative data on such unsteady flow phenomena.

Figure II.1 (Top) Sketch of the turbulent water motion by Leonardo da Vinci (Codex Atlanticus), showing the unsteady eddy motions. (Bottom) Ludwig Prandtl with his fluid test channel, 1904.

Today, a century after Prandtl's experiments, it's simpler to extract quantitative information about the instantaneous flow velocity field from the same types of images that Prandtl had access to in 1904.

We begin with Taylor, 1935 analysis in his book “Statistical Theory of Turbulence”. Taylor measured the distribution of energy in a pipe over its cross section with a series of hot-wires. Direct estimation of the viscous dissipation, $\epsilon = \nu\overline{(\partial_j u_i')^2}$, requires resolutions down to the Kolmogorov scale. Local probes, such as hot-wires, can attain this resolution but require a complex array configuration to compute velocity gradients. Indirect measurement techniques such as hot-wire have the advantage of being simple to use and relatively low cost. They have the problem of disrupting the flow or fluid characteristics, which can lead to measurement mistakes (Raffel et al., 2018). Optical measurement techniques have been developed to overcome these limitations by allowing sensors to be placed outside of the flow. These techniques were previously restricted to point-wise velocity measurements, such as Laser Doppler Velocimetry (LDV), the first optical measuring technique. It requires tracer particles that faithfully follow the flow motion. A first laser Doppler device was provided by (Yeh and Cummins, 1964). Twenty years later, the term "Particle Image Velocimetry" (PIV) had its first appearance in the literature (Pickering and Halliwell, 1984).

PIV piqued the interest of many researchers since it provided a novel and promising method of examining the structure of turbulent flows. This purpose influenced the method development decisions significantly. Turbulence is a natural phenomenon that happens on a wide range of physical scales, from the largest scales of the flow down to the Kolmogorov scale. As a result, an effective measurement technique must be capable of measuring throughout a wide dynamic range of length and velocity scales. With the development of PIV, it became possible to measure two components of velocity to confirm Kolmogorov's $-5/3$ law prediction (Kolmogorov, 1962b, Ullum et al., 1998). However, the flows that exists in nature are three dimensional. PIV has been quickly extended to the measurement of 3D components of the velocity because of its capability to capture the instantaneous flow organization, also known as coherent structures, observed in turbulent flows. Current existing techniques of three-dimensional velocimetry, using illumination by laser, can be divided into three main families according to (Raffel et al., 2018):

- (0D-1,2 or 3C): the point wise velocity measurement techniques.
- (2D): Two dimensional methods:
    - (2D-2C): the two components velocity measurement using one camera in a plan.
    - (2D-3C): the two-dimensional methods which allows the measurement of the three components of the velocity in a plane. It consists mainly of the stereoscopic PIV method. Stereoscopic-PIV was first introduced by (Arroyo and Greated, 1991). It needs two cameras to extract the 3rd component of the velocity.
- (3D-3C): the three-dimensional techniques that make it possible to find the three components of the velocity in a volume. These techniques unlike the other two techniques, allow the measurement of the gradient tensor of instantaneous velocity without using additional hypothesis. It consists of scanning PIV (David et al., 2012) and tomographic measurements introduced by (Elsinga et al., 2006). This family also includes 3D-PTV techniques (Maas, 1992).

Introduced by (Elsinga et al., 2006), tomographic Particle Image Velocimetry (Tomo-PIV) relies on a tomographic reconstruction of the particle distribution and a subsequent three-dimensional cross-correlation. On the other hand, 3D PTV-methods (Maas, 1992) triangulate particle positions and try to find matching occurrences in successive time steps in order to form Lagrangian track (the method is also called 4D-PTV as it provides time information). The advantages of Tomo-PIV are the evaluation on an Eulerian grid that allows easy computation for flow components and the possibility to use high seeding densities concentration. However, the main problem associated to this method is the high percentage of ghost particles and its high computational cost due to cross correlations and volume reconstruction.

Unlike Tomo-PIV which involves spatial averaging over the interrogation window, 4D PTV can inherently reach higher spatial resolution as it yields a vector for every tracked particle position. It also gives the Lagrangian representation of the flow field. However, as the number of particles increases, identification of overlapping particles and its corresponding 3D reconstruction becomes challenging, which leads to a tradeoff between spatial resolution and reconstruction accuracy.

II.1.1 Particles Tracking Velocimetry

In the early age of PIV, researchers were working on statistical methods based on auto correlation of double exposure images (Adrian, 1984) but by 1985, the computers performance were limited (128 KB of RAM and a 30 MB hard drive as standard). Two-dimensional Fourier transforms and two-dimensional correlation analysis were practically impossible to perform on such machines. As a result, non-statistical methods (using optical Fourier transform) such as tracking particles individually sparked a lot of interest.

PTV is one of the oldest techniques of flow measurement. The acquisition of quantitative information of high density at reasonable effort has only become possible with use of computers. Since the 70s, the methods and applications reported in the literature show a transition from systems with completely manual data processing (i.e., a human operator measures coordinates and defines correspondences) towards completely automated systems. Chiu and Rib, 1956 reported an early application based on stereoscopic imaging. Their method requires manual measurements in the images, which took 20 hours to track 70 particles. In the 60's, Boyle and Smith, 1970 invented the charge-coupled device, which is now known as CCD cameras. Their invention was a major breakthrough in imaging systems, and they were awarded the Nobel Prize for it. In 1989 Kobayashi et al., 1989 used two CCD cameras to measure a flow between rotating disks. An average of 51 simultaneous velocity vectors were obtained. Further, a Japanese group at Tokyo University has developed a completely automatic 3D PTV that allows the determination of up to 440 simultaneous velocity vectors (Nishino et al., 1989). This was particularly useful for measuring complex three-dimensional turbulent flows. The 3D PTV system was first developed in 1987 (Malik et al., 1993). It was based on digital photogrammetry methods and three synchronized CCD cameras recording particle image sequences. It has been applied to the measurements of velocity fields in test volumes of $12 \times 120 \times 15$ to $200 \times 200 \times 40\ mm^3$ seeded with about $1000 - 1500$ particles in a $24\ m$ laboratory channel and in a stirred aquarium. In 1993, Maas et al., 1993a used high-resolution high-speed CCDs with up to 4096 x 4096 pixels to record up to 1000 images per second and

track up to 1000 particles simultaneously. This paper demonstrated how hardware evolutions will have a significant impact on PTV results.

However, the main disadvantage of 3D-PTV is that it is typically used with a low density of particles due to difficulties not only for particle tracking but also for individual-particle detection, which can result in a higher ghost to true particle ratio.

On this account, the goal with PTV systems was to achieve applicability to higher density particle images, and some new ideas have been reported in the literature in this regard. The hybrid PIV/PTV method (Cowen et al., 1997) is an example of this, in which standard cross-correlation (PIV) is used prior to individual-particle tracking to estimate the local velocity to be measured by the PTV system. Another example is the hybrid PIV/CFD method (Kaga and Yamaguchi, 1997) which involves iteratively checking particle-velocity data against theoretical fluid-flow data. In that way the trajectories can be validated by numerical simulations of a flow with same physical properties. The year 1998 marked the introduction of one of the most important algorithms of PTV, the relaxation method. It is based on binary image cross correlation method and it was introduced by Japanese researchers (Ohmi and Li, 2000). The most significant advantage of this method is that it is based on the probability of particle matching between the first and second frames, which is defined for each possible pair of particles, including the probability of no match. The number of erroneous (ghost) particles was reduced according to their findings. However, the number of ghost particles does not appear to be negligible in some of their experiments. This is especially true when the particle distribution density is high and/or the flow is subjected to strong shearing motions. As a result, the method needs to be improved for use in more complex turbulent flows. But the conclusion was that this PTV technique can be applied to a much higher density of particle distribution than previously thought.

Recent advances in reconstruction algorithms, such as Iterative Particle Reconstruction (IPR) (Wieneke, 2013) and "Shake the Box" (STB) (Schanz et al., 2016a), have improved the accuracy of 3D PTV significantly. IPR constructs a projected image using a triangulation-based reconstructed field, then minimizes the intensity residuals in the image plane by shaking the particles in world coordinate location. For seeding densities up to 0.05 particles per pixels, this process achieves better positional accuracy, a lower fraction of ghost particles, and reconstruction accuracy comparable to the intensity-based Multiplicative Algebraic Reconstruction Technique (MART) (Elsinga et al., 2006). This concept is further developed in 4D-STB, which uses temporal information for a time-resolved measurement to predict particle location in future frames and iteratively corrects the predicted position with IPR. For synthetic experiments with high particle concentrations, such measurements have successfully resolved flow structures (up to $0.125\ ppp$ (Schanz et al., 2016a)) . As a result of these capabilities, 3D PTV measurements have gained renewed attention and applicability in many experiments.

II.2 General PIV/PTV principles

PTV like other laser velocimetry methods, works by seeding the flow with particles that are illuminated by a laser and whose images are captured by cameras. The particle displacements and velocities can be determined by processing the acquired images.

II.2.1 Typical setup for 3D PTV

A laser and 3 cameras at least are required in a typical 3D PIV setup, as shown in Figure II.2. Three cameras are essential for the establishment of stereoscopic correspondences because of ambiguities that occur when multiple candidates are found in a search area using only two cameras. These ambiguities can only be solved if a third (or even a fourth) camera is being used. A laser beam can be shaped using optics like lenses and mirrors to create a laser beam with the proper thickness and dimensions for the volume in question. PIV lasers are usually pulsed and must be synchronized with the cameras. The laser and cameras are connected to a computer which, by the help of a PTU synchronizer (Programmable Timing Unit), controls the acquisition parameters, and the recorded images are transferred to this computer for analysis. The idea is to acquire images with a short time step dt and measure particle displacements over that time to calculate their velocity.

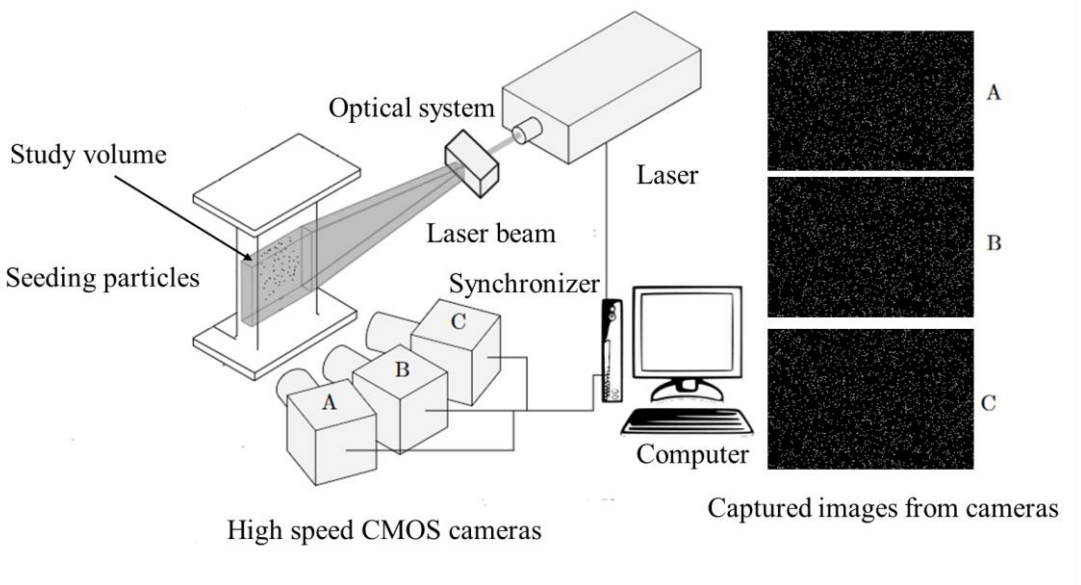

Figure II.2 Typical experimental setup of PTV system to track particle trajectories.

II.2.2 Tracer particles

To measure the velocity of a fluid flow represented by tracer particles, sufficiently small particles are needed. These particles must be neutrally buoyant. Meaning that, a solid particle in a fluid is in equilibrium due to gravity and Archimedes principle's upward buoyant force. The difference in density between the fluid and the solid particle plays a role in this equilibrium. If the particle density is the same as the fluid, it will not move when the fluid is at rest. As a result, the particle must be as dense as the probed fluid in order to be a reliable tracer. Furthermore, the goal of turbulence research is to investigate all of the structures in the turbulent cascade, all the way down to the Kolmogorov dissipative scale. A solid particle with a diameter of $dp > \ell$ cannot probe a structure of size ℓ. Intuitively, we can expect a large particle to completely cover a structure. Thus, in order to probe structures as small as η, the particles must be as small as possible and necessary much smaller that η. Additionally, if we want to resolve a structure of size ℓ the particles displacement needs to be less than $\ell/2$ (Shannon's criteria) (J M Foucaut et al., 2004).

II.2.2.1 Mechanical considerations

The first quantity used to qualify the tracer particles is the Stokes number. It compares the particle response time to the characteristic time of the fluid.

$$S_t = \frac{\tau_{paricle}}{\tau_{fluid}} \qquad (II\text{-}1)$$

A Small Stokes number, $S_t \ll 1$, describes a particle which "reacts" faster than the fluid, and will be able to follow the smallest flow fluctuations. On the other hand, by solving the equation of motion of a settling particle submitted to its weight, buoyancy and drag force, the particle characteristic time appears $\tau_{particle} = \frac{dp^2 \times \rho_p}{18\mu}$ where dp *and* ρ_p are the particle size and particle density. Thus, the Stokes number can be expressed as:

$$S_t = \frac{dp^2 \rho_p}{18\mu\tau_{fluid}} \qquad (II\text{-}2)$$

In turbulence, τ_{fluid} should be the time scale at the smallest resolved scale of the flow. In our case, it should be of the order of the Kolmogorov scale or even less.

The most critical conditions are met when particle tracers are immersed in turbulent flows at high Reynolds number, where a wide range of turbulent scales is present. Therefore, attention should be made to the size of the particle since the Stoke's number increases with particle size (equation (II-2). Figure II.3 shows the behavior of a particle within a small-scale vortex. By increasing the Stoke's number the sensitivity of a particle to the fluid dynamics decreases. On the other hand, the size of the particles cannot be arbitrarily decreased otherwise they would not scatter enough light to be visible (see the next section II.2.2.2).

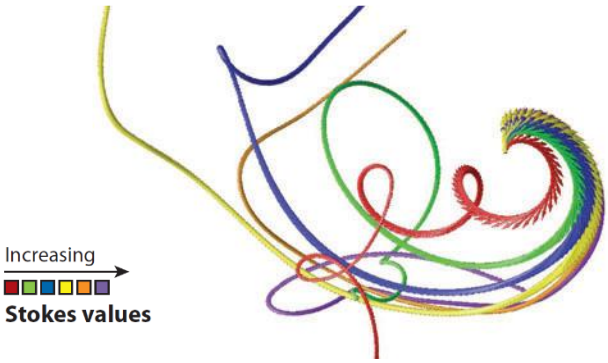

Figure II.3 Image from Toschi and Bodenschatz, 2009: Trajectories of heavy particles with different inertia. When released within a small-scale vortex filament (matching the velocity of the underlying fluid), particles with different inertia respond to vorticity differently. Particles with large Stokes numbers are almost insensitive to the presence of the vortex. The red line represents a fluid tracer, whereas the green, blue, brown, and yellow lines correspond to increasing Stokes values, respectively.

Sedimentation is another issue that can arise when the particle density is higher than the fluid density. It causes a systematic error in the velocity because it adds a drift component

to the particle velocity in addition to the fluid velocity. Furthermore, as a result of this sedimentation, the density of the seeding gradually decreases over time, necessitating new seeding or vigorous stirring to re-suspend them. The falling speed v_g of the particles in the fluid characterizes this phenomenon. Once the particles (assumed spherical here) have reached their falling speed in a fluid at rest the falling speed is found to be:

$$\overrightarrow{v_g} = \frac{dp^2(\rho_p - \rho)\vec{g}}{18\mu} \qquad \textit{(II-3)}$$

where $\vec{g}$ is the gravitational acceleration.

II.2.2.2 Scattering properties

The illumination of the measurement area is generally achieved using a laser beam expanded using a set of optics generating a collimated beam of the measurement volume thickness. Scattered light by small particles follows the theory of Mie (Gouesbet and Grehan, 1999a). Mie scattering is the scattering of light from spherical particles with diameters that match the wavelength of the incident light, as described by the generalized Lorenz-Mie theory (Gouesbet and Grehan, 1999a). The average intensity of scattered light in Mie scattering is proportional to the square of particle diameters. Large particles scatter more light and are therefore more visible in a PIV image. The cross section of scatter light is presented by (Melling, 1997) in the figure below. Seeding particles used in PIV have diameters in the range $1 - 10\mu m$ (Raffel et al., 2018).

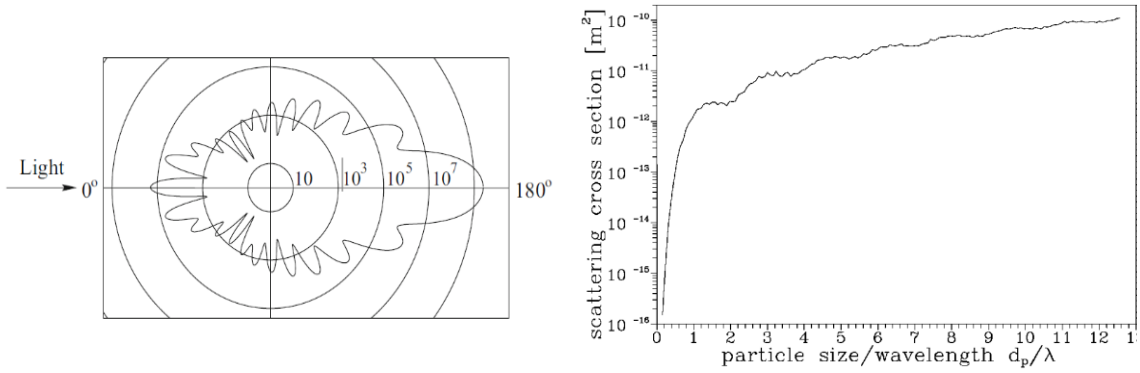

Figure II.4 (Left) Polar plot of light scattering by a 1μm oil particle in air (source (Gouesbet and Grehan, 1999b)). (Right) The scattering cross section as a function of the particle size normalized by the wavelength (refractive index n = 1.6) (source (Melling, 1997))

II.2.3 Imaging of small particles

Two aspects are important when imaging small particles for 3D PIV applications. First, the particles are usually imaged by cameras in focus, so the focal depth δ_z (see Figure II.5) should be larger or equal to the depth of field of the illuminated volume. The equation of the focal depth is given by (Solf, 1978):

$$\delta_z = 4.88 f_{\#}^2 \left[\frac{|M|+1}{M}\right]^2 \lambda \qquad \textit{(II-4)}$$

where:

- $f\# = \frac{f'}{D_a}$ is the aperture of the lens. It can be found by the ratio of the focal length f' over the diaphragm diameter of the camera D_a.
- $M = \frac{\overline{p'a'}}{\overline{pa}} = \frac{f'}{f'+p}$ is the magnification of the set up. $\overline{pa}$ and $\overline{p'a'}$ are the object and its corresponding image.
- λ is the wavelength of the emitted light.

On the other hand, For any particle within the focal depth, assuming diffraction limited imaging and a Gaussian intensity distribution of the particle image, its particle image diameter d_τ can be estimated as follows (Adrian, 1997):

$$d_\tau = \sqrt{\left(M \times d_p\right)^2 + d_{diff}^2} \qquad \textit{(II-5)}$$

When the diameter of the particle geometric image, $M \times d_p$, is considerably smaller than d_{diff}, this expression is dominated by diffraction effects and reaches a constant value of d_{diff} (Raffel et al., 2018):

$$d_{diff} = 2.44 f\#(|M|+1)\lambda \qquad \textit{(II-6)}$$

The diffraction spots must have a diameter d_{diff} of maximum 3.5 pixels and less than 2 pixels is optimum (Raffel et al., 2018).

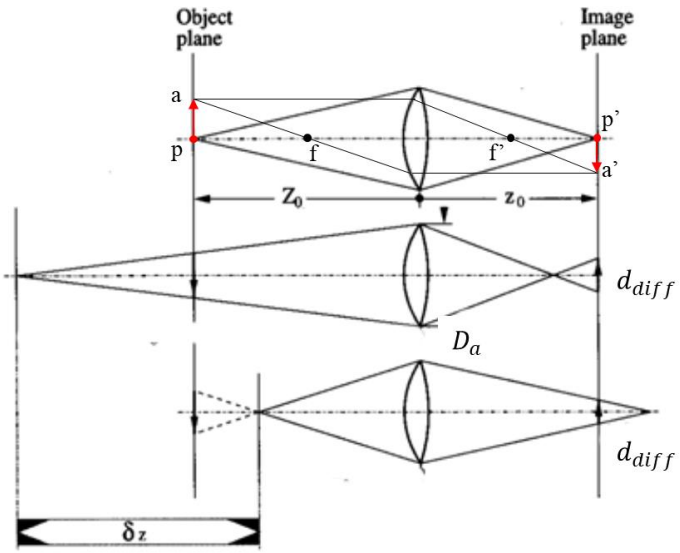

Figure II.5 Representation of optical system dimensions used for imaging small particles. δ_z is the focal depth and d_{diff} is the diffraction diameter.

Additionally, if there is a change in the medium that a light is traversing, the equation (II-4) can be modified as (Debue, 2019):

$$\delta_z = 4.88 f_\#^2 \frac{n_i}{n_e} \left[\frac{|M|+1}{M}\right]^2 \lambda \qquad \textit{(II-7)}$$

where the optical index of the medium containing the observed field is n_i, while the optical index of the external media where the camera is positioned is n_e. For a fixed magnification M, if $n_i > n_e$, the focal depth is greater than for the case where both optical indices are equal.

II.2.4 Calibration of cameras

The 3D PIV reconstruction is based on the relation between the 3D actual physical space (or world reference system) and the image space. The calibration provides mapping functions. Two main functions exist in the bibliography: Pinhole model (Tsai, 1986) which is the physical model of the camera and an approximated polynomial model (Soloff et al., 1997). Recently, the calibration optical transfer function (OTF) (Schanz et al., 2013a) became an additional option to minimize the calibration errors of the two camera models.

Pinhole model

We use bold italic letters for vectors and matrices (such as rotation array $\boldsymbol{R}$) in R^3. All the definitions used in the following are illustrated in Figure II.6. The world coordinate system is denoted $(O;\ X,Y,Z)$, while $(C;\ X',Y',Z')$ is the camera coordinate system. Extrinsic parameters refer to the 3 angles defining the rotation of the camera frame relative to the world frame, denoted by the 3×3 array $\boldsymbol{R}$, and to the translation vector $\boldsymbol{T} = \overrightarrow{OC}$, defined as the coordinates of the optical center C expressed in the world frame. As a result, for a point P of coordinates $\boldsymbol{X} = [X,Y,Z]$ in the world frame and $\boldsymbol{X'} = [X',Y',Z']$ in the camera frame, the following equation holds:

$$\boldsymbol{X'} = \boldsymbol{R^{-1}}(\boldsymbol{X} - \boldsymbol{T}). \qquad \textit{(II-8)}$$

Here the inverse $\boldsymbol{R^{-1}}$of the rotation matrix $\boldsymbol{R}$ is equivalent to its transpose since $\boldsymbol{R^T}\,\boldsymbol{R} = I$ (i.e. $\boldsymbol{R}$ is orthonormal). The intrinsic parameters characterize the projective transform. The intersection point "A" of the optical axis with the image plane is referred to as the principal point with coordinates c_x and c_y in pixel units (coordinates (0,0) is top left in the pixel coordinate of the camera). The focal length $f = \left|\overrightarrow{CA}\right|$ is the distance from the optical center to the image plane, leading to f_x (respectively f_y) when converted into horizontal (resp. vertical) pixels units. f_x and f_y might be different if the field is not squared.

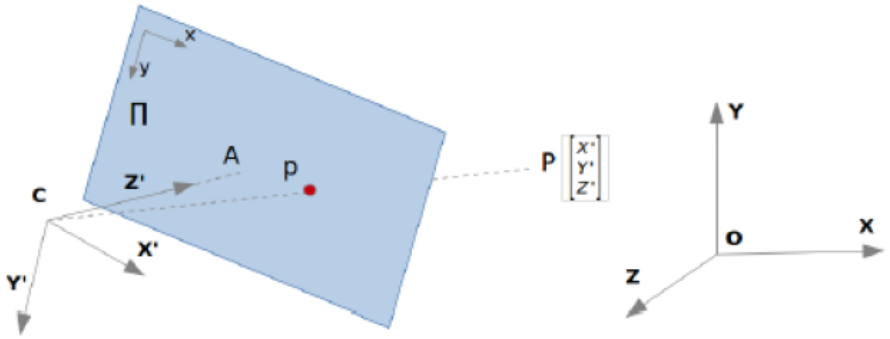

Figure II.6 Coordinate reference system of the camera in a pinhole model. $(O;\ \boldsymbol{X},\boldsymbol{Y},\boldsymbol{Z})$ is the world coordinate system and $(C;\ \boldsymbol{X}',\boldsymbol{Y}',\boldsymbol{Z}')$ is the camera coordinate system (Figure extracted from (Cornic, 2016)).

The pinhole model assumes the paraxial approximation. This means that a point "P" with coordinates $\boldsymbol{X}' = [X', Y', Z']$ in the camera frame, its image "p" onto the image plane "Π" and the optical center "C" are aligned.
Since p ∈ Π, its coordinates in the (metric) camera frame are p$= [u, v, f]$. Using the law of similar triangles, it was found that:

$$\begin{cases} u = f\,\dfrac{X'}{Z'} \\ v = f\,\dfrac{Y'}{Z'} \end{cases} \qquad \textit{(II-9)}$$

When converted to pixel coordinates, the image coordinates $[x, y]$ of 'p' are obtained:

$$\begin{cases} x = f_x\,\dfrac{X'}{Z'} + c_x \\ y = f_y\,\dfrac{Y'}{Z'} + c_y \end{cases} \qquad \textit{(II-10)}$$

If this projection is a linear transformation, then it can be represented as a product of a matrix and the input vector (in this case, it would be $P(X', Y', Z')$). However, from equation (II-10), we see that this projection is not linear, as the operation divides one of the input parameters (namely Z'). Still, representing this projection as a matrix-vector product would be useful for future derivations.
One way to solve this problem is to change the coordinate systems. For example, we introduce a new coordinate, such that any point p(x, y) becomes $(x, y, 1)$. This augmented space is referred to as the homogeneous coordinate system. Using homogeneous coordinates, we can formulate:

$$\alpha \times p = \alpha \times \begin{bmatrix} f_x \frac{X'}{Z'} + c_x \\ f_y \frac{Y'}{Z'} + c_y \\ 1 \end{bmatrix} = \begin{bmatrix} f_x & 0 & c_x \\ 0 & f_y & c_y \\ 0 & 0 & 1 \end{bmatrix} \begin{bmatrix} X' \\ Y' \\ Z' \end{bmatrix} = KP \qquad \textit{(II-11)}$$

where α is determined by the equation obtained on the last line and $\boldsymbol{K}$ is the intrinsic array or **camera matrix** defined as:

$$\boldsymbol{K} = \begin{bmatrix} f_x & 0 & c_x \\ 0 & f_y & c_y \\ 0 & 0 & 1 \end{bmatrix} \qquad \textit{(II-12)}$$

Polynomial model (Soloff model)

The Soloff model is more suitable to map complicated refraction geometries (in cases without strongly severe distortions). The model is given by a least-squares polynomial with cubic dependence in X and Y, and quadratic dependence in the depth Z. The mapping function can be given as:

$$\begin{aligned} \Omega = {} & a_0 + a_1 X + a_2 Y + a_3 Z + a_4 X^2 + a_5 XY + a_6 Y^2 + a_7 XZ \\ & + a_8 YZ + a_9 Z^2 + a_{10} X^3 + a_{11} X^2 Y + a_{12} XY^2 + a_{13} Y^3 \\ & + a_{14} X^2 Z + a_{15} XYZ + a_{16} Y^2 Z + a_{17} XZ^2 + a_{18} YZ^2 \end{aligned} \qquad \textit{(II-13)}$$

where Ω is either pixel coordinate x, or y, $i.e.$ one polynomial for x and one for y to determined)

Scheimpflug condition

Scheimpflug condition is needed when the optical axis is not orthogonal to measurement plane or volume. The full field of view cannot be focused on the same image plane (perspective effect). By tilting the camera, then all points in the a given plane will be focused. The Scheimpflug condition must be respected for 4D PTV as different viewing angle are required.

II.2.5 Volume self-calibration

Before volume self-calibration, we use recorded images of a plate with known markers position on at least two planes. These recordings allow us to obtain the image coordinates in pixels of some points in the physical space to fit the selected camera model seen in section II.2.4

However, after calibrating the cameras using a calibration plate, the maximum calibration error is typically around ~0.4 pixels (based on the experiments done in this thesis). It should be less than 0.1 pixel to perform proper 3D PTV, hence the need of the "Volume Self Calibration" (VSC) (B. Wieneke, 2008). The technique is based on the correction of the mapping functions Ω (this mapping function is defined from the calibration plate using pinhole or polynomial model) using the particle images. These errors come from inaccurate calibration plates, inaccurate plate movement, mechanical instabilities and optical distortions that are not accounted for by the mapping function.

Preferably, VSC should be done on low image densities to correct the system errors. Then it can be corrected iteratively for higher densities if needed. The technique starts by choosing the brightest particles from the image $(x_i, y_i)_{orig_n}$ and triangulating the

matching particles to their 3D positions (X_i, Y_i, Z_i) (see section II.3.2 for the basics of this triangulation method and section II.4.1 for the method used in this thesis). A best fit of the 3D world position is usually done by minimizing the distance between the original image and its back projection $(x_i, y_i)_{proj} = \Omega_n(X_i, Y_i, Z_i)$. The triangulation error represented in Figure II.7 by the cyan vectors is what is called disparity vector. The disparities, d_n, for all particles throughout a sub-volume are then used to correct the mapping functions for all cameras. For a perfect line of sights, the disparity should be equal to zero as no correction is needed.

$$\Omega_n(X,Y,Z)_{new} = \Omega_n(X,Y,Z)_{orig} - d_n(X,Y,Z) \qquad \textit{(II-14)}$$

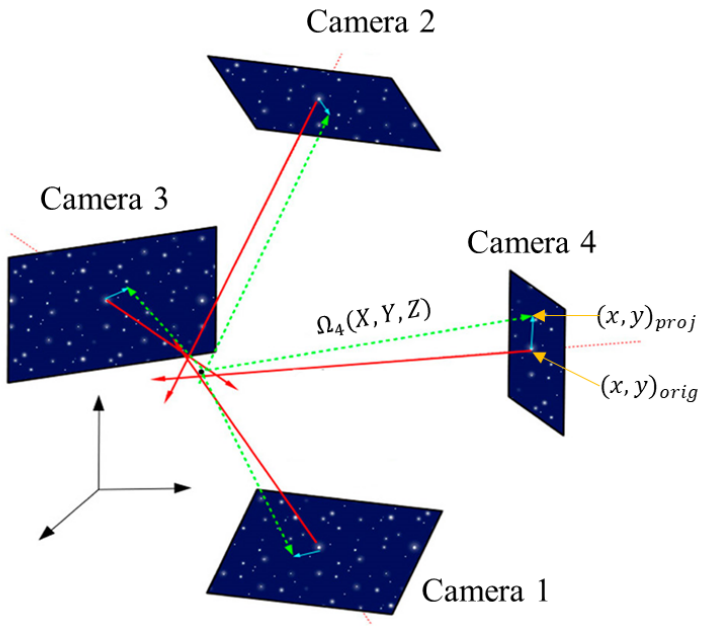

Figure II.7 Illustration of the disparity. Red lines: computed lines of sight through the particle. Black dot: triangulation of the particle. Dashed green lines: projection of the triangulated particle. Cyan arrows: disparity. Figure is extracted from (Cornic, 2016)

The calculated disparities $d_{n,i} = \left(d_{ix}, d_{iy}\right)_n$ are displayed as a small 2D Gauss blob of maximum intensity of 1 for all particles. Finally, disparity maps are summed for multiple recorded images and mapping functions are updated by the equation (II-14).

II.3 Working principles of 3D PTV

II.3.1 Coordinates of particles images

The first step, which is essentially the first part of any 3D-PTV, is to locate 2D particle positions in each camera image to be able to find later on the corresponding 3D particle positions through matching and triangulation.

Every local maximum in image intensity above a certain threshold is assumed to be a particle. Choosing the center of this local maximum pixel is the simplest method for determining a particle center. This method is relatively fast, can handle overlap, and is

noise-resistant. Weighted averaging (Maas et al., 1993a) (Dracos, 1996) is a very simple technique and is therefore widely employed in PTV. To represent single particles, camera images must first be segmented into adjacent groups of bright pixels. The center of the pixel groups coordinates $(x_c,\ y_c)$ are then calculated by averaging the positions of all the pixels in the group, weighted by their intensity. If we consider $I(x,\ y)$ to be the pixels intensity at $(x,\ y)$, x_c is given by (similar for y):

$$x_c = \frac{\sum_p x_p I(x_p, y_p)}{\sum_p I(x_p, y_p)} \qquad \textit{(II-15)}$$

As previously stated, we consider every local maximum of intensity (above a threshold) to be a particle. As a result, we assume that a group of pixels with N intensity maxima contain N particles when segmenting the camera image into groups of contiguous active pixels for averaging. Maas' algorithm (Maas et al., 1993a) includes a preprocessing step that divides such pixel groups into N subgroups, each with only one intensity maximum. The subgroups are formed by assuming that the intensity of pixels in a particle image decreases monotonically as the distance from the particle center grows. The contiguous subgroup containing the brightest local maximum is arbitrarily assigned to local intensity maxima.

If we know the functional form of the intensity profile of the particle images on the detector, a fit of this function to the image would produce a very accurate determination of the particle center. However, the functional form is not known. Instead, it is common to approximate it as a Gaussian (Mann et al., 1999).

$$I(x,y) = \frac{I_0}{2\pi\sigma_x\sigma_y}\left\{-\frac{1}{2}\left[\left(\frac{x-x_c}{\sigma_x}\right)^2 + \left(\frac{y-y_c}{\sigma_y}\right)^2\right]\right\} \qquad \textit{(II-16)}$$

where σ_x and σ_y are the Gaussian widths in the horizontal and vertical directions. If a pixel group contains N local maxima, the sum of N Gaussians is fitted to the group. Bear in mind that if particle images start to overlap, the detection of individual particle images is difficult and the uncertainty of the fit increases.

II.3.2 Particles 3D reconstruction (Establishment of 3D correspondences)

Once the image coordinates of all particles in all images have been determined, correspondences between data of the different images have to be established to be able to reconstruct the 3D coordinates. The epipolar geometry is used to solve this problem, knowing the orientation parameters of the cameras from a calibration. This is a standard and well known method described in (Maas, 1992).

From a point P' in one image, an epipolar line in another image can be calculated using the orientation parameters of the cameras from the calibration procedure; the corresponding point must then be located on this line. The epipolar line is a straight line in the strict mathematical formulation, but it will be slightly curved in the more general case with convergent camera axes, non-negligible lens distortion, and multimedia

geometry (Figure II.8). A small two-dimensional area with tolerance ε (due to data quality) serves as the search area for the corresponding particle image.

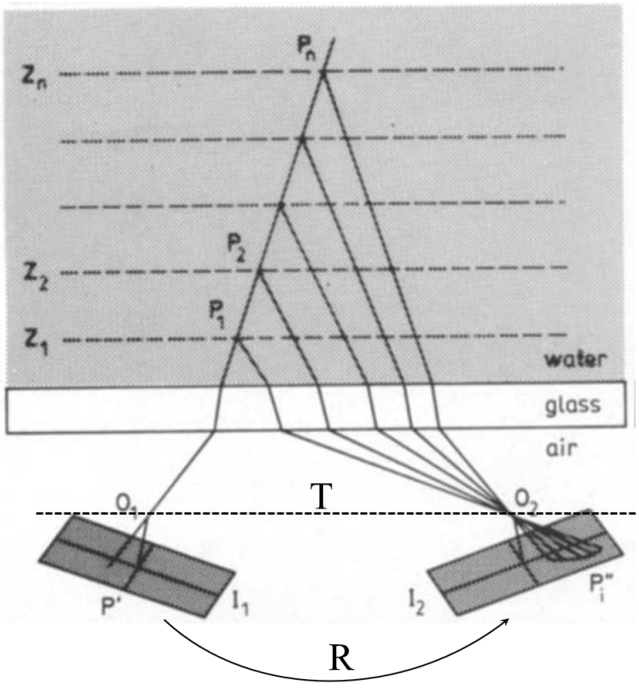

*Figure II.8 The epipolar constraint on two corresponding image points P' and P'' which are the projection of the scene point P. Point P'' must lie on the epiploar line with a defined tolerance ε. **T** and **R** are the translation and rotation vectors respectively (Figure extracted from (Maas, 1992)).*

In the calibrated environment we capture the geometric constraint in an algebraic representation known as the essential matrix. With two views, the two camera coordinate systems are related by a rotation $\boldsymbol{R}$ and a translation $\boldsymbol{T}$. The essential matrix can be found to be:

$$E = \begin{bmatrix} 0 & -t_z & t_y \\ t_z & 0 & -t_x \\ -t_y & t_x & 0 \end{bmatrix} . R \qquad \textit{(II-17)}$$

where $\boldsymbol{T} = \left(t_x, t_y, t_z\right)^T$. The essential matrix relates the corresponding image points expressed in the camera coordinate system. This relation allows us to find the depth information. Development of this method in recent years include the use of 3 cameras at least to decrease the possibility of having wrong/ghost particles. This method is called "Iterative Particle Reconstruction" (IPR) (Wieneke, 2013) and it is based on the same fundamentals of the method introduced by (Maas, 1992). The difference basically lies in the use of "residual images" that verifies the detection of all possible particles. This method is described later on in this chapter in greater details.

II.3.3 Particle tracking

After both finding the 2D positions of the tracer particles and 3D matching them to find the full 3D positions, the particles must be tracked in time. In its most general form, the problem of tracking many particles over many frames is a multidimensional assignment problem. There is therefore no known tractable algorithm for solving the full problem. Particle tracking algorithms are instead forced to approximate the optimal solution of the full assignment problem by restricting the temporal scope of the tracking, considering only a few frames at a time.
If x_i^n denote the i^{th}particle position in the n^{th} frame a tracking algorithm attempts to find an x_i^{n+1} for each x_i^n such that x_i^{n+1} is the position of the particle in frame $n+1$ that was at the position x_i^n in frame n. Multiple algorithms are explained and qualitatively compared in the interesting thesis of Ouellette et al., 2006. Additionally, Chenouard et al., 2014 have tested many tracking algorithms where different highly challenging scenarios were experienced from particle shape size to images frame rate and nonuniform background. Their results indicated that none of the methods can be considered as the best for particle tracking in any situation. However, new algorithms came to surface in another challenge for different PIV methods (Kähler et al., 2016). In this work, it was found that PTV algorithms can outperform state of the art PIV algorithms in terms of uncertainty. Furthermore, PTV-based methods with oriented particle search and refinement seem to overcome classical algebraic reconstruction and cross-correlation-based methods, at least on synthetic images without noise (Schanz et al., 2013c).

II.4 'Shake the Box'

Shake the box (Schanz et al., 2013c) (Schanz et al., 2014a) (Schanz et al., 2016a) was found to be the best method in PIV challenge (Kähler et al., 2016). It is probably one of the most advanced particles tracking method available today. Its most distinct feature is the accurate tracking of tracer particles at highest possible seeding densities so far.

Shake the box applies an advanced triangulation techniques compared to the ones found in literature. This step is called Iterative Particle Reconstruction (IPR). It uses the residual images created by back projecting the triangulated particle cloud. Describing the imaging properties of the particles is important to avoid artificial residuals. For that, the use of a calibrated Optical Transfer Function (OTF) is a must for this method (Schanz et al., 2013a). Finally, the Shake-The-Box algorithm introduces temporal information into the IPR processing of each time-step by predicting a particle cloud for each consecutive time-step (Time-resolved STB). Trajectories of tracer particles are identified with a high spatial accuracy due to a nearly complete suppression of ghost particles. The STB method is illustrated in the figure below. Details of each step are explained in the following subsections.

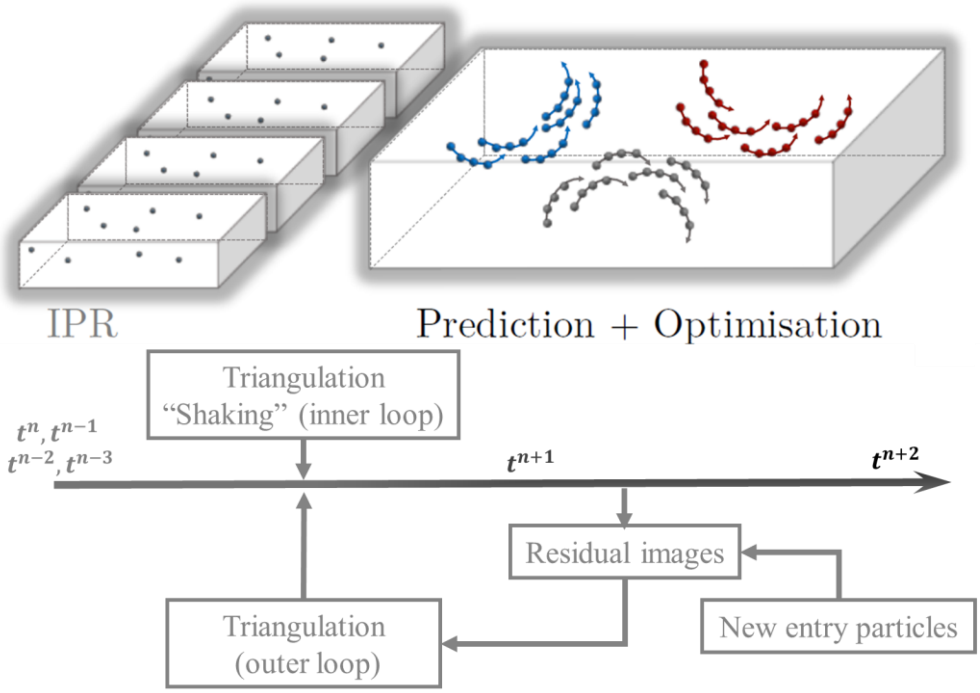

Figure II.9 4D-PTV flowchart starting from particle reconstructions in four frames using IPR (Wieneke, 2013). Then it goes to the prediction and optimization phase by triangulating new particles found in residual images. (Figure adapted from (Khojasteh et al., 2021)).

II.4.1 Iterative particle reconstruction 'IPR'

Iterative particle reconstruction (Wieneke, 2013) starts with finding the particles using a standard 2D gaussian fitting-based (section II.3.1). The particles are then triangulated to 3D positions using a sophisticated 3D-triangulation algorithm in order to obtain possible 3D-particle locations (B. Wieneke, 2008). Wieneke improved the algorithm of (Maas et al., 1993b) which fails at high seeding densities. The triangulation procedure illustrated in the Figure II.10 is explained further downstream.

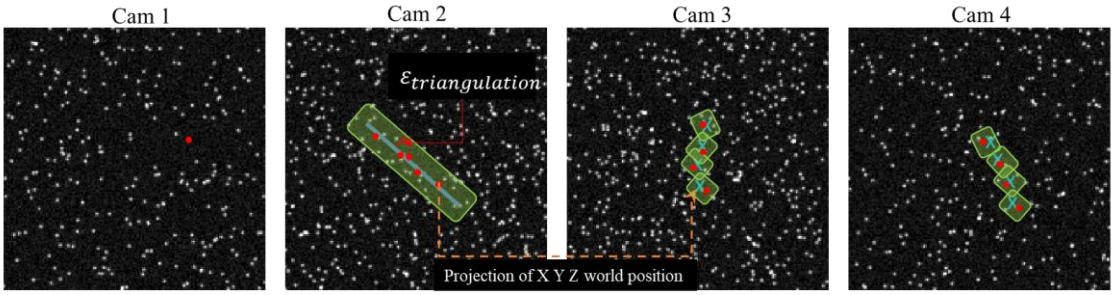

Figure II.10 Illustration of the triangulation procedure. Red dots depict selected peaks, green depicts the searching area. The algorithm first selects one peak on Cam 1. The corresponding 3D line of sight (blue) is calculated and projected onto Cam 2. On Cam 2 all peaks within a given tolerance, $\varepsilon_{triangulation}$, (allowed triangulation error) around this line-segment (green area) are queried. For all found peaks, a 3D position is projected to Cam 3 and Cam 4 images. Then particles are found around a squared area of the same allowed triangulation error.

The line-of-sight for each pixel is known thanks to the perspective volume calibration, which is of primary importance in particle identification. A beam can be projected through 3D space starting with the position of a single particle in camera 1 (the red particle in far left) and knowing the line-of-sight for each pixel. This beam will form a straight line on the sensor in camera 2. This line is known as the epipolar line (second image from the left). However, the matching particle cannot be expected to be located exactly on top of this line, as described before in section II.3.2, due to an unknown amount of remaining calibration errors. That is why instead of looking for matches only on a line, particles are searched around an area of maximum allowed triangulation error. All particles in this area are possible matches for the single particle that has been selected from camera 1. Each particle position within the stripe is used to do a triangulation to get a hypothetic 3D position for that combination. If the 3D particle position is correct, then matching particles in a specific area of interest must be present in cameras 3 and 4. The hypothetic 3D position is mapped to cameras 3 and 4 (using known lines of sight calibrations) to calculate the central position of the area of interest. A squared section with a size of $\left(2 \times \varepsilon_{triangulation}\right)^2$ is investigated around this central position to find possible matching particles (see Figure II.10, Cam3 and Cam4). This method is also used for Volume-Self-Calibration (see section II.2.5).

A new optimized IPR technique was introduced by (Jahn et al., 2021). They apply triangulation error linearly increasing with the number outer iterations instead of the fixed triangulation error:

$$\varepsilon_{triangulation}^{adjusted} = \varepsilon_{triangulation}^{initial} + \frac{i}{N_{IPR} - 1} * \Delta\varepsilon_{triangulation} \qquad \textit{(II-18)}$$

where N_{IPR} is the number of outer iterations of IPR and $\Delta\varepsilon_{triangulation}$ is a second parameter allowing the triangulation error to increase slightly at each outer iteration. According to this paper, this approach minimizes the creation of ghost particles, especially at the first iterations where the residual image is still very populated. This new triangulation was not applied in the algorithm used in this thesis.

The next step is to perform triangulation iterations. This step is done after particles have been detected. The particles detected on Cam2 and verified by Cam3 and Cam4 are back projected to Cam1 to verify the correspondence of the found particle with the original one. If the position is not exact, residual images are calculated. The method described below are summarized in Wieneke 2013 and Schanz et al. 2016. Consider a particle p projected into the image of camera i with coordinates X, Y, Z and intensity I_p . Thanks to the OTF and the mapping functions, a projected image on camera i of this particle can be obtained noted $I^i_{part}(x_i, y_i, I_p)$. By summing for all particles p in the volume their projected image $I^i_{part}(x_i, y_i, I_p)$, a projected image of the volume is obtained for camera i noted I^i_{proj}. Then a residual image I^i_{res} is calculated by subtracting the original image from the back-projected image I^i_{proj}.

$$I^i_{res}(x_i, y_i) = I^i_{orig}(x_i, y_i) - I^i_{proj}(x_i, y_i) \qquad \textit{(II-19)}$$

where I^i_{orig} is the recorded image of cam i.

The aim of the triangulation algorithm is to minimize this residual image by finding the good values of all particles p positions (X, Y, Z) and intensity I_p. This is done locally for each particle by minimizing the residual with a "shaking" approach. For each particle p (approximate position X, Y, Z), a metric R is constructed as follow:

$$R(X', Y', Z', I_P) = \sum_i \sum_{\substack{pixels\ around \\ projected\ point}} \left[I^i_{res+p} - I^i_{Part}\left(X', Y', Z', I_p\right) \right]^2 \qquad \textit{(II-20)}$$

With $I^i_{res+p} = I^i_{res} + I^i_{Part}(X, Y, Z, I_P)$. To minimize the metric, in X direction first, the metric is evaluated for $X' = X - \Delta$, X, $X + \Delta$, where Δ is the shaking parameter of typically 0.1 to 0.5 voxel. Then a quadratic polynomial is fitted to the 3 values to obtain the new X position of the particle. Then the same is done in Y and Z directions. For each shake iteration, the particle intensity needs to be updated according to (II-21)

$$I_{P,new} = I_P \times \sqrt{\frac{\sum_i \sum_{\substack{pixels\ around \\ projected\ point}} (I_{res+p})}{\sum_i \sum_{\substack{pixels\ around \\ projected\ point}} (I_{Part[X_{new}, Y_{new}, Z_{new}, I_P]}}} \qquad \textit{(II-21)}$$

In case the intensity $I_{P,new}$ falls below a specified threshold (usually 10% of the average particle intensity – this is a parameter that could be adjusted in the GUI of the Lavision STB algorithm), it is assumed that the particle was lost, and the shake process is not converging to the true particle position. In that case, the particle is deleted.

The name "Shake the Box" comes from this part of the algorithm since it consists of shaking the particle for multiple iterations to update its position. The shaking is typically of 0.1 voxel. This iterative process has an outer loop that adds new particles and an inner loop that refine the position of the added particles (see Figure II.9). Each inner iteration of the **inner** 'refine' **loop** updates the particle position ('shaking') and intensity. The greater the number of iterations, the greater the precision, but also the longer the computation time. In the **outer loop**, new particles are added using remaining particles

from the residuum. The more outer loops, the higher is the possibility to detect particles from the residuum as for the inner loop. On the other hand, more loops can increase the processing time significantly as for the inner loop.

II.4.2 Optical transfer function 'OTF'

The Optical Transfer Function (OTF) is a complex-valued function describing the response of an imaging system as a function of spatial frequency. As we have seen in previous section, IPR and other reconstruction methods rely on accurate reprojection of 3D particle positions. An accurate calibration of the camera lines of sight, which is ensured by performing a Volume Self Calibration, is an important precondition for this step. However, in describing the back-projected image of a particle, not only the precise location of the projection point is important, but also the shape of the particle image. Even if the particle position is perfect, the back projection cannot fit the recorded particle image if a circular Gaussian peak shape is assumed but the real shape is distorted due to astigmatisms or small depth of field compared to illuminated volume. Astigmatic distortions are common when viewing through interfaces with change of refractive index at non perpendicular angles.

The method of OTF is as follow: it selects particles in specific subvolumes, and it identifies their shape using a two dimensional gaussian peak:

$$w(x,y) = p.exp\left(-\frac{1}{2}(ax^2 + 2bxy + cy^2)\right) \qquad \textit{(II-22)}$$

Where x, y are the particles pixel position and a, b, c, p are parameters that determine the shape and particle intensity of the image. The OTF in a particular subvolume is determined for all cameras by averaging the obtained parameters over several particles coming from the same area of space. Figure II.11 shows an example of particle patterns calculated for different slices in z direction. The particle pattern shows how important OTF could be to describe particle patterns in the volume. The use of an OTF with the existing volume self-calibration showed that it can significantly reduce the ghost particles (Schanz et al., 2013b).

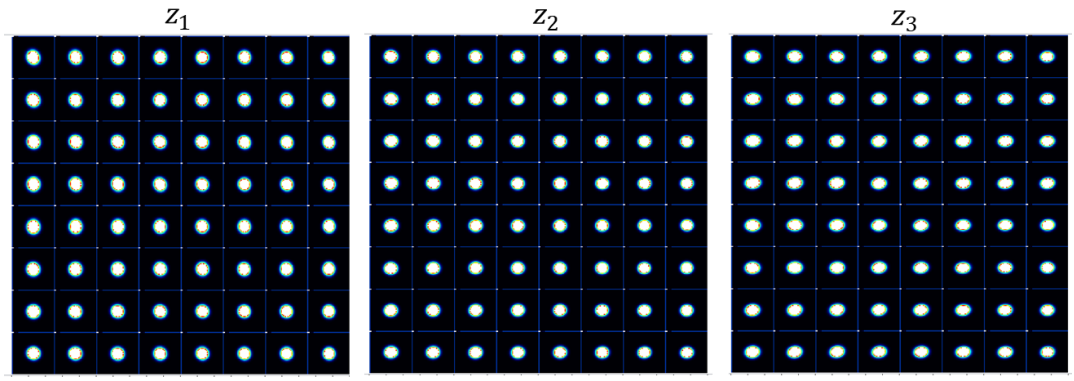

Figure II.11 Example of particle pattern for one camera and for 3 different planes in z direction for the experiment done in Chapter V. The volume is divided to $8 \times 8 \times 3$ *subvolumes.*

II.4.3 Initialization of tracks

Following the particle identification, trajectories need to be extracted from the distributions of particle candidates for the first 4 time-steps as shown in Figure II.9. The approach is not discussed in the original 'Shake the Box' paper but it is mentioned that it is a very simple algorithm based on finding matches in consecutive frames by applying a search radius around the particle position. The details of some of the methods are discussed and tested in the thesis of (Ouellette et al., 2006). Also, an implementation of a predictor could be used by performing a Tomo-PIV evaluation of the first time steps.

At the end of this phase, all tracks of 4 time steps in length found by the tracking system (see Figure II.12) are validated using thresholds of velocity and acceleration.

II.4.4 Prediction of the particle positions

The particles being tracked at t^n are extended to time step t^{n+1} by applying a Wiener filter (Wiener 1949) for extrapolation as described by Schanz et al 2016. The filter parameters are determined with the positions of particles at previous time step. Then the predicted particles locations are evaluated at time t^{n+1} thanks to these obtained filters from previous known positions t^{n-3}, t^{n-2}, t^{n-1}, t^n (see Figure II.12).

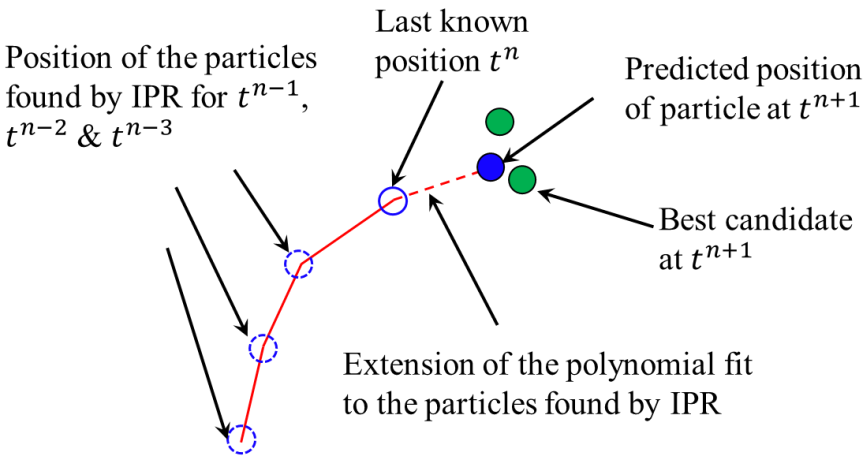

Figure II.12 Illustration of the prediction algorithme. Knowing the past positions of a particle, the next is estimated by a wiener filter fit to the past. The closest particle to the estimated position is saved to the track for time step t^{n+1}.

The closest particle to the predicted one is selected for the track. Every particles position at t^{n+1} is then 'shaked' to its correct position and intensity again by the IPR procedure (triangulation inner loop, Figure II.9).

During this phase, as not all particle tracks have been found yet, the residual images will still show a significant amount of particle images. New particle candidates are triangulated from the residual images using allowed triangulation error (see Figure II.13). This is the outer loop phase of the STB algorithm.

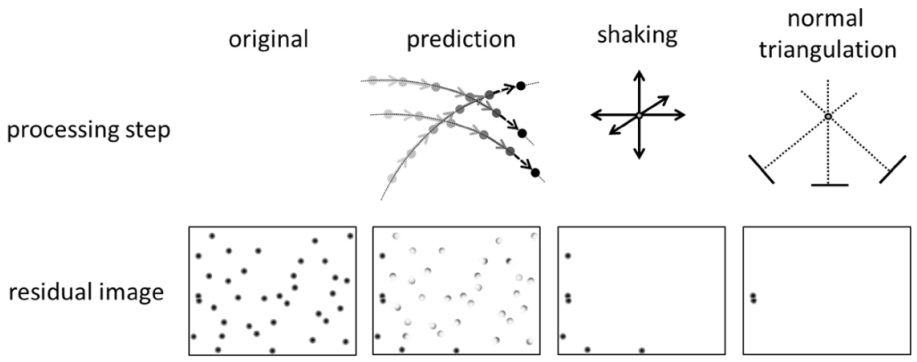

Figure II.13 Schematic description of the Shake-The-Box procedure for one time-step in the converged state by illustrating the effects of the different computation steps on the residual image of a single camera (out of multiple). After performing some iterations of shaking, the residuals of the tracked particles vanish (nearly) completely. The not found particles in the residuals are then tackled by the triangulation/IPR process until all possible particles are found (Schanz et al., 2016a).

The algorithm continues with time-step t^{n+2} and so on. This process of finding tracks/identification of new ones, will continue until (nearly) all true particles are tracked. At this point, convergence is reached.

II.4.5 Software parameters

Shake the box method is a black box algorithm, which was only available for us through a software from Lavision. The version used for processing in this thesis is DAVIS 10.1.0.56724. The parameters are grouped in three main windows are:

1- General

As general parameters, we have first of all to specify the volume where particles may be detected. Using the "max" buttons will automatically add the x y and z limits found using the calibration plate after the Volume-Self-Calibration. Then we have to iteratively adjust the optimal intensity threshold for all cameras for the detection of particle peaks. Finally, the allowed triangulation error ($\varepsilon_{triangulation}$) that is necessary for the IPR process is specified here.

2- Iterative particle reconstruction

We specify in this window the parameters of the shaking process with first the inner and outer loops number of iterations (4 and 4 by default). The "Shake particle position" parameter defines the spatial distance that is used to 'shake' the particle around to find the optimal position which minimizes the residuum (see section II.4.1. By default, it is fixed to 0.1 voxel). Also, we can allow the algorithm to remove a particle if its calculated 3D position is very close to an already existing particle (fixed to 1 voxel in this thesis work). This parameter requires a special attention, especially for high particles images densities. The effect of this parameter will be shown in chapter IV section IV.8. Finally, weak intensity particles are removed if they fall below a threshold (parameter fixed by default to 10% of the particle intensity). The intensity of predicted and triangulated particles is adapted in each iteration using equation (II-21).

3- Tracking

In the tracking process, we can specify first the minimum time steps of the particles detected by IPR process to initialize a track before starting the process of prediction. The adjustable range is from 4 to 10 time steps. A smaller value results in more tracks, a higher number ensures longer tracks with sometimes less noise. A special attention should be made to the velocity limit parameters which have to be defined in this tab. If the flow has a non-zero mean component, the expected shift can be entered here. Then we can adjust the dynamic range of the expected shift. This parameter specifies the maximum shift between two particles from a times step to another. It has to be large enough to capture all existing particle shifts in the flow. However, if this parameter is too high, processing may take much longer and false (spurious) tracks may be detected.

The outlier vectors can be drastically decreased by using a median filter. This filter can be applied iteratively ranging from 1 to 10 iterations. The median filter considers each particle in the flow and looks at its neighbors to decide whether or not velocity is conceivable with respect to the median velocity of its neighbors. The filter compares the difference of the velocity of the point and the median velocity of its neighbors with the standard deviation of the velocity of its neighbors. If the difference exceeds the standard deviation of the neighbors by some factor (also defined by the user), the particle is removed. Three parameters control the behavior of the median filter:

1- **Number of neighbors used**: Determines the number of nearest neighbors that are used to calculate the deviation from the median.
2- **Max search range**: determines the maximum search range for neighbor particles. Depending on the seeding concentration a smaller or bigger range may be necessary to find enough neighbors. The first parameter can restrict this region if more particles than the parameter "number of neighbors used" defined are present in this region. The filter takes then "number of neighbors used" particle the closest to the point considered.
3- **Remove if standard deviation** >: The particle in question is removed, if its velocity from the median of the neighbors is bigger than the value of this parameter times the standard deviation of the neighboring velocities.

II.5 Tracks smoothing

For the investigation of turbulence flows, determining the position is important but having access to an accurate estimation of velocities and acceleration is essential. The derivatives to find velocity and acceleration amplifies exponentially the errors of the positions thus, polluting the higher-order turbulent statistics based on both temporal and spatial small-scale quantities. For that reason, a smoothing method for the trajectories is necessary to brush off the errors. Smoothing can be done through least square polynomial fitting (Savitzky and Golay, 1964). This method is briefly discussed in section II.4.4.

On the other hand, a more rigorous method is what is called "Splines" introduced by (Bézier, 1986) as follow is used:

$$C(t) = \sum_{j=0}^{n'} b_{j,n'}(t) P_j \qquad \textit{(II-23)}$$

- Bézier curves are smooth curves defined using control points P_j (see figure below).
- n' is the degree of Bézier curves. A Bezier curve of degree n' is defined by $n' + 1$ control points P_j.
- $b_{j,n'}(t)$ are called the basis functions.

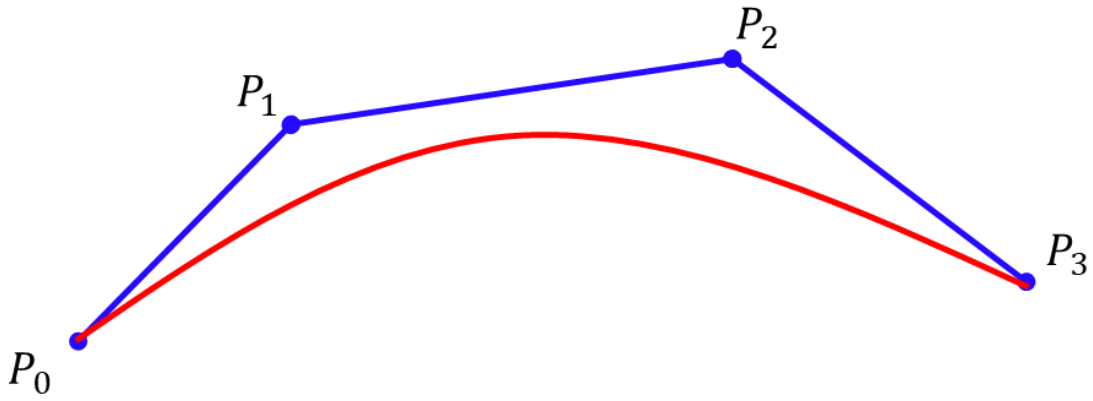

Figure II.14 Example of a cubic Bézier curve defined by four control points.

Now, B-splines (short for **Basis Splines**) (De Boor, 1978) use several Bézier curves joined end to end. A n' degree B-spline curve defined by $n + 1$ control points will consist of $n - n' + 1$ Bézier curves. In that way, we can have cubic B-spline defined by more than 4 control points for example, contrary to a cubic Bézier curve that could be only defined by 4 control points.

When deriving a B-spline, one should ensure the continuity and continuity of derivative up to a second order.

The equation of a B-spline is as follow:

$$S(t) = \sum_{j=0}^{n} b_{j,n'}(t) P_j \qquad \textit{(II-24)}$$

Where $(P_0, P_1, \ldots . P_n)$ are control points and $b_{j,\mathrm{n}'}$ are the basis function defined as:

$$b_{j,0} = \begin{cases} 1 \;\; if \; t_j \leq t < t_{j+1} \\ \\ 0 \qquad Otherwise \end{cases} \qquad \textit{(II-25)}$$

$$b_{j,n'} = \frac{t - t_j}{t_{n+j} - t_j} b_{j,n'-1}(t) + \frac{t_{j+n+1} - t}{t_{j+n+1} - t_{j+1}} b_{j+1,n'-1}(t)$$

The smoothing method we are discussing in this section is defined by Gesemann et al., 2016 and consists of minimizing the least square between the noisy data p_i and the fitted B-splines. Consider the regression $n + 1$ data points. The least squares function to minimize is:

$$l = \sum_{i=0}^{n} \left\{ P_i - \sum_{j=0}^{n} b_{j,n'}(t_i) P_j \right\}^2 \qquad \textit{(II-26)}$$

Finally, one need to introduce a penalty on the third order derivative of the fitted curve to avoid high frequency oscillations (Cheminet et al. 2021). This penalty term ($\Delta^3 P_i$) is multiplied by a parameter λ_s which control the smoothness of the fit.

$$l = \sum_{i=0}^{n} \left\{ P_i - \sum_{j=0}^{n} b_{j,n'}(t_i) P_j \right\}^2 + \lambda_s \sum_{i=0}^{n-3} \{\Delta^3 P_i\}^2 \qquad \textit{(II-27)}$$

Error on the noisy data.

Regularization/Smoothing term.

where $\Delta^3 P_i = P_{i+3} - P_i$

If λ_s is equal to zero, no smoothing is applied. If λ_s is large the regularization/smoothness is dominant.

This smoothing method acts as a low pass filter. Like any such filter, it has a transfer function $H(f)$, defined as the ratio of the Fourier transform of the smoothed data and the Fourier transform of the raw unfiltered data. Knowing $H(f)$ allows to define the cutoff frequency f_c. Deriving the filter response to a sinusoidal signal (Cheminet et al., 2021) found an analytical estimation of transfer function:

$$H(f) = \frac{1}{1 + \left(\frac{f}{f_c}\right)^6} \quad , \quad fc = \frac{1}{\pi \lambda_s^{1/6}} f_N \qquad \textit{(II-28)}$$

where f_N is the Nyquist frequency (in our case, as we will smooth the trajectories $X(t), Y(t), Z(t)$ and as we acquire the images at a frequency f_{aq}, f_N will be $\frac{1}{2} f_{aq} = \frac{1}{2\Delta_t}$). An example of noisy DNS compared to noise free DNS spectrums are shown in Figure II.15. The question that arises is how to find the cut off frequency f_c in order to determine the smoothing parameter λ_s? The noise is thought to be at high frequencies and can be considered a white noise. Two methods were used to find the cutoff frequency either by doing an intersection between an estimate signal spectrum (extrapolation of the linear part of the spectrum in loglog plot corresponding to a power law before the noise dominates) and an estimation of the noise spectrum (value of the plateau at the higher frequency where the white noise dominate. This point is called fc_1). This is not exactly where the signal to noise ratio (SNR) is equal to 1 (overestimation of the cut-off frequency). Another idea was to find the maximum spectrum curvature[2] (point f_{c2}). We see that the f_{c2} point is even further away than the frequency where the SNR=1.

[2] The curvature κ measures how fast a curve is changing direction at a given point: $\kappa = \frac{|f''(x)|}{(1+[f'(x)^2])^{3/2}}$

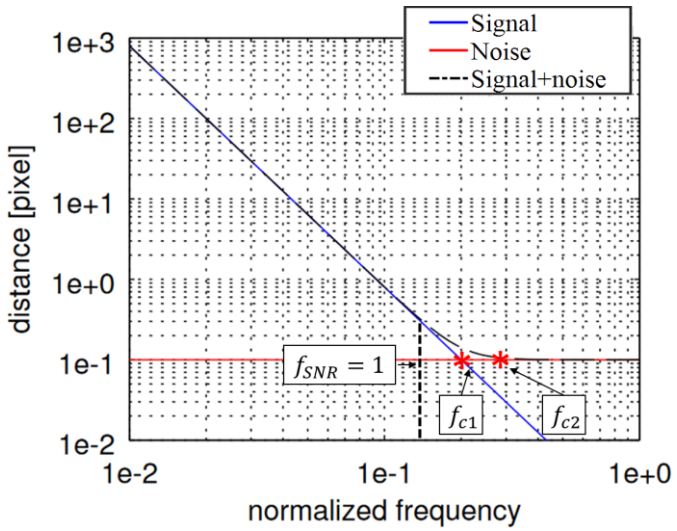

Figure II.15 PSD of particle positions for actual signal, noisy data (measured) and the added noise to the signal. Figure extracted from (Cheminet et al., 2021)

(Cheminet et al., 2021) proposed a better solution to the problem by using Tikhonov regularization for ill-posed problem (Tikhonov, 1977). The method requires to minimize the following fuctional:

$$\|y - kx\|_2^2 + \lambda_s \|x\|_2^2 \qquad \textit{(II-29)}$$

Where the left term is the error on the data fit and the right term is the regularization parameter. Several techniques were developed to circumvent this issue Cheminet et al., 2021 tested two of them on synthetic data, namely the $\mathcal{L} - curve$ criterion (Hansen and O'Leary, 1993) and the Normalized Cumulative Periodogram (NCP) criterion (Hansen et al., 2006). They have shown that low value of λ_s faithfully reconstruct high signal gradients. The conclusion is based on PSDs of positions, velocities and acceleration as well as PDFs of curvatures.

They have also shown that the use of smoothing parameter based on the NCP criterion is the best to smooth the positions data. Overall, this study showed that the Trackfit smoothing method based on B-spline and equation (II-27) is a very powerful tool to reduce noise in Lagrangian trajectories. Furthermore, the smoothing tuning strategies can be based on a desired accuracy and on the physical behavior of the measured quantities a one wishes to focus on.

Chapter III Preparatory experiments

Contents

III.1 Optimization of experimental parameters – introducing the Small Water Tank (SWT)

This chapter seeks to summarize two of the experiments carried out during the thesis. These two experiments have for objective to prepare the main experiment on the GVK. The experimental setup is first described in detail. Then, the principles of operation of the experimental techniques associated with PTV and tracks reconstruction are explained, and the main solutions chosen for both experimental (optical access, particles etc.) are discussed and justified. The results are presented and analyzed in the following chapter.

After presenting the overall objective of the EXPLOIT project in Chapter I as well as the past related work; we decided to optimize the different parameters that can improve the particles tracking results. For this reason, we decided to build a replica of the GVK with the same geometrical characteristics but with simpler technical solutions (see Figure III.1). From this point on we will call this replica SWT (Figure III.2) which stands for "Similar Water Tank". The interest of making this test is to optimize the parameters to prepare the experiments on the GVK, located at CEA Saclay. The idea was to build this replica in Lille as the LMFL was in charge of this parameter optimization within the EXPLOIT project.

A schematic view of GVK is shown in Figure III.1 (left). The apparatus mainly consists of an outer tank formed by 16 faces placed in a circular way with 22.5 degrees angle between each face (see Figure III.1 (right)). On each side, five windows with a thickness of $6mm$ are positioned vertically and serve as optical access points. It was decided for the first campaign on the GVK to use the middle access window for all 4 cameras to take measurements at the volume center. All the data presented in this thesis are measured at the center of the volume for GVK & SWT.

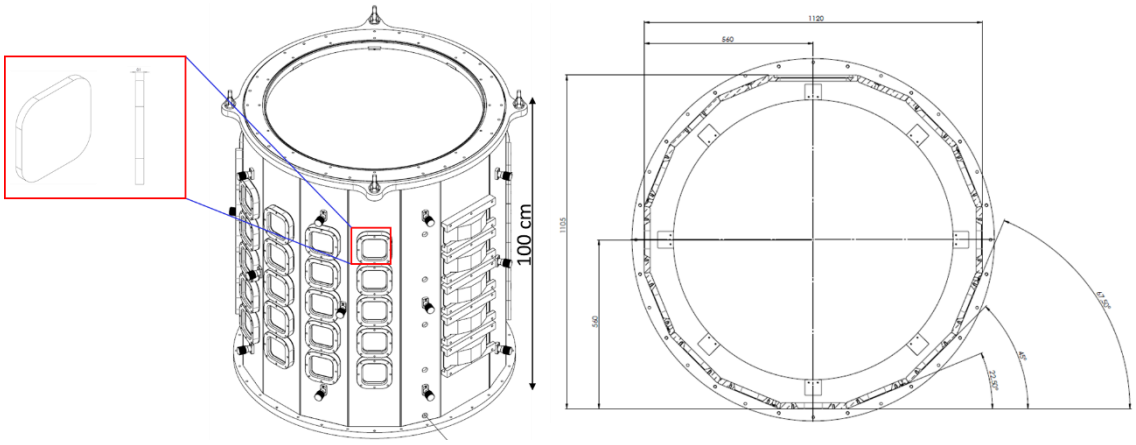

Figure III.1 Views of the GVK (CEA Saclay) experiment. ***(Left)*** *Perspective view with dimensions of the windows. The experiment is 100 cm tall.* ***(Right)*** *Top view that shows the angles of each window of the outer tank.*

An outer tank with same configuration was designed for the replica experiment. The faces are made of glass with same thickness of $6mm$. Since we are only interested in measurement properties factors and not the actual flow, the SWT is only $25cm$ in height compared to $100\ cm$ of the GVK. Another very important difference between these two experiments is the presence of a glass cylinder placed inside the outer tank of GVK as

seen in the top view of Figure III.1. This cylinder has a thickness of $10mm$. The gap between the tank and the cylinder is filled with water. We tried to get a cylinder for SWT in order to keep the same optical access compared to GVK, but we couldn't find a cylinder at a reasonable cost to put inside of our replica. However, the internal cylinder should not significantly modify the focus in the center of the volume. A simple calculation of the focal length of the cylinder gives a value of $f_{cylinder}$ of $-200\ m$. In other words, we think that the focus plane won't be affected by the presence of the cylinder since we want to measure at the center of the volume at $0.5m$.

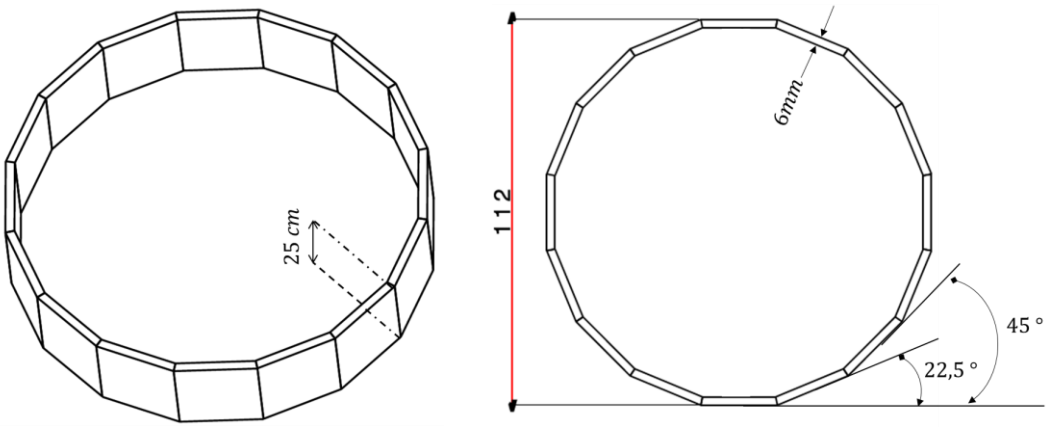

Figure III.2 Views of the SWT experiment (LMFL Lille). ***(Left)*** *Perspective view.* ***(Right)*** *Top view with the indication of the angles of each side of the tank.*

III.2 Experimental setup of SWT

The SWT was designed to test key parameters, as previously stated. The tank shown in Figure III.2 (left) has 16 faces. These glass faces are glued to a bottom template to form a tank; a top template was used to close the tank once it was filled with water to keep the dust out. To insert the calibration plate, the top template had to be removed. Special attention was paid to keep the water as clean as possible throughout the process. Three fish tank pumps were installed inside SWT, facing the volume center where we planned to measure. The aim of these pumps was to generate a turbulent flow. As the replica do not contain any propeller and internal cylinder, the flow of GVK could not be reproduced. However, this mismatch of the flow is not critical to test most of the measurement parameters.

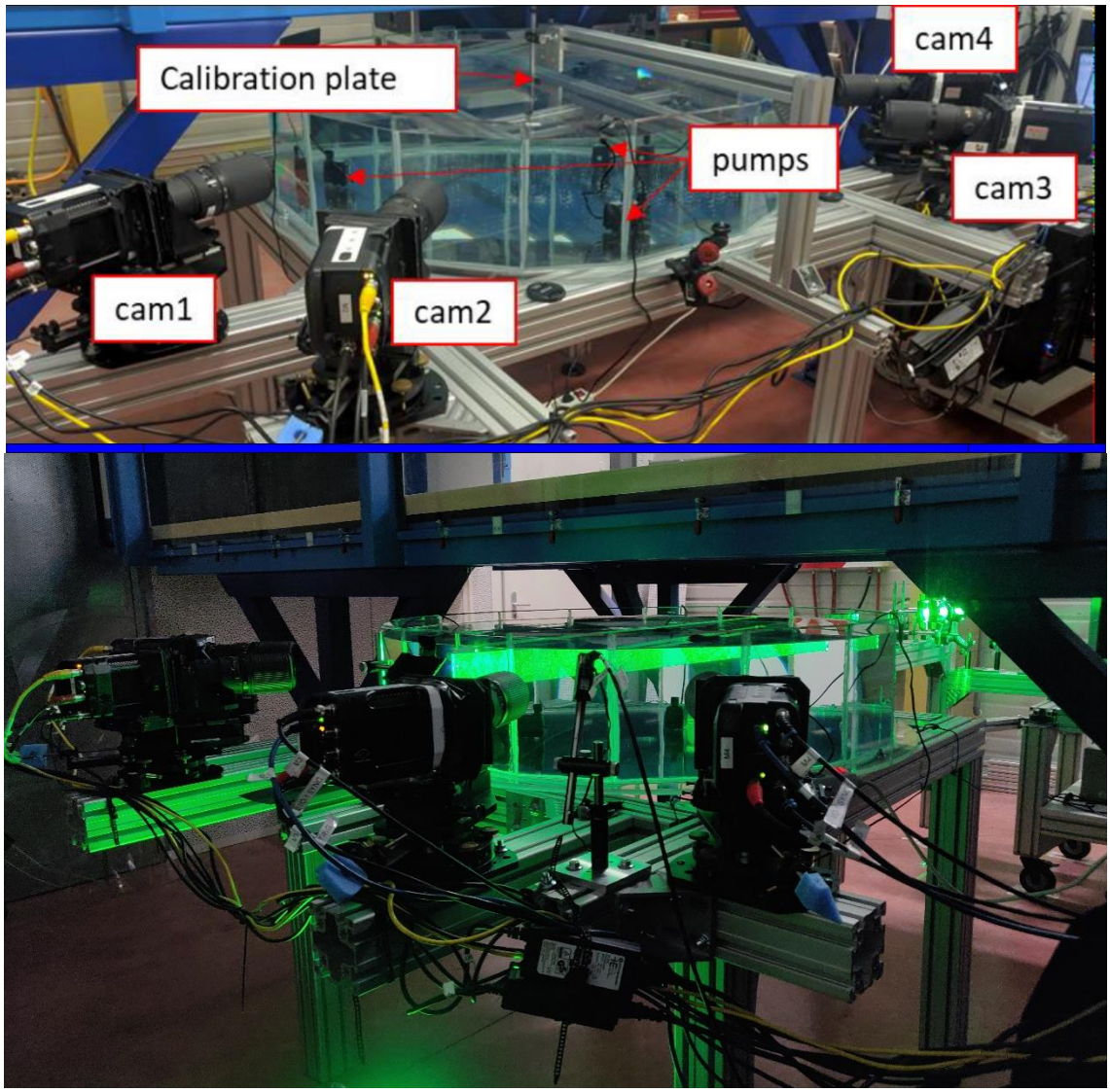

Figure III.3 Photograph of the SWT tank and the four cameras at their correct position. A calibration plate is placed in the center of the volume (top photograph corresponds to calibration phase). Three fish tanks pumps are used to generate a flow at the center of the volume

III.2.1 Cameras and illumination

The cameras used for the experiments are Phantom Miro 340. They record images at a rate of 800 frames per second for a maximum resolution of $2560px \times 1600px$. The cameras can operate at 1200 frames per second by reducing the resolution to $1600px \times 1600px$. The latter was used for this experiment with a maximum of 3226 frames recorded per run of about 2.7 seconds at 1.2kHz.

The cameras are (CMOS) with pixels size of 10 μm and a dynamic range of 12 bits. The image format is Cine RAW. Connectivity is via gigabit ethernet for control and fast data

downloads. In this chapter we study two different configurations. The main difference is the cameras angles with respect to the laser beam.

The Scheimpflug conditions states that the lens plane, the image plane, and the object plane have to intersect in a common line for each camera. This can be achieved by tilting the camera relative to the lens with a so called Scheimpflug adapter, as can be seen in Figure III.4. It is an important criterion in order to have a sharp focus on the whole object plane. The cameras were equipped with macro Nikon 200 mm lenses. The magnification was fixed to $M = 0.37$ and the apperture at $f\# = 11$ to be able to obain a good focus on the full depth of the volume of 6 mm.

Table III-1 Characteristics of the camera and their spatial positions for both configurations tested in this chapter.

Camera	$lens(mm)$	M	$f\#$	Config1	Config 2
1	200 mm	0.37	11	$+67.5°$	$+45°$
2	200 mm	0.37	11	$+45°$	$+22.5°$
3	200 mm	0.37	11	$-45°$	$-22.5°$
4	200 mm	0.37	11	$-67.5°$	$-45°$

The cameras will only record particle images when the light source is on, and therefore all the cameras will record images at exactly the same instant. We use a Quantronix Darwin duo Q-switch Nd:YLF laser that provides green light at a wavelength of $527nm$ and for frequency from 1 to $10kHz$ with maximum 25 $mJ/pulse$ or $50W$.

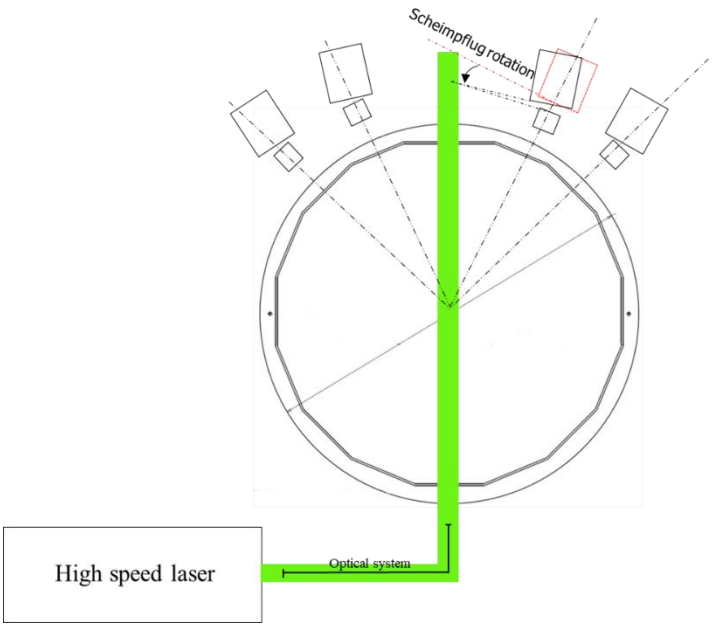

Figure III.4 Positions of laser beam and cameras to the SWT experiment.

As presented in Figure III.4, the cameras are placed in forward scattering positions to optimize the particle intensity signal for the same laser power and camera lens aperture than for backward scattering. For mixed forward and backward scattering setup, we would need to send the laser beam back using a mirror so that each camera get the same signal, one way the laser in forward scattering and the other way in backward scattering.

The propagation of the laser beam through the $1m$ radius of the experiment reduces energy, and one should tune the laser strictly parallel for at least more than 1 m.

III.2.2 Field of view

An optical system (see Figure III.4) made by 4 lenses allow us to obtain an illuminated volume of $45 \times 45 \times 6\ mm^3$. The first two lenses represent a telescope. We use a Galilean telescope which consists of negative spherical lens and positive spherical lens separated by the sum of their focal lengths. Since one of the lenses is negative, the separation distance between the two lenses is short (see Figure III.5). This telescope gives us the radius of the laser beam, $r_2 = 11mm$ (beam of $22\ mm$ diameter). They are positioned just after the exit of the beam from the laser cover. Then, two mirrors were used to align the laser beam with the experiment along the optical path as presented in Figure III.5. A third lens, a cylindrical diverging one, is placed to open the beam vertically. It is followed by a vertical slit to cut the border of the beam in order to optimize the energy distribution of the beam as close as possible to a top hat profile from a gaussian shape. After the slit, we place a convergent cylindrical lens at $205mm$ from the previous one. The convergent lens makes the beam slightly diverging with a radius at output $r_3 = 23\ mm$ (laser beam of 46 mm height) as presented in the sketch of Figure III.6. In this direction, the beam was tuned slightly diverging as no focal lens above 300 mm was available to retain only the high energy center part of the laser to get uniform light distribution in the full height of the volume. The laser beam is finally cut to $6mm$ thickness by a horizontal slit (again only the central part of the beam is conserved to obtain quasi top hat profile). The beam is sent to the SWT and reaches the center of the volume passing through glass and water. Finally, the beam exits from the other side of the experimental bench through a glass window. A mirror is fixed to reflect light to the ground in a bucket full of water to dump the energy of the laser for security purposes.

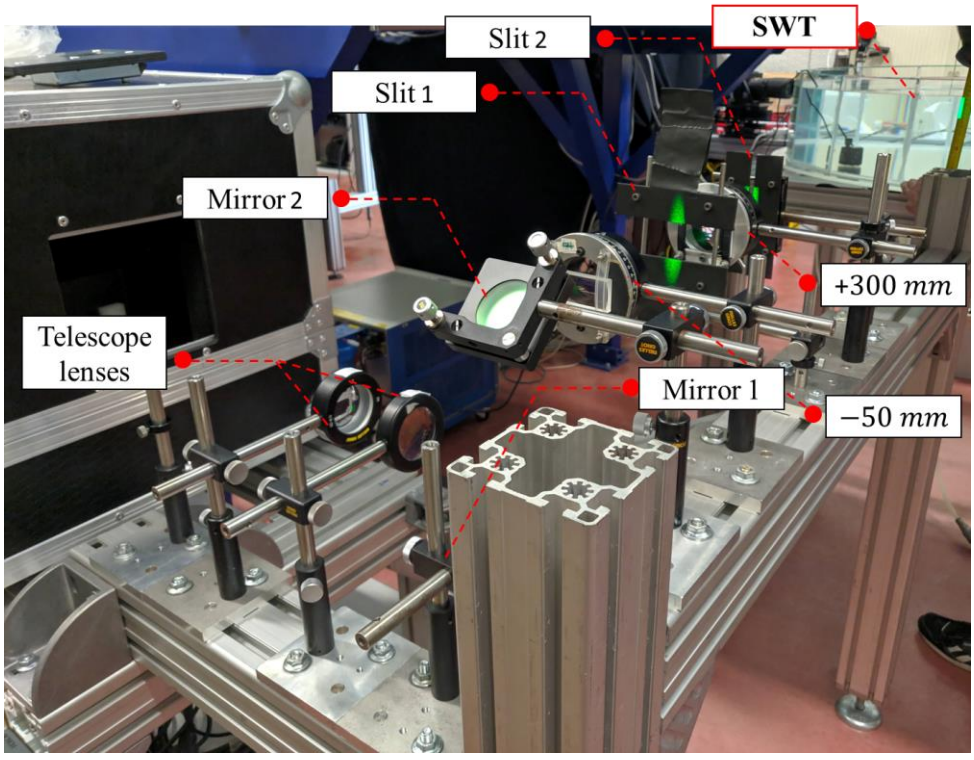

Figure III.5 A photograph of the optical configuration for SWT.

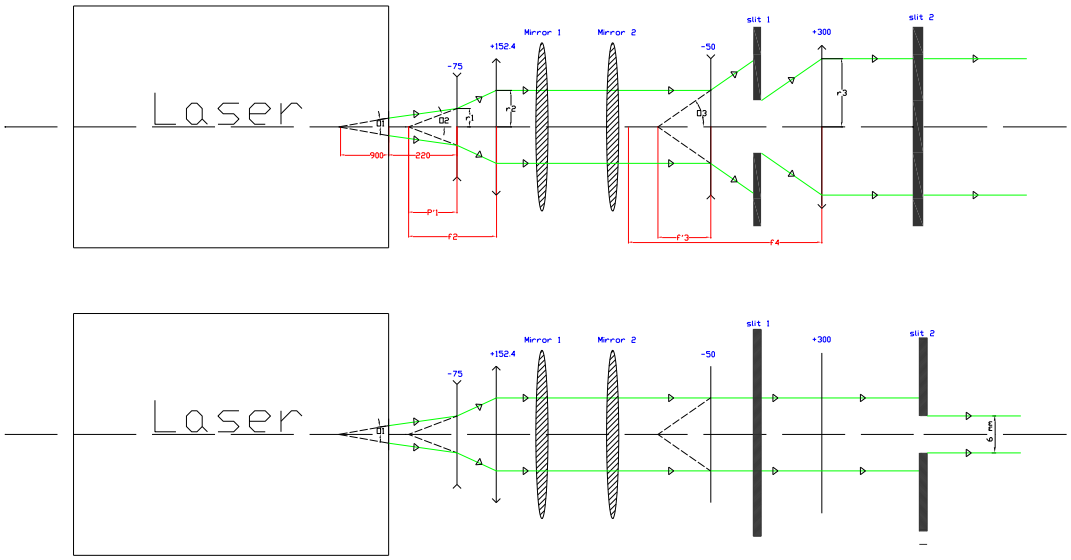

Figure III.6 (Top) side view. (Bottom) top view of a sketch of the optical system used to create the desired laser beam.

III.2.3 Calibration of cameras

The calibration of the system is carried out using the recorded images of a calibration plate. We open the upper template of the SWT, and we place the calibration plate in the center of the volume as presented in Figure III.3. During positioning, a particular attention is paid to verify the alignment between the laser beam and the calibration plate.

The known geometry of the calibration plate allows the mapping of the physical space to the image plane with projection functions. The model used is a polynomial model (see section II.2.4). The application of a calibration correction (Volume-Self-Calibration) between each acquisition is important to calibrate the cameras to the images of the particles. The correction procedure is explained in detail in section II.2.5 Volume self-calibration. This correction leads to an average error in the $8 \times 8 \times 3$ subvolumes of less than $0.02\ pixels$ and maximum of $0.2\ pixels$.

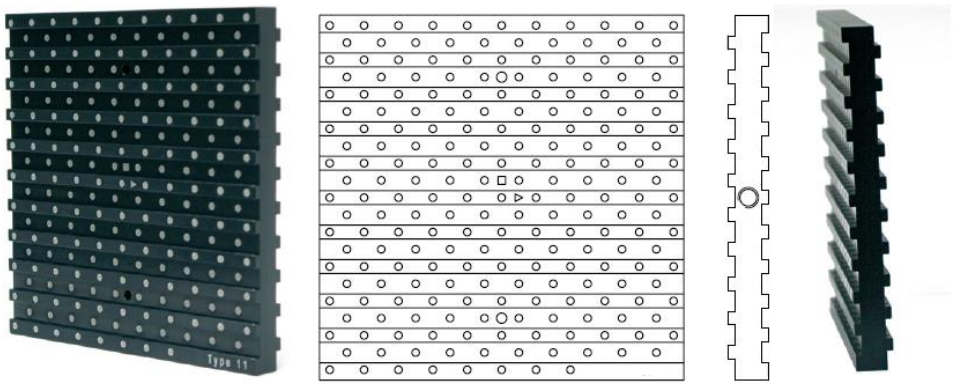

Figure III.7 Two levels 058-5 Lavision 3D calibration plate.

The calibration plate used for all experiments in this thesis is presented in the Figure III.7. It is a two-level double-sided 3D Calibration Plate provided by Lavision of size of $58 \times 58\, mm$ and with a level separation of $1mm$. The separation of the round markers are 5 by 5 mm.

III.3 First cameras configuration

The primary objective of this first testing is to assess our setup optical behavior and its impact on STB results. For this configuration we use 4 cameras spatially aligned at angles of ± 45 and ± 67.5 degrees around the axis of the laser beam. According to the Mie theory (section II.2.2.2) we see that there is a factor of around $3-4$ lower for the light scattered between a point of view at an angle of 67.5 compared to 45 degrees (for better understanding check Figure III.13). This factor increases the overall mean intensity of the cameras at 45° by a factor of two compared to cameras at 67.5°. Examples of particles images for these cameras are presented in Figure III.8 where the $colorbar$ is the intensity in counts. Camera 2 and 3 that are at angles of $\pm$ 45° have a mean intensity of $150\ counts$ compared to $75\ counts$ for cameras at $\pm 67.5°$.

III.3.1 Seeding particles used for this configuration

We utilize the same particles that were used on the VK2 (Debue et al., 2018) & (Valori et al., 2021). The particles are from Lavision. They are glass hollow spheres with diameter ranging from minimum 1 to maximum 30 μm, with the average of 10 μm (Distribution of the particles size is presented in Figure III.9). Their density is $1.1 g/cm^3$. The choice of these particles was based on the image quality obtained during the little Von Karman experiment (VK2), as well as the fact that they were cheap and easy to obtain.

III.3.2 Particles Images quality

During particles images acquisition, we realized that we needed to increase the laser energy to higher levels than in the VK2 experiment (Debue et al, 2018) due to the longer distance that the laser beam had to travel through the radius of SWT ($R_{SWT} = 50cm$) compared to VK2 ($R_{VK2} = 10cm$) and mainly because we have enlarged more the laser beam to be closer to a top hat profile. We also noticed that the background noise has increased (more than VK2) to the point where even the smallest impurities in the water could be seen (down to the minerals of the water used). Figure III.8 shows that when the threshold is set to 100 counts, we can only see a few particles for Cam1 and Cam4 because of the elevated background noise level. Also, the intensity difference is high between (Cam2 & Cam3) and (Cam1 & Cam 4). This could present an issue for the STB algorithm as we can only set one threshold for all cameras. In Chapter IV we will discuss in greater depth the choice of the optimal threshold for our experiment.

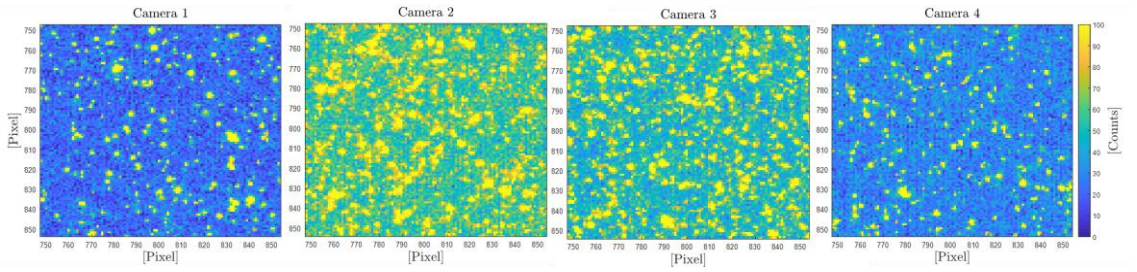

Figure III.8 Examples of images from cameras 1 to 4 at a density of $0.05ppp$ *with same color bar range (100 counts). Images are* 106×106 *pixels.*

On the other hand, all cameras show clusters of particles, probably linked to not well dissolved dry particles powder in water (the dry particle powder make some clusters due probably to static electricity which are hard to break, even if they were mixed hard in a small bottle with water before being injected in the experiment). The polydisperse particle size shown in Figure III.9 has an added effect on the particle images obtained on the four cameras. As scattered light is proportional to dp^2 (see Figure II.4, with dp the diameter of particle), cameras 1 and 4 (67.5° scattering angle) have less particles visible than 2 and 3 as only the bigger ones are visible. So only the brightest ones will be reconstructed, and the smallest ones will contribute to noise. Increasing the laser power cannot solve the problem as then small impurities and dusts in water become visible in cameras 2 and 3 when the small particles become visible in cameras 1 and 4.

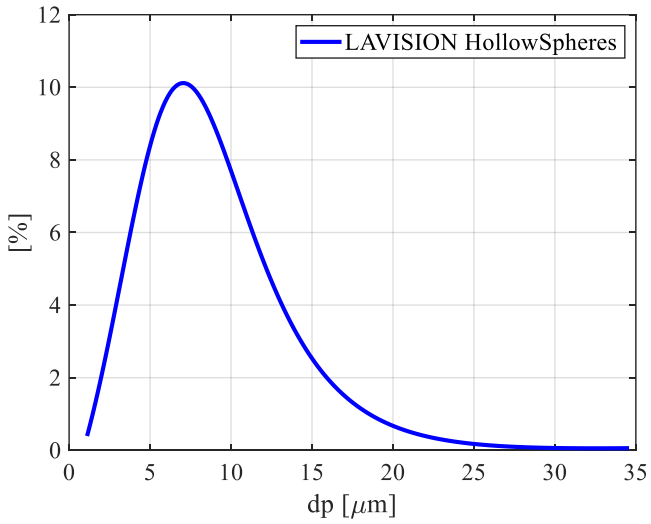

Figure III.9 Histogram distribution of Lavision HollowSpheres particles size with mean dp *of* $9 - 13$ μm *(source Lavision technical sheet)*

Moreover, as bigger particles scatter more light, their particle images will be larger due to the nonlinear digitalization of the camera chip. Indeed, the tail of the particle image intensity distribution is always cut by the camera background noise. So, particle image of smaller particles are more reduced than the bigger ones as the maximum intensity level is closer to the camera background noise than bigger ones. This raises concerns regarding the particle quality. The error in particle tracking is highly dependent on the particle image size in pixels. An analysis of STB results applied to synthetic images in Chapter IV shows that the quality in particles tracking strongly depends on the particle image diameter.

Further, we use a correlation-based method to detect the particles size on PIV images directly. From the raw images we take a window of 64×64 $pixels$ and we correlate it with itself. Then the peak of this window is fitted with a 2D Gaussian equation. Finally, the diameter shown in the Figure III.10 is the module of dp_x & dp_y (the particle diameter in x and y directions defined by 4 times the standard deviation in the corresponding direction of the gaussian distribution fit as defined by (J. M. Foucaut et al., 2004) for 100 randomly selected images for each of the 4 cameras. In this figure we observe that the particle images for most cameras is higher than the recommended particle size. According to the researchers who are working on the STB development, we need to aim for a constant image size of around 2.4 pixels (see (Wieneke, 2013) and (Novara et al., 2016)). Hadad and Gurka, 2013 showed that the size of seeding particles had the largest influence on velocity and acceleration results in comparison to the other parameters in PTV in particular.
Figure III.10 shows that camera 2 has higher particle image size comparing to the other cameras. This can also be noticed on the images of camera 2 in Figure III.8. This could be due to a variety of optical access-related factors like camera focus, lens aberrations etc; More attention should be paid to the focus of the cameras.

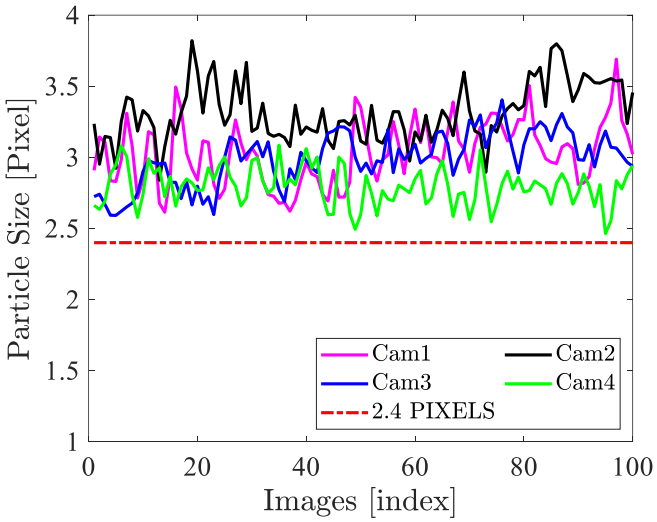

Figure III.10 Mean particles size for 100 images and for all cameras. Particle size is estimated by fitting a 2D gaussian to the peak of correlation of one image by itself. Window size used for correlation is 64×64 *pixels.*

The second feature of the particle image that we noticed during acquisition is that the software (Davis) was unable to detect higher concentrations than 0.02 ppp, despite our efforts to increase the images density to 0.05 by adding more particles inside the volume. For this reason, we wanted to check the particles density using a simple code that detect the particles images. We use a MATLAB built in function to expand the image pixels using a user defined structuring element (here square 3 by 3 pixels element). The function is called "`imdilate` [3]". Then, we use a logical operation to find where the dilated image grey level is equal with the original image and where the original image is above a certain intensity threshold (in counts). The number of values equal to 1 in this logical image obtained is then the number of particle. The method is summarized as follow:

[3] For more information about the function "imdilate": https://fr.mathworks.com/help/images/ref/imdilate.html

```
Finding image density
 1:  loop on all Orig_image
 2:              New_Image = imdilate(Orig_image, [3 × 3]) Figure III.11 (b)
 3:       then
 4:              do a logical operation where:
 5:              Final_image=(New_image == Orig_image)
 6:              &
 7:              (Orig_image>= defined_Thresold)
 8:       then
 9:              find the illuminated pixels (x,y) in Final_image
10:              Calculate the density from Final_image.
11:  end loop
```

An example of each step of the procedure is presented in the Figure III.11. The first figure is the original image, (b) is the dilated image using "`imdilate`" where the particles in a $3px \times 3px$ window are expanded over the area of the window using the biggest intensity peak in the same window and (c) is the final image that is used to calculate the density of the image. We use this approach to have a common method of detection for all the images in this thesis.

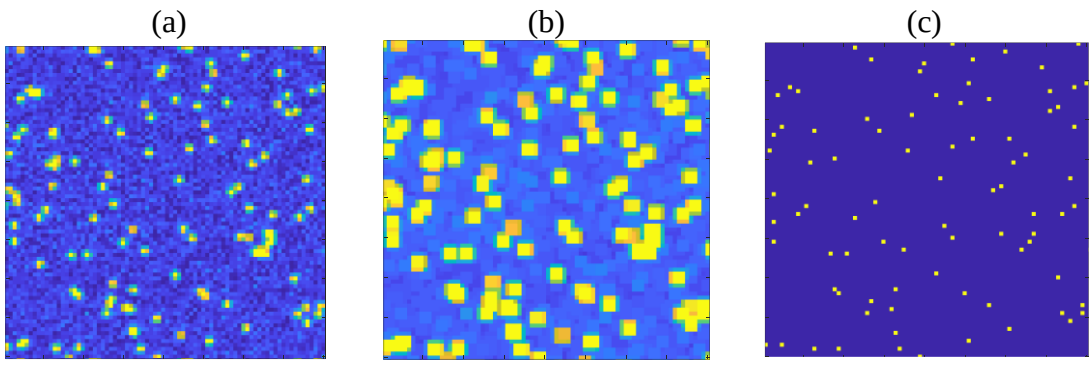

Figure III.11 (a) Original_image. (b) New_image with pixels expanded using "imdilate" from Original_image and (c) result of the logical operation between Original_image and New_image for a specific threshold.

The results are presented in the Figure III.12 for two camera images with physical density of $0.05ppp$ estimated from the weight of particles in a known volume of water supposing the camera is perpendicular to the FOV (field of view). Camera 1 and Camera 2 are at 67.5° and 45° respectively with respect to the laser beam. The concentration detected for Camera 1 is $0.008ppp$ on average (equivalent to 23,000 particles per time step) for all time steps for a threshold of 70 counts and is $0.02\ ppp$ for Camera 2. This result is compatible with the software's estimation. As a result, we're faced with the challenge of improving image quality. It will be shown in Sections III.5 that only a small fraction of the particles are tracked by the STB algorithm.

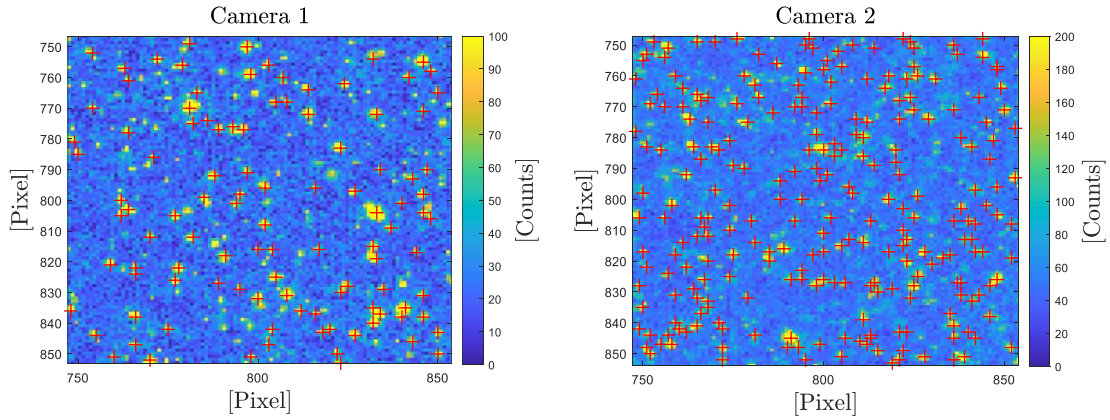

Figure III.12 Examples of images from cameras at a density of $0.05\ ppp$ *with a colorbar of 100 counts for camera 1 and 200 counts for camera 2; Red plus signs* (+) *are the particles detected by our detection procedure used to compute the density of particles in the images.*

III.4 Second cameras configuration with monodisperse particles.

A second test was performed with different position of the cameras. In the first configuration (previous section) the cameras were placed at angles of 45° & 67.5° with respect to the x axis (the laser beam axis). Placing the cameras at angles of 22.5° & 45° might improve this setup because these angles get more scattered light as illustrated in Figure III.13. The particles we are using in this section are half the size of the particles used before. Light scattering is related to particle diameter squared (d_p^2), by dividing the particle size by 2, one needs to increase the laser intensity by a factor of four to compensate and ensure that the particles are adequately illuminated. By placing the cameras at 22.5° *and* 45°, we increase the laser energy by 33% only compared to the 1st configuration. This was not an objective by itself, but we do know that the less energy we use, the less background noise we will have.

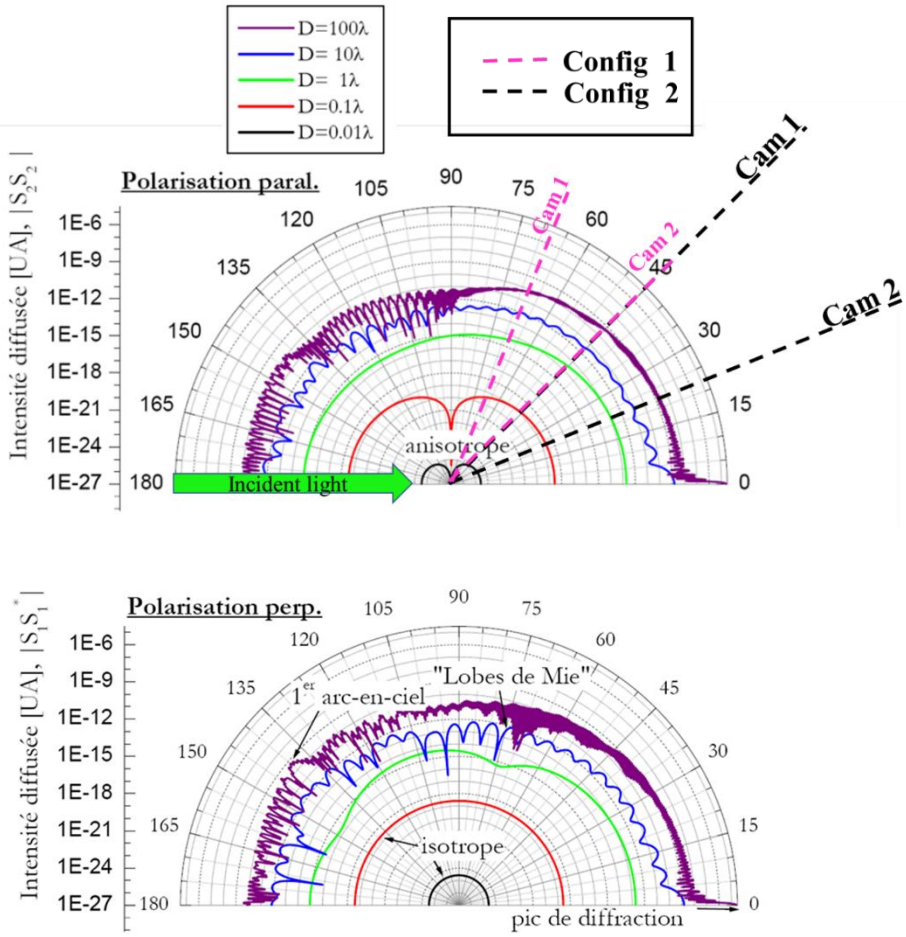

Figure III.13 Mie polar chart of scattering lights for different particles size in function of the light wavelength. (Top) Mie chart for parallel polarization incident light. (Bottom) Mie chart for perpendicular polarization incident light. The position of cameras for the first and second configurations are indicated with pink and black dash lines respectively on the top figure.

It is also possible to reduce background noise by improving the quality of the water used in the SWT. The noise level we observed in the previous section was most likely caused by a lack of water quality. For the first configuration, we used pure water, but we had to transport it in containers. This minor detail has probably affected the quality of the water. To bypass this difficulty, a specialized filtration system was installed close to the experiment. The filter used is Polyamide demineralizator E300 with $22L$ of resin that can filter up to $600L$ of water. The volume of our water tank is $200L$ so this filter can produce clean water for 3 full fillings. The system has a flow rate of $250L/h$, it consists of a prefiltration unit of 5 μm, then 2 ion exchange columns by a mix of cationic plus anionic resins, finally a 1 μm final post-filtration, the purpose of which is to avoid the possible release of resin.

III.4.1 Improved seeding particles

The second and most important concern, as mentioned before, is the particles properties. The particle size used in the first configuration is sparse, ranging from 3 to $30\mu m$ as we see in the distribution of particles diameter of the Lavision HollowSpheres (Figure III.9). To lower the levels of background noise that may come from small particles ($\leq 1 -$

$3\mu m$) as well as the number of particles clustering together, it was decided to invest in new particles with improved monodisperse properties.

The particles used for this second configuration are Polystyrene particles with mean diameter of $d_p = 5.09\ \mu m$ from Spherotech, *Reference: PP-50-10*. These particles are composed of linear polystyrene without any cross-linking agent. They have sulfate groups on their surface. As a result, these particles are negatively charged which can help to avoid clustering problems. Microscopic photo of perfectly sphere-shaped polystyrene particles are shown in Figure III.14 to illustrate the uniformity of their size. Also, a very important advantage of these beads is that they are protein coated which can substantially increase their longevity specially in the water (according to Spherotech Inc).

Further about these particles, they cannot tolerate organic solvents such as toluene, xylene, chloroform, methylene chloride, acetonitrile, dimethyl formamide or acetone. However, Spherotech polystyrene particles are stable in the presence of some water miscible solvents such as dimethyl sulfoxide and alcohols.

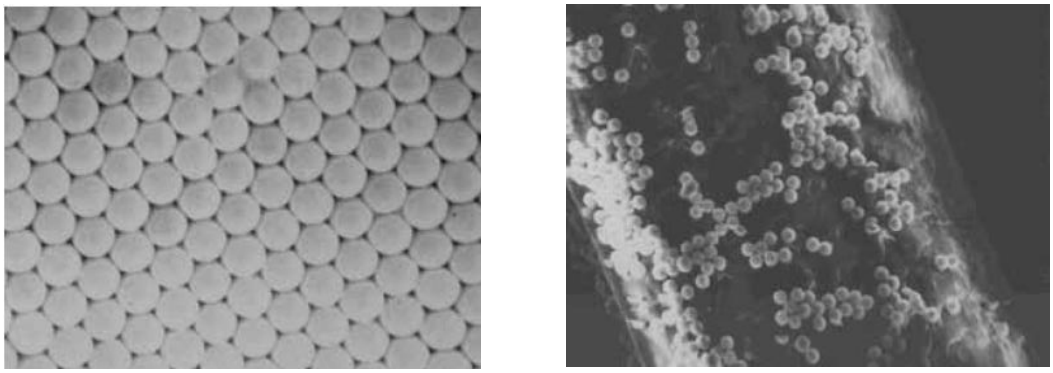

Figure III.14 3 Sphero polystyrene 5.09 *µm diameter particles (Reference: PP-50-10)*

These beads are significantly more expensive than the Lavision one used before, nonetheless they are important to ensure better quality images and tracking results. They are shipped in a solution of 10 or 100 ml with 5% weight to volume ratio. Summary of their characteristics are included in the Table III-2. Also Figure III.15 is the histogram of particles number as function of their diameter. This plot shows a maximum particle size $dp = 7.5\ \mu m$ and a minimum of $dp = 4.8\ \mu m$ (A tight size range of Spherotech polystyrene particles is maintained by monitoring size according to Spherotech).

Table III-2: Properties of Spherotech PP-50-10 particles.

Mean diameter	5.09 (μm)
Particle shape	Spherical
Particle material	Polystyrene
Solution (ml)	10 or 100 (5% particles)
Density	1.05 (g/cm^3)
Price	160 € (10ml) or 1260 € (100ml)

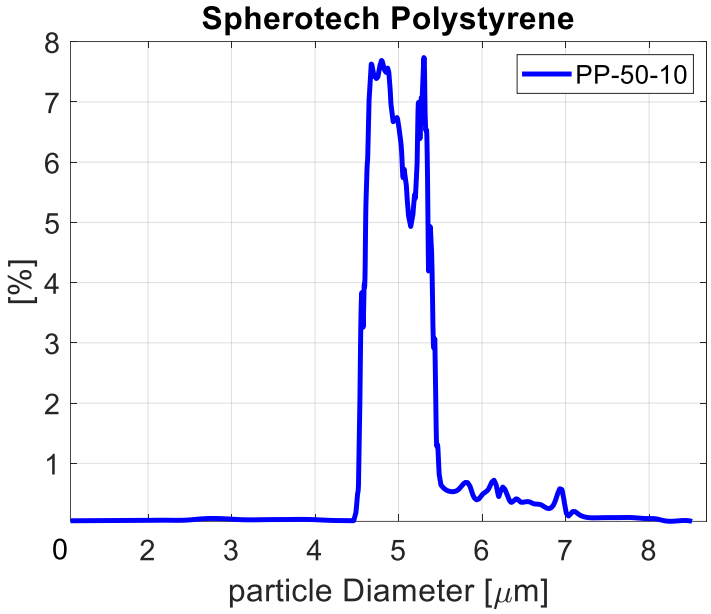

Figure III.15 Histogram distribution of Spherotech Polystyrene particles size with mean diameter of $5.09\ \mu m$.

III.4.2 Impact of configuration changes to image quality

For the second configuration we used the same optical setup as the one described in Figure III.5 but we increased laser energy by 33% compared to the first configuration to get sharp images of the particles on all cameras. Figure III.16 shows the difference in particle size recorded on images employing the new particles versus the old particles used for the first configuration. The size of the particles is clearly closer to the recommended size of 2.4 pixels as can be seen in Figure III.16 and closer to $2px$ estimated by the diffraction formula (II-6). Additionally, the size variations in each image are lower than the values reported previously. This proves that when it comes to clean and sharp images, good quality monodisperse particles are essential. The mean size computed on 3226 images of the Spherothech polystyrene particles is 2.6 pixels for all cameras compared to 3.2 pixels for Lavision HollowSphere particles. It should be noted that the particle image should have, in theory, the same size on the images since the magnification is the same $(M = 0.37)$. However, since the particle size is estimated by the correlation method mentioned in section III.3, the estimated particle size depends on the signal of the autocorrelation. To put it another way, it is determined by the highest correlation peak at the center of the specified window which is influenced by the biggest particles inside the window (more intense so more weight). Because the Spherotech particles are monodispersed, the signal of particle image obtained is more homogeneous (less fluctuating) as shown in the Figure III.16(left).

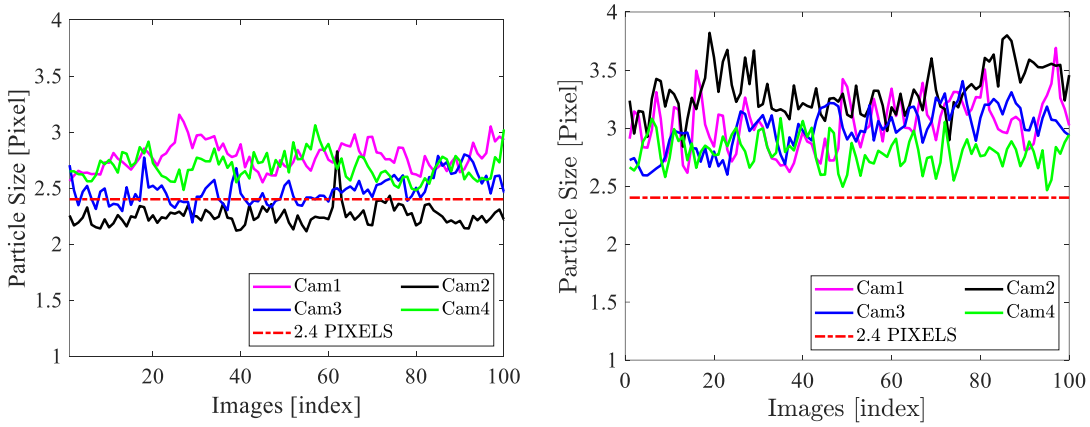

Figure III.16 Particles size for 100 random images. ***(Left)*** *Spherotech (second configuration).* ***(Right)*** *Lavision particles (first configuration). Particle size is estimated by fitting a 2D gaussian to the peak of correlation of one image by itself. Window size used is* 64×64 *pixels.*

From the Figure III.17, that represents a probability density function of the camera images (including background noise), one can notice a change of intensity as a belly shape appears for the camera images of the second configuration for an intensity of 500 to 1000 counts (more visible for camera at 45°). This shape could be an indicator that we have more actual particle images, and the peak of low intensities (background noise) is comparable for all cameras (around 60 counts).
Further, by comparing the cameras of the same angles, 1st Config 45° and 2nd Config 45°, we notice that for intensities higher than ~1200 counts, the intensity for the 2nd configuration is lower than the 1st configuration. This implies that we have less big particles scattering high levels of light, hence it validates the narrow distribution claimed by the particles manufacturer. The two other lines are not comparable because of angle difference.

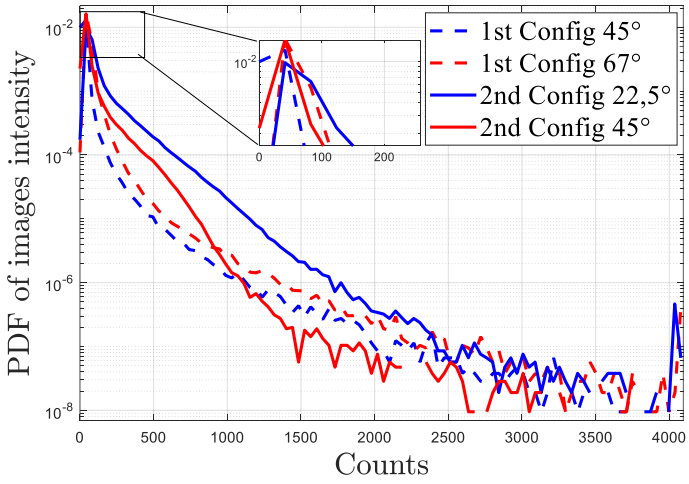

Figure III.17 Comparison between PDFs of images intensity of Camera1 and Camera2 for the first and second configurations.

III.5 Shake the Box results for both configurations

Aside from image quality, the properties of Shake the Box tracks are the most important to compare the two configurations. The major goal is to assess the tracking algorithm efficiency by comparing the results of these two configurations. To analyze the full potential of STB, we compare the results of several sets for one configuration. Cases were acquired at multiple images density ϕ_{im} increasing the spatial resolution as much as possible without compromising the track numbers and track length. Finally, the presence of erroneous tracks (ghost tracks) is an important factor and should be lessened as much as possible. In this section, we present STB results for three image densities 0.02, 0.05, and $0.07 ppp$.

Also, to look at the influence of the mean displacement of the particles, multiple displacements have been tested to check if we can improve the quality and quantity of the tracks. The displacement can be modified by skipping a specific number of images during the STB processing, 1dt represents the original sampling rate, 2dt is done by skipping one image and 3dt by skipping 2 images. The table below summarize the parameters of the 8 tests, 3 tests for first configuration and 5 for the second configuration. Higher densities have been tested for the second configuration as the property of the particles seems to improve the quality of the images.

Table III-3: Total number of tests done for each configuration.

ϕ_{im} $[ppp]$	Displacement	1st configuration	2nd configuration
0.02	$1dt$	☑	☑
0.05	$1dt$	☑	☑
	$2dt$	☑	☑
	$3dt$	-	☑
0.07	$1dt$	-	☑

The parameters of the Shake the Box were tweaked to maximize the number of tracked particles. Parameters were tested rigorously before choosing the perfect set, mainly particle count threshold, allowed triangulation error, shaking loops (see IPR section II.4.1) and velocity limits in order to get the tracks with the best properties. No image preprocessing was applied, and median filter was left off since the tests showed no visual spurious vectors (more info about median filter is included in section II.4.5). These tracks can be detected visually on the results by an incoherent displacement of particle compared to neighbors as well as illogical velocity magnitudes compared to maximum velocity of the majority of tracks. The volume needs to be carefully inspected before settling for a set of parameters. After testing, IPR parameters were left as default (4 inner and outer iteration loops) for both configurations.

III.5.1 STB Comparison between the configurations.

We present in Figure III.18 a 2D visualization of tracks for 1st and 2nd configurations of particles that are tracked with 10 time steps for each track plotted. Quick examination to these two snapshots of tracks shows a higher tracks density in the results of the second

configuration and for the same **estimated** image density (density is estimated by calculating the number of particles to put inside the volume to reach a specific concentration in particle per pixel ppp).

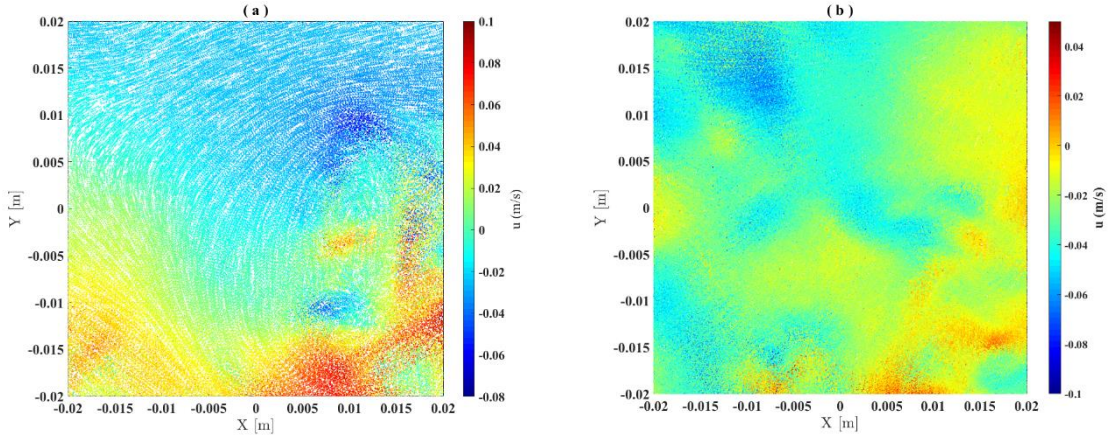

*Figure III.18 2D representations of tracks for $\phi_{im} = 0.05\ ppp$ for **(a)** first configuration and **(b)** second configuration. Tracks are plotted with 10 time steps. Both are color coded with u component (velocity in x direction).*

Figure III.19 is the number of tracked particles per time steps for all cases presented in Table III-3. The difference is high between dotted blue line (1st Config) and solid green (2nd config) for an estimated image density of $0.05ppp$. Precisely, we are talking about an average of 1.9×10^4 and 9.0×10^4 tracked particles per time step, resulting to a ratio of tracked particles over particles inside the volume of $1.9 \times 10^4 / 1.28 \times 10^5 = 14\%$ and $9.0 \times 10^4 / 1.28 \times 10^5 = 70\%$ for the 1st and 2nd configurations respectively where 1.28×10^5 is an estimation of the total number of particles in the measured volume and per time step for $0.05ppp$. For an estimated image density of $0.02\ ppp$, the tracking ratio for the 2nd configuration is 90% while for the 1st configuration the tracking ratio is only 20%. The difference is outstanding between the results of these two configurations at least from the point of view of number of tracked particles.

Looking at the histogram of track length for the 2nd configuration results in Figure III.20 ($\phi_{\text{im}} = 0.02, 0.05$ & $0.07ppp$) we surprisingly notice that the track length for $0.07ppp$ and $0.02ppp$ are longer than $0.05ppp$, this result can be due to too many factors mostly related to the actual flow field (different runs for each concentration and statistics are not converged for one run of 2.6s). In other words, we cannot really conclude on the track length results. Similar remark can be said by comparing the 1st configuration results in Figure III.20.

Finally, the spectrum of raw position (Figure III.21) data for track of minimum length of 100 time steps is also tricky to analyze considering the unknown properties of the flow captured for each specific set, but it is noticeable that the energy at low frequencies increases by increasing the images density which could indicate that increasing the ppp increases the length of track in the large scale structures. We can consider that the plateau reached at high frequency can give an idea of the random error level. In the figure it is clear that the second configuration give systematically less noise than the first one and the error increases a little with the concentration due to the more difficult tracking (higher probability of overlapping particles or hidden particles by other).

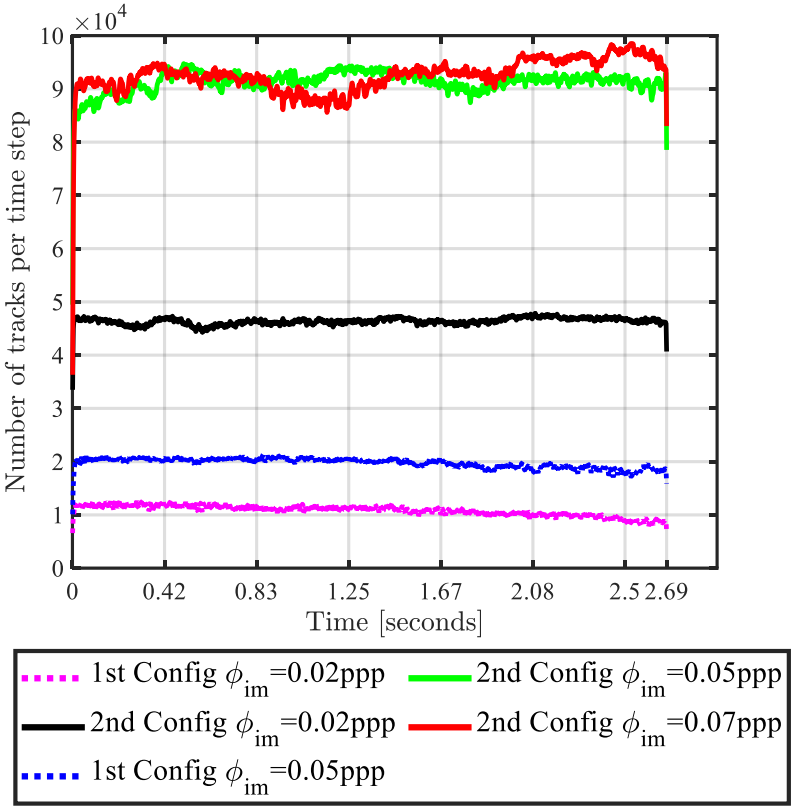

Figure III.19 Comparison of number of tracked particles per time step for a total of 3226 images for different image densities $\phi_{im} = 0.02$ & 0.05 ppp for 1st configuration and $\phi_{im} = 0.02, 0.05$ & 0.07ppp for the 2nd configuration. All results showed are for a displacement of 1dt.

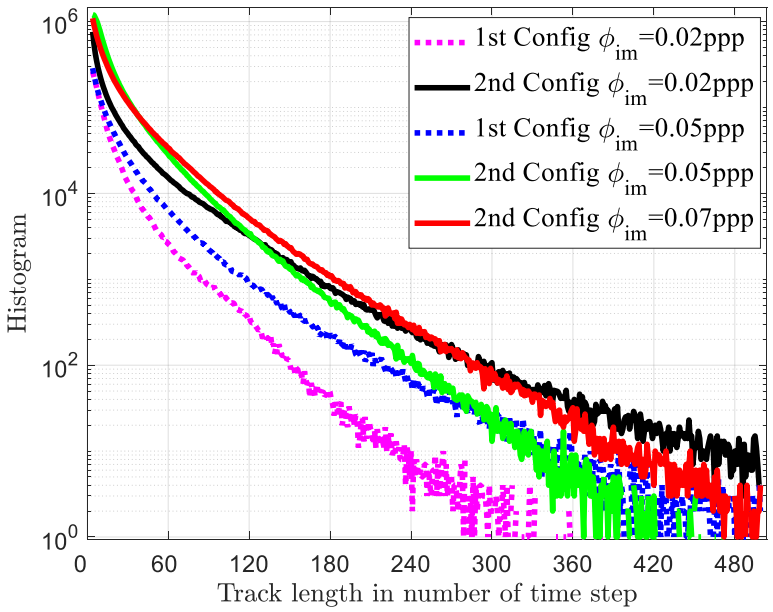

Figure III.20 Histogram of track length as function of ϕ_{im} for displacement of 1dt.

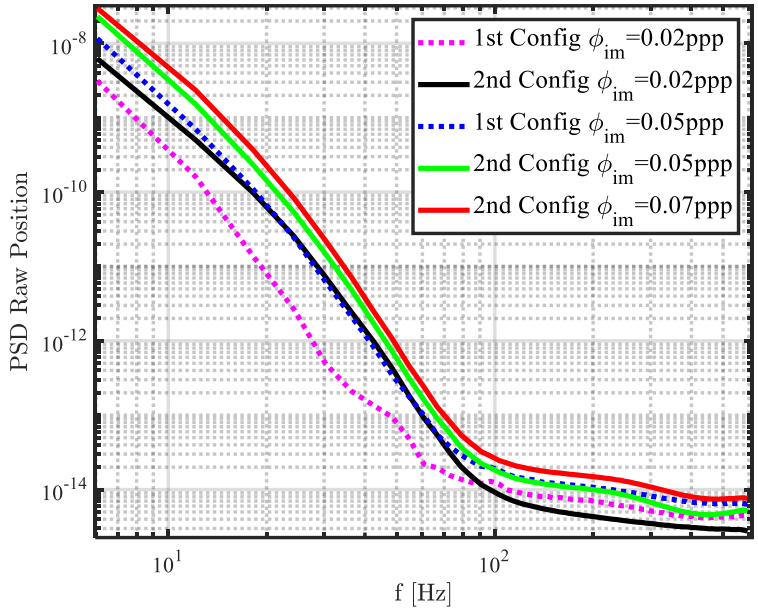

Figure III.21 Power spectrum of raw positions of tracked particles for several images densities ϕ_{im} and for displacement of 1dt

III.5.2 Effect of mean displacement.

The mean particles displacement in pixel for all the cases at 1dt (original sampling) don't exceed 2.8 pixels (Table III-4). The data could be oversampled, meaning the displacement between two snapshots are too close to track efficiently the next time step of a track. (Schanz et al., 2014b) used synthetic images with a mean displacement of $6vx$ (and maximum displacement of $11vx$) and they were able to detect 99,6% of particles even for a $\phi_{im} = 0.125\ ppp$. This seems to indicate that a mean displacement around $6vx$ is possibly suitable for STB algorithm.
In the following, we check whether a displacement of $2dt$ (mean displacement of around 4.1 to $4.8vx$) and $3dt$ (mean of around $7vx$) could help to improve the STB outcome.

Results from 1st Config

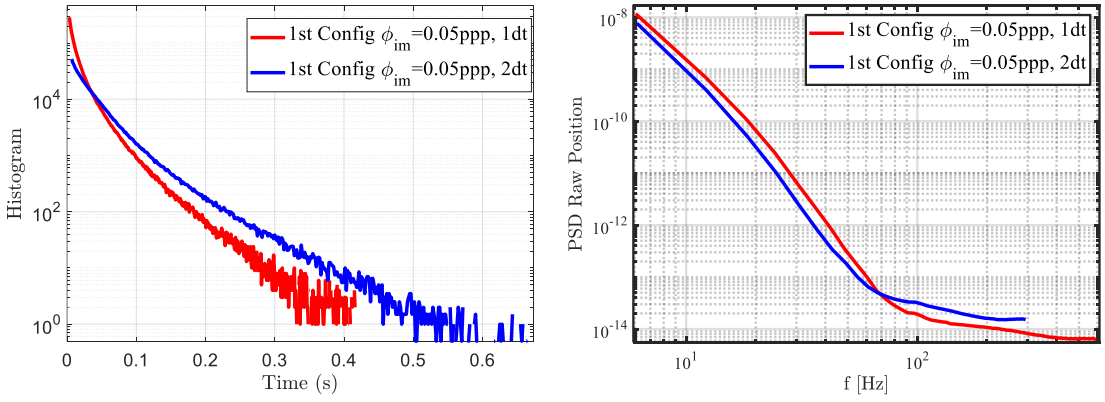

*Figure III.22 **(Left)** Histogram of track length for displacement of 1dt and 2dt. **(Right)** spectrum of raw positions for the same two cases.*

The first configuration in Figure III.22 (left) shows an improvement in track length by increasing mean displacement (case 2dt), with fewer small tracks and longer tracks that go up to $0.6s$, corresponding to particles being tracked over 350 images with 2dt as well as a slight increase in the number of tracked particles of 5% (Table III-4) (keep in mind that particles are always entering and leaving the volume). This slight increase in number of tracked particles could be explained by the sampling improvement. Indeed, the fit extrapolation created by the STB algorithm to predict the position of a particle in the following time step is better due to ratio of noise on particle positions of previous time steps over particle displacements which becomes smaller. The less systematic and random error on the past positions of a particle, the better is the estimated position of a new particle in a trajectory by the fit extrapolation. As a result, the rest of the tracks extrapolation procedure will be improved, giving more chance to the algorithm to track the particles at the next time step.

Results from 2nd Config

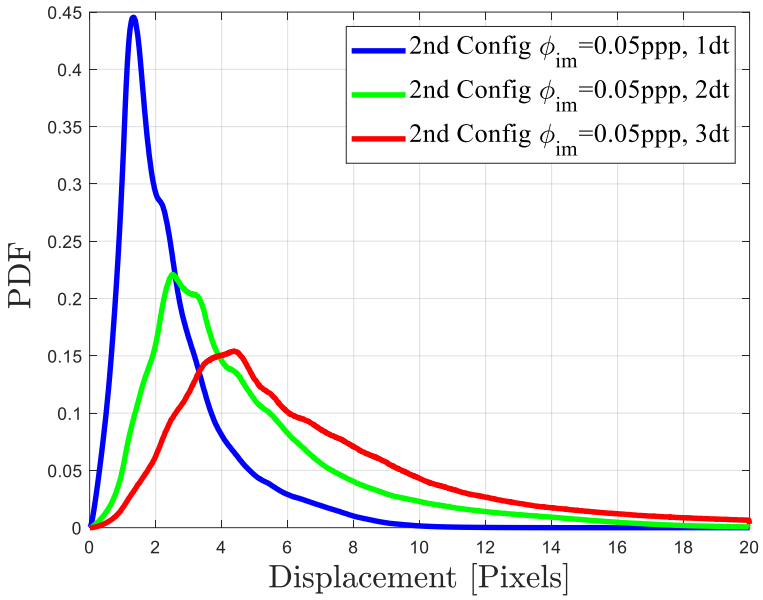

Figure III.23 Probability density function of displacement in pixels for the same run of the 2nd configuration but for several dt obtained by skipping images.

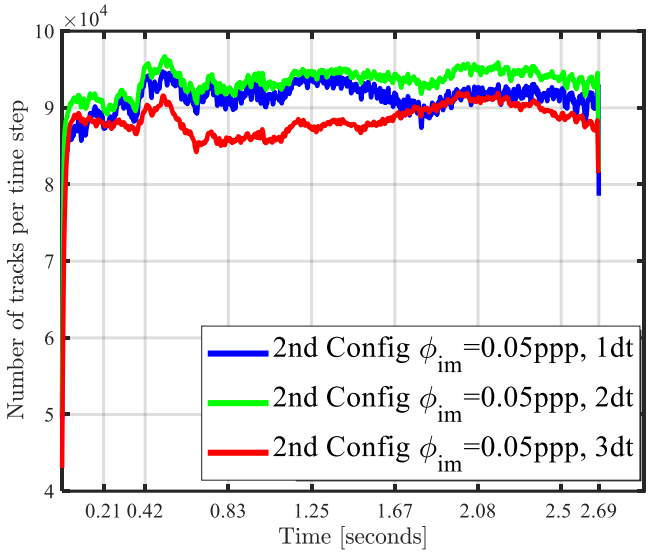

Figure III.24 Comparison of number of tracked particles per time step for different displacements $1dt, 2dt$ *and* $3dt$ *(2nd configuration).*

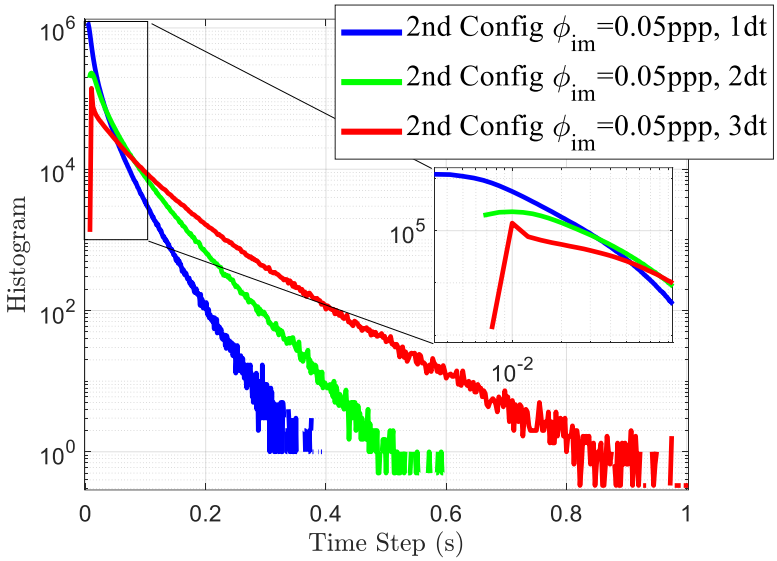

Figure III.25 Histogram of track length as function of displacement of 1dt, 2dt and 3dt.

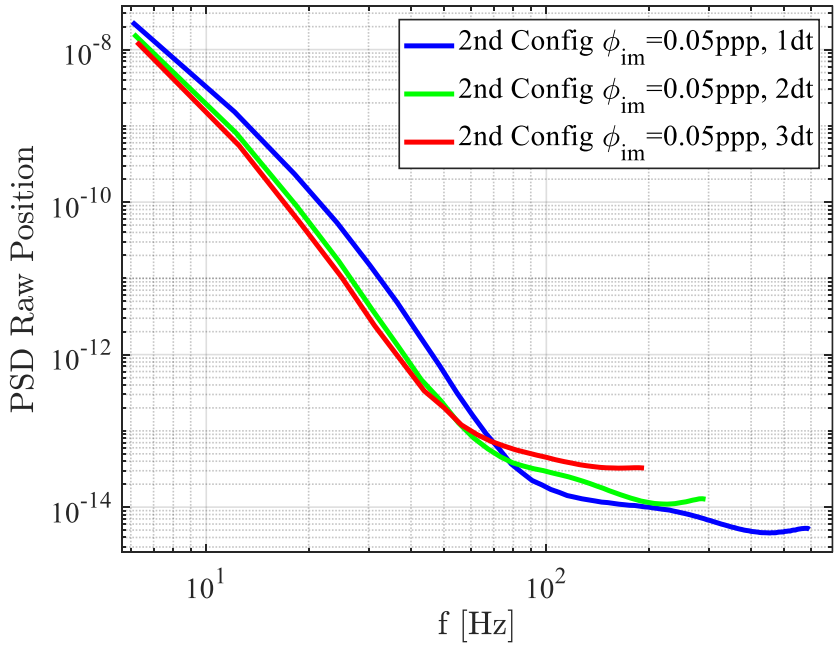

Figure III.26 Spectrum of raw positions for three displacements 1dt, 2dt and 3dt (2nd configuration).

Figure III.25 confirms the findings of Figure III.22 (left). Both figures indicate a clear improvement of track length by increasing the time steps of the STB analysis. On the other hand, when comparing the 1dt and 2dt plots of tracked/identified particles in Figure III.25, it is remarkable to see that there are more tracked particles at each time step for the case of 2dt, owing to the fact that the tracks are longer, and hence more tracked particles are added at each time step. The average number of particles tracked per time step is 9.3×10^4 for $2dt$ compared to 9.1×10^4 for $1dt$.

On the other hand, increasing the displacement to $3dt$ shows a significant increase in the track length. However, particles number decreased slightly to 88×10^3 per time step, and we saw some spurious vectors are detected as shown in Figure III.27. These ghost/wrong tracks were not visible for the cases of 1dt and 2dt. Results could be improved for this specific case, but without having a reference it is difficult to tune the parameters of STB. This leads us however to suggest that the 2dt displacement is the best compromise.

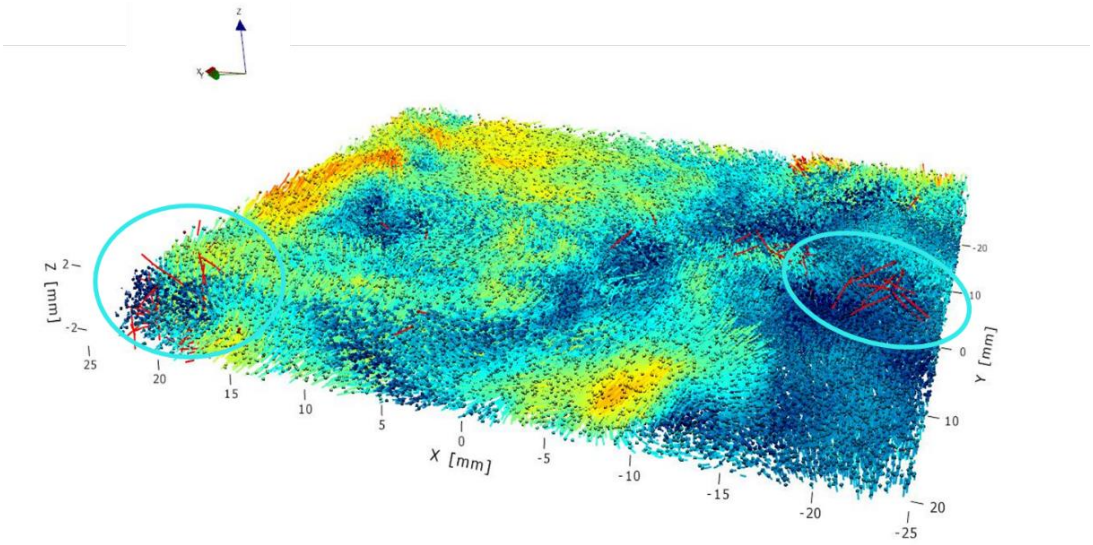

Figure III.27 3D view of the tracks for the case of $\phi_{im} = 0.05ppp$ and displacement of 3dt between time step number 1137 and 1150. Regions with more spurious tracks are indicated with blue circles.

III.6 Conclusion

The experimental configurations presented in this chapter were essential to tune multiple parameters. What we learned is that water and particles quality are crucial for better Raw images. On the other hand, the second configuration of cameras seems to be the better solution, especially when using smaller particles because smaller particles require more laser energy. Hence the advantage of the second configuration that offers cameras closer to the direct incident light.

Shake the box results were compared at different images densities to test the optimal spatial resolution that we can reach without compromising the quality of tracks. From table below, the ratio of particles tracked for $0.02ppp$ can reach 90%, 70% for $0.05ppp$ and 55% for $0.07ppp$. The sampling comparison suggests that an optimal displacement could be around $4-5\,px$ (2dt in our case). But using this information alone it is not simple to estimate the optimal density and displacement for our application. For that reason, one can ask the following questions: What is the error on the particles position as function of different ppp and STB parameters? What is the percentage of ghost particles/tracks?

Conclusions are difficult to draw since we don't have a reference with ground truth. Moreover, the code we are using (STB) is a black box with multiple parameters (allowed triangulation error, particles grey level threshold, IPR, median filter etc.) which happens to be very sensitive on the results. For this reason, we decide to go deeper in the investigation using synthetic PIV images generated using a solution obtained by a Direct Numerical Simulation (DNS) of the Navier-Stokes equations.

Table III-4: Summary of the STB results of configurations 1 & 2.

Cases		**1st Configuration**		**2nd Configuration**		
ϕ_{im} [ppp]		0.02	0.05	0.02	0.05	0.07
Estimated particle per Time Step. $\times 10^3$		51	128	51	128	170
1dt	Average of tracked particles / Time Step $\times 10^3$	10	19	46	91	93
	Average of track length [**Time Step**]	15	21	24	19	23
	Average of displacement [**px**]	1.5	2.1	2.2	2.4	2.8
2dt	Average of tracked particles/Time Step $\times 10^3$	-	20	-	93	-
	Average of track length [**Time Step**]	-	21	-	20	-
	Average of displacement [**px**]	-	4.1	-	4.8	-
3dt	Average of tracked particles /Time Step $\times 10^3$	-	-	-	88	-
	Average of track length [**Time Step**]	-	-	-	23	-
	Average of displacement [**px**]	-	-	-	7.2	-

Chapter IV Accuracy assessment of ‘Shake the Box’ 4D-PTV using synthetic images.

Contents

List of symbols for this chapter:

ϕ_{im}	Image density $[ppp]$.
N_{DNS}	Number of DNS (reference) particles.
N_{STB}	Number of STB tracked particles.
N_{match}	Number of matchings from the tracked particles.
N_{gh}	Number of ghost particles.
n_{DNS}	Number of DNS (reference) tracks.
n_{STB}	Number of STB tracks.
n_{match}	Number of matching STB tracks.
n_{gh}	Number of STB ghost tracks.
$GTML$	Ghost tracks mean length.
ψ	Particles matching ratio of STB with DNS; $\psi = \frac{N_{match}}{N_{DNS}}$.
ε	Systematic position error between a reference particle and a matching particle.
C_T	Coverage of an STB track - The number of detected particles per one STB track compared to DNS track.
f_r	Fragmentation of an STB track - How many STB track(s) matching with one DNS track.
d_p	Mean particle image size [in μm or pixel].
dx_{DNS}	DNS spatial resolution.
dx_{expe}	Experiment spatial resolution $= \Gamma \times dx_{DNS}$. Γ is a factor we use to control the transformation from DNS to experiment.
Δ_{PTV}	Mean displacement of particles positions between two frames $[vx]$.

IV.1 Introduction.

In this section, we describe the principles of the synthetic PTV tests that we performed to assess the impact of several factors on the reconstruction quality of 'Shake the box'. We will focus on the description of our image generating process, the STB tracking as well as quality evaluation metrics that we will consider. To this end a generator of synthetic tracks from DNS was used, allowing the creation of tracks at different seeding densities. Projections of such tracks on virtual cameras are used as input data for a STB analysis. All the tests were performed with a set of 250 images.

The quality of results is assessed by means of statistical results: matching ratio ψ with respect to the synthetics (ground truth) tracks n_{DNS}, systematic position error ε, and the percentage of ghost particles. For this end, multiple tests were done using different sets of synthetic images. Most of these tests are defined by changing particles images densities, ϕ_{im}, particles image diameter dp and by adding background noise to the synthetic images. Another parameter to be tested is the effect of the mean displacement, Δ_{PTV}. Original mean displacement is about $6vx$, where all the 250 images are used. Increasing the mean displacement is done by skipping one image while processing in "*DAVIS 10.1.0.56724"* software which gives a mean displacement of $12vx$. By Skipping two images we end up with a mean displacement of $18vx$. On the other hand, we wanted to test a mean displacement that is close to the ones of the configurations of Chapter III. For this, intermediate particles positions were interpolated by spline interpolation to create a set of 500 images and mean displacement of $3vx$. Another very important parameter is the particle size of the images that can be modified by changing the point spread function (PSF) (section IV.3.2) of the particles images which increases the diffraction spot of the particle. Three different particles images sizes were tested with mean size of $dp = 2.4px, 3.8px$ and $4.8px$. A summary table of the test to be performed are provided in the Table IV-1 for four particles densities ranging from $0.01ppp$ to $0.07ppp$. We did not push the density further in this section as it is already challenging for the actual experiments to exceed $0.05\ ppp$ as we saw in Chapter III.

The difference of this study to its counterpart found in the bibliography is the fact that we apply STB to synthetic images as if they were real PIV images recorded by the cameras (DNS of turbulent flow as input for particle positions and synthetic calibration images were generated). Then, we follow all the steps of STB processing from the calibration process to volume self-calibration. The studies of (Schanz et al., 2014a) & (Schanz et al., 2016b) are rather an assessment of the STB algorithm assuming a perfect calibration and self-calibration results which can explain the difference in outcomes between our results and their results.

Table IV-1: Experimental parameters tested on synthetic images.

ϕ_{im} $[ppp]$	Noise	Displacement				Particle size		
		$0.5dt$	$1dt$	$2dt$	$3dt$	$2.4\ px$	$3.8\ px$	$4.8\ px$
0.01	☑	-	☑	☑	☑	-	☑	-
0.03	-	-	☑	☑	☑	-	☑	-
0.05	☑	☑	☑	☑	-	-	☑	☑
0.07	☑	-	☑	-	-	☑	☑	-

IV.2 Description of the DNS used to create synthetic images.

Synthetic images were created using Lagrangian positions and velocity fields from a Direct Numerical Simulation (DNS) of the Navier-Stokes equations solved with a pseudo spectral code.

The DNS is forced with Taylor Green vortex integrated on a triply periodic domain using a pseudo spectral code with a 2^{nd} order Runge-Kutta scheme with a time step of $\Delta t_{DNS} = 0.001$. Up to 60 millions particles are integrated using 2^{nd} order Runge-Kutta scheme associated to a tri-linear interpolation of the velocity at the position of the particles. The position of the particles is saved every 4 time steps ($\delta t_{DNS} = 0.004$). The simulation was performed on a 768^3grid in physical space and a $2/3$ rule is used for the desaliasing.

Table IV-2: DNS parameters used for creating PIV images

Space discretization $dx_{DNS} = 2\pi/768$	$dx_{DNS} = 0.00818$
Taylor Reynold number Re_λ	$Re_\lambda = 68.9$
Integral scale	$l = 0.829$
Kolmogorov length scale	$\eta_k^{DNS} = 0.02219$
DNS resolution	$k_{max} \times \eta_k^{DNS} = 5.7$
Δt_{DNS}	0.001
δt_{DNS}	0.004

The Table IV-2 provides the DNS parameters. The resolution of the DNS can be computed to be 5.7 or $dx_{DNS}/\eta_k^{DNS} = 0.367$ which means that the Kolmogorov scale is discretized with 3 meshes.

For creating the synthetic tracks, we select a domain of the same size of the one in the experiment of Chapter III ($45 \times 45 \times 6\ mm^3$) projected on four cameras with same resolution of 1600 by 1600 pixels, with a given spatial resolution η_k^{expe} (η_k^{expe} is the Kolmogorov scale in the synthetic experiment):

$$\eta_k^{expe} = \eta_k^{DNS} \times \Gamma = 0.02219 \times 0.0302 = 0.67mm$$

And time conversion factor is simply: *(IV-1)*

$$\delta t_{DNS} \times \Gamma$$

where Γ is defined as the transformation factor that transforms DNS coordinates to the desired experimental coordinates (η_k^{expe} was selected to match values that we will get on the large Von Karman experiment at CEA). Then we vary at the same time the particles number to solve as much as possible the Kolmogorov scale. For example, for synthetic PIV image density of $0.02ppp$ we can resolve one Kolmogorov scale and up to $\eta_k^{expe}/1.42$ for a concentration of $0.05ppp$. This was calculated by defining the PTV resolution Δ_x^{PTV}as the ratio of the volume of the experiment over the number of particles to the power 1/3 (for example for a concentration of $0.05ppp$, $\eta_k^{expe}/\Delta_x^{PTV} = 1.42$).

The Lagrangian velocity spectrum of the DNS tracks is shown in Figure IV.1. The -2 slope is typical for Lagrangian velocity spectra using the Kolmogorov hypothesis (see Yeung et al., 2006 and Tennekes and Lumley, 1972).

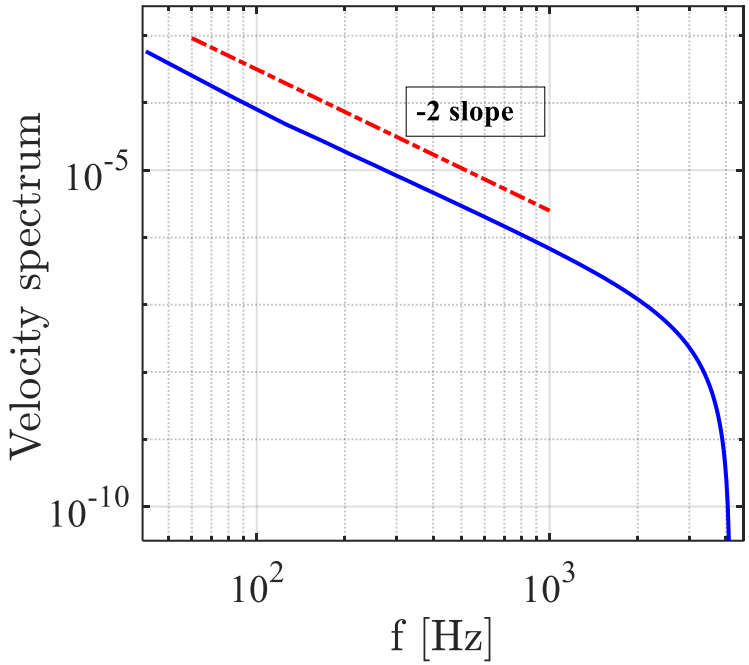

Figure IV.1 Velocity spectrum of the Lagrangian DNS tracks used to create the synthetic tracks.

IV.3 Simulator of PIV images

In order to reproduce the second configuration discussed in Chapter III, the virtual cameras are distributed in forward scattering positions symmetrical to the x axis. Cam1 and Cam4 are positioned at an angle of $\pm$ 45° and Cam 2 and Cam3 are at an angle of $\pm$ 22.5° with respect to the x axis as shown in Figure IV.2. The size of the cameras image is 1600×1600 pixels as for the experiment.

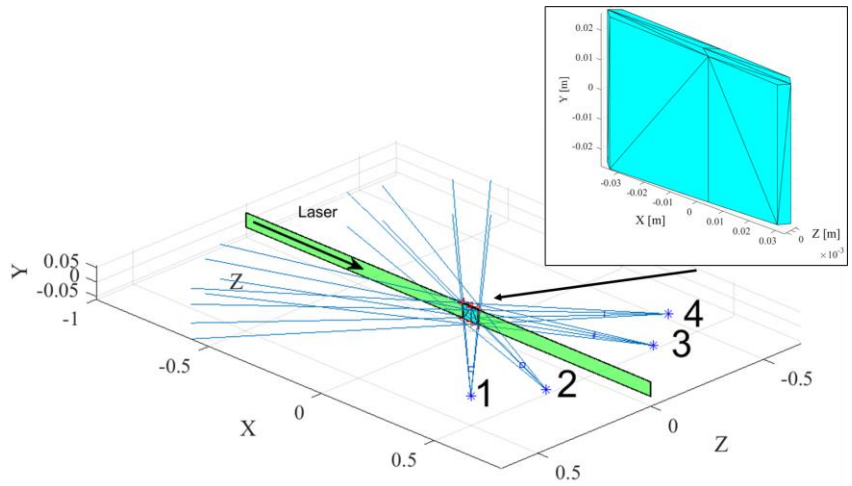

Figure IV.2 Positioning of the cameras setup for synthetic experiment. Top right corner is the intersection of line of sights of all cameras limited by a volume of thickness 6mm.

A pinhole model is assumed for the cameras, without Scheimpflug adapter for simplicity, (for a model that account for Scheimpflug angles check (Cornic et al., 2016)) and calibration is supposed to be perfectly known and to obey a pinhole model. The intersection of the line of sights from a pinhole model and with the 6 mm thick virtual light sheet creates the desired volume of investigation.

IV.3.1 Cameras parameters

The pinhole camera parameters are designed as follow; we start by calculating the projection of the focal length in both directions from:

$$f_x = N_x/2/\,tan\left(\frac{H_{fov}}{2}\right)$$
$$f_y = N_y/2/\tan\left(\frac{V_{fov}}{2}\right)$$

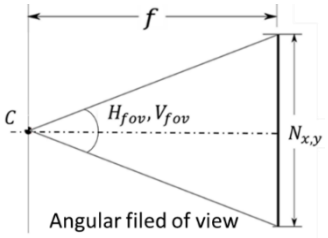

(IV-2)

Where N_x and N_y are the image size in pixel. In our experiment we choose a squared image of $N_x = N_y = 1600\,px$ leading to equal angles of field of view in horizontal and vertical direction $H_{fov} = V_{fov}$ with square pixel of size $c = 10\mu m$ for all cameras. The angle H_{fov} and V_{fov} in the experiment was 4.58°. For the synthetic images they were fixed to same value.

The intersection of the optical axis with the image plane is referred as the principal point with coordinates c_x and c_y in pixel units (see section II.2.4). In our case $f_x = f_y = 2 \times 10^4 px$ and $c_x = c_y = 800.5px$.
The 3D world positions of the cameras are defined in the translation vector $\boldsymbol{T}$ where the Y position is equal to zero since the position of cameras optical center is supposed to be in X, Z plane as shown in Figure IV.2.

Copying our real experiment, virtual cameras are positioned with camera origin frame C at $0.74m$ from the center of the volume defining the physical origin (0,0,0). Hence, the magnification M is equal to 0.37, so the magnification factor is equal to $\frac{c}{M} = 2.7\ 10^{-5} m/px$.

IV.3.2 Synthetic particles

We will consider a traditional approximation which considers the scattered light as proportional to the square of the particle physical diameter dp and determines the intensity of a particle by its diameter and its position in the light sheet only via:

$$E_p \propto dp^2 e^{-\frac{z^2}{2\sigma_{Laser}^2}} \qquad \textit{(IV-3)}$$

Assuming a Gaussian distribution of the laser beam with standard deviation of σ_{Laser} (taken here as 22 mm as in the experiment of Chapter III). On the other hand, the particles physical diameters are randomly drawn in the $[mindp\ ,\ maxdp\ ]$ segment, according to a Gaussian distribution law with mean m_{dp} and standard deviation σ_{dp}, with $mindp = 0.5\,\mu m$, $maxdp = 2.5\,\mu m$ and $m_{dp} = 1.5\,\mu m$. The distribution is controlled by $\sigma_{dp} = 0.3px$.

Then for the final particle image intensities, we follow the work of (Champagnat et al., 2014) where they developed an imaging model that reconstruct point-like particles rather than blobs. This model is better suited for particle tracking velocimetry.

We consider a set of P particles, each of which is denoted by index p and located at $\mathbf{X_p}$ in 3D space. The imaging model is based on the concept of Point Spread Function (PSF). Any source point located at $\boldsymbol{X}$ in 3D-space has a geometrical image located at $F(\boldsymbol{X})$ in the focal plane of a given camera. Considering particles with intensity E_p located at point $\boldsymbol{X_p}$ in 3D-space, the intensity distribution of the projected image is given by:

$$I(\boldsymbol{x}) = \sum_{p=1}^{P} E_p . h\left(x - F\left(\boldsymbol{X_p}\right)\right) \qquad \textit{(IV-4)}$$

Where $\boldsymbol{x} = (x\ ,\ y)$ denotes any location in the image plane, F is the geometric projection function in the image (obtained with a pinhole model presented in section II.2.4), and h the so-called PSF which models the aperture limited diffraction and pixel integration.
All the synthetic experiments performed in this chapter assume a Gaussian PSF with standard deviation σ_{PSF}:

$$h(x,y) = \frac{1}{4}\left(erf\left(\frac{x+0.5}{\sqrt{2}\,\sigma_{PSF}}\right) - erf\left(\frac{x-0.5}{\sqrt{2}\,\sigma_{PSF}}\right)\right) \qquad \textit{(IV-5)}$$

$$\times \left(erf\left(\frac{y+0.5}{\sqrt{2}\,\sigma_{PSF}}\right) - erf\left(\frac{y-0.5}{\sqrt{2}\,\sigma_{PSF}}\right)\right).$$

where $\mathrm{erf}(x) = \frac{2}{\sqrt{\pi}} \times \int_0^x e^{-t^2} dt$ is the error function used to integrate the Gaussian intensity distribution of a particle over a pixel.

Synthetic images that were created with PSF made of a Gaussian with standard deviation $\sigma_{PSF} = 0.6$, gives a mean particle image diameter of around $dp = 3.8\, pixels$. The PDF of the final intensity of the particles images is presented in dotted lines in the Figure IV.3 (Bottom Right). The constant of proportionality in the particle intensity formula (IV-3) was adapted so that the mean particle diameter of 1.5 µm gives a grey level count of 50 (8 bits images generated). The mean particle size for the synthetic particles, using the method described in section III.3.2, is measured at around 3.8 pixels (this value validates the estimation method used). This particle size is used for most of the tests done in this chapter. This size is slightly higher than for the real experiments as the mean diameter of SWT first configuration was 3.2 px and for the second configuration it was estimated to be 2.6 pixels. Smaller particles will be tested later in this chapter.

IV.3.3 Background noise added

The effect of image noise is simulated by adding to each pixel a random intensity from a normal distribution with variance σ and mean μ. Two cases are studied starting from noise free ideal particle images $[\sigma = 0, \mu = 0\ ]$ to noisy images with $[\sigma = 3\ , \mu = 5]$ (8 bits images generated). These values were chosen to have a similar signal to noise ratio compared to the real experiment. In the graph at the bottom right of the Figure IV.3 the effect of the noise appears as a “bump” added to the intensity PDF. In this figure we can see that at the intensity of 20 counts, the PDFs of cameras with and without noise start to superpose since the maximum added noises intensity is around 20 counts.

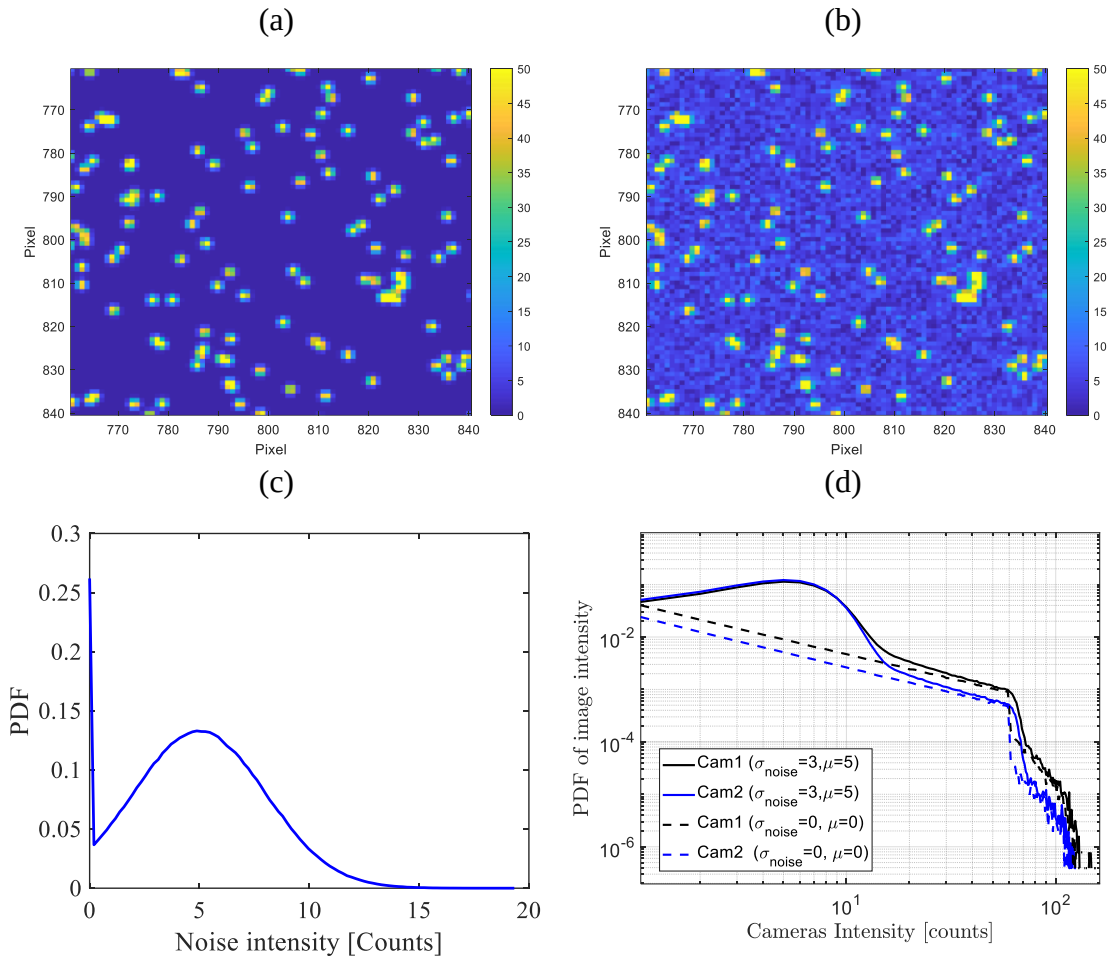

Figure IV.3 Particles images without noise (a) and with noise [σ=3 ,μ=5] (b). Gaussian distribution of the added noise (c). PDF of images intensity for two cameras (cam 1 at 45° and Cam 2 at 22.5°) (d). Cameras with and without noise are represented with solid lines and dash lines respectively.

IV.3.4 Particles coordinates & images density

Seeding densities ranging from 2 to 15 particles per cubic millimeters corresponding to an effective image density of 0.01 *ppp* to 0.07 *ppp* were tested by selecting a certain number of the DNS tracks among the ones available randomly. The number of actual particles range approximately between 25,000 and 180,000 for each of the 250 time steps. Figure IV.4 shows a subset of a camera image for three seeding densities.

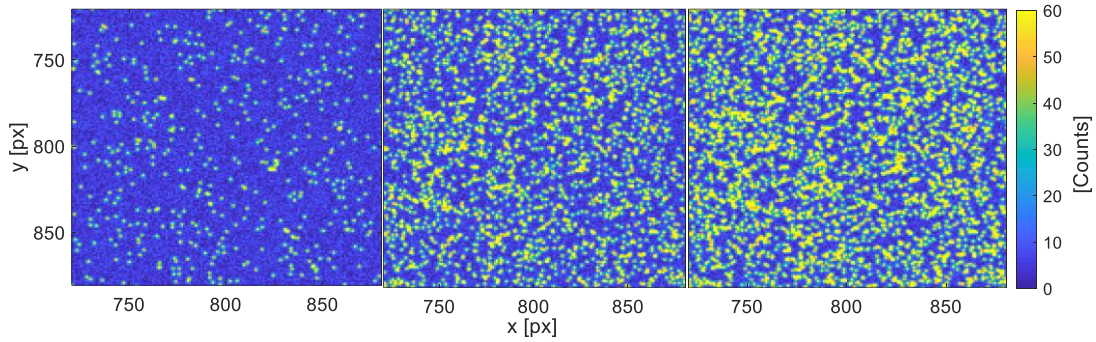

Figure IV.4. Zoom of camera images for 0.01, 0.05 and 0.07ppp (from left to right) for a mean particle size of 3.8 pixels. All images are with background noise added.

We chose this range of concentration because we observed in Chapter III that exceeding $0.05ppp$ in real experiments is difficult. Moreover, increasing the image density from 0.05 to 0.07 did not result in a substantial increase in the number of particles detected, as shown in Table III-4 of Chapter III.
The image density, ϕ_{im}, in ppp is calculated by taking the whole number of particles taken from DNS and then finding the number of particles existing in the volume. Subsequently, the ppp is the number of particles divided by the number of pixels in the image = 1600×1600.

Table IV-3: N_{DNS}, number of particles that are present in the volume seen by all 4 cameras for a volume of thickness 6mm and the corresponding seeding densities ϕ_{im} of 0.01 ,0.03, 0.05 & 0.07 ppp.

Total particles taken from DNS $\times 10^6$	**Number of Particles in volume $\times 10^3$**	**Seeding density ϕ_{im} [ppp]**	$particle/mm^3$
1.8	25.6	0.01	2
5.6	76.8	0.03	6
9.3	128	0.05	10
13	179	0.07	15

IV.3.5 Displacement range

The original sampling rate for our study corresponds to 1dt resulting in a mean and maximum particle displacement of around 6 and 15 voxels respectively (equivalent to a velocity of 1.5 and 3.5 m/s in the real experiment). The PDF of displacement is shown in Figure IV.5. Acquisition frequency used for STB is 8267 Hz with the scale factor Γ used to scale the DNS (see equation (IV-1)). The acquisition frequency is calculated as follow:

$$f_{acquisition} = \frac{1}{\delta t_{DNS} \times \Gamma} \qquad (IV\text{-}6)$$

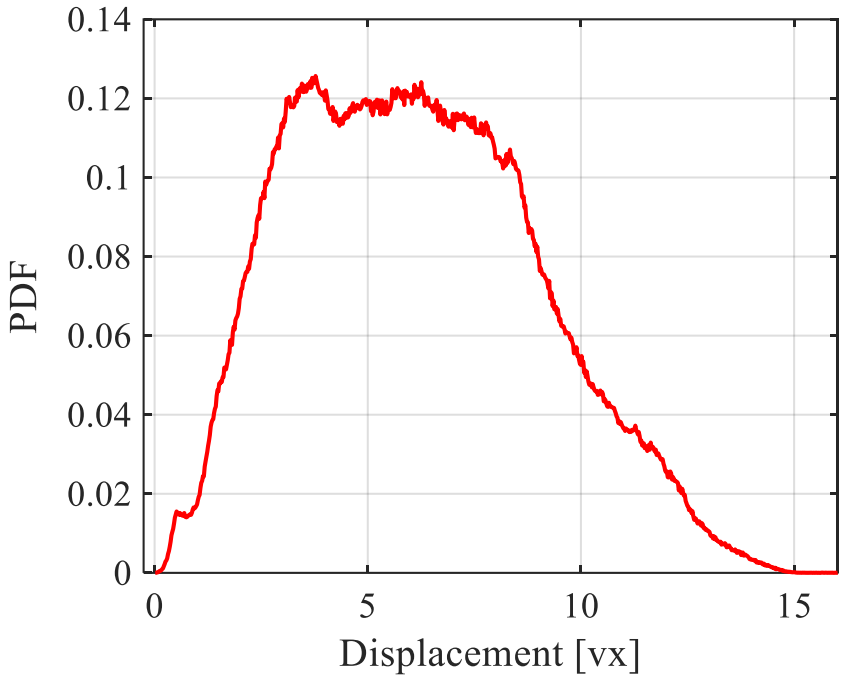

Figure IV.5. PDF of displacement magnitude for 1dt increment.

As mentioned in Table IV-4 the displacement tested are $0.5dt$ $(3vx)$, $1dt$ $(6vx)$, $2dt$ $(12vx)$ and $3dt$ $(18vx)$. Displacement larger than 1dt are obtained by skipping images when performing STB in DAVIS software.

IV.4 Reconstruction of tracks using STB

IV.4.1 Synthetic calibration target

For reconstruction, object-to-image correspondence are obtained from images of planar synthetic calibration target consisting of grid of a known pattern. We use a planar grid containing dots identical to the calibration target used in Chapter III. The calibration images are obtained by placing particles at the desired marker position in physical space and the same method as for generating the synthetic images of particles are used, using much larger standard deviation in the point spread function. Then extraction algorithms of Lavision software Davis like in real experiment recover the marker positions from the images of the plate and assign proper world (physical) coordinates to them. For the calibration tests described herein, grids of regularly spaced dots were used (see Figure IV.6). We are seeking to reconstruct a volume with thickness of $6mm$ which here is accounted for by performing calibration using multiple calibration plate images at different volume depths starting from $-5mm$ to $10mm$.

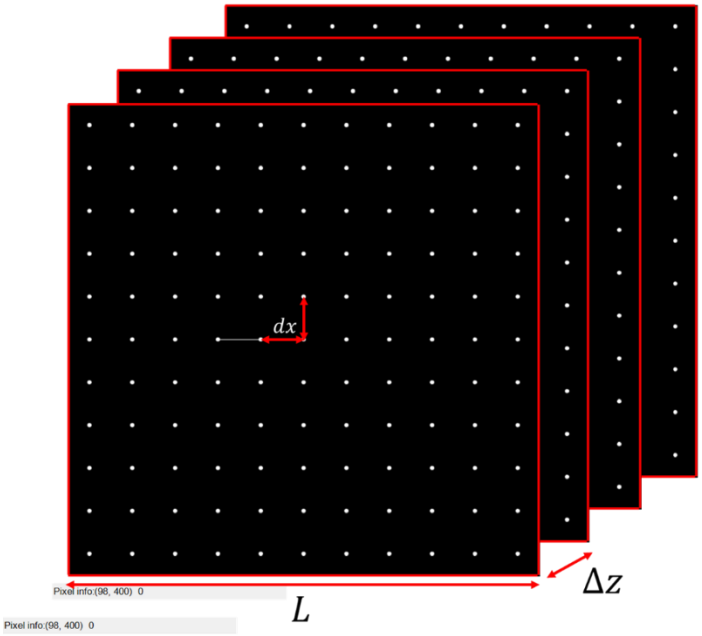

Figure IV.6 Synthetic calibration plate, L is the length of the plate $L = 200mm$. $dx = 4.5mm$ *is the space between dots in x and y direction and* $\Delta Z = 5mm$ *is the spacing between planes created where total thickness calibrated is* $3\Delta z = 15mm$

In the built-in algorithm of Lavision the dots are detected by cross-correlation with a similar-shaped template. Grid reconstruction is then performed on the recovered collection of dots using three user-positioned guide markers that roughly define the origin and first grid points along the major axes.
To be coherent with the tests done on real experimental images of Chapter III we choose a 3rd order polynomial-based reconstruction method to map the camera. (Willert, 2006) concluded that the choice of camera model has only a minor influence on the estimate of the camera (pinhole) position.

IV.4.2 Tracks reconstruction algorithm (STB)

Shake the Box algorithm was applied to the particle images originating from synthetic tracks. For initialization, the first four time-steps were treated with IPR as follows: the original (default) allowed triangulation error was set to $0.5\ vx$ (unless determined otherwise) for all iterations. Each triangulation iteration was followed by 8 shake-iterations, 4 outer loops for adding particles and 4 inner loops to refine (shake) particles positions in the resulting particle distributions. The minimum track length was set to 4 time steps to trigger the algorithm to start predicting/shaking the particles. One parameter we have to tune carefully is the velocity limits which depends on the reference velocity and the image acquisition frequency you choose. All STB parameters are mentioned in the Table IV-4.

Table IV-4: STB parameters applied to synthetic images. The parameters in bold are the parameters that are fixed in section IV.7.

General parameters					
Threshold $[counts]$	No Noise added	1			
	With Noise added	$10 - 15 - 20 - 25 - 30$			
Triangulation $[\mathrm{v}x]$		$0.3 - 0.4 - 0.5 - 0.6 - 0.7$			
Iterative particle reconstruction (IPR)					
Adding particles (outer loop)		4			
Refine particle and position (inner loop)		4			
Shake particle position $[\mathrm{v}x]$		0.1			
Tracking					
Displacement		$0.5dt$	$1dt$	$2dt$	$3dt$
Velocity Limits $[\mathrm{v}x]$		10	20	40	60
Median filter		off			

The reference tracks for a low seeding density case of 0.01 ppp are shown in Figure IV.7 (top). Total number of reference tracks in the volume is 1.52×10^5. The 1.56×10^5 corresponding detected tracks by STB for the same concentration are shown in the bottom figure. The number of STB detected tracks are higher than the tracks of DNS because of ghost tracks. Further, some of the good trajectories could be also fragmented to more than one track hence increasing the total number of detected tracks.

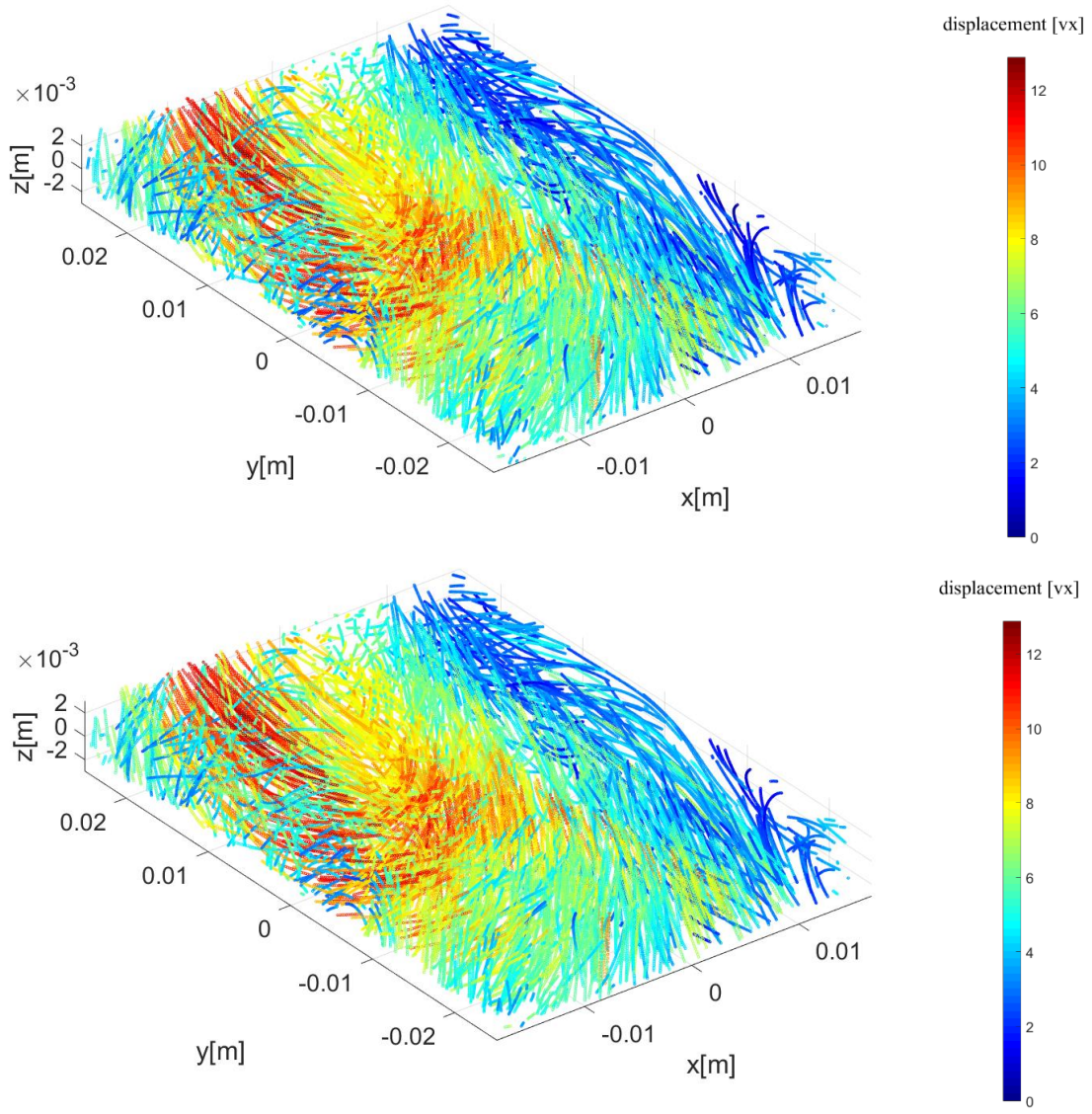

Figure IV.7. (Top) Reference particle tracks from the DNS (Bottom) Particle tracks reconstructed by STB. Overlay of 100 time-steps, color coded by particles displacement. Not all tracks are shown for visibility.

IV.5 Matching STB tracks to DNS reference

IV.5.1 Matching process

In this section we discuss more in depth the novelty of this study where we used a matching procedure based not only on the spatial information of particles but also on the information provided by the tracks.
The steps of the matching procedure are the following:

```
Matching Algorithm
 1:  loop on all particles P_i of all DNS reference tracks
 2:    loop on all STB particle P_j with same time and a position error less
 3:    than a given value Err_pt
 4:      Compute the mean position error ⟨Err⟩ of all particles of the STB
 5:      tracks Tr(P_j) having common times with reference DNS track Tr(P_i).
 6:      If    [ the mean position error ⟨Err⟩ is less than a given value
 7:            "Err_tr" and the evaluated STB track Tr(P_j) not yet matched
 8:            with a reference DNS track]
 9:            or
10:            [the mean position error ⟨Err⟩ is less than the mean position
11:            error of the STB matching track already associated to the
12:            reference track Tr(P_i)]
13:      then
14:            match temporally the STB track Tr(P_j) with the reference track
15:            Tr(P_i)
16:      end if
17:    end loop
18:  end loop
```

Ghost particles are divided into two types. The first type is a ghost particle that is a part of STB track that matches with a DNS track. In the Figure IV.8 they are represented by the yellow asterisk marked by arrows. They spill out of the DNS track where the STB algorithm overestimate the actual track length. The number of these type of ghost particles is $N_{gh,tr}$. The second type ghosts are the ghost particles that are part of a ghost track that does not have any reference match. The summation of all particles of these two types of ghosts is N_{gh}.

In addition, we define N_{DNS} , N_{STB} & N_{match}, the number of particles of DNS, number of tracked particles of STB and number of STB particles matching with DNS. Consequently, the total number of tracked particles is $N_{STB} = N_{gh} + N_{match}$.

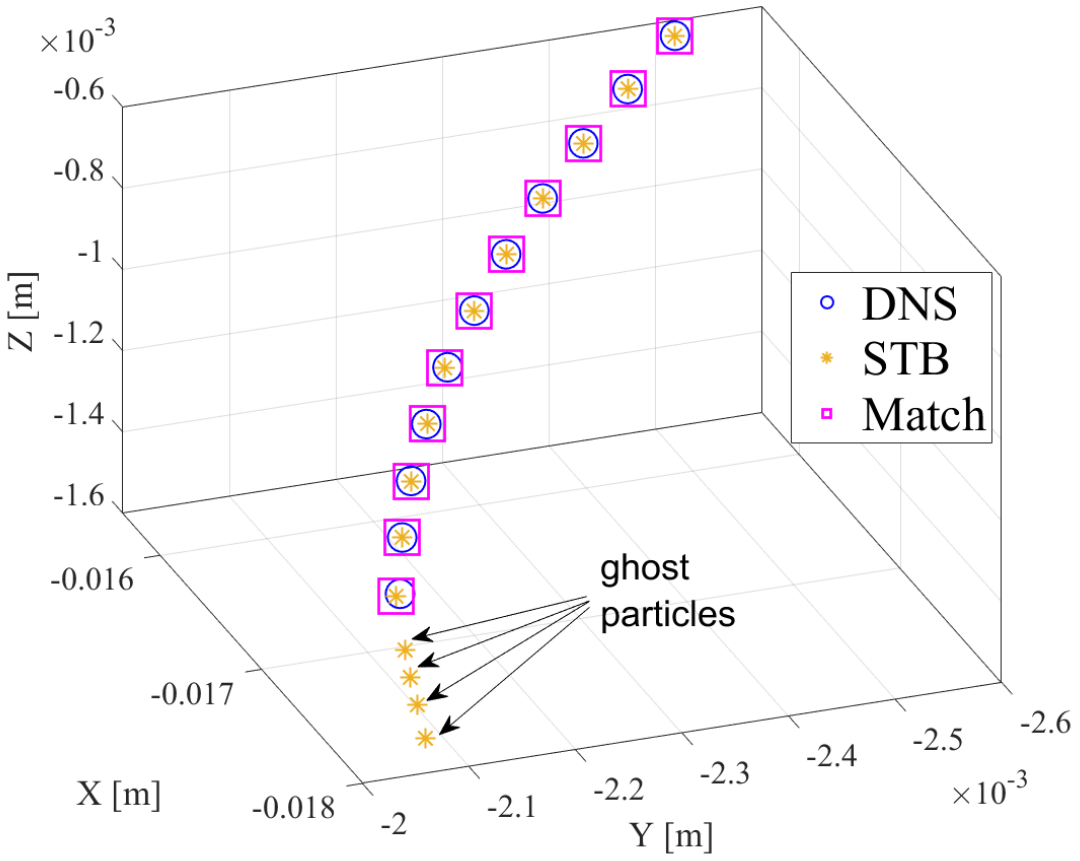

*Figure IV.8 Example of STB particles (✳) tracked over multiple time steps to form an STB track. The track is matched by its DNS counterpart (**o**). The STB track is overestimated by Shake the Box. These particles are considered as ghosts type "gh, tr"(and their total number is $N_{gh,tr}$). They don't exist in the reference, but they are still part of a track that exists in the reference. The squared particles (■) are type "$match$. These are the type of particles used for comparison between DNS and STB.*

We examine using an example how the algorithm is able to match particles to a DNS track that is fragmented into two or more STB tracks as we see in the Figure IV.9. In this example we see that the red STB track is matched with its DNS reference (the blue circles) The deviation of this STB track from the DNS track is noticeable compared to the green track. This increase significantly the error calculated on the track. For that reason, when two particles of these two tracks should match with the same DNS particle, the matching algorithm chooses the particles from the green STB track (see Figure IV.9 bottom). Obviously the 4 red asterisk marked with arrows that does not match with DNS are considered as ghost, type "gh, tr".

Finally, we analyzed the dependence of the matching results on the two parameters Err_{pt} and Err_{tr} of the matching algorithm above. These two default errors were set as mentioned before to 1 & $\sqrt{2}\ vx$ respectively as shown in Table IV-5.

Table IV-5: Matching performance as function of search parameters, Err_{pt} & Err_{tr} , of the Matching algorithm.

$Err_{\mathrm{pt}}\ [vx]$	$Err_{\mathrm{tr}}\ [vx]$	Matching percentage	$\bar{\varepsilon}$ [Pixel]
1	$\sqrt{2}$	91.4%	0.2349
0.6	$\sqrt{2}$	91.2%	0.2335
0.3	$\sqrt{2}$	89.5%	0.2244
0.6	$0.6\sqrt{2}$	88.1%	0.2169
1.3	$1.3\sqrt{2}$	92.2 %	0.2408
2	$2\sqrt{2}$	92.6 %	0.2457

The default parameters of Err_{pt} and Err_{tr} (1 and $\sqrt{2}\ vx$ respectively) gives a matching ratio of 91.4% and a mean error (i.e. position error between reference particle and matching particle) of $0.2349\ vx$. By decreasing the search area of the first particle from $1\ vx$ to $0.6\ vx$ the matching ratio decreases to 89.5%. Decreasing both parameters to 0.6 and $0.6\sqrt{2}\ vx$ reduces the matching ratio defined in equation (IV-7) by 3%. There is indeed not a great influence of these two parameters. This behavior proves that the matching procedure is well designed as the matching efficiency should be as little dependent on external parameters as possible. Even if we go up to 2 and $2\sqrt{2}\ vx$, the results remain comparable on the matching ratio and the mean error. This is the benefit of our matching algorithm which evaluate the best matching track and do not match particles of track one by one.

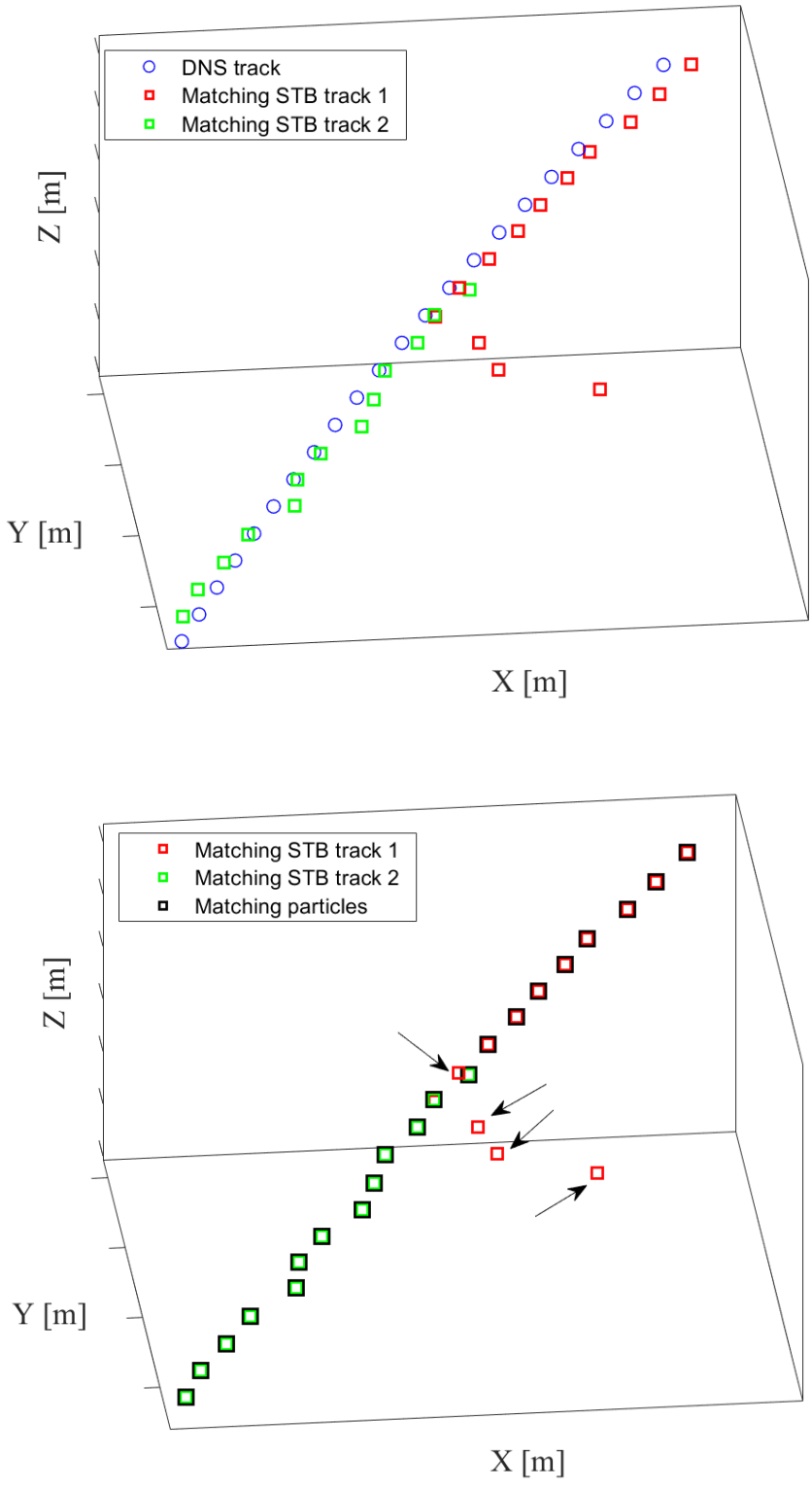

Figure IV.9 ***(Top)*** *Example of a DNS reference track (0) that is fragmented into two different STB tracks, (STB track 1 □ and STB track 2 □).* ***(Bottom)*** *a representation of the particles that are considered as matching particles (□)(from both STB tracks).*

An important question is why we have ghost particles type $N_{gh,\mathrm{tr}}$ and more importantly why we have ghost tracks that are completely wrong and does not match with any reference track?

Even though $N_{gh,\mathrm{tr}}$ are wrongfully tracked particles, they are at least part of a track that exists; on the other hand, our first assumption for the completely incorrect tracks represented by the tracks number n_{gh}, is that they are the result of a wrong threshold setting where the STB algorithm tracks pixels from background noise or different wrong particles which by bad luck are close to predicted positions for some time steps. In section IV.6 we fixed all different parameters and changed the threshold to investigate in more details the effect of this parameter on the percentage of ghosts.

IV.5.2 Evaluation metrics

To evaluate the quality of the tracking results, each track identified by STB is matched with a synthetic track. In order to evaluate the quality of the STB algorithm, four evaluation parameters will be computed and analyzed in detail:

Matching Ratio: The percentage of tracked particles that match with synthetic (reference) particles. The ratio is calculated for all tracks and all time steps.

$$\psi = \frac{N_{DNS}}{N_{match}} \qquad \textit{(IV-7)}$$

Matching error: It is the systematic error between detected and synthetic matching particles. It is related to the calibration error as well as the triangulation and tracking (shaking and predicting) of the particles over time. The matching error is calculated for every matched particle for all time steps.

$$\varepsilon(i) = |\boldsymbol{x}_{match}(i) - \boldsymbol{x}_{DNS}(i)\,| \qquad \textit{(IV-8)}$$

And the mean is calculated over all time steps:

$$\overline{\varepsilon} = \frac{1}{N_{match}} \sum_{i=1}^{N_{match}} |\boldsymbol{x}_{match}(i) - \boldsymbol{x}_{DNS}(i)\,| \qquad \textit{(IV-9)}$$

Coverage index: For each DNS track, the coverage C_T is the ratio between the total number of all STB particles matching with a reference DNS track and the length of this reference track. Maximum value of C_T =1, represents a reference track that is fully detected by STB (even if several STB tracks are needed).

Fragmentation index: This index measures the brokenness of a track. It is the number of STB matching tracks with a single reference track.

In the Figure IV.10 (top right insert) we see an example of track where a part of it is detected by STB, exactly 13 positions tracked with respect to 21 actual DNS positions (C_T =62%). On the same figure an example of probability distribution function of C_T at a concentration of $0.01ppp$ where 73% of the tracks are nearly fully recovered ($C_T \geq 0.95$). Additionally, only 4% of tracks are covered at 50% or less. Results of coverage for different image densities are included in the Figure IV.29 **(a)** and **(b).**

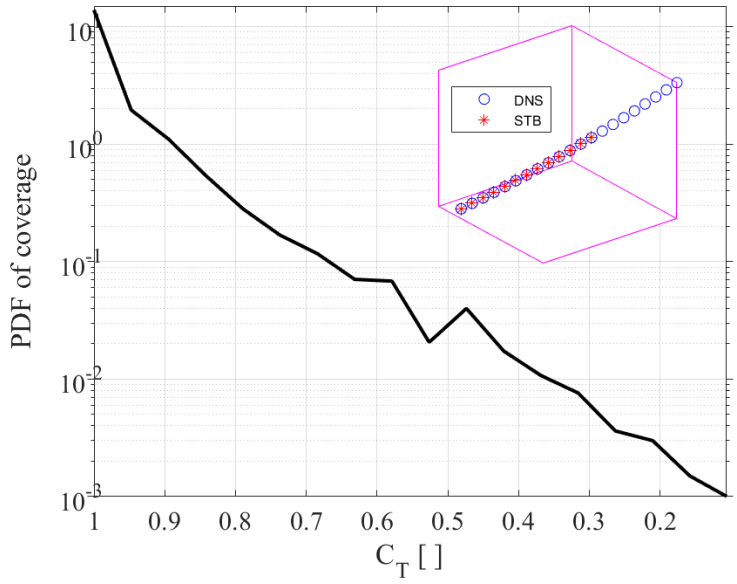

Figure IV.10 Probability distribution function of tracks coverage C_T for a concentration $\phi_{im} = 0.01$ ppp. An example of a track that is covered at $\frac{13}{21}$ is shown in the top right insert.

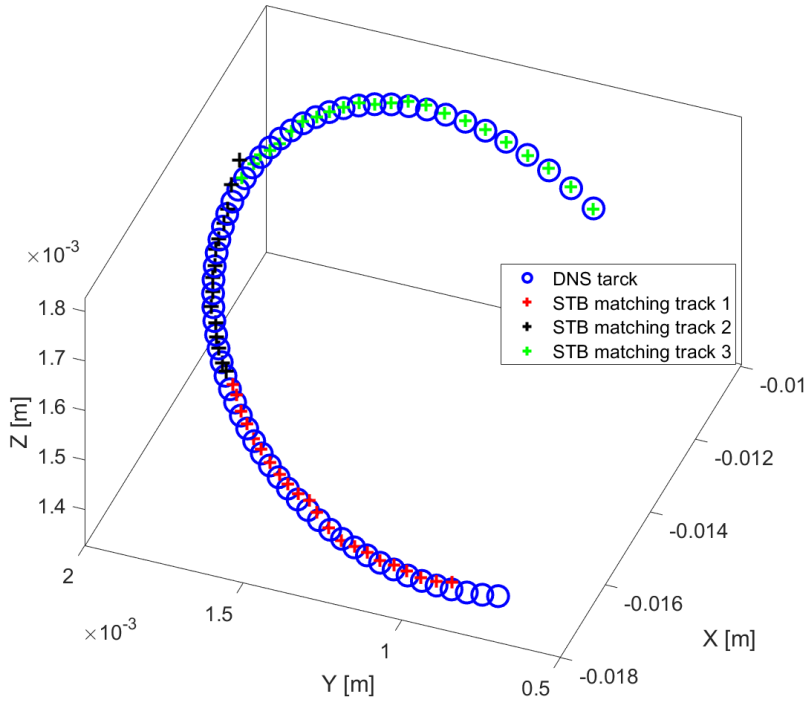

Figure IV.11 An example of a track that is fragmented into 3 different STB tracks;($f_r = 3$). The DNS track extends over 60 time steps. The length of STB track 1 (+), *STB track* 2 (+) and *STB track* 3 (+) are 22, 15 and 23 respectively.

The fragmentation of a track , f_r, quantifies the number of detected segments for a single original synthetic track. The larger f_r is, the shorter will be the detected tracks. The new version of DAVIS 10.2.2 includes a track-connecting parameter, but it was not used for the time being to avoid overprocessing position data and to avoid using two different versions for the analysis done in his chapter. Figure IV.11 includes an example of a synthetic track fragmented to 3 different STB tracks. In this example, the red plus is a trajectory of particle being tracked over 22 time steps, the black plus signs is 15 time steps long and green plus signs is 23 time steps. The total number of detected particles is therefore 60. On the other hand, the actual DNS track is 65 time steps long. Note that matching ratio for this track (or C_T) is not 60/65 for this track, it is actually 57/65 because some particles of the three STB tracks overlap over the same DNS particle.

In addition, we investigate why STB does not detect all the particles of a reference track as shown in the example of Figure IV.12 (left) where several time steps were not tracked. In order to answer to this question, we start to examine some characteristics of the cutoff points where the STB track comes to a pause before starting again after several time steps. In the Figure IV.12 (right) we find the nearest point from another DNS track, and we plot it. In this case, this nearest track (the black points) is at 0.2 voxels from the empty dark circles of DNS reference track in the Figure IV.12 (left). This may be a source of perturbation for STB. The projection of these two points (cut off and nearest) on the images plane shows that these two particles overlap on all 4 cameras (see Figure IV.13). This finding motivates the study of the optimal image density we can reach without having many fragmented tracks.

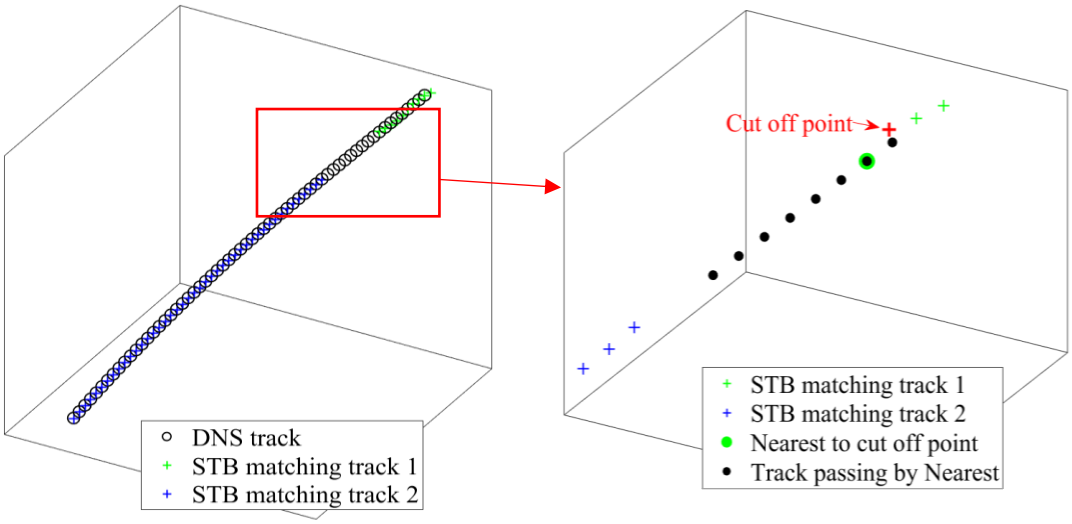

Figure IV.12 (Left) Example of a DNS track fragmented to two different STB tracks where the STB matching track 1 stops at a cutoff point (highlighted in the right figure). Several time steps later, the DNS track is found by STB matching track 2. Additionally, a different DNS track passing by the nearest to cut off point is added.

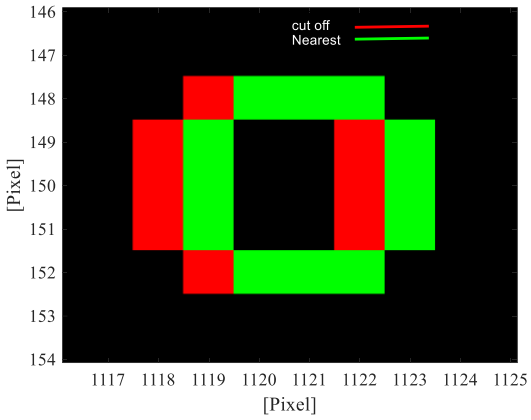

Figure IV.13 Projection to camera images plane of the Cut off and nearest points shown in Figure IV.12 with a particle size found to be of 4 pixels (mean particle size of the set is 3.8 px).

IV.6 Optimization of 'Shake the box' parameters

In this section, we will test the optimal grey level threshold to detect particle and allowed triangulation error parameters of the STB algorithm. Once optimized, these two factors will be fixed starting section IV.7.

The velocities provided by the Trackfit included in the software are not very accurate as can be seen from the PSD of the velocities in Figure IV.14. Trackfit parameters of the Lavision Davis STB black box are limited to two: order of the polynomial and length of the polynomial track fit. Without a deep understanding of these parameters, and in order to evaluate only the properties of the STB algorithm, we decide to analyze exclusively the raw positions of tracked particles.

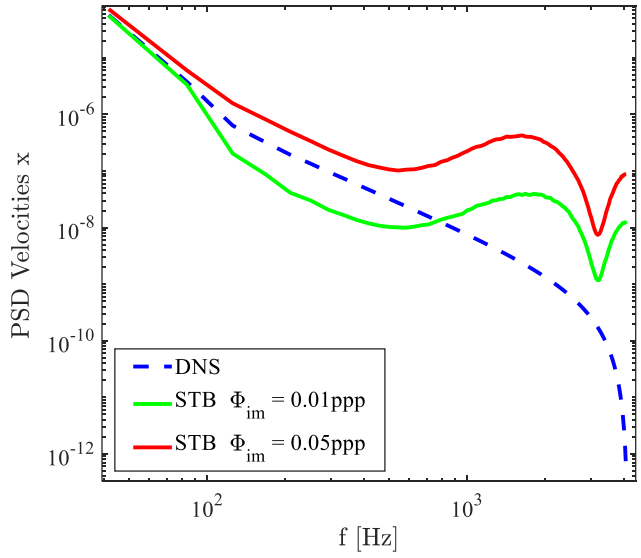

Figure IV.14 Power spectral density of the velocities in x direction for two image densities 0.01 and 0.005 ppp. The velocities are the output of the Trackfit included with the Davis software.

IV.6.1 Effect of threshold

First and foremost, we want to determine the best particle grey level threshold and allowed triangulation error parameters for our setup. The threshold corresponds to the minimum intensity of particles which are considered for the STB analysis. We start testing with different thresholds on the case with image density of $0.05\ ppp$ with a displacement of $1dt$ (corresponding to $6vx$). The effect of thresholds is analyzed on noisy images only for the series mentioned in Table IV-1. The threshold is chosen within a range of $20\ counts$ (equivalent to around 3σ, with σ being the standard deviation of the background noise added to the synthetic images) since it is the maximum background noise added to the images. Results are presented in the Figure IV.15.

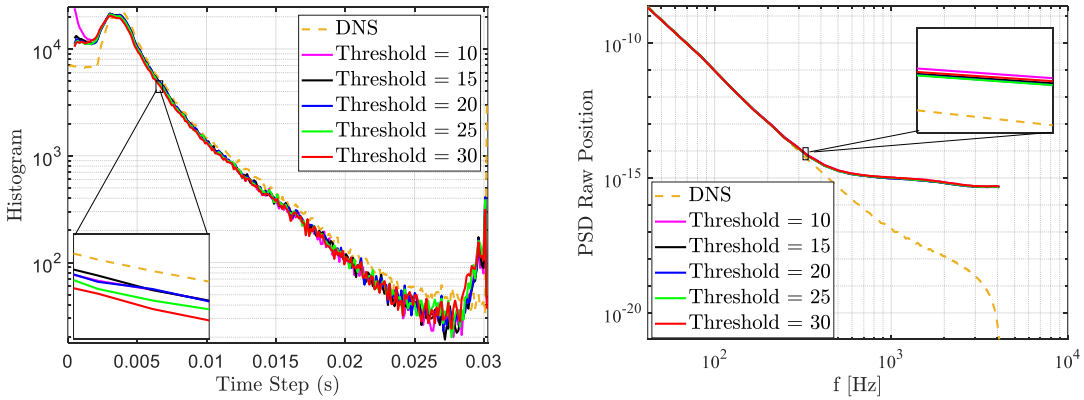

Figure IV.15 (Left) Track length histogram as function of the threshold, for a given concentration $\phi_{im} = 0.05\ ppp$ and a displacement of 1dt. (Right) Power spectral density of the same case.

Figure IV.15 shows that a threshold of 10 counts may be too low because it leads to a large fraction of very small tracks less than twenty times steps as compared to the DNS. Moreover, the error on the raw positions is higher than for other thresholds tested. On the other hand, for an increasing threshold larger than 20, the histogram of track lengths starts to depart more from the DNS reference. In addition, as displayed in Figure IV.16, the number of particles detected for various thresholds agrees that a good threshold is between 15 and 20 counts. Finally, by looking at the PDF of errors, the peak of position error ε is maximum for a threshold of 15-20 counts indicating that less particles have much larger errors. For all these reasons we chose to continue the analysis by using a threshold of $20\ counts$ which corresponds to the maximum value of background noise added to the images

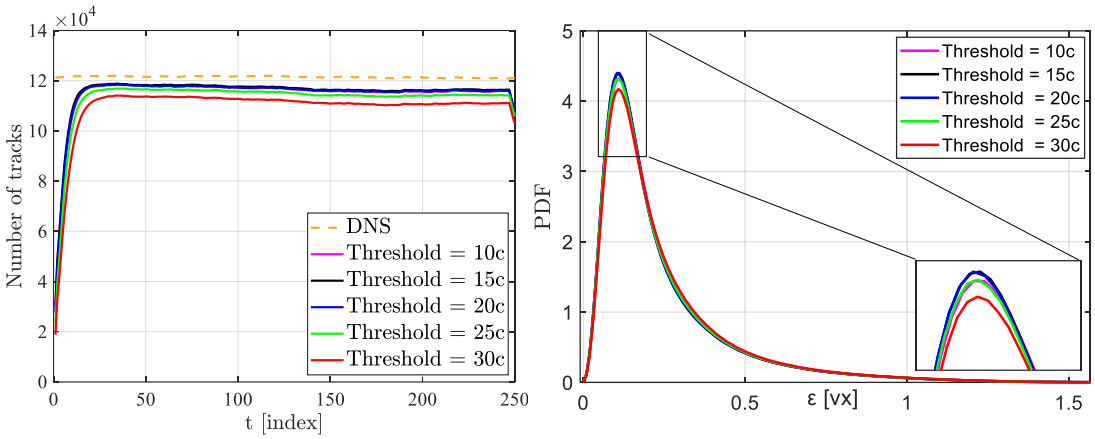

Figure IV.16 (Left) Comparison of the number of tracks detected as a function of time steps for different thresholds for a given concentration $\phi_{im} = 0.05\ ppp$ and displacement of 1dt. (Right) Probability distribution function of position error ε in voxels for different thresholds.

By increasing the threshold from 20 counts (maximum noise added to the particles images) to 30 counts which is larger than the noise added to the images, we find no significant decrease for ghost tracks which are 9000 and 7000 for a threshold of 15 counts and 30 counts respectively. Also, the overall ghost particles decrease slightly from 0.6% to 0.5%.

Table IV-6: Comparison of detection track statistics as function of several thresholds for the case of $\phi_{im} = 0.05\ ppp$ and a mean displacement of 1dt (corresponding to $6vx$).

threshold [*counts*]	N_{STB} $\times 10^6$	N_{match} $\times 10^6$	ψ	$\overline{\varepsilon}$ $[vx]$	$\frac{N_{match}^{\varepsilon<0.2}}{N_{match}}$	$\overline{C_T}$	$\frac{N_{gh}}{N_{STB}}$	*GTML [Time step]*
10	18.564	18.384	95.6 %	0.194	66.9%	0.84	1.4%	10
20	18.602	18.492	96.5 %	0.192	68%	0.85	0.64%	12
30	17.911	17.826	93.5 %	0.200	67%	0.80	0.5%	13
40	16.147	15.964	83.3 %	0.223	60%	0.68	10%	17

We conclude from the results of the Table IV-6 that a too low estimate or too high estimate of threshold increases the percentage of ghost particles. Especially a high threshold increases a great deal the percentage of ghost and the ghost tracks mean length (GTML). This is due to the reduction of the low intensity particles signal by an aggressive threshold. In that situation the STB algorithm may have problems differentiating the particles from different tracks as some particles can disappear at some time step by the high threshold when its intensity is close to it, hence, increasing ghost ratios. The threshold selected for the rest of the tests done in this chapter will be 20 counts.

IV.6.2 Effect of allowed triangulation error

Allowed triangulation error is more complicated to test as there is no clear guidelines. The default allowed triangulation error suggested by Lavision ($0.5vx$) was used on all the analysis of the SWT. We decided to test multiple allowed triangulation errors around this value in the range $[0.3vx, 0.7vx]$.

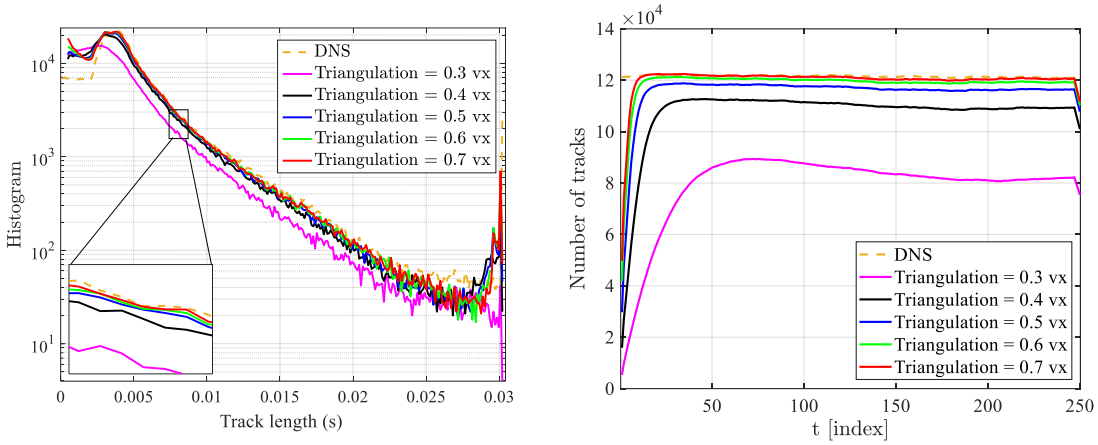

Figure IV.17 (Left) Track length histogram as function of triangulation, for a given concentration $\phi_{im} = 0.05\ ppp$ and displacement of 1dt (6vx). (Right) Number of tracks as function of time steps for the same cases.

Figure IV.17 (left) shows that a low value of the allowed triangulation error ($0.3vx, 0.4vx$) strongly affect the track length and track number. These results drive us to question if we also underestimated the allowed triangulation error of 0.5 vx that was used for SWT. On the other hand, an over estimation doesn't look to affect a lot the deviation from DNS results. One must keep in mind that a higher allowed triangulation error significantly increases the STB processing time (from 1 hour 6 minutes for 0.5 vx to 1 hour 45 minutes for $0.7vx$ for only 250 time steps). This value increases exponentially with data sets of thousands of images.

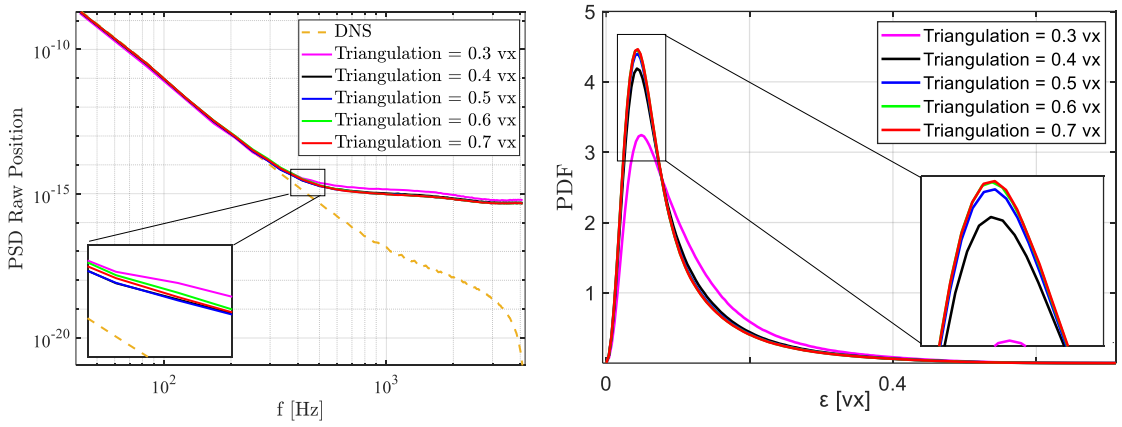

Figure IV.18 (Left) Power spectrum distribution as function of allowed triangulation error for a given concentration ϕ_{im} of 0.05 ppp and displacement of 1dt. (Right) Probability distribution function of position error for the same cases.

By looking at the PSD of raw positions and PDF of errors Figure IV.18 we can safely conclude that triangulations of $0.5vx$ to $0.7vx$ are the best candidates for our application at a concentration of $0.05\ ppp$ and a mean displacement of $6vx$. We present more statistics in the Table IV-7. By increasing the triangulation from $0.5vx$ to $0.7vx$, the matching ratio increases by 2%. Additionally, the mean position error $\bar{\varepsilon}$ slightly decreases. Finally, the ratio of particles detected with position error less than $0.2vx$ (6th column), increases with the allowed triangulation error parameter.

Table IV-7: Comparison statistics between $0.5vx$ & $0.7vx$ using the case of $\phi_{im} = 0.05\ ppp$ and a mean displacement of $6vx$.

triangulation $[vx]$	N_{STB} $\times 10^6$	N_{match} $\times 10^6$	ψ	$\bar{\varepsilon}$ $[vx]$	$\frac{N_{match}^{\varepsilon<0.2}}{N_{match}}$	$\overline{C_T}$	$\frac{N_{gh}}{N_{STB}}$:
0.5	18.602	18.492	96.5 %	0.192	68%	0.85	0.64%
0.7	18.946	18.829	98.3 %	0.189	70.5%	0.90	0.66%

Also it is worth to mention that during allowed triangulation error tests that were done on the data of VK2, it seemed that $0.5vx$ is giving better results for the STB data (Ostovan et al., 2019) and (Cheminet et al., 2021)

To conclude on this part and from this point forward, the allowed triangulation error will be set to a value of $0.5vx$ for the rest the analysis even though it might seem that $0.7vx$ is better for our application and it should be considered for the processing of GVK data.

IV.7 Optimization of experiment parameters

IV.7.1 Optimal particle size

In this subsection, we will focus on reproducing the effect of the particle size in synthetic images with noise. Increasing the size of particles introduces non negligible STB problems since it increases the chance of particles overlapping, hence increasing the number of undetected/ghost particles which make it more difficult to identify and track the particles. The effect is reproduced by varying the σ_{PSF} in the equation (IV-5). We tested three different σ_{PSF} of $0.3, 0.6$ and $0.8px$. The case with σ_{PSF} of $0.3px$ was only tested with $0.07\ ppp$ and σ_{PSF} of $0.8px$ was only tested with a concentration of $0.05\ ppp$ (see Table IV-1).

Once again, we use the correlation-based method to estimate the mean diameter of the particles in each direction. For simplicity we will represent the mean diameter which is the average of both directions. For σ_{PSF} of 0.3, 0.6, and $0.8px$, the mean particle size is $2.4px, 3.8px$ and $4.8px$ respectively. Figure IV.19 represents a $30px \times 30px$ zoom of images with image density of $0.05\ ppp$ and for different particle sizes. The three snapshots correspond to the same physical space. The effect of the mean particle size is clear as the particles increase in size as well as they tend to blend more with the background noise. On the real experiments the particle size can be adjusted by the magnification and mainly by changing the lens aperture, but this is a tricky parameter to

adjust since it affects the depth of field too. Additionally, a special attention should be made (during real experiment) to focusing the particles into crisp and defined images on the sensor where they are recorded. This is done using the focus adapter of the cameras lenses and tuning perfectly the Scheimpflug angle. The calibration and OTF check results with multiple iteration is necessary during the experimental tuning.

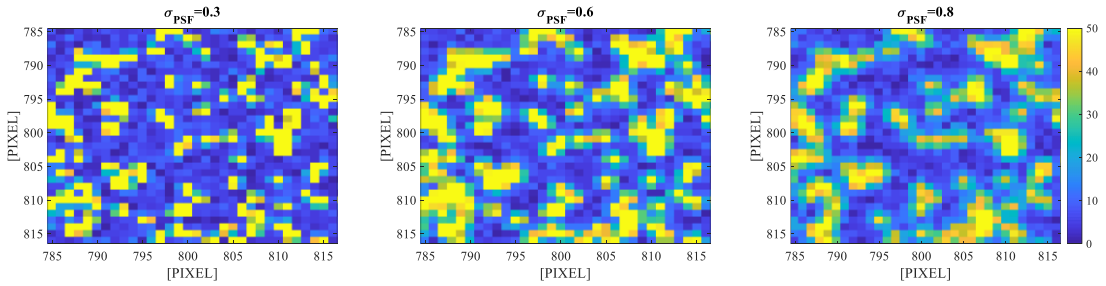

Figure IV.19 Example of images with a mean particle size of $2.4px$, $3.8px$ *and* $4.8px$ *(from left to right respectively). The three images are at the same time step and represents the same portion of the image* $30px \times 30px$.

0.05 *ppp* case with noise:

Using image density of $0.05ppp$ with added noise and a mean displacement of $6vx$, we compare the STB results of two different cases with different particles diameter, $dp = 3.8px$ and $4.8px$.

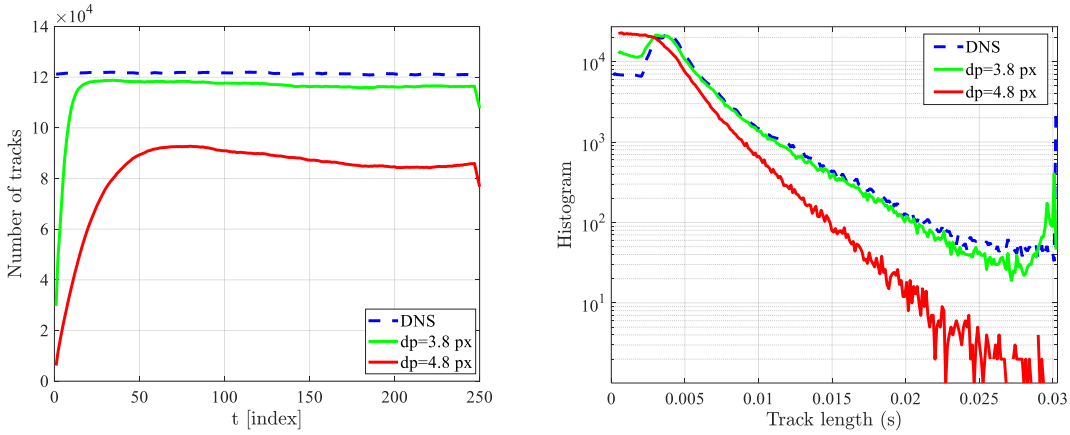

Figure IV.20 (Left) Number of tracks as function of time for a concentration $\phi_{im} = 0.05$ *ppp and a displacement of 6vx for different dp. (Right) Track length histogram as function of dp for the same cases*

From Figure IV.20 and Figure IV.21 we conclude that for image density of $0.05ppp$ the optimal particle size is definitely smaller than 3.8 pixels. The quantitative comparison is presented in Table IV-8. The number of tracked particles decreases considerably by increasing particles size. the matching ratio drops from 68% to 22.4%. For the mean particles size of $4.8px$ the tracks are shorter in length in general and mean fragmentation is 23% higher. Moreover, the mean position error is 150% higher. In addition, for particle diameter of $3.8\,px$ only 6% of tracks are fragmented into 2 or more STB tracks, while for a particle diameter of $4.8px$, 23% of tracks are fragmented to at least two STB tracks.

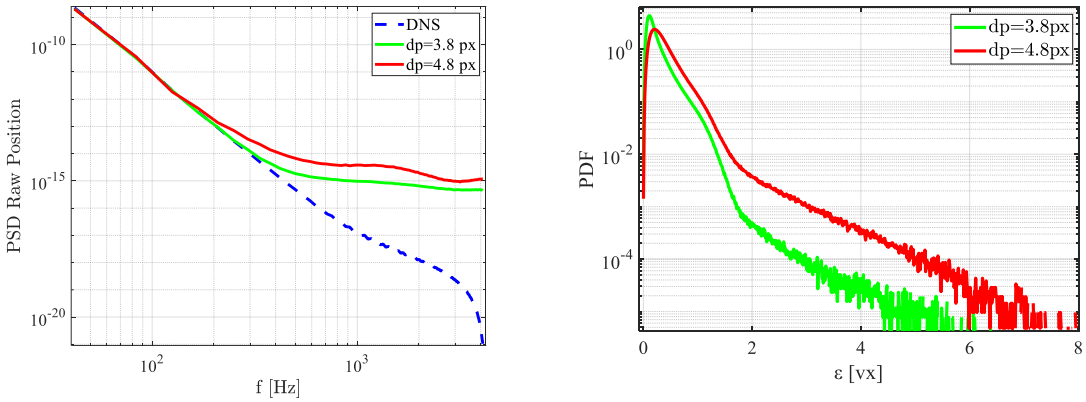

Figure IV.21 (Left) Power spectral distribution in function of d_p, for a given concentration $\phi_{im} = 0.05\ ppp$ and displacement of 1dt (6vx). (Right) Probability distribution function of position error ε for the same cases.

Table IV-8: Comparison statistics between two different particle diameters for the case of $\phi_{im} = 0.05\ ppp$ with a mean displacement of 6vx.

dp $[px]$	N_{STB} $\times 10^6$	N_{match} $\times 10^6$	ψ	$\bar{\varepsilon}$ $[vx]$	$\frac{N_{match}^{\varepsilon<0.2}}{N_{match}}$	$\overline{C_T}$	$\overline{f_r}$	$\frac{N_{gh}}{N_{STB}}$:
3.8	18.602	18.492	96.5 %	0.192	68%	0.85	1.06	0.64%
4.8	14.324	12.735	66.4%	0.326	22.4%	0.51	1.23	8.4%

0.07 *ppp case with noise:*

For the cases with a higher concentration, Figure IV.22 shows that decreasing the particle size from 3.8 px to 2.4 px improved the STB performances. The number of tracks detected increased from 140,000 to 160,000, resulting in a matching ratio of 79 to 90% respectively. On the other hand, we can see a slight improvement for track lengths and PDF of errors. The PSD of position follows the reference DNS up to frequency of $f = 250Hz$ for a particle size of $2.4px$ whereas it starts to depart from the reference at $f = 150Hz$ for the case with mean particles size of $3.8px$. Moreover, the number of particles with a position error of less than 0.2 pixels increases by a factor of three as presented in Table IV-9 for particle image of 2.4 px compared to 3.8 px.

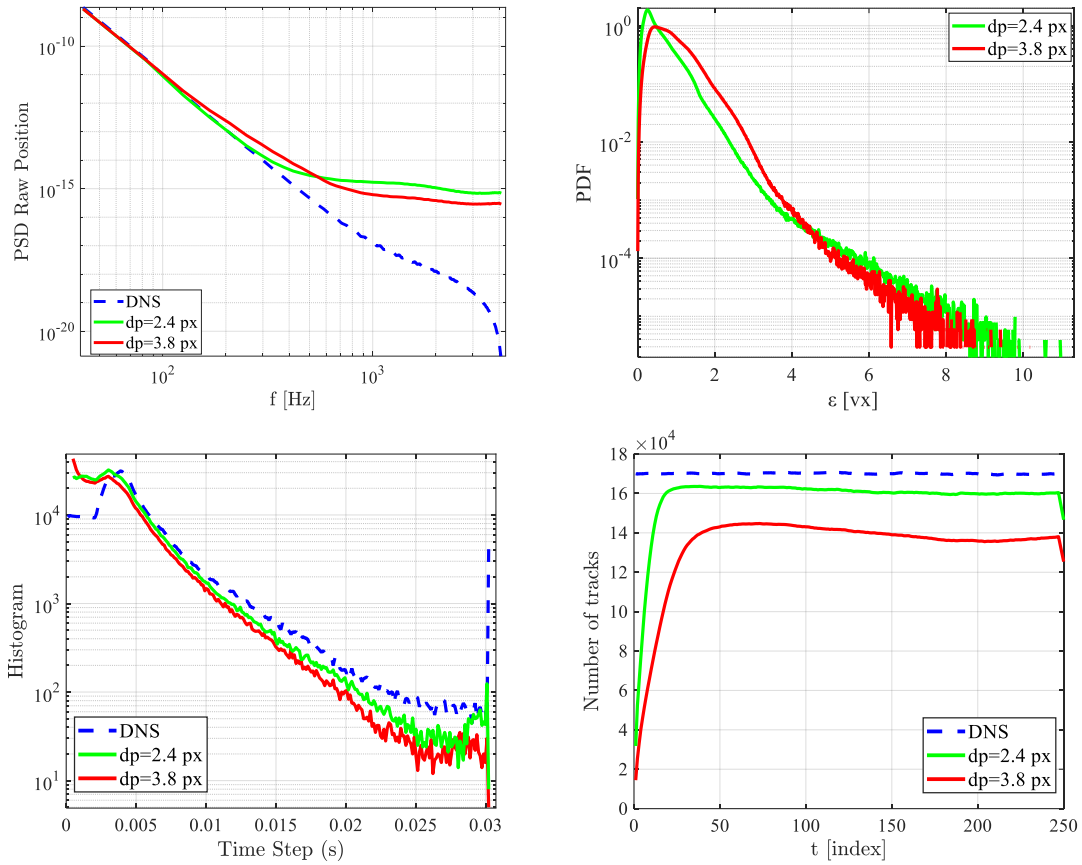

Figure IV.22 Effects of particle image size dp on (Top left) PSD of tracks position. (Top right) PDF of error. (Bottom left) Track length histogram. (Bottom right) number of tracks as function of time steps. All figures are for the same case of $\phi_{im} = 0.07$ ppp and displacement of 6vx.

Table IV-9: Comparison statistics between particle image size of $2.4px$ & $3.8px$ for the case of $\phi_{im} = 0.07ppp, mean\ displacement = 6vx$.

dp $[px]$	N_{STB} $\times 10^6$	N_{match} $\times 10^6$	ψ	$\bar{\varepsilon}$ $[vx]$	$\frac{N_{match}^{\varepsilon<0.2}}{N_{match}}$	$\overline{C_T}$	$\overline{f_r}$	$\frac{N_{gh}}{N_{STB}}$:
2.4	25.991	24.337	90.7 %	0.478	17%	0.76	1.11	6.3%
3.8	22.785	21.223	79.1%	0.783	5.3%	0.59	1.10	6.1%

Knowing the difficulty to track particles at such high concentration, the results seem to suggest that a particles size of 2.4 pixels is probably close to the optimum one for this concentration.

The findings of this section confirm those of Chapter III, in which we found that smaller particle images produced better overall results. It is worth to mention that we didn't try σ_{PSF} of 0.3 (dp of 2.4 px) on $0.05ppp$ cases even though the STB results on $0.07ppp$ case show that we can improve their quality. But when we look at the ratio of points with a position error less than $0.2vx$, the highest value achieved for $0.07ppp$ is 17 %, or 30×10^3 particles out of 180×10^3 possible per time step. On the other hand, the ratio

of position error less than $0.2vx$ is 68% for a concentration of $\phi_{im} = 0.05ppp$ and $dp = 3.8\,px$, which is equivalent to 87×10^3 particles out of 128×10^3 per time step. What this tells us is that with arguably worse conditions for $0.05ppp$ (particle size of $3.8px$ as compared to $2.4px$ for $0.07\ ppp$), the results are already better when it comes to detected particles with less systematic error on space positions. In addition, unlike the results of Figure IV.21 (left); the PSD position of the case $0.07\ ppp$ for different particle sizes in Figure IV.22 (top left) is difficult to analyze. The error for dp of 2.4 px is less than error for dp of $3.8px$ for a frequency less than 600 Hz. The opposite is observed for high frequencies. This result leads us to question if the ideal image density is somewhere between 0.05 and $0.07ppp$. The next section will be devoted to the analysis of image density. This will be achieved by fixing all other parameters.

IV.7.2 Optimal image density ϕ_{im}.

Particle concentration is an important factor for our PTV resolution. For our synthetic experiment based on DNS at $Re_\lambda = 70$, Figure IV.23 shows that we need a particle concentration around $0.02ppp$ to resolve at least one Kolmogorov scale (we remind that the STB resolution is defined by $1/C^{1/3}$ with C the concentration of particles in the volume of $45 \times 45 \times 6\ mm^3$). For a concentration of $0.05ppp$ we are able to resolve scales that are 43% smaller than Kolmogorov scale η_k^{expe} for the DNS experiment.

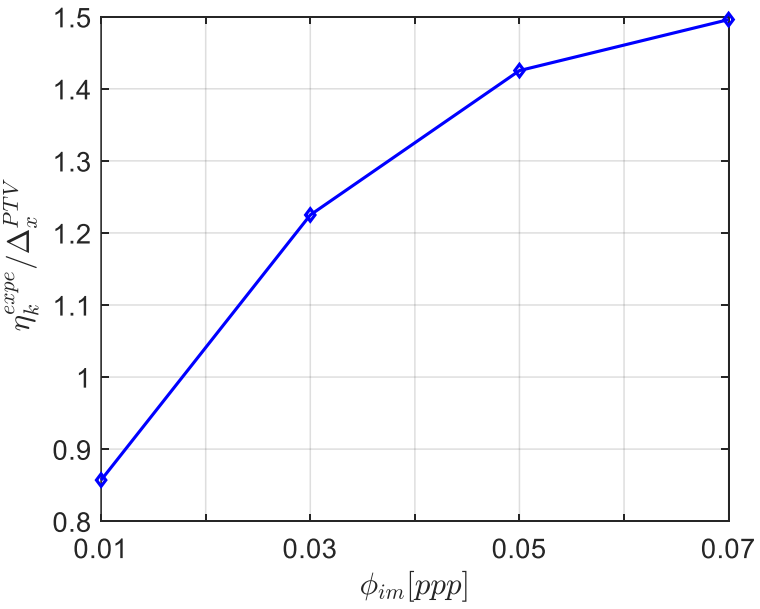

Figure IV.23 Ratio of Kolmogorov scale for the "DNS experiment" and PTV resolution as function of the image density.

Effect of particles concentration for images without noise:

First, we want to see the limits of STB for noise free images with particle size of 3.8 pixels and a displacement of $1dt$ $(6vx)$. The different concentrations of particles are obtained by selecting a certain number of tracks randomly among the available ones in the DNS to generate the synthetic images.

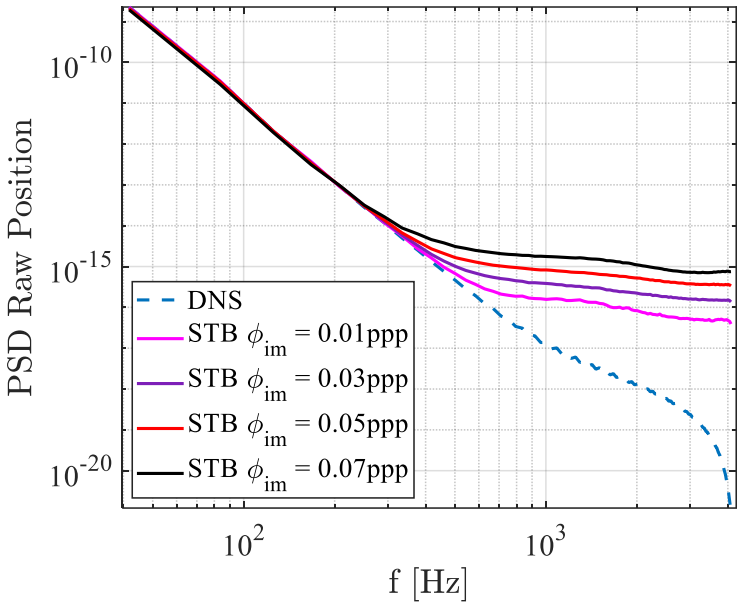

Figure IV.24 Power spectrum distribution of positions as a function of image density ϕ_{im} for a given particle size of 3.8 pixels and a displacement of $6vx$.

Figure IV.24 shows clearly that the higher the image density, the higher the error on the raw positions (plateau at high frequencies represent nearly the noise which increases with increasing ϕ_{im}). The question then is what maximum concentration can we reach without compromising too much the quality of results? When looking at the histograms of track length in Figure IV.25, the deviation from DNS is small until $0.05ppp$ and becomes more and more significant until it goes completely off at $0.07ppp$ with much more very short tracks.

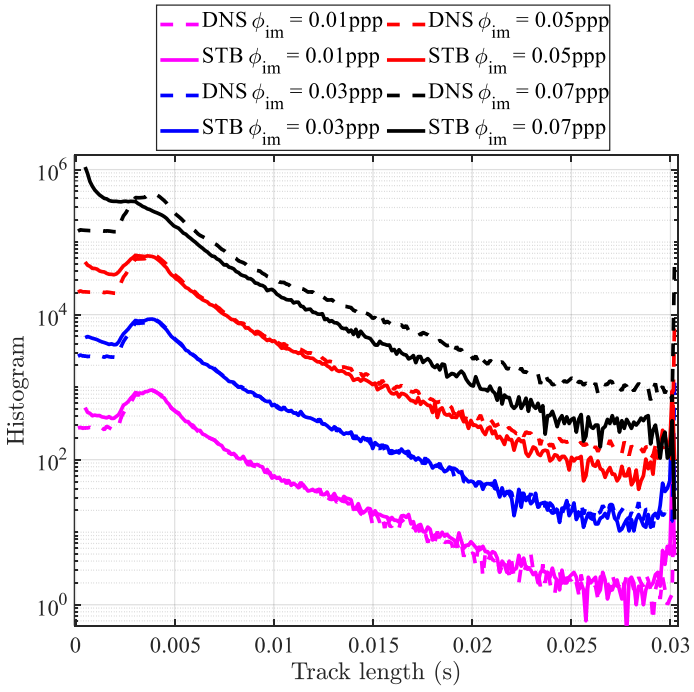

Figure IV.25 Track length histogram for several image densities for the case with a given particle size of 3.8 pixels and displacement of $6vx$. The plots are shifted by one decade for visibility (reference plot is case 0.01ppp).

Impact of Noise for a given ϕ_{im}

We decided to study specifically the case of $0.05ppp$ as it seemed that it is the maximum image density for noise free images. The histogram and PSD of raw position in Figure IV.26 show that the background noise added causes serious problems for STB compared to the case $0.01ppp$.

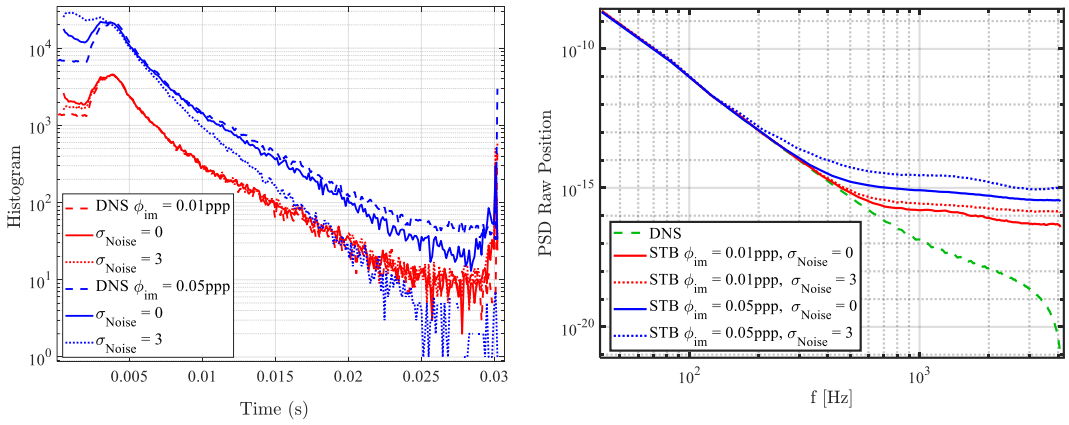

Figure IV.26 (Left) Track length histogram for two image density with and without added noise. (Right) PSD for the same cases ($\sigma_{Noise} = 3,\ \mu = 5$).

From the PDF of position errors (Figure IV.27), for three image density, we see that the peak noise for $0.05ppp$ is less than 0.2 pixels which is still acceptable. On the other hand, $0.07ppp$ the PDF is shifted toward much higher error.

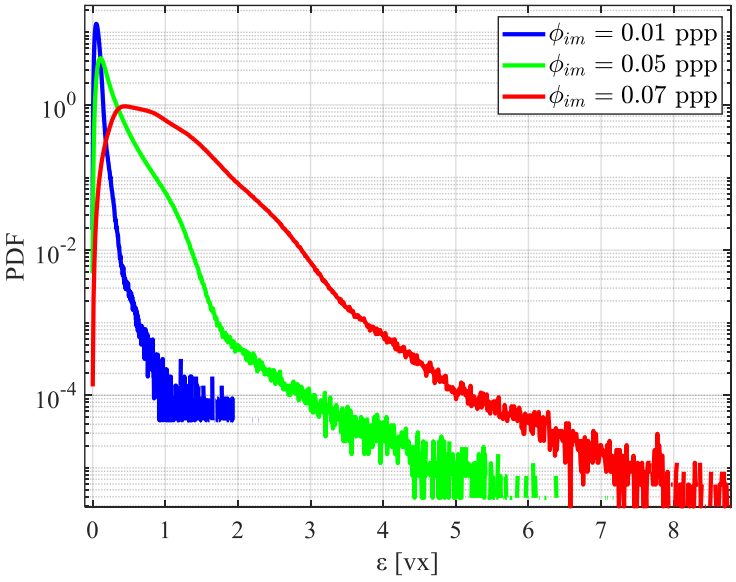

Figure IV.27 Probability distribution function of error for different images density with background noise added ($\sigma_{Noise} = 3,\ \mu = 5$).

From Table IV-10, the matching ratio drops drastically between $0.05ppp$ and $0.07ppp$ from 96.5% to 79%. It is worth to recall that, the matching ratio for $0.07ppp$ can be increased to 90% for a particle size of 2.4 $pixel$ as we saw in the previous section. Nonetheless, the ratio of position error less than $0.2vx$ is still far from the $0.05ppp$ case whether we compare it with images at 0.07 ppp with mean particle size equal 3.8 px or $2.4px$. For 0.05 ppp we calculate the number of particles with an error less than $0.2vx$,

we found $87 \times 10^3$for a concentration of $0.05ppp$. This number drops to 30×10^3 for the $0.07ppp$ case.

Additionally, number of tracks that are fully detected (see column number 7 in Table IV-10) is around 50 % for an image density of $0.05ppp$. In other words, a total of 400k track for all time steps are found and detected by STB. On the other hand, this ratio is 18% for the case of $0.07ppp$ for a dp of $3.8px$ and 29% for a dp of $2.4px$ meaning that in both cases the actual number of fully covered tracks is less than 4×10^5. One should keep in mind that these fully covered tracks can still be fragmented to two or more STB tracks.

Table IV-10: Comparison statistics for images with background added noise ($\sigma_{Noise} = 3, \mu = 5$) in function of image density for particle size of 3.8px and mean displacement of $6vx$.

ϕ_{im}	N_{STB} $\times 10^6$	ψ	$\bar{\varepsilon}$ $[vx]$	$\frac{N_{match}^{\varepsilon<0.2}}{N_{match}}$	$\overline{C_T}$	$\frac{n_{match}^{c_T=1}}{n_{match}}$	$\bar{f}_r$	$\frac{N_{gh}}{N_{STB}}$:
0.01	3.785	99.3%	0.059	99%	0.93	70%	1.002	0.05%
0.05	18.602	96.5%	0.191	68%	0.85	46%	1.06	0.6%
0.07	22.785	79. %	0.783	5.3%	0.59	18%	1.10	6%

For all the reasons mentioned above, $0.05ppp$ seems to offer qualitatively and quantitatively acceptable results. A complete summary of some key parameters that compares the effect of images density with and without noise can be seen in Figure IV.28 and Figure IV.29.

In Figure IV.28 (bottom) we can see that matching ratio and mean position error for images without noise (full lines) respectively decreases and increases exponentially with images density, the optimal concentration seems to be between 0.04 and $0.05ppp$ for noise free images. Obviously for real experimental images, noise can come from different sources (background noise, focus, intensity difference etc). So, the question that surfaces is what is the limit of image density that can be used for images with noise? Second observation is the exponential decrease of matching ratio as well as the increase of position error for images with noise at density of $0.05ppp$ and higher (Figure IV.28 (bottom)). Also, the particles number detected by STB start to be noticeably deviating from DNS one whether it is for the case with or without added background Noise (Figure IV.28 (top)).

Additionally, the same observation can be made about $\overline{C_T}$ (Figure IV.29 **(a)**) and the fraction of ghost particles (Figure IV.29 **(d)**) where the slope increases gradually as the image density increases for both images with and without added background noise. The fraction of the fully recovered tracks by STB ($C_T = 1$) decreases from 55% for $\phi_{im} = 0.05ppp$ to less than 30% for $\phi_{im} = 0.07ppp$, meaning that 403×10^3 total tracks are fully covered by STB for $0.05ppp$ and 257×10^3 for image density of $0.07ppp$, when it should be higher by 40% (the ratio of particles number between these two cases). Moreover, we have more ghost tracks for the $0.007ppp$ case (145×10^3) as compared to the $0.05ppp$ (27×10^3) for all time steps.

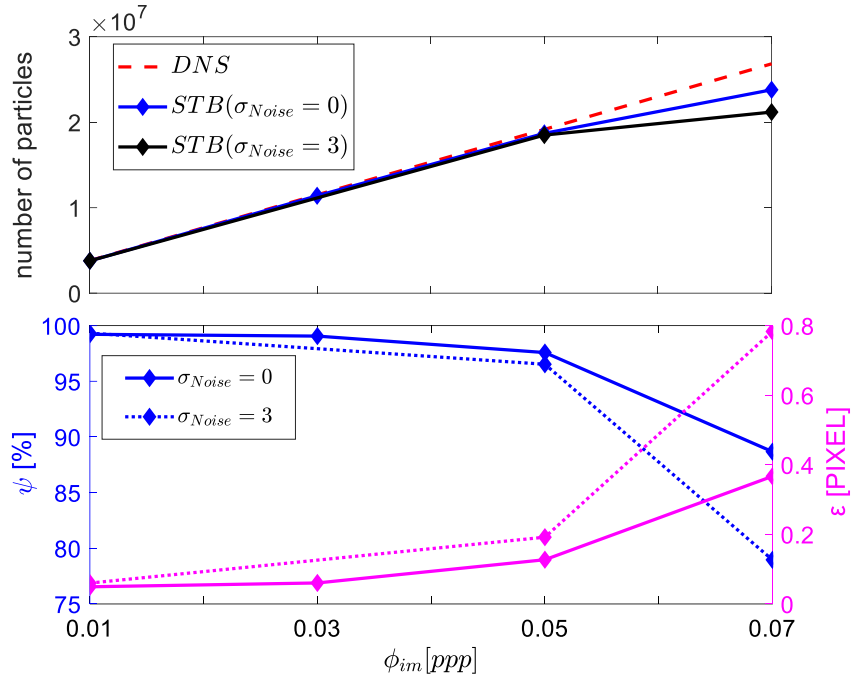

Figure IV.28 (Top) STB matching and reference DNS number of particles per time step for images with and without noise. (Bottom) Matching ratio in blue and average position error of matching particles in purple for images with and without noise.

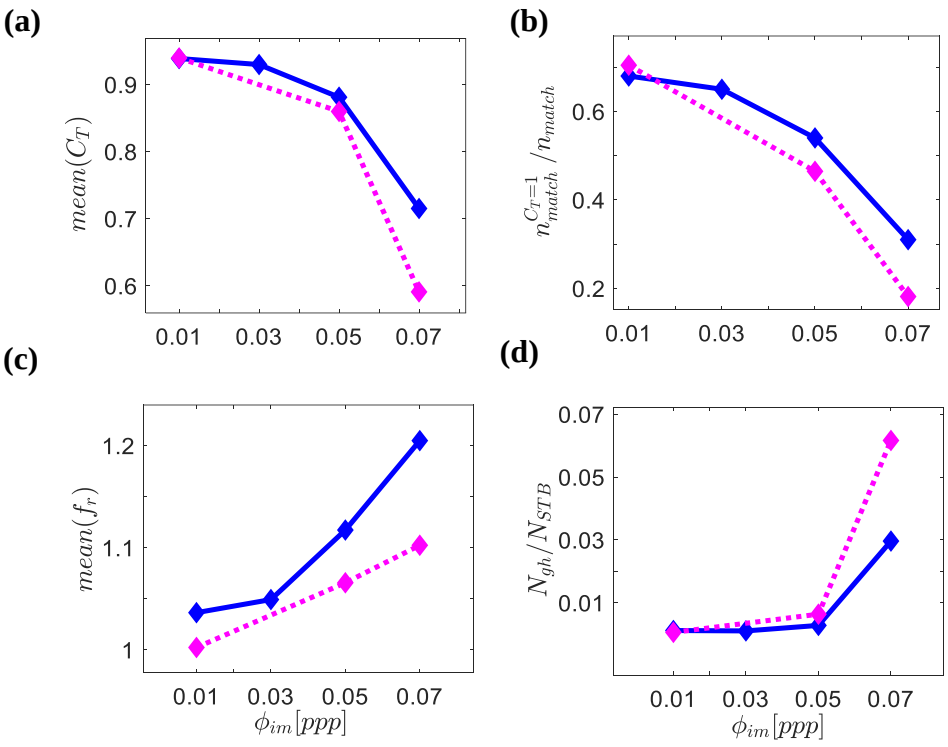

*Figure IV.29 Statistics of the STB results as function of image density for images without noise (blue) and with noise (purple). **(a)** Mean of coverage **(b)** fraction of fully recovered tracks by STB ($C_T = 1$). **(c)** Average fragmentation **(d)** fraction of all ghost particles relative to the tracked particles.*

Since $0.05ppp$ seems optimal for our application, we try to find the distance between two particles (from center to center) for this concentration and for a mean particle diameter of

3.8 pixels. The distance is calculated from the three dimensional distributions for each particle to all the other particles. We find that the mean distance between two particles is around $3vx$ for this case. Given that the mean particle size is 3.8 pixels, this means that two particles overlap on average. Precisely, by making statistics on the particle images generated with image size of 3.8 pixels and concentration of 0.05ppp, we found 32 % of the 3D distribution of particles which overlaps over a quarter of other particle image and 4% of particles overlaps at 50%. Figure IV.30 represent overlapping values as function of image densities. A comprehensive analysis for different particle sizes is provided by (Cierpka et al., 2013).

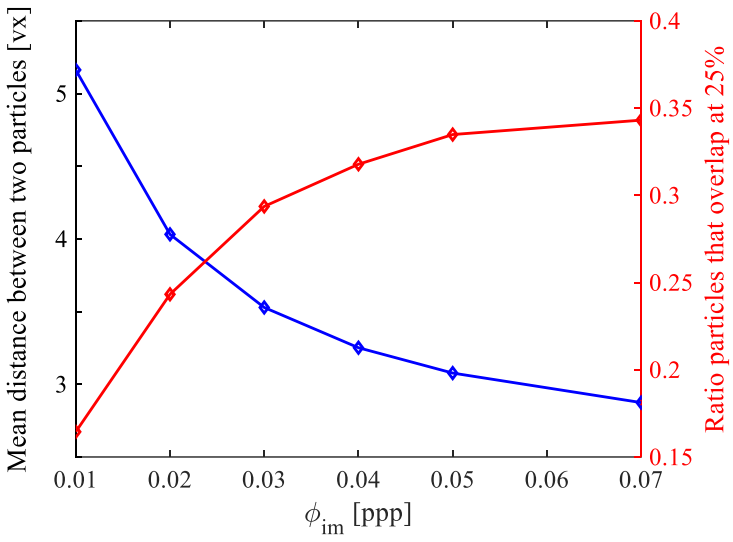

Figure IV.30 Average mean distance of particles in 3D worlds in vx (blue line) and ratio of particles overlapping at 25% of their diameter in the camera images (red line).

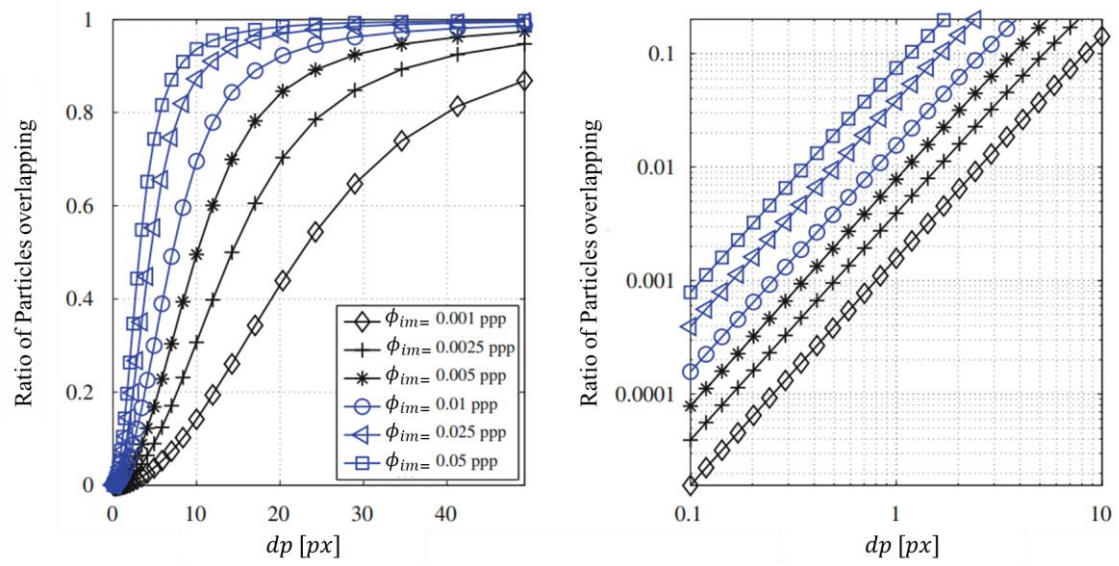

Figure IV.31 Ratio of the number of overlapping particle images versus the total number of particle images for different particle image diameters and particle image concentrations ϕ_{im} in particles per pixel. The right bottom plot shows the region for $dp \leq 10px$ in logarithmic scale. Bottom figures extracted from (Cierpka et al., 2013).

IV.7.3 Intensity difference between cameras

Another effect we found on the images from SWT is the intensity difference between cameras at different angles (check Figure III.8). The mean intensity of all images for cameras at $\pm 22.5°$ is almost double as the one from cameras positioned at $\pm 44.5°$. We recreate this effect by multiplying the overall images intensity of images of second and third cameras by a factor of two, which is of course not totally similar as getting more light in real life experiment. The effect of energy difference between cameras has a clear effect on the statistics of tracks length and the PSD of particle positions. Figure IV.32 (b) shows a clear deviation from the reference DNS data. In addition, the PDF of errors shows, a similar behavior from the reference for $\varepsilon < 1.5\, vx$ but more particles have a higher systematic error.

As consequence, image preprocessing must be applied for the real images case, where a time series filter is applied to subtract the mean from the images. Additionally, the images are normalized to have similar background noise. For the current analysis we consider that all cameras receive the same amount of light from the illumination source.

($\boldsymbol{a}$)

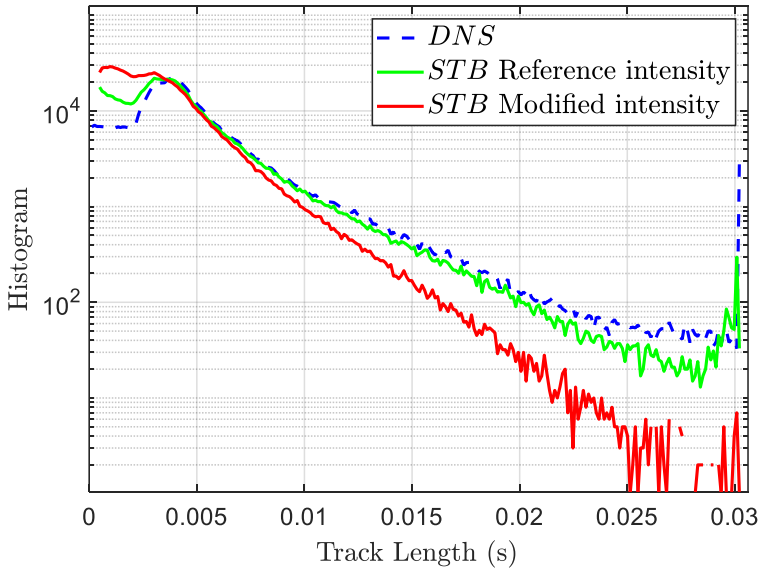

($\boldsymbol{b}$)

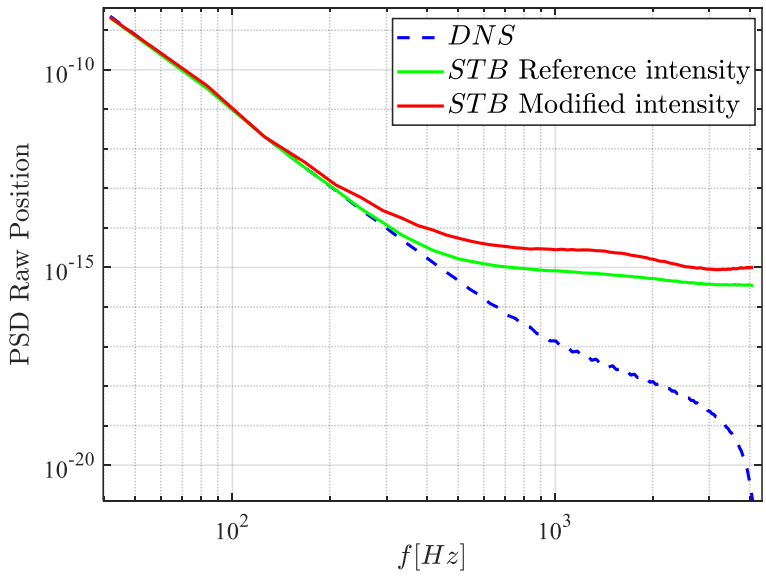

(***c***)

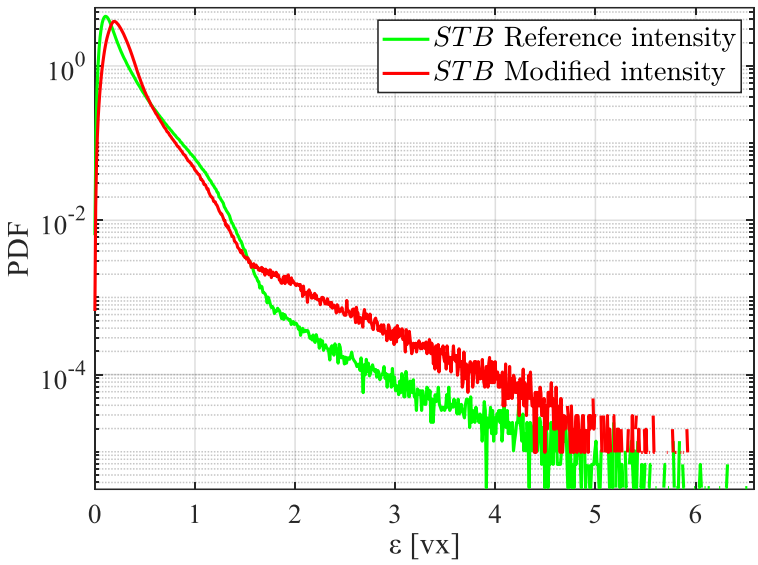

Figure IV.32 (a) Track length. (b) PSD of position and (c) PDF of error for two cases with Noise and reference intensity, and with Noise and modified intensity on cameras 2 and 3.

IV.7.4 Effect of displacement

In this section the aim is to test the effect of average displacement between two consecutive time steps for the STB analysis to determine the sampling rate that should be tuned for the main experiment (GVK). We use synthetic images of 0.05ppp and particle image size of 3.8px. For this test, three time separations will be investigated: the original time sampling of 1dt corresponding to around $6vx$ displacement, 2dt corresponding to $12vx$, and finally particles positions were interpolated by simple spline interpolation to create a 0.5dt case with an average displacement of $3vx$. All figures presented in this subsection are for tracks of the same physical time length whatever the mean displacement value.

A potential problem for the STB algorithm is slowly moving particles where the position accuracy of the involved particles is compromised due to the increased difficulty in the prediction phase of the algorithm, resulting in noisy tracks.

In Figure IV.33 **(a)** we see clearly that a displacement of 2dt ($12vx$) is not optimal since the number of tracked particles is reduced. Hence the matching ratio decreased from 96,5% to 88,9% for the 1dt and 2dt cases respectively. Additionally, the 2dt case leads to high percentage of ghost tracks.

The 0.5dt case is comparable to the 1dt case of chapter 3 and seems to confirm the findings of the SWT experiment. In Chapter III we found that a displacement of around $4.5vx$ is better than a displacement less than $3vx$. In this test on synthetic images, a $3vx$ displacement (corresponding to 0.5 dt of the original 1dt sampling) leads to high positions errors as seen in the same Figure IV.33 **(c)**. Also, the ghost ratio doubles, and ghost mean track length raises to 24 time steps (see Table IV-11). Furthermore, by visually looking

at the tracks for different image densities and multiple displacements, we see the evolution of spurious/ghost tracks for displacement larger than $2dt$ (see Figure IV.34).

(***a***)

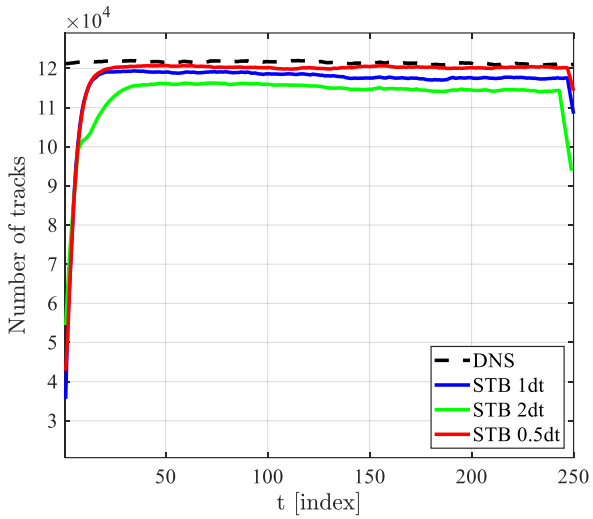

(***b***)

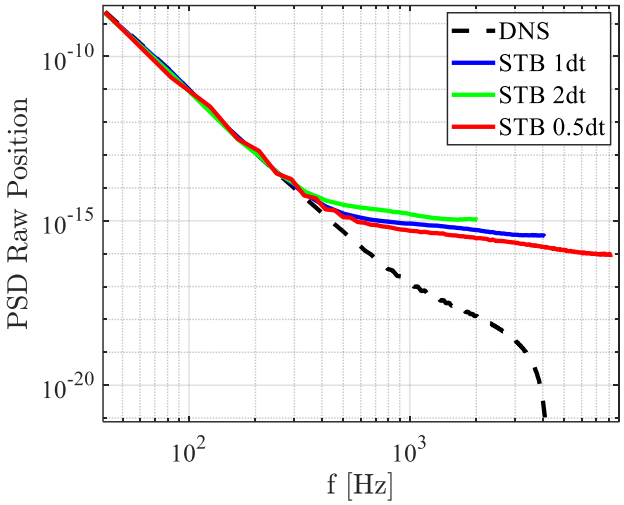

(c)

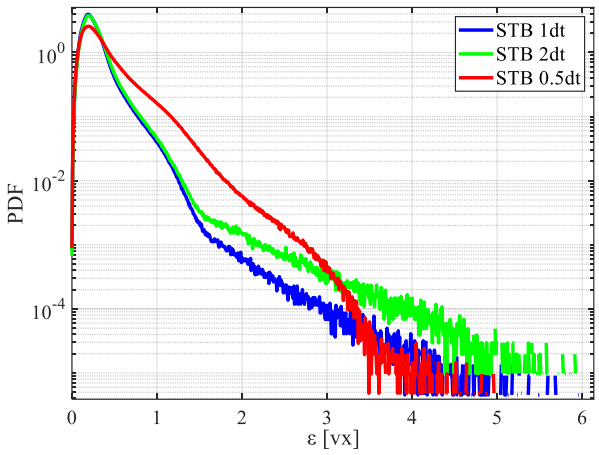

Figure IV.33 (a) Number of tracks. (b) PSD of position and (c) PDF of error for three cases 1dt 2dt & 0.5dt.

Table IV-11: Comparison statistics for images with background added noise ($\sigma_{noise} = 3, \mu = 5$) as function of particle displacement for particle image size of 3.8px and particle image concentration of 0.05ppp

Displacement	ψ	$\bar{\varepsilon}$ $[vx]]$	$\frac{N_{match}^{\varepsilon<0.2}}{N_{match}}$	$\overline{C_T}$	$\frac{n_{match}^{c_T=1}}{n_{match}}$	$\overline{f_r}$	$\frac{N_{gh}}{N_{STB}}$:	$GMTL$ *[TS]*
$3vx\ (0.5dt)$	96.3%	0.35	31%	0.79	35%	1.17	1.3%	24
$6vx\ (1dt)$	96.5%	0.19	68%	0.85	46%	1.06	0.6%	12
$12vx\ (2dt)$	88.9%	0.26	36%	0.74	40%	1.05	5.1%	5

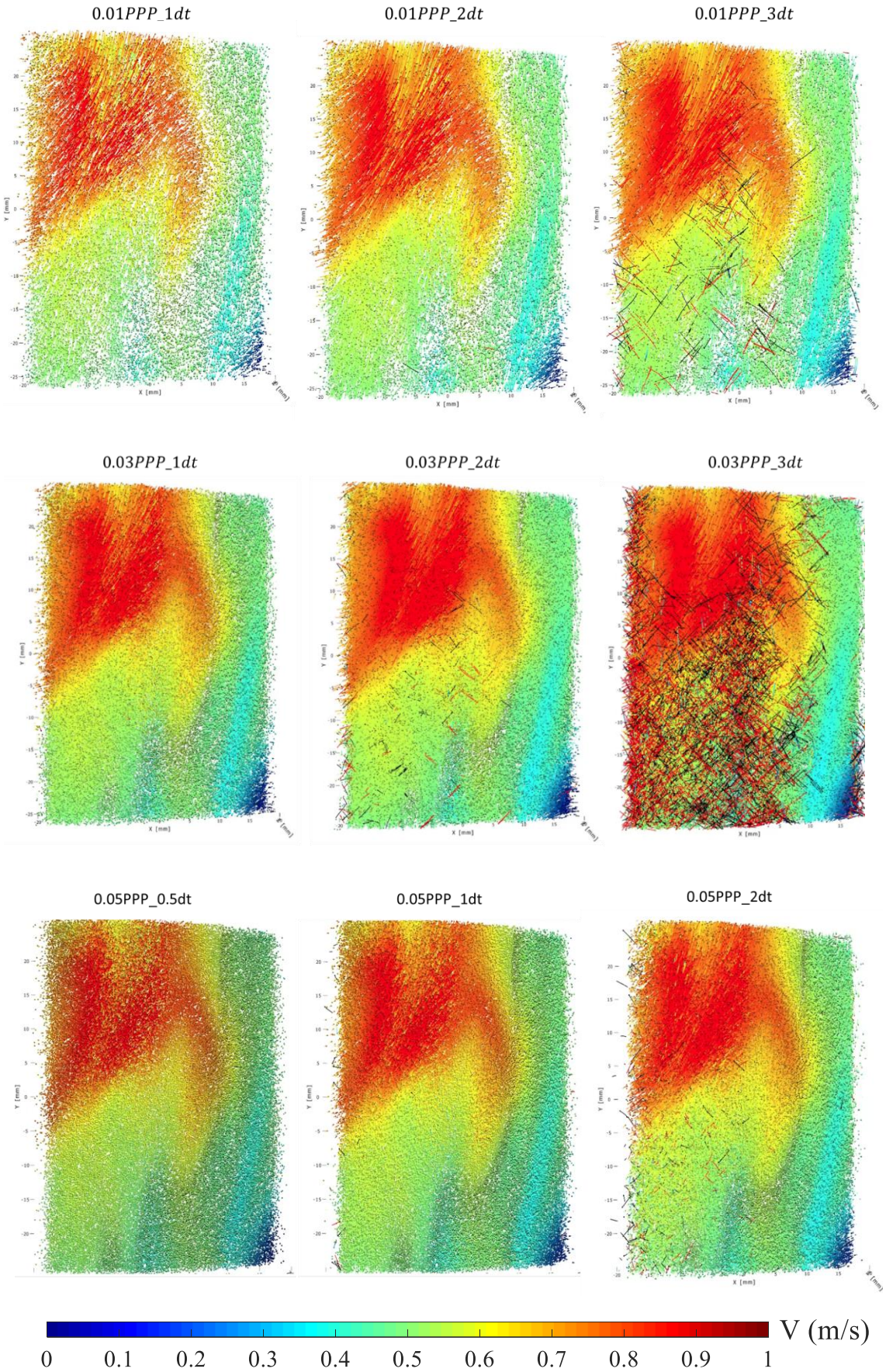

Figure IV.34 STB tracks for different displacement and images densities. 7 time steps only of all tracks presented in this figure are shown for visibility.

IV.8 Error investigation

For the error investigation, we will focus on the case of $\phi_{im} = 0.05\ ppp$ with added noise and mean displacement of $6vx$ $(1dt)$. This case is arguably the best for our applicaltion on the GVK experiment. First we analyze the error as function of time steps and how it does evolve in time. Figure IV.35 (Bottom) that presents the mean error by time step, gives us insights into STB. The first 4 time steps are the IPR phase prior to STB phase where the method updates the coordinates and intensity parameters of particles with their tracks extrapolation as predictor. This explains the increasing mean error for time steps 2 to 5. STB starts at time step number 5 where we can see the highest recorded mean error. Also we can see that the later time steps, from 220 to 250, have slightly more error, especially the last time step. In addition, in Figure IV.35 (top) we plot the PDF of errors for each time step. This time step number 5 leads to less particles with small errors and more particles with higher values of error. This is understandable considering that these particles are the first "tracked" particles. The error stabilizes after 10 to 20 time steps. This result shows that it is preferable to discard the first 20 time steps for correct statistics. For a set of 3226 images in our GVK experiment that should not be problematic.

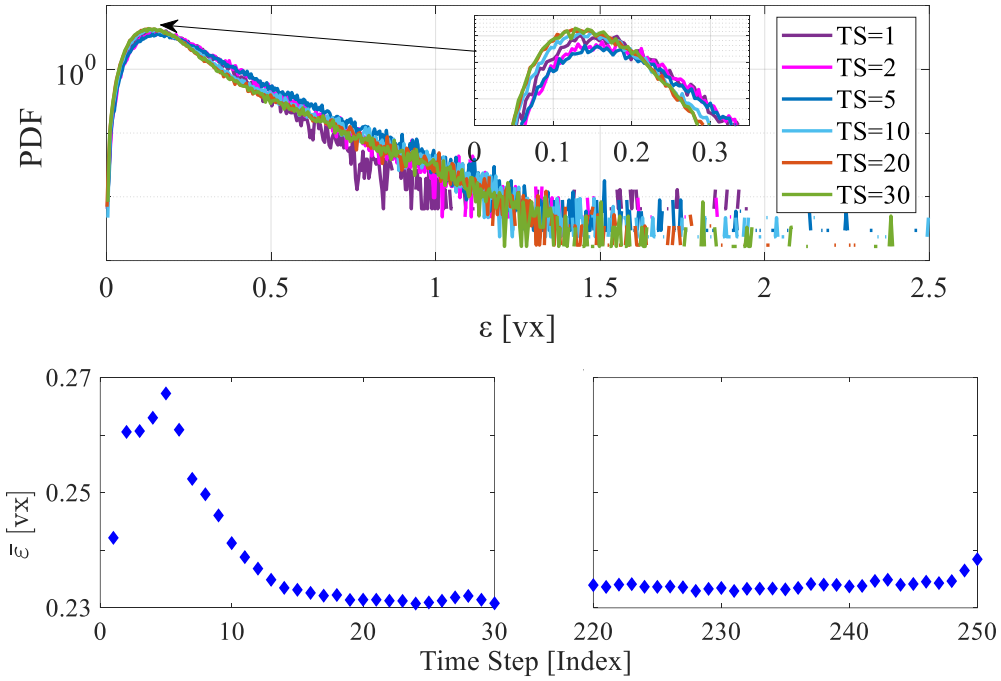

Figure IV.35 (Top) PDF of systematic error of all the points at a given time step (time step=1 to time step=30). (Bottom) The mean error ($\bar{\varepsilon}$) of all points at a given time step and (left) for the first and (right) for last 30-time steps. Both plots are for the case of $\phi_{im} = 0.05\ ppp$ with added noise and mean displacement of 6vx (1dt).

It's also worth noting that one of IPR characteristics is that a particle is removed when its position is within one pixel of another particle (Wieneke, 2013). We confirm this feature by finding the distance between one particle to all other particles at one time step. We then plot the PDF of these distances between a particle and its nearest in voxel space at a given time step. The result is presented in Figure IV.36. This figure shows that STB tends to filter some of the particles that lies at a distance less than 2vx from another particle. This could be another explanation of why STB fails to find the remaining part of the track in Figure IV.12. In that example, the nearest particles to the "cut off point" is at $1.28vx$

from it, hence increasing the possibility that this particle was filtered by the STB algorithm. On the other hand, and since we are using the case which gave us the optimal results, we might introduce a criteria that could be helpful to detect the reliability of STB results. The criteria is the distance between two particles where it should represent a plot that, more or less, have similar properties to the figure below where the peak is at $9vx$ and standard deviation is $5vx$.

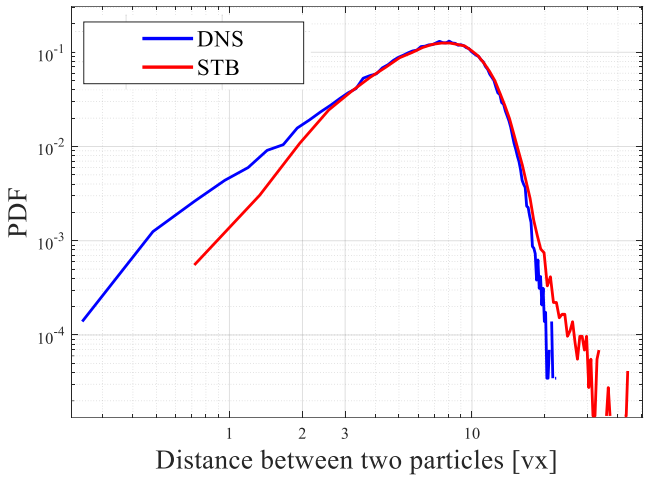

Figure IV.36 Comparison of PDFs of distances between a particle and its nearest in voxel space for the DNS and STB at Time step number 125 for the case of $\phi_{im} = 0.05$ *ppp with added noise and mean displacement of 6vx (1dt).*

Looking to the histograms of errors, the blue line in Figure IV.37 represents the histogram of error for $\phi_{im} = 0.01$ & $\phi_{im} = 0.05ppp$ from left to right. The dashed red line represents the histogram of error for all matching points of a track minus the first, last and second last matching point of the same track. The idea is to see the contribution of the error of each of these points to the global histogram of errors. The last matching point of a track (as we saw the cut off point in Figure IV.12) is usually where an unknown source of perturbation affects the space positioning of it and leads to the end of the tracking. From Figure IV.37 we see that "Last match of track" has more contribution to the high error values. Also the 2nd last matching contributes to these errors. On the other hand the first match doesn't seem to have a particular characteristic, besides having a lesser mean error.

Furthermore, from Figure IV.37 (right of error histogram) we see a belly shape for $0.6vx < \varepsilon < 1.3vx$ that start to form for images density of $0.05\ ppp$. We investigate more these points to verify if they have a particular positioning in our volume or if they represent a specific range of displacements values.

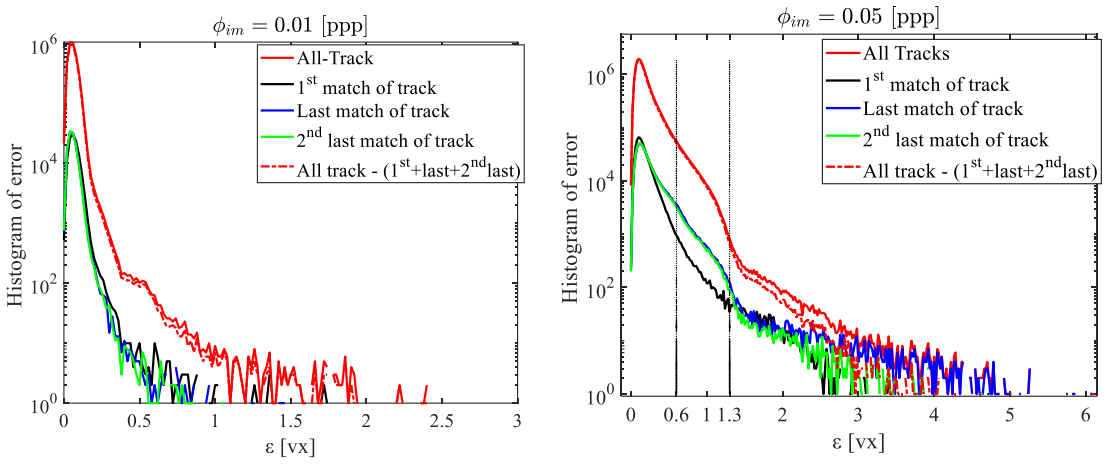

Figure IV.37 Histogram of systematic error ,ε, for: all matching point of a track (solid red line), first matching point of a track (black line), last match of a track (blue line), second last match of a track (green plot) and finally the histogram of error for all points matching in a track except the first, last and second last matching point in a track (red dotted line).

First by looking at the PDF of coordinates in the volume for all time steps in Figure IV.38 (top) we see that the error are mostly grouped in x positive, z negative and distributed across y coordinates but mostly in y positive. The same information could be deduced from the distribution of particles at the single time step (Time step number 125) in Figure IV.38 (bottom).

Finally in the Table IV-12 we see that the last match of a particle in a track contributes the most to the noise on the position of the particles. The table represents the percentage of particles with error less than 0.2 vx. Last match has the least percentage of particles with low error. Eliminating the last match of a track should reduce the noise on the real experiment where we expect higher magnitude of errors due to multiple experimental factors that contribute to the position uncertainty of a particle.

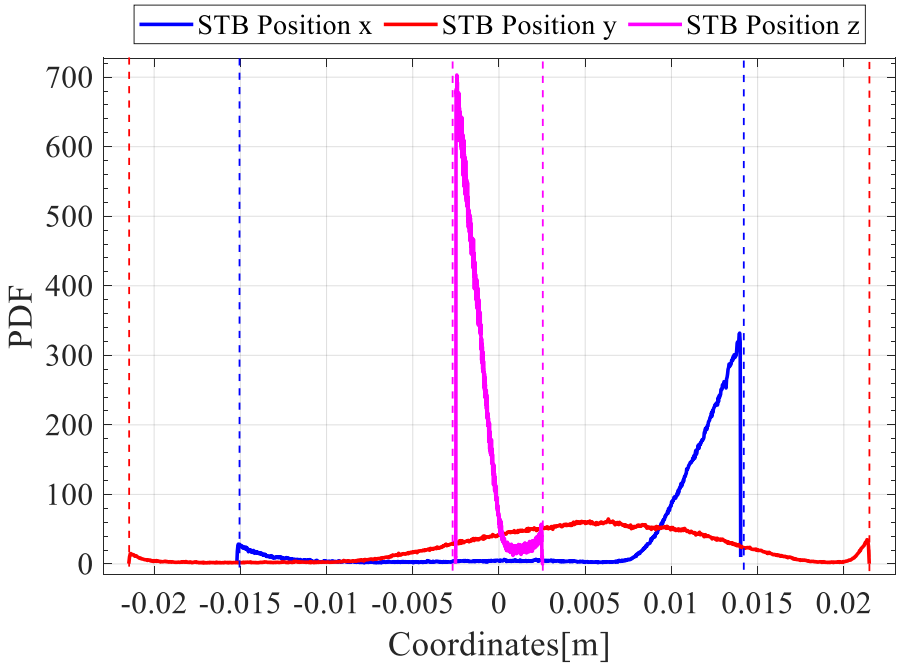

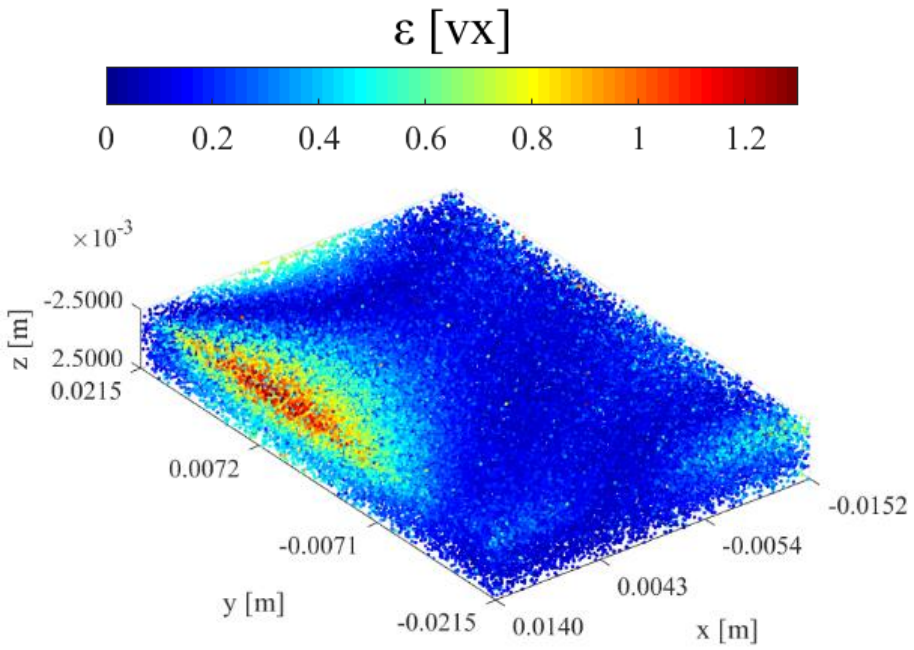

Figure IV.38 (Top) PDF coordinates for STB particles at all time steps ($from\ 1\ to\ 250$), the dotted vertical lines represent the boundaries of the volume. (Bottom) Is the distribution of particles in the volume color coded module of ε [vx] at time step number 125 for clarity. Both cases are for the case of $\phi_{im} = 0.05\ ppp$ with added noise and mean displacement of 6vx (1dt).

Table IV-12: Percentage of particles with systematic error less than $0.2vx$ $\left(\frac{N_{match}^{\varepsilon<0.2}}{N_{match}}\right)$ *as function of their position in a track and for different images densities*

Percentage of particles with error less than 0.2 vx

	0.01 [ppp]	0.05 [ppp]	0.07 [ppp]
All match tracks	99%	68.3%	6.05%
First match of tracks	99.01%	70.89%	1.95%
Last match of tracks	97.2%	56.4%	2.5%
second last match of tracks	97.3%	58.1%	3.07%
All match tracks except (1st , last & 2nd last)	99.3%	69.02%	6.4%

On the other hand the joint PDF of systematic error in x, y, z directions as function of the the displacement $[vx]$ in Figure IV.39 shows that most of errors in y direction are related to small diplacements. This result is somehow compatible with our findings in Chapter

III where we saw that a mean displacement of around 2.8 vx was oversampled. A displacement of 2dt (around 4.5 vx) was optimal for application on the 2nd configuration.

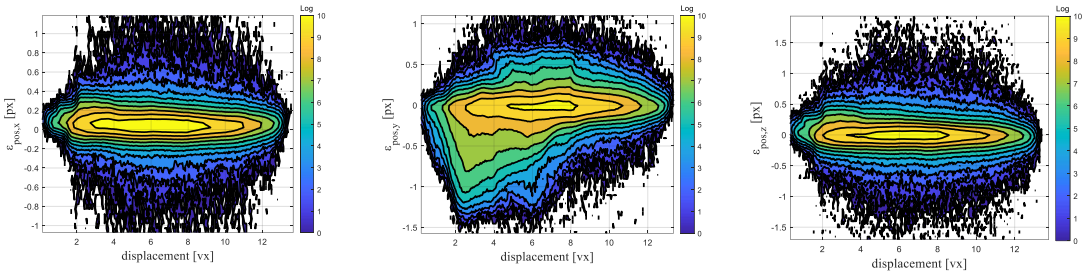

Figure IV.39 Joint PDF of error $\varepsilon_x, \varepsilon_y, \& \varepsilon_z$ with displacement $[vx]$ for all time steps combined for the case of $\phi_{im} = 0.05$ ppp with added noise and mean displacement of 6vx (1dt).

IV.9 Ghost tracks characteristics?

Even if the ghost level is remarkably low (0.6% for $\phi_{im} = 0.05\ ppp$ with background noise and for a displacement of $6vx$ (see Table IV-10)), it is however important to try to remove these last residues. Such unphysical tracks leads to wrong velocity data potentially biasing velocity and acceleration statistics. The first characteristic we find is the fact that ghost tracks have a higher displacement than the matching points of STB. The peak displacement of matching points is somewhere around $5vx$ while the peak of displacement of ghost particles is around $10vx$. This can be explained by the fact that ghost tracks are formed by unphysical particles. For a moderate density of particles, these unphysical particles forming ghosts are not as dense as the real particles. This means that a larger displacement is expected to form these ghost tracks, probably linked with the extrapolation of tracks to predict positions at next time step of STB algorithm.

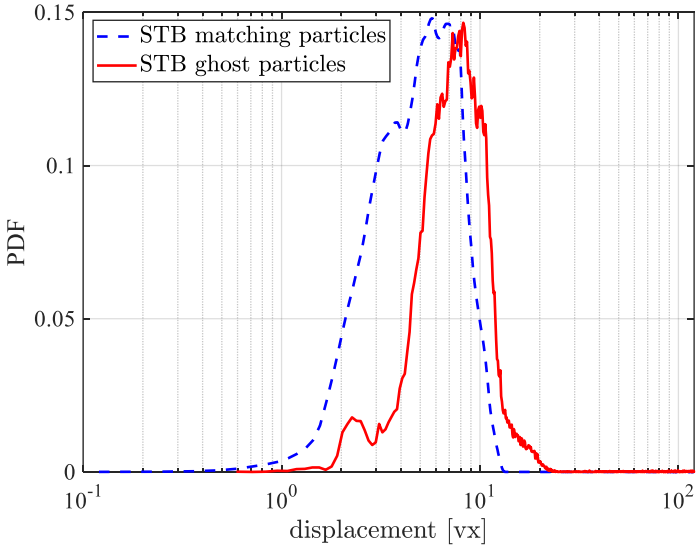

Figure IV.40 PDF plot of displacement of STB ghost particles compared to STB matching particles for the case of ϕ_{im}=0.05 ppp with added noise and mean displacement of 6vx (1dt).

Additionally, we have calculated the mean displacement of ghost particles for different image densities, we found $8.2vx$, $9vx$, $10vx$ and $11vx$ for image densities of $0.01, 0.03, 0.05$ and 0.07 ppp respectively (where the mean displacement of all densities for all particles is 6 vx). The particles in ghost tracks always have a mean displacement larger than the matching particles with DNS.

On the other hand, we plot the PDFs of ghost tracks length, it is remarkable to see some of ghost tracks (completely wrong) can be tracked up to 250 time steps which is the maximum number of time steps (see Figure IV.41). The minimum ghost tracks length is 5 since IPR deletes tracks that are smaller than 4 time steps.

Finally, by looking to a comparison between ghost tracks length, we remark in Figure IV.41 that by increasing the image densities we have less small ghost tracks. On the other hand, we have more 'illogical' tracks that are longer.

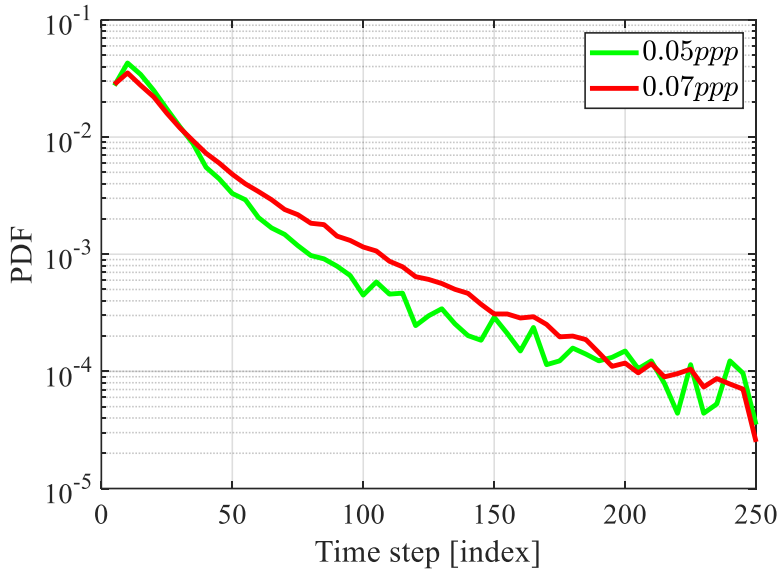

Figure IV.41 PDF plot of ghost tracks length in function of image density ϕ_{im}.

IV.10 Summary & Conclusion

A performance assessment of the iterative STB approach is carried out by means of the analysis of synthetic experiments. The availability of ground-truth particle and flow fields allows for the quantification of measurement errors in terms of position and the evaluation of the number of actual particles identified by STB. Evaluation metrics are provided to qualify STB parameters as well as experimental parameters (grey level threshold, allowed triangulation error, seeding density, image noise and particle displacement). Finally, some insights are given concerning errors and ghost tracks.

Results show the capability of STB to detect up to 99% of particles for an image density of 0.01ppp. This matching ratio decreases slightly to 97% for images density of 0.05 ppp. But the mean position error increases with a factor of 4 (from 0.051 vx to 0.194 vx for $\phi_{im} = 0.01$ ppp to 0.05 ppp respectively). From these results we conclude that image density choice is very important. For our application and using a mean particle size of $3.8px$, it seems that we pushed the density thresholds to its limits. The average distance between two particles in 3D space was found to be 3vx (for 0.005ppp and particle size of

3.8px). It should be taking into account a smaller density than $0.05ppp$ if mean particle size is bigger than $3.8px$.

Particle size tests shows that this parameter is the most crucial parameter to optimize around a mean diameter of $2.4px$. It was shown that this parameter affects significantly either quantitatively or qualitatively the STB results. Ghosts ratios increase substantially, and matching ratio decreases with increasing particle image size.

Displacement trials were not very clear to interpret and to find an optimal displacement range. On the other hand, we showed that a high displacement values drastically affect the results and increases the number of spurious vectors. Nonetheless, we showed that a mean displacement of $6vx$ seems optimal. Also, it is interesting to see that for images density of $0.05ppp$ the matching ratio increases slightly from 95.6% to 96.3% for a smaller mean displacement $(3.1vx)$ but the mean error records a maximum of $0.358\ vx$ between all the tests done on the same $0.05ppp$ image density, this could be a first indication to the optimal displacement that we should aim to on the real experiment.
Finally, we test multiple image densities, and we see that the matching ratio drops 3.7% from $0.01ppp$ to $0.05ppp$, and then drops 16.5% from $0.05ppp$ to $0.07ppp$. $0.05\ ppp$ seems to be the limit of image density. Percentage of ghost tracks as well as ghost tracks length agrees with these findings. Furthermore, higher error magnitudes appear to be linked to small displacements rather than large displacement. Ghost particles, on the other hand, have higher displacements compared to other particles. Almost a factor of two higher.

The main findings of the error investigation (section IV.8) is the fact that these errors are not linked to specific properties of the flow.
One might need to delete the first 15 to 20 time steps of each track since they present the highest recorded errors $< \varepsilon >$. Further, the last match of a track contributes the most to the big errors in the PDFs shown in this section.

Finally, grey level threshold and allowed triangulation error should be chosen carefully. The allowed triangulation error especially needs to be kept as defaults (0.5vx) if not sure of the value to use. On the other hand, grey level threshold needs to be as close as possible to the real background noise. This can be done by investigating visually the images. Low threshold increases the fragmented/small tracks ratio while a high threshold decreases the number of detected particles.

To wrap up this section, the most important factors that affect STB results in descending order are:

	Experimental characteristics	STB limits	Comment
1	Mean particle size	Maximum 3.8px (if 0.05ppp is the goal images density)	If particle size bigger than 3.8px, images acquisition at lower images densities is required.
2	Intensity difference between cameras	The mean intensity difference between cameras should not present big differences.	If mean intensity difference between cameras is higher than a factor of 2; image preprocessing is absolutely needed.
3	Images density	Maximum 0.05ppp (if particle size is close to 3.8px)	Any optical aberration recorded (astigmatism etc.) requires decreasing the ϕ_{im}.
4	Displacement range	Roughly between 4vx to 6vx	We could not say for sure what is the optimal choice. Deeper investigations must be done. But too small is clearly a problem.

Table IV-13: Summary table of the parameters with basic results of the comparison with respect to synthetic tracks from DNS.

Δ_{PTV} _$Noise_d_p$	$part/mm^3$	η_k^{expe}/Res_{PTV}	$[\mu_{dp}\ \sigma_{dp}]$ $[vx]$	Threshold [count]	Trian-gulation $[vx]$	Results N_{match} $\times 10^6$	Results ψ	Results $\bar{\varepsilon}$ $[vx]$
0.01ppp DNS			**[5.97, 2.38]**					
1dt_3.8px	**2**	**0.86**	[5.8, 2.4]	1	0.5	3.78	99.3%	0.051
2dt_3.8px			[11.6, 5.2]	1	0.5	1.86	97.7%	0.054
3dt_3.8px			[17.7, 9.4]	1	0.5	1.2	95.3%	0.057
1dt_Noise_3.8px			[5.8, 2.4]	10	0.5	3.78	99.3%	0.059
0.03ppp DNS			**[5.96, 2.38]**					
1dt_3.8px	**6**	**1.22**	[5.8, 2.4]	1	0.5	11.4	99.1%	0.063
2dt_3.8px			[11.7, 5.2]	1	0.5	5.58	97%	0.067
3dt_3.8px			[17.7, 9.4]	1	0.5	3.46	89.5%	0.073
0.05ppp DNS			**[5.96, 2.38]**					
0.5dt_3.8px	**10**	**1.42**	[3.1, 1.3]	1	0.5	18.7	97.7%	0.298
0.5dt_Noise_3.8px			[3.1, 1.3]	10	0.5	18.5	96.3%	0.358
1dt_3.8px			[5.8, 2.4]	1	0.5	18.7	97.5%	0.249
2dt_3.8px			[12.6, 6.9]	1	0.5	8.5	88.9%	0.263
1dt_Noise_3.8px			[5.8, 2.4]	10	0.5	18.3	95.6%	0.194
			[5.8, 2.4]	15	0.5	18.6	96.5%	0.191
			[5.8, 2.4]	20	0.5	18.4	96.3%	0.192
			[5.8, 2.4]	25	0.5	18.2	95.2%	0.194
			[5.8, 2.4]	30	0.5	17.8	93.0%	0.200
			[5.8, 2.4]	15	0.3	12.9	67.4%	0.244
			[5.8, 2.4]	15	0.4	17.6	91.9%	0.200
			[5.8, 2.4]	15	0.6	18.7	97.8%	0.189
			[5.8, 2.4]	15	0.7	18.8	98.2%	0.188
1dt_Noise_4.8px			[5.8, 2.4]	30	0.5	12.7	66.4%	0.326
0.07ppp DNS			**[6, 2.38]**					
1dt_3.8ox	**15**	**1.5**	[6, 2.75]	1	0.5	23.7	88.5%	0.496
1dt_Noise_3.8px			[6, 2.75]	15	0.5	21.2	79.1%	0.783
1dt_Noise_2.4px			[6, 2.75]	15	0.5	24.3	90.7%	0.478

Chapter V GVK experiment.

Contents

V.1 Von Kármán mixing tank - GVK description and setup

The GVK experiment was specifically designed to study turbulence experimentally at high Reynolds number in a large-scale mixing tank. The name of this experiment is also known in the community under the name “French washing machine”. It consists of two counterrotating impellers made of aluminum and immersed in a cylindrical tank filled with water as shown in Figure V.1. The fluid contained into the cylindrical tank is mechanically stirred by the two coaxial impellers and driven by two independent motors. The impellers generate a region of axisymmetric shearing near the middle of the tank, generating high levels of turbulence with a weak mean flow approaching zero near the center of the tank. The cylindrical tank is made of two plates of plexiglass, the final cylinder has a thickness of $1cm$ as in VK2 and an inner diameter of $1\ m$. This tank is placed in another hexadecagon tank formed of 16 faces as previously shown in Figure III.1. It is made of aluminum and holds the cylindrical tank while connecting the bottom and top of the set-up to ensure that the plexiglass cylindrical tank is not stressed. The inner and outer tanks are separated by four centimeters. There are two kinds of openings in the outer tank: windows and prisms as shown in Figure V.2. Both are removable and made of optical anti-refractive glass. The windows will be used for volume measurements in the tank center at several heights. They act as access points for the laser beam and image acquisition. The prisms will be used to observe a measurement volume near the wall (not included in this thesis work). A metal structure holds the tank and another one holds the bottom and the top engines. Siemens electrical asynchronous engines were chosen. Each motor has a rated power of $7kW$, a torque of $45N.m$, and a rotation frequency of $1500\ rpm$. They are paired with reduction gears with a $20{:}1$ reduction ratio. Two pulleys of different sizes are provided for each engine, allowing the entire range of working parameters to be achieved. Transmission to the impellers is ensured by belts. The total height of GVK (when it is closed) is $2.2\ m$, the length is $3m$ and the width is $1.3\ m$. The inner radius of the cylinder is $R = 500mm$ and the distance between the inner face of the impellers is $H = 1000mm$, which gives an aspect ratio of $H/R = 2$.

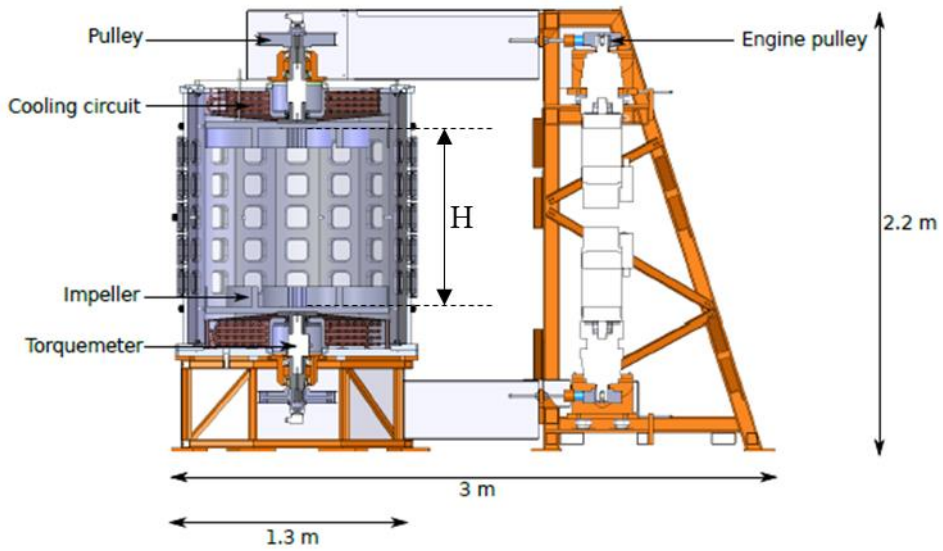

Figure V.1 Vertical cross section of the GVK setup designed by GP concept.

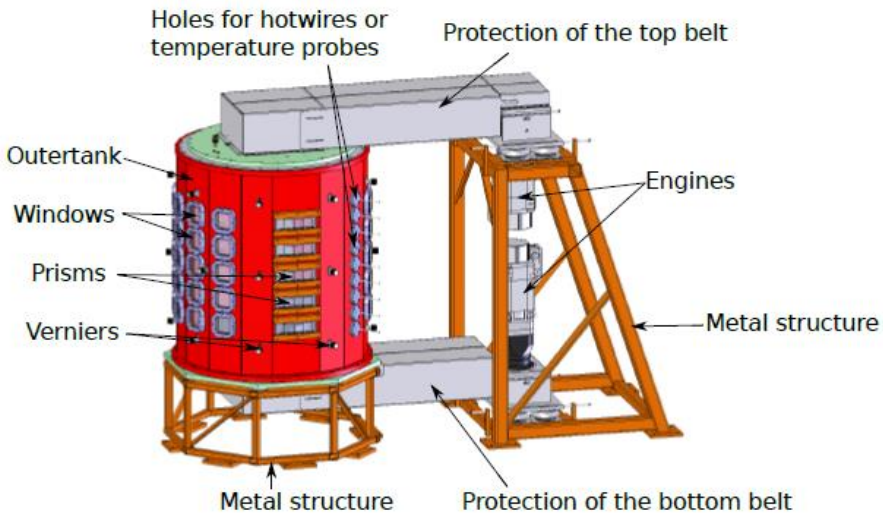

Figure V.2 3D view of the GVK setup designed by GP concept.

V.1.1 Global quantities and scaling relations

The considered von Kármán flow is characterized by a Reynolds number based on the cylinder radius R, the impeller revolution per second F and the fluid kinematic viscosity ν as follows (Kuzzay et al., 2015b):

$$Re = \frac{\omega R^2}{\nu} = \frac{2\pi R^2 F}{\nu} \qquad (V\text{-}1)$$

where F is the frequency of rotation of the impellers. The Reynolds can be varied by increasing F or by changing the fluid. Some tests were done on VK2 using a mixture of water and glycerol. As the mixture kinematic viscosity is larger than water, the Reynolds decreases leading to an increase of the Kolmogorov scale which can be better resolved. The small Reynolds numbers were created by a low frequency of impellers. We only use water for the time being for this first GVK campaign.

Starting by an approximation of energy dissipation using torque measurements, one can get an accurate estimate of the global power injected into the flow. The input energy must balance the rate of energy dissipation within the flow. Following the work of (Kuzzay et al., 2015b) and (Rousset et al., 2014) the dissipation rate is estimated to:

$$\epsilon = \frac{2\omega T}{m} \quad \text{With } m = \rho\pi R^2 \times H \qquad (V\text{-}2)$$

where m is the mass of the fluid in the cylinder and T is the average torque (over time) applied on the fluid by one impeller. The total applied torque is $2T$ and the total power is $2\omega T$.

Following the procedure described in (Marié, 2003), a non-dimensional value of the torque K_p is computed as:

$$K_p = \frac{T}{\rho R^5 \omega^2} \qquad (V\text{-}3)$$

Then from equation (V-2) we find:

$$\epsilon = \frac{2\omega^3 K_p \rho R^5}{\rho \pi R^2 \times H} = \frac{2\omega^3 R^3 K_p}{H\pi} \qquad (V\text{-}4)$$

And the estimated Kolmogorov length scale is computed from the Kolmogorov's scale definition

$$\eta = \left(\frac{\nu^3}{\epsilon}\right)^{\frac{1}{4}} = \left(\frac{H\pi\nu^3}{2\omega^3 R^3 K_p}\right)^{\frac{1}{4}} = \left(\frac{H\pi\nu^2}{2\omega^2 R K_p}\frac{1}{Re}\right)^{\frac{1}{4}} \qquad (V\text{-}5)$$

Finally, the Kolmogorov time scale is:

$$\tau_\eta = \left(\frac{\nu}{\epsilon}\right)^{\frac{1}{2}} = \left(\frac{H\pi\nu}{2\omega^3 R^3 K_p}\right)^{\frac{1}{2}} \qquad (V\text{-}6)$$

V.1.2 Experimental setup

Here we present the setup of the first campaign done on the GVK hoping for more successful campaigns to come. The experiment is shown in Figure V.3 as well as the PTV system. On the left of the figure, we can vaguely see the metal chassis holding the GVK and the engines. The top impeller is removed to add particles and water that is provided from a water tank situated in the same room (see right side of the Figure V.4). Also, the removable top allows us to introduce the calibration plate at the center of the volume for recording cameras calibration images. We make sure to cover the water tank with nylon sheet to prevent dust from entering the experiment. Control room including data acquisition systems is separated by curtains from the GVK for laser safety purposes.

The experimental conditions are those presented previously in Chapter III. Cameras are placed symmetrically around the experiment following exactly the 2nd configuration (see section III.4) and to be in forward scattering to the source of light (for more information about the cameras see Table III-1). To enable optical measurements, the flow is seeded with particles of polystyrene of average size 5.09 μm from Spherotech, we use the same particles tested in chapter III inasmuch of their proven quality. The third row windows are used to record images at the center of the volume. A calibration plates is introduced at the center of GVK using a mechanical system specially designed to accurately tune its position from outside of the tank to minimize as much as possible the possibility of polluting the water inside GVK.

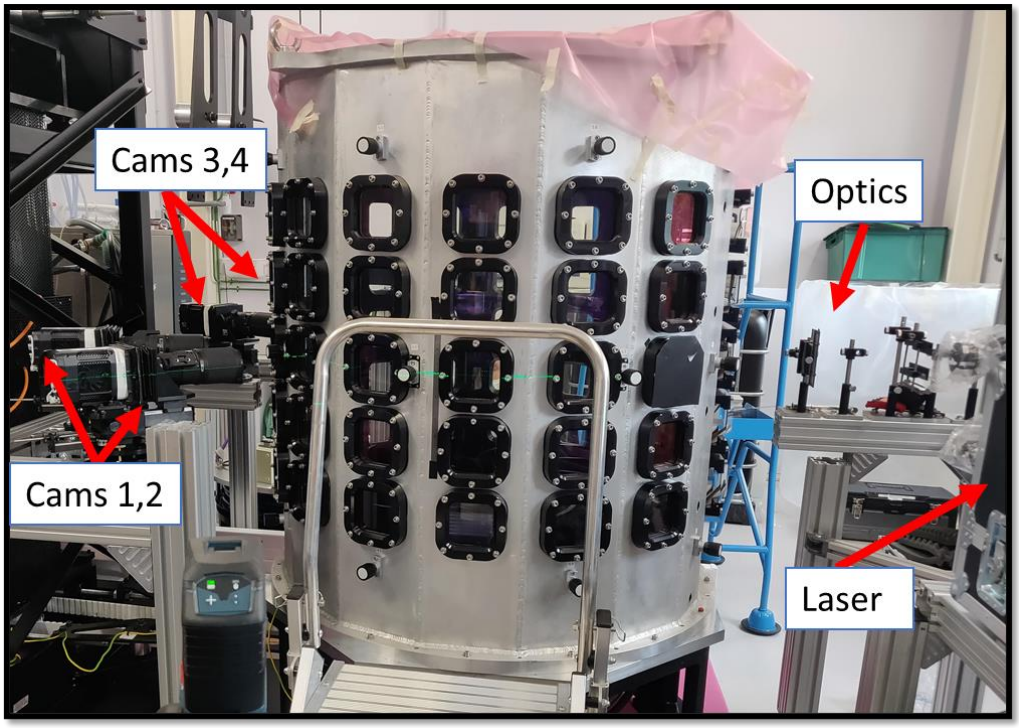

Figure V.3 The outer tank of the "Grand Von Karman" (GVK) with cameras mounted around.

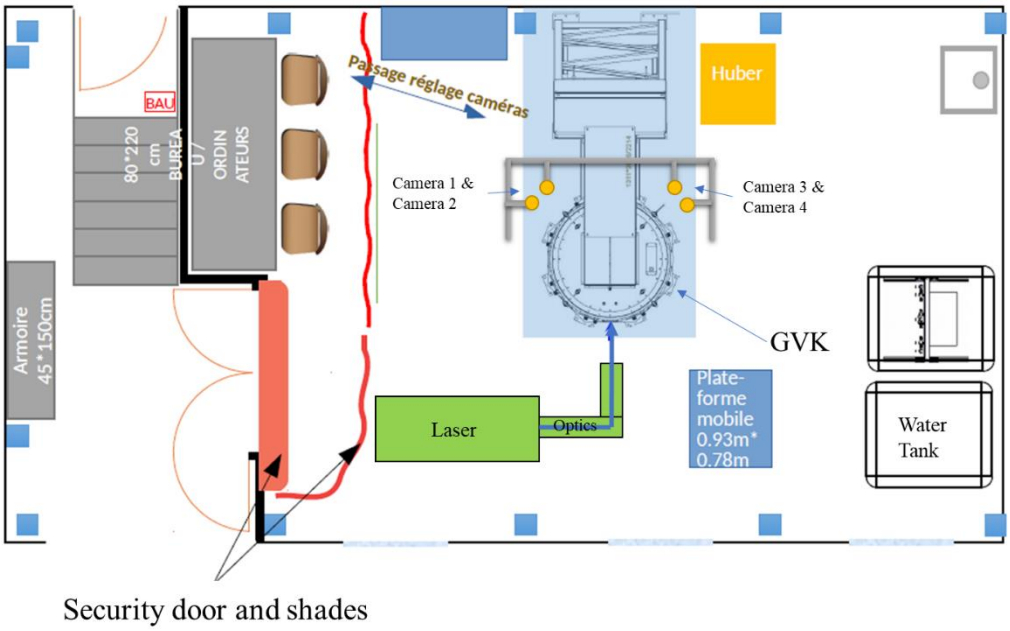

Figure V.4 A sketch of the material placement inside the GVK room illustrating the GVK and the placement of the symmetrically located cameras. This sketch also shows the laser location and the optics that were used to create the beam that enters towards the cameras into the GVK through the middle window.

During image acquisition, we observed some astigmatism effects for all cameras, but specially for camera 2 and camera 3. This optical aberration could be due to the presence

of a small cylindrical lens formed by a slight bend of the glass windows of GVK which might be a result of the mechanical constraints applied on the access windows by the screws which compress the gasket. As a consequence, the volume in focus becomes shifted in both directions hence, causing the image formed on the camera sensor to be distorted. Given that we had one week timeline to finish the experiment, we decided to close the aperture (i.e increase the value of $f\#$) from 11 to 16 for cameras 2 and 3 where the astigmatism was too strong on the edge of the volume. The cameras properties are presented in Table V-1.

Table V-1 Characteristics of the cameras and their spatial positions for the configuration used in this chapter.

Camera	Angle with Laser beam	$lens(mm)$	M	$f\#$
1	$+45.5°$	200 mm	0.37	11
2	$+22.5°$	200 mm	0.37	16
3	$-22.5°$	200 mm	0.37	16
4	$-45°$	200 mm	0.37	11

By increasing the fstop number, we increase the depth of field from 5.27mm to 11mm to limit the blurred images in one direction on both edges of the volume, the drawback is that it increases the particle size. This by itself presents a problem since the real particle size obtained in SWT experiment configuration 2 (same optical set-up as here) at $f\# = 11$ was already around the optimal at 2.4 pixels (see Figure III.16). The minimum particle diameter for camera 2 and camera 3 is estimated to be 2.9 pixels (see Table IV-2). Now astigmatism increases this number, and one must keep in mind that the diameter of the diffraction spots is bigger due to small blurring of the particles located on the edge of the illuminated volume. For that reason, it is ideally necessary to have a diffraction spot diameter around 2 pixels at the center. Another serious disadvantage of having different $f\#$ values between cameras is the fact that cameras with lower $f\#$ (camera 1 and camera 4) get more light. But since these two cameras are at $\pm 45°$, they get less scattered light already than ones at 22.5°. However, to minimize the background noise from reflections inside GVK, we played on the polarity of the laser. The optimum was reached for a polarity different than in SWT experiment. As the scattering light is highly sensitive to the polarity of the laser (see Figure III.13), we obtained much higher difference of particle intensities for cameras 2 and 3 (22.5°) compared to camera 1 and 4 (45°) than in SWT experiment. In SWT experiment (all cameras with same $f\# = 11$) was about 2. Here, we obtained a factor about 4, even with the higher $f\#$ use for cameras 2 and 3. This difference can also be explained by the presence of coated glasses which can increase the transmitted light for 1 polarization. Probably a better compromise could have been found.

Also, for camera 1 and camera 4 our image is not focused on the totality of the desired $6mm$ thickness as we see from the estimated δ_Z in Table V-2. The minimum particle diameter for these two cameras is estimated to be 2 pixels at focus plane contrary to camera 2 and camera 3 for which it is $2.9px$.

In conclusion, for all cameras, the particle image size obtained is too large compared to optimum value. This can be improved by correcting the astigmatism problem and playing on the polarity of the laser. However due to a risk of breaking a GVK glass windows or introducing leaks, we have not iterated on these points. Probably improvement can be found there. As the particle image diameter obtained here is larger than optimum one

found in chapter 4, the seeding density has then to be lower than the optimum 0.05ppp found. It was then decided to fix the concentration at $0.04\ ppp$.

Table V-2: Particle image minimum diameter and the depth of field as a function of the $f\#$. The results are for a given magnification factor M=0.37. d_{diff} is the particles diffraction diameter.

$f\#$	$d_{diff}(pixel)$	$\delta_Z(mm)$
8	1.45	2.8
11	2	5.27
16	2.9	11
22	3.98	21.1

V.1.3 Images acquisition

In this section we present the experimental data sets that are acquired during the timeline of this thesis. We use STB to track particle given by one standard deviation of velocity positions at the center of the turbulent von Kármán flow generated in the GVK set-up (Figure V.5). We use the Lavision software "Davis" for data acquisition. The acquisition frequency is adjusted for each rotation frequency of the impellers. In the previous work on the VK2; Debue, 2019 defined a criterion to estimate the acquisition frequency.

$$f_{acq} = \frac{\omega R a}{5\left(\frac{c}{|M|}\right)} \qquad (V\text{-}7)$$

Where a is equal 0.4 for Anti and 0.35 for Contra cases and 5 pixels is the targeted average displacement of particles given by one standard deviation of velocity between two successive frames. This displacement is around the optimum value based on our previous tests on synthetic images.

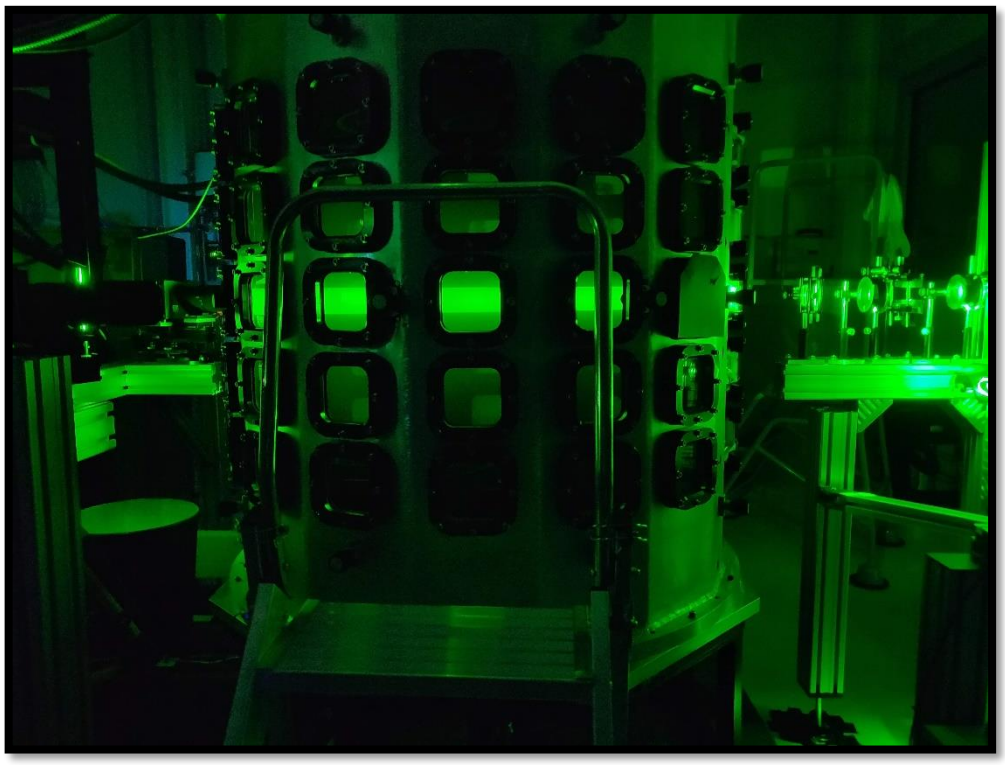

Figure V.5 Photograph of the PTV experimental setup. A laser beam of thickness 6mm created by a set of optic described in Chapter 3 Figure III.5, is entering the GVK through a window and is exiting from the left side of the figure.

Eight cases were recorded at different Reynolds numbers in order to vary the Kolmogorov scale and therefore to probe different scale ranges. The Reynolds numbers of the different cases are given in Table IV-2 for the Contra and Anti configurations, along with the corresponding flow parameters and the acquisition frequencies. This frequency is the value estimated to reach an average displacement of 5vx.

Table V-3: Physical parameters of GVK for the 8 different cases. F is the rotational speed of the impellers, Re is the Reynolds number of experiment (V-1), Kp is the torque coefficient (V-3), T_i is the integral time scale, $T_i = R/(2\pi RF)$, with R being an estimate of the integral length scale and $2\pi RF$ the maximum velocity of the flow, ϵ is the dissipation (V-4), η is the Kolmogorov length scale (V-5), τ_η is the Kolmogorov time scale (V-6) and f_{acq} is the sampling frequency of the STB experiment.

Case	Anti	Contra	Anti	Contra	Anti	Contra	Anti	Contra
$F\ (Hz)$	0.004		0.01		0.025		0.1	
Re	6.3×10^3		1.5×10^4		3.9×10^4		1.57×10^5	
K_p	0.135	0.047	0.135	0.047	0.135	0.047	0.135	0.047
$T_i\ (s)$	40		16		6.4		1.6	
ϵ $(10^{-6}\ m^2/s^3)$	0.34	0.12	5.3	1.85	83.3	29	5330	1855
η (mm)	1.3	1.7	0.66	0.86	0.33	0.43	0.12	0.15
$\tau_\eta\ (s)$	1.71	2.9	0.43	0.73	0.11	0.18	0.013	0.023
f_{acq}	37	32	92	81	232	203	929	813

The Kolmogorov length scale is of the order of 1 mm at the lowest Reynolds. This makes fully spatially resolved measurements possible with our PTV system as the resolution of PTV system is estimated to $0.5mm$ for image concentration of 0.04ppp which is largely feasible (see Chapter IV). The actual acquisition frequencies that we use for the Anti-Contra cases are 100, 150, 400 and 1200Hz for the 0.004, 0.01, 0.025 and 0.1Hz impellers rotation frequency. The frequencies are intentionally set higher than the estimated frequencies in order to avoid having too large displacement values. As shown in Chapter IV large displacements can be problematic for the STB algorithm. We therefore decided to take some security margins on our frequency estimation to be in the safe side as it was the first experiment on GVK, and we were not sure that the estimation formula obtained for VK2 (V-7) is valid in GVK. Moreover, the minimum laser frequency above which the same optical set-up can be used to generate the same volume light sheet is 100Hz. For the four frequencies of impellers investigated (0.004, 0.01, 0.025 and 0.1 Hz) and the two configurations contra and anti of GVK, 40 runs of full memory (3226 time steps) were recorded for each of these 8 cases. For each case, the total recorded time corresponds to about 30 integral time scales for the 0.004Hz configurations and about 50 to 60 for the others. This allows then to start computing turbulence statistics by averaging in time and space (homogeneous flow). The volume of recorded raw images is about 12 TB.

V.2 Particles images quality

As briefly discussed before, we noticed a problem in the image particles of the cameras, especially for camera 2 and camera 3. The particle images look elongated in x or y directions for different depth of fields. This effect which was noticeable to the naked eye at first was quantified by the OTF 2D map for different slices in the volume (in z direction). Astigmatism distortions are troublesome as it increases the mean particle size significantly. As we saw in the previous Chapter IV, this parameter might be the most important for STB reconstruction. Another important factor that plays big role in the quality of STB results is the image intensity factor between different cameras. From the particles images, we found that the average intensity for images of camera 1 to camera 4 are 90, 415, 352 and 100 counts respectively. Indeed, the difference is unacceptable between camera 1 & camera 2 and camera 3 & camera 4. We have learned from Chapter IV that even a factor of two could be detrimental for the results. For this reason and before to process by STB, the images have to be corrected to reduce the intensity difference between different cameras that are at different angles with respect to the source of light. Additionally, the image preprocessing will help reduce the cameras background noise. In this way we achieve nicely shaped particle images with close to zero background noise. Finally, it is very important to use these processed images for the calculation of the optical transfer function and for the Shake-the-Box calculation. Otherwise, the optical transfer function will not fit to the new processed images and STB will suffer to track the particles.

The image preprocessing is as follow: a spatial filter is used to remove the image background by subtracting the local minimum from each pixel. The size of the region used for this phase is $11px \times 11px$ (i.e the $1600px \times 1600px$ images are divided into 145 sub windows). The mean intensity of images of cameras 1 to 4 becomes almost equal to 45 counts. In Figure V.6 (bottom) we see the PDF of intensity for 1000 images for all cameras before and after image preprocessing. The effect of image preprocessing is clear for camera 2 and camera 3. The peak becomes closer to the one observed for camera1 and camera 4. Furthermore, an added value of the image preprocessing is the reduction in particle diameter due to a cut of the tail of the gaussian distribution of particle intensity by the background subtraction. In Figure V.6 (top) we show the estimated particle size for all particles over 1000 images. The mean particle size before image preprocessing was 3.2px, 5.4px, 4.8px and 3.3px for camera 1 to 4 respectively and reduced to 2.9px, 4.6px, 4px and 2.9px for camera 1 to 4 after processing.

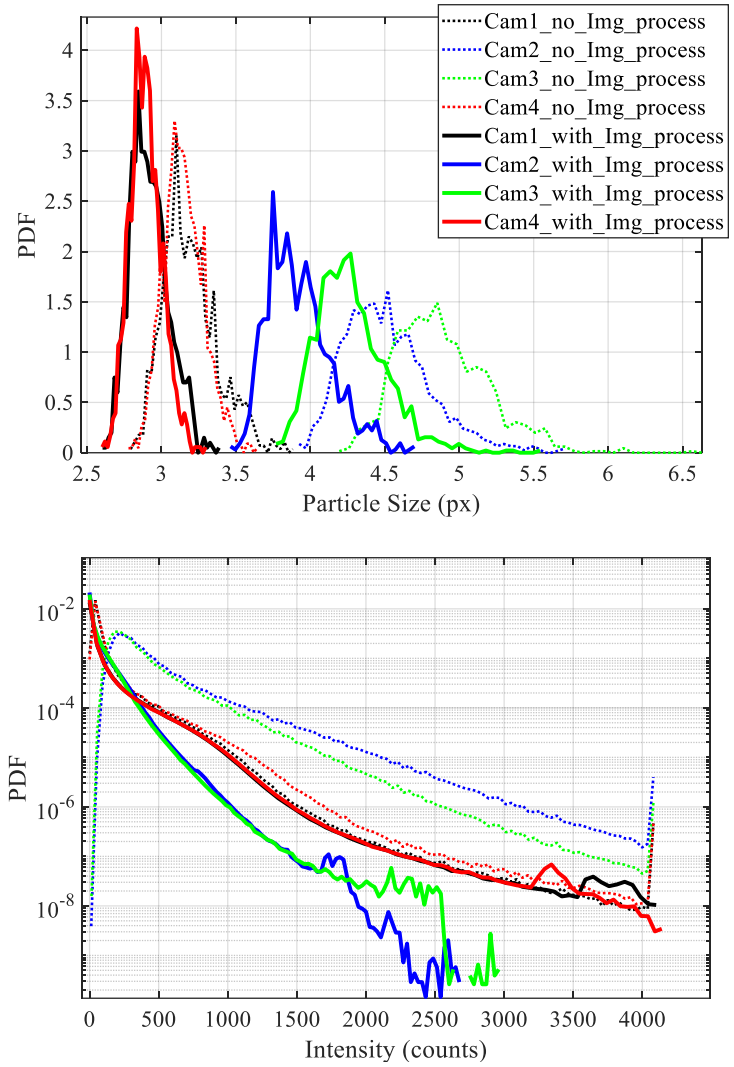

Figure V.6 (Top) PDF of particle size estimated from 1000 images. (Bottom) PDF of images intensity. Both figures are for images before and after image preprocessing Particle size is estimated by fitting a 2D gaussian to the peak of correlation of one image by itself. Window size used for correlation is 64×64 pixels.

Finally, the particle size quality can be qualified using the OTF map. Figure V.7 show an OTF example at the center of the volume for camera 2. The OTF calculated for images before image preprocessing (left figure) present oddly shaped particles especially in the far right subvolumes. This effect could be greater for slices far from the center that could be not totally in focus due to optical aberrations and/or not covered with the depth of field (out of focus plane). On the other hand, the OTF for images after processing (right figure) is much better (blurred part close to background noise suppressed and intensity difference reduced) but not fully optimal as compared to the results of Chapter III.

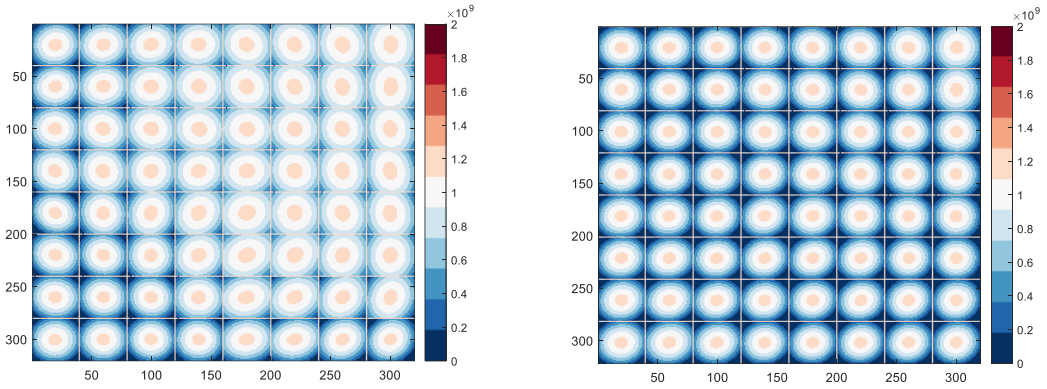

Figure V.7 Optical transfer function (OTF) that represents the particles pattern for a selected slice into the volume (z=0 the center of the volume). The left figure is the optical pattern calculated from the run #20 of the case 0.1Hz Anti before image pre-processing. The right figure is the optical pattern for the same run after image pre-processing.

V.3 STB Analysis

After processing the images, we carried out 4D Lagrangian particle tracking using the STB algorithm as described in detail previously. The first results of STB tracking are presented in this thesis. Here we try to optimize the tracks as much as possible before they can be exploited to search for some possible quasi-singularities in the turbulent flow. Our main goal in this chapter is to confirm if the spatial resolution has been improved compared to VK2 experiment (Debue et al 2019). This could be achieved by investigating the velocity spectra to check that the smallest scales exhibit a better signal to noise ratio.

The STB parameters are adjusted and adapted to each of the 8 cases presented in Table V-3. The main difference between the results presented here and the results presented before in Chapter III is, as discussed before, the use of preprocessed images instead of raw images. Another difference is the use of a median filter (filter explained in section II.4.5) to reduce the number of spurious vectors. As this filter was not used before for the lack of necessity (no spurious vectors), the exact effect of each parameter of the filter used were unknown for us. We use here the suggested parameters from Lavision STB manual that are adapted to our values of displacement and *ppp* (Max search range = 60 vx, number of neighbors used = 10, threshold = 2). The effect of median filter is shown in the figure below. It does visually suppress spurious tracks with velocity completely different from neighbors as expected (see Figure V.8) without compromising the number of tracks (70×10^3 in average per time step for both cases). On the other hand, it does have a negative effect on the track length histogram with much shorter track (see Figure V.9 (top)) but reduces the noise levels for frequencies larger than 2 Hz (see bottom figure).

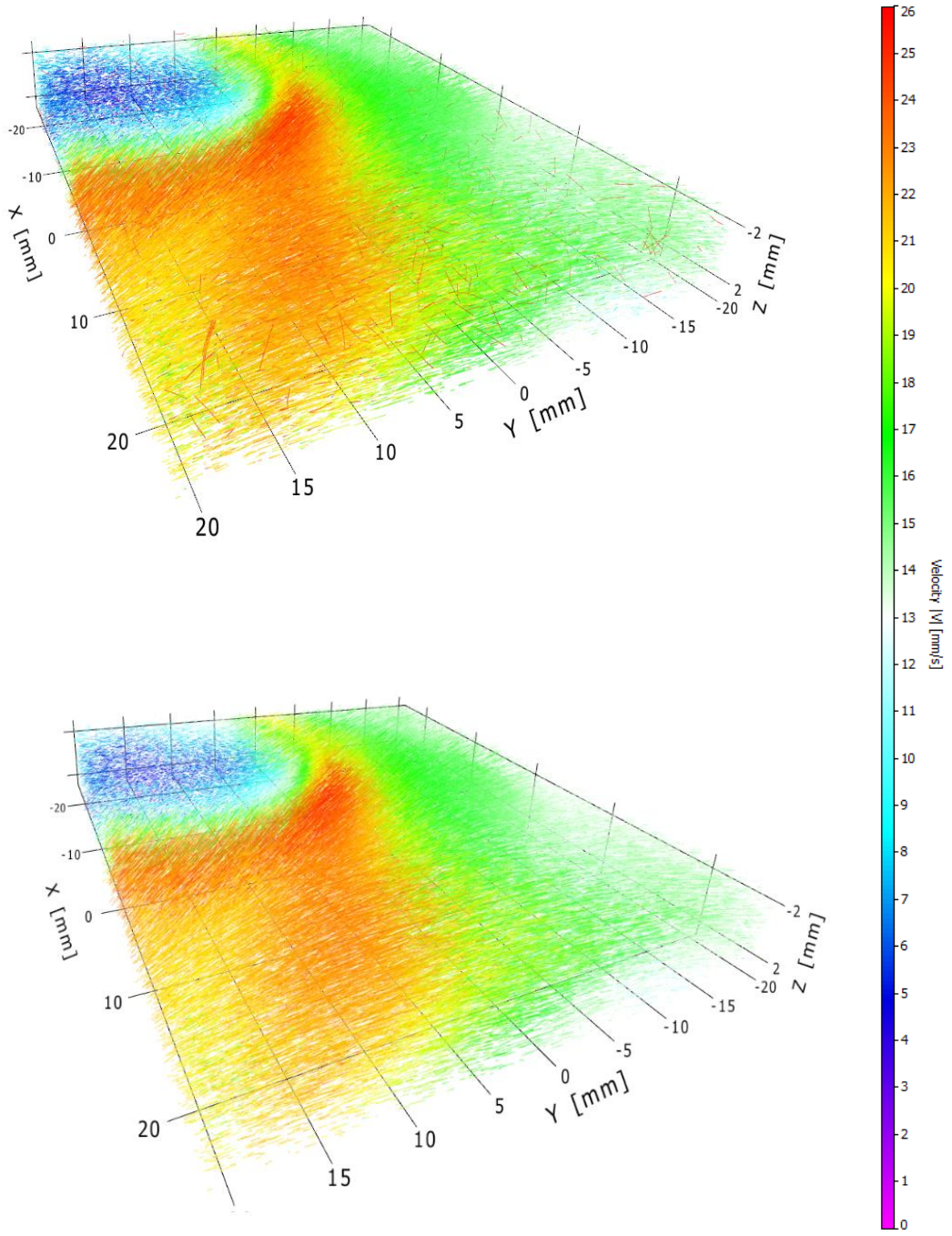

Figure V.8 Particle tracks reconstructed by STB with median filter OFF(Top) and with median filter ON (Bottom). Overlay of 11 time-steps are presented and color coded by particles velocity module.

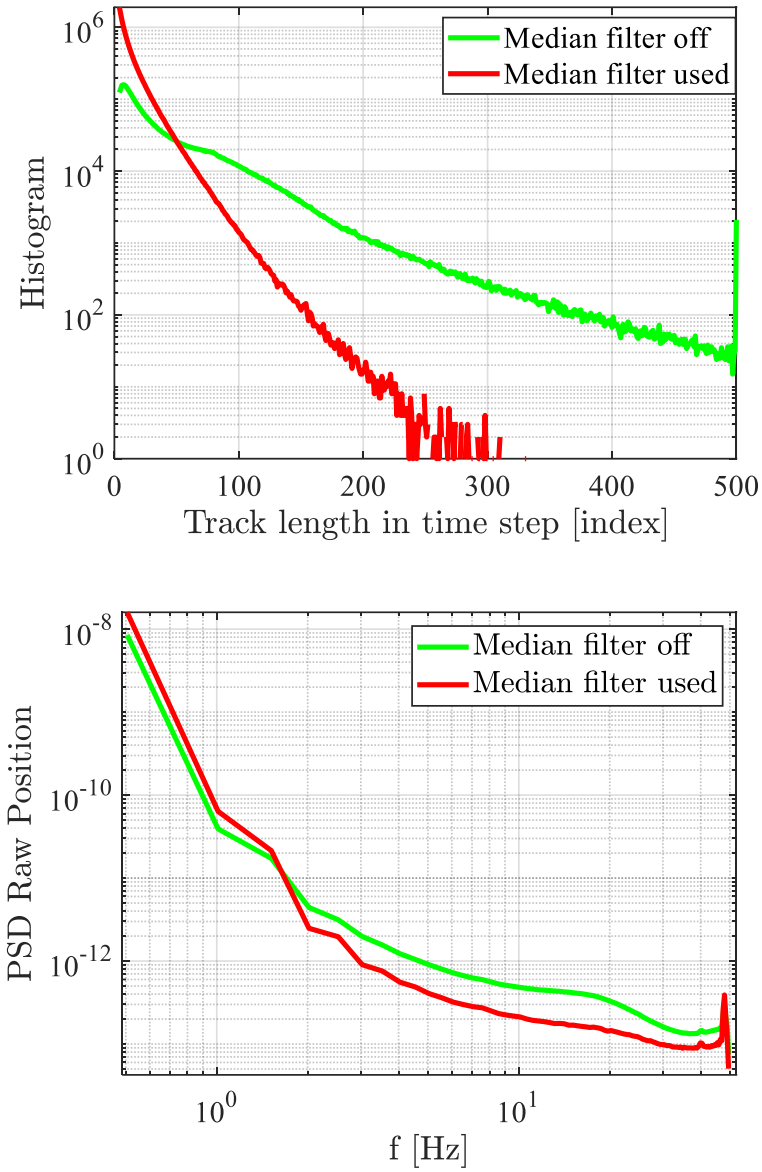

Figure V.9 (Top) Comparison of track length histogram for the case Anti 0.004Hz (run #20) where the STB is calculated with and without the use of a median filter. The images density is 0.04ppp. (Bottom) Power spectral density of the same cases.

The median filter parameters used for all the recorded cases are the following:

1- Number of neighbors used: 10.
2- Max search range: 60 voxels.
3- Threshold =2.

Most probably the values of the median filter used are rather strict and the threshold could have been increased. Indeed, the parameter selected cut the tracks into smaller ones (See Figure IV.9 (top)), so probably the filter detects some particles inside some tracks which deviate just too much compared to the neighbors and removes these particles, fragmenting the tracks into several ones. Keeping these particles leads to longer track, so better turbulence information which can be extracted from, but with higher noise linked with these particles. A better compromise can probably be found.

From the previous work of (Debue, 2019), (Ostovan et al., 2019) and others we know that the disparity map should be refined iteratively over the runs. As a standard practice, the disparity and OTF maps were refined every 10 runs. Initially, we did the same but after

every third run, the number of tracked particles started to fall off noticeably. This might be a result of the quality of our particle images that we discussed before or slight change of camera positions to each other due to small thermal dilatation of the large bench (about 5 min between runs). As a consequence, we decided to test refining the OTF and disparity every run vs refining it every third run to see if there is a big difference. The results of these tests showed that there is no significant difference between both STB results therefore we didn't refine the disparity and OTF every run because of the significant increase of the CPU and human time needed for refining the disparity.

V.3.1 STB results for multiple cases

At this stage, three points have been established: first, the images must be pre-processed; second, self-calibration and OTF must be refined at least every 3rd runs; and third, a median filter on tracks should be used when processing the images by STB algorithm. The results discussed in this chapter are only the "Anti" cases from Table V-3 due the enormous amount of data to present. In Figure V.10 and Figure V.11 STB results are analyzed and averaged for 40 runs for the following cases: Anti 0.04 Hz, 0.01Hz, 0.025Hz and 0.1 Hz. The histogram of the average displacement in x, y, z directions is presented in Figure V.10. The peak of all cases nearly collapses around 3 to 4 voxels excepts for Anti 0.004Hz case which is around 2 vx due to minimum laser frequency of 100Hz which was imposing large oversampling compared to frequency estimated with equation (V-7). We calculated the RMS of the module of the velocity of the STB results, we found that our estimation (i.e $\omega Ra,$ see equation (V-7) with a $= 0.35$ for contra cases and a $= 0.40$ for anti ones) is close to the calculated RMS of all cases except the 0.004Hz case where it is 35% smaller. This validate then the equation (V-7) to estimate the required acquisition frequency.

In Chapter IV we saw that big displacement values will affect the STB results, on the other hand, the results weren't clear for small displacements. However it is advised by (Schröder et al., 2015) who developed the STB algorithm to fix an average displacements of about 5vx. In Figure V.11 (a) we see that the number of tracked particles for the case Anti 0.1Hz is the highest in comparison to the other cases (the peak of the histogram of displacement is around 5vx). Then again, we see that the case of 0.004Hz represents the second best results when it comes to the number of tracks. This contradicts our expectancies to some extinct. This case was recorded first then Anti 0.01 Hz 3 days after, then 0.025 Hz 2 days after 0.01 Hz and then 0.1 Hz 1 day after 0.025 Hz. For the case 0.1Hz, new particles were added. This could indicate that the lifetime of particles to get very good image quality in GVK is about 1-2 days. This could then explain why 0.004 Hz gets more tracks than 0.01 and 0.025 Hz which is surprising for low displacements tuned for this case.

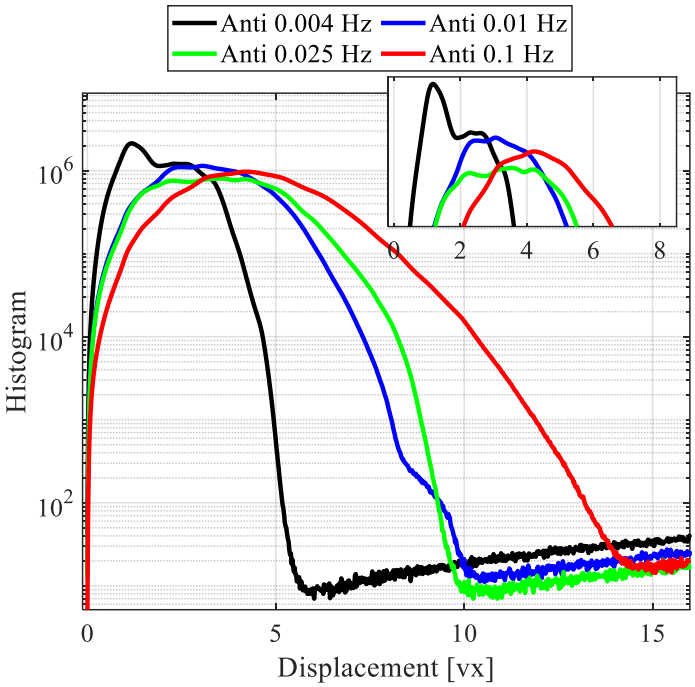

Figure V.10 Histogram of the module of displacement for different cases. The histogram is an average for 40 runs for each case to extract valuable statistical results of turbulence both in Lagrangian and Eulerian framework.

The histogram of track length in Figure V.11 (b) is more or less comparable for all cases though, with slight advantage of the Anti 0.025Hz case, probably linked to less tracked particle (i.e.only the most bright particles are tracked and can be followed on more time steps as their intensity level have less chance to become close to background noise of images). The track length is very important this is why our main objective by setting the parameters of STB is to get long trajectories.
Although we have on average 20,000 more particles than with VK2 experiment for the same particle image density, there are much more tracks smaller than 10 time steps which increase the spatial noise levels. This conclusion is based on the result we also found in Chapter IV where we saw that the first 15 to 20 time steps of any trajectory are noisy all along with the last couple of time steps of a trajectory (check Figure IV.35). That is why we have to delete tracks that are very small if we want low noise data since they contribute to increase the noise.

Finally, the PSD of raw positions in Figure V.11 (c) presents a strange peak at 48 Hz for all cases except the Anti 0.1Hz. This peak is small compared to the signal (about 3 decades less) and it is systematically of 48 Hz. It cannot be linked to the rotation frequency which varies for each case. However, it could be linked to mechanical natural frequency of the system. Until now we have no more idea of the origin of this peak, but this question is to be answered before the next GVK campaigns.

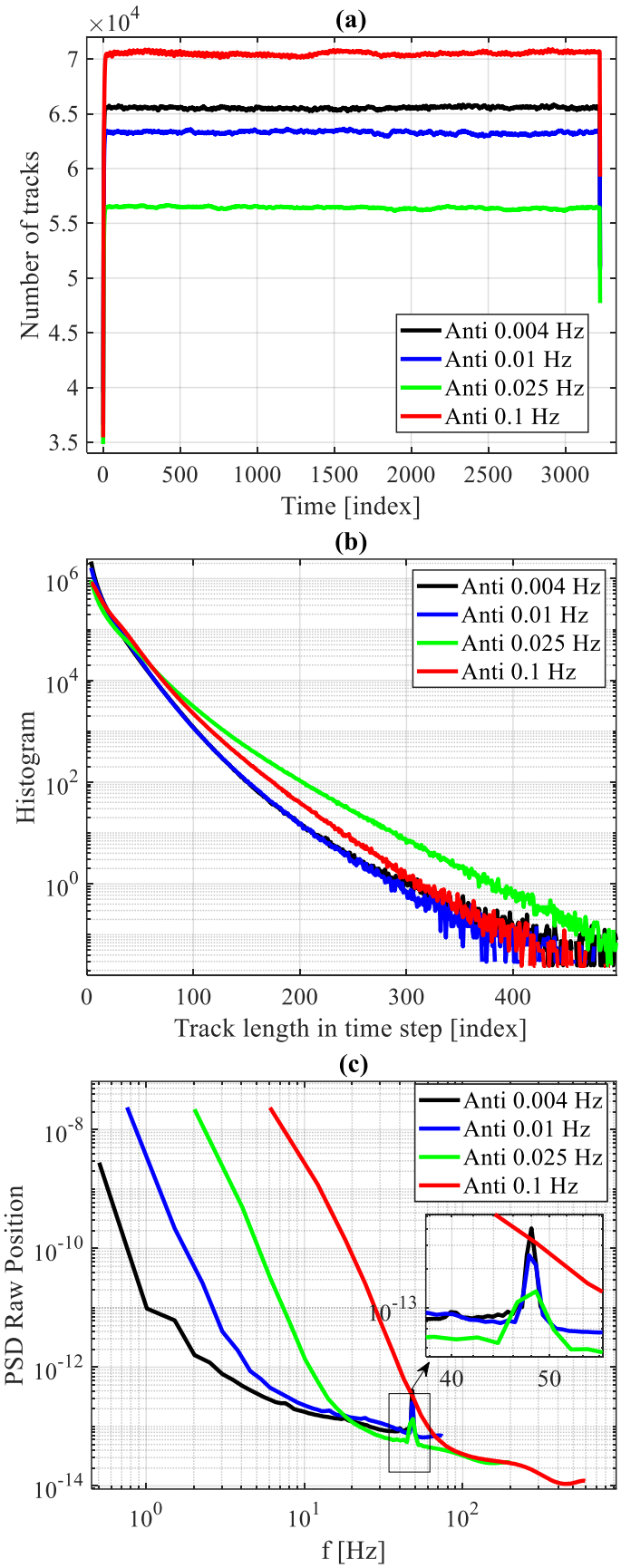

Figure V.11 (a)Average number of tracks per time step. (b) Histogram of track length and (c) PSD of position for the Anti cases with disparity and OTF refined every 3rd runs. The STB results are for images with density of 0.04ppp. The statistics presented in this figure are an average for 40 runs.

V.4 Velocity determination (smoothing STB tracks)

We have seen in previous results that the Lagrangian velocities provided by Shake the Box black box are very polluted with noise. For that reason, a post-processing software written in MATLAB language, was developed by (Cheminet et al., 2021) in the framework of EXPLOIT project. TrackFit showed that is a very powerful tool to recover denoised Lagrangian trajectories. The smoothing tuning strategies can be determined by the experimenter taking into account the desired accuracy and the physical behavior of the measured quantities.

The PSD of positions and velocities are depicted in the Figure V.12 for case Anti 0.1 Hz. It was calculated using tracks that have at least 100 time steps. We can learn a lot about the temporal resolution of our measurements and the particle position error by examining the Lagrangian spectrum. By examining the level of the noise region of the spectrum at high frequencies, one can determine the extent of the spatial noise. The frequency at which the noise appears in the spectrum determines the temporal resolution.

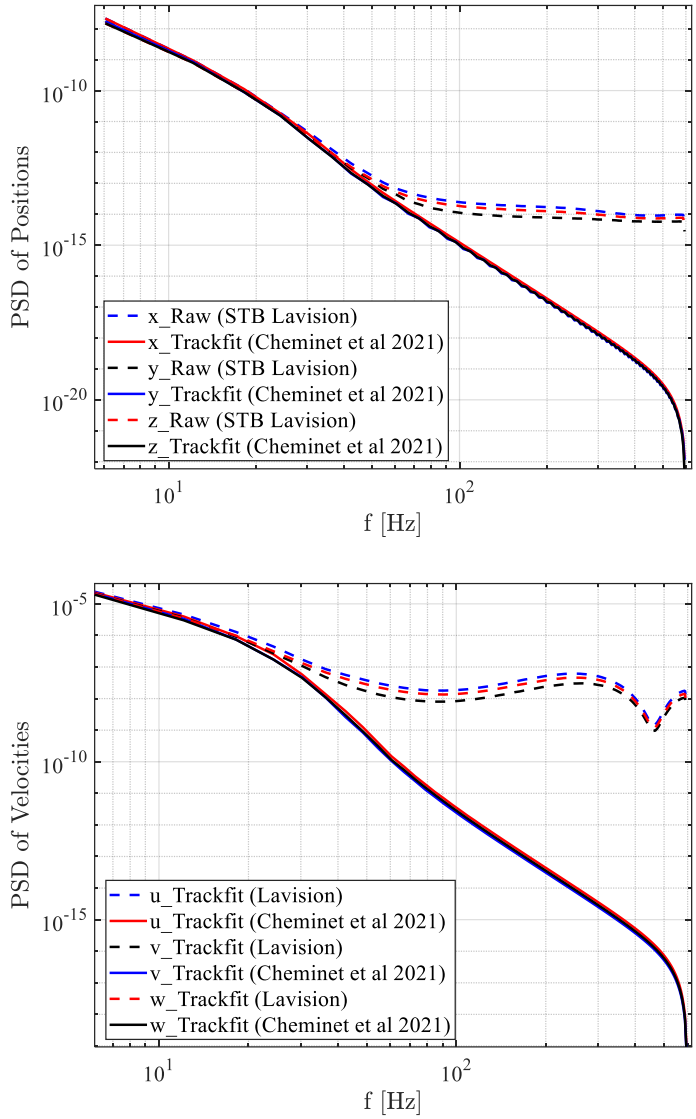

Figure V.12 (Top) Power Density Spectrum of Lagrangian particles positions. A comparison is made between Raw positions obtained by STB and TrackFit applied to the same Raw data. (Bottom) Power Density Spectrum of Lagrangian particles Velocities obtained using Trackfit and averaged over 10 runs of case ANTI 0.1Hz.

Furthermore, with the TrackFit tool developed at LMFL, it is obvious that we reduce the noise levels for the velocity spectrums specially after 20 Hz. One should keep in mind that smoothing tracks filter also the turbulence at small scale. That is a problematic since the main objective of the GVK is to search these regions for possible quasi singularities.

V.4.1 Eulerian spatial spectrum

After passing the data through the Trackfit software, instantaneous Eulerian velocity fields were computed by means of a linear interpolation (griddata routine of MATLAB) from the smoothed tracks as well as the raw data from Lavision. Flow details can be observed in 2D plots showing samples of instantaneous velocity fields on the middle plane ($z = 0$) of the volume (see Figure V.13, case anti 0.1 Hz). There is a clear discrepancy in the level of noise between the results from Trackfit of Lavision and Trackfit of Cheminet et al., 2021. This difference is quantified in the spectrum presented

in Figure V.14 where we can see that the noise level is reduced after $k = 250\, m^{-1}$ (corresponding to wave length of 4 mm) as compared to the results obtained with Trackfit of Lavision.

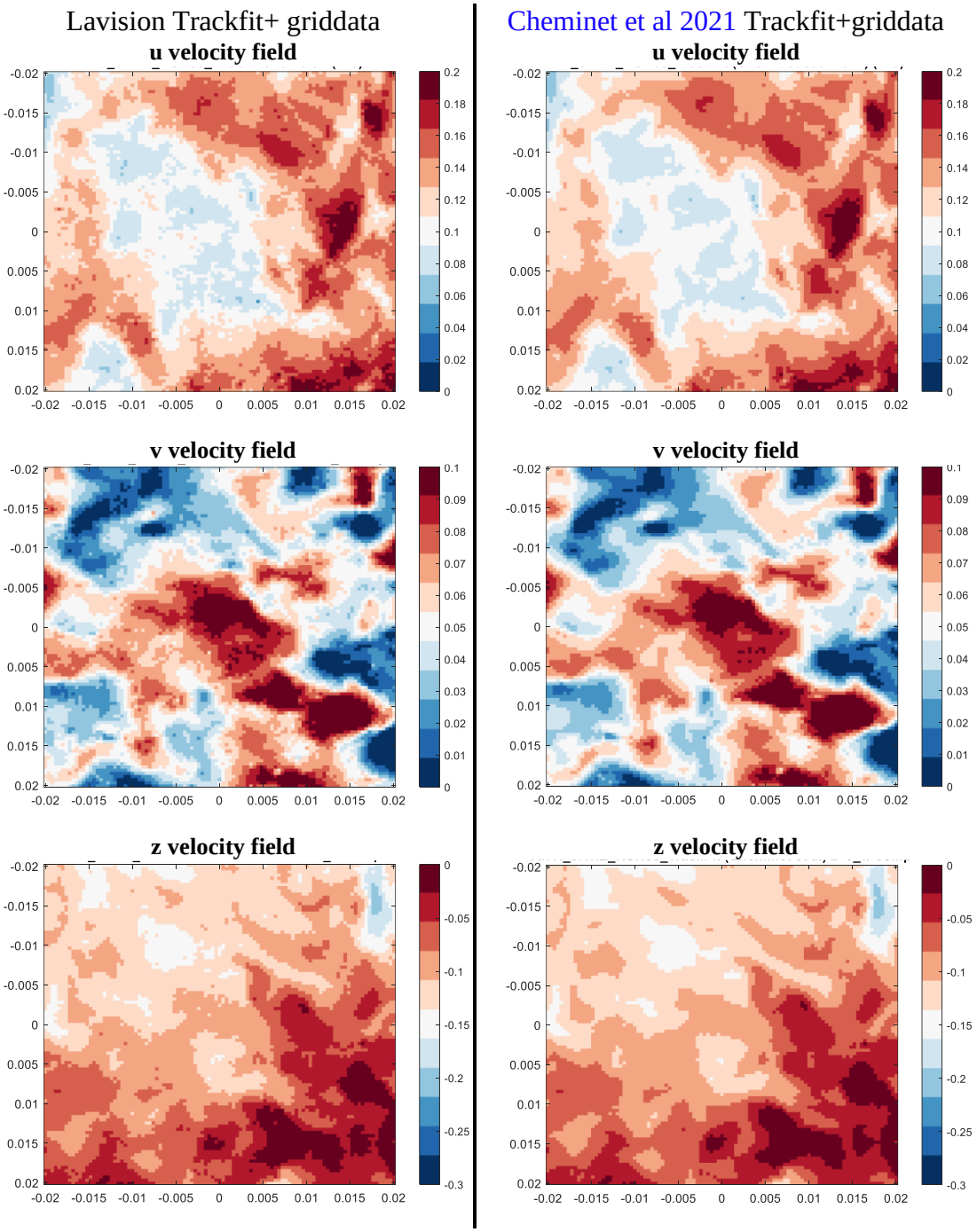

Figure V.13 Three components of the instantaneous velocity fields (Time step #20) on the middle plane (z=0) of STB measurements of the "Grand Von Karman" experiment, case Anti 0.1Hz. The left column represents the u,v,w velocity fields interpolated with griddata using the Lavision track fit data. The right column represents the u,v,w velocity fields interpolated the same way but using Cheminet et al., 2021 track fit data.

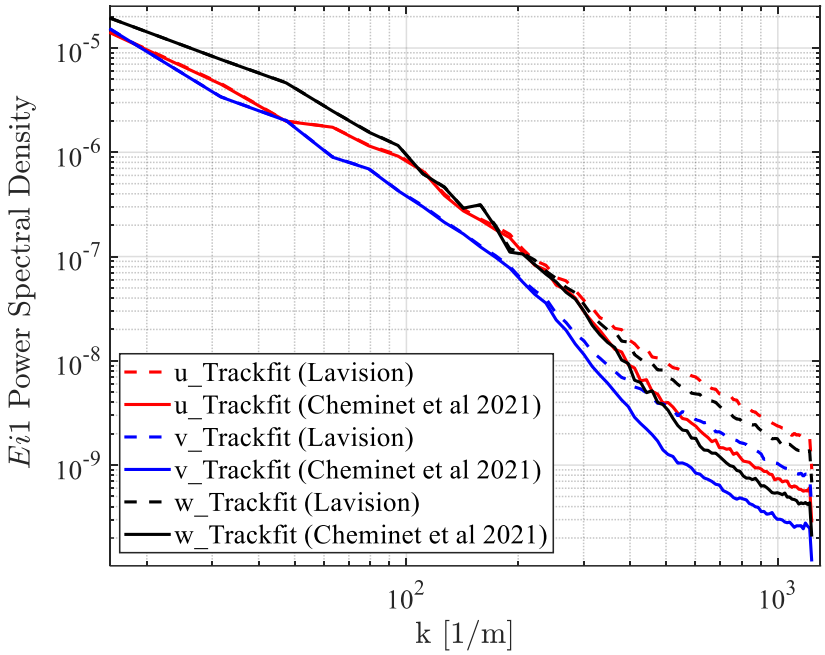

Figure V.14 Comparison between the E_{i1} Power Spectral density of velocities u,v,w interpolated with griddata routines from using smoothed tracks from Lavision Trackfit and Cheminet et al., 2021 track fit. The spectrums are calculated from instantaneous velocity fields of case Anti 0.1Hz and averaged for 10 time steps and in y and z directions.

V.5 Conclusion

The first experiment done on GVK was not perfect nor the success we expected since we did not obtain the same quality of images as SWT that allowed us to track more particles and with less error. Complicated experiments like GVK present always new experimental challenges and the two weeks constraint have prevented us to take the time to solve problems to improve images quality, especially the surprising astigmatism problem. Nonetheless, we have created a database at different Reynolds numbers (larger than *Re* created using VK2) and for different rotation directions, Anti and Contra of a Von Karman flow that are better in term of spatial resolution from what was done before in the framework of the EXPLOIT project. We also showed that the STB raw data are noisy and need to be smoothed before interpolating the velocity or acceleration. For this purpose, we presented the capabilities of the TrackFit tool to reduce the noise level of the raw data.

Chapter VI Conclusions and perspectives

In the first section of conclusions, we will talk about the different objectives that have been targeted and the various contributions that we have made in the studied problematic. The second section encompasses the different ideas, written in the form of perspectives that could improve the proposed methods in order to consider a continuation of our research work. The conclusion and perspective sections will be divided in two parts, the first part is experimental related conclusions and perspectives, and second is conclusions and perspectives related to the improvement of STB results.

VI.1 Conclusions

Experimental conclusions

The “Grand Von Karman” experiment presents many practical challenges, especially to carry out optical measurements inside to extract turbulence information. The goal of the project was to fine study the turbulence generated by this GVK at very high Reynolds numbers. As the turbulence is a 3D phenomenon, the "Shake the Box" (STB) method was selected as it provides information about the 3 velocities components in a volume as function of time. For that reason, a mimic experiment that reproduces the optical access we have for GVK was used with an objective to fine tune all the possible experimental barriers that we might face on the main experiment $i.e$ GVK. First of all, we tested two possible configurations for camera placements around the quasi-cylindrical experiment to examine the optical performance. Optical access points were designed at 22.5°, 45° and 67.5° from laser volume illumination. First tests were done using the windows at 45° and 67° with Lavision $10\mu m$ Hollow sphere particles for seeding. Laser energy needed for cameras at 67.5° was important in this experiment and background noise recorded was high. Particles images were fluctuating in size and clusters were observed everywhere on the images. For that reason, we thought that it was worth it to invest in better quality particles.

Second configuration was tested by changing the cameras positions at $\pm 22.5°$ and $\pm 45°$ from volume illumination. Additionally, we used different particles for seeding from Spherotech (PP-50-100) with smaller mean diameter ($5.09\mu m$) and more monodisperse (i.e. narrower probability density function). These new particles, from the best of our knowledge, were not used for PIV before and they showed a great capability to enhance the measurements. Moreover, and due to high noise levels observed before linked with small impurities less than 1-3 µm present inside the water, we decided to use a water filtration system installed in the room of the experiment to reduce any contamination of the water by dust or plastic fibers of containers used for transportation of the water. The water quality is of great importance and precautions need to be taken into account when opening the top of the experiment. It is probably not possible to work with a “clean room” type of precautions, but it is necessary to pay a lot of attention when manipulating around and inside the facility to avoid hairs and other dusts to penetrate into the tank. In the figure below we show an example of the precautions used when manipulating the GVK.

The intensity difference visible on the different cameras as a result of their positions in forward scattering angles is one experimental parameter that could not be changed. This is problematic as it decreases the STB quality results as seen in Chapter IV. This phenomenon can be attenuated by closing more the aperture of cameras which get less light, but this increases the particle image size which can also deteriorate the STB results. The perspective offers some propositions/solutions to this issue.

Based on images quality as well as STB results of the second configuration proposed as optical measurement solution in chapter III, it was decided to use this solution in the GVK campaign. During the measurements, we observed astigmatism effects on all 4 cameras but specially for the cameras at angles $\pm 22.5°$. This could be due to mechanical constraints applied on the access glass windows of GVK, hence damaging its optical properties. For that reason, we were left with an "undesired" solution to increase the fstop number of cameras 2 and 3 to get a better compromise on the particle image size in the full volume. This change increases the particle images size substantially hence making it more difficult for STB to identify (OTF +IPR) and track (extrapolation) the particles as shown in Chapter IV. The STB results obtained in GVK during this PhD is then not as good as expected compared to ones obtained with the optical set-up tests presented in Chapter III.

To obtain good 3D velocities measurements with STB, a nearly perfect calibration is needed (B Wieneke, 2008). For that, the disparity map obtained with volume self-calibration should be as low as 0.02vx on average in the full domain. To be as close as possible to this goal, it was shown that a self-calibration refinement was needed every 3 runs (i.e. every 15 min of recording interval). As this cannot be automatized, it required a lot of human time for processing the large data base acquired.

Despite all the barriers, a large database of STB data in GVK to study its turbulence was generated during this PhD. For the four frequencies of impellers investigated (0.004, 0.01, 0.025 and 0.1 Hz) and the two configurations contra and anti of GVK, 40 runs of full memory were recorded for each of these 8 cases with a STB spatial resolution of about 0.6 mm. For each case, a total of about 30 integral time scale is available for the 0.004Hz configuration and about 50 to 60 for the others. The raw data images correspond to 12TB, and the processed data (raw tracks from STB) to about 6 TB to post-process.

STB conclusions

Tracks qualities were exploited for both experimental and synthetic data. We start by a comparison between STB results for 1st configuration and 2nd configuration tested on

similar water tank of GVK (SWT). We recall the main differences between these two configurations. For the first configuration, cameras were at $\pm 67.5°$ and $\pm 45°$ and we used Lavision glass hollow spheres with diameter ranging from 1 to maximum 30 μm. For the second configuration, cameras were at $\pm 45°$ and $\pm 22.5°$ and we used Spherotech polystyrene particles with diameter ranging from 4.5 to maximum 7 μm. Then we tested the STB algorithm on synthetic data to understand the effect of different parameters as well as to try to push the method to its limits. Finally, we conducted the GVK experiment based on the conclusions obtained on the SWT and synthetic tests.

First of all, the particles that were bought for the second configuration along with changing the configuration of cameras, had a massive impact on the quantity and quality of STB tracks. For a given particle per pixel concentration of 0.05ppp, we were able to track 80,000 more particles than the first experiment done on SWT. Also, the overall quality of tracks and level of noise were much better even though comparing different runs may be misleading in a sense that the flow characteristics could affect the STB results and the experiment reproducibility was poor. For that reason, we decided to investigate in depth the effect of different "experimental" parameters as well as STB processing parameters by means of synthetic PIV images created using Lagrangian tracers integrated from a DNS. This synthetic experiment simulates to a great deal what we had tested before on SWT 2nd configuration such as magnification factor, cameras positions, cameras lens etc. Scheimpflug condition was not taken into account. The STB results were compared to the ground truth DNS with a novelty matching procedure not only based on particles but also on track information. These tests showed that:

1- The particle size is the most important factor to tune around 2.4 pixels.
2- Intensity difference in cameras images creates problem for the tracking scheme and significantly decreases the length of tracks. This intensity difference between cameras has to be as low as possible.
3- STB has a very strong limitations to image particle density for a given mean particle image size. For example, it is shown that $0.05ppp$ seemed a bit too much for the value of the particle size we had of about 3.8 pixels on average.

Additionally, these tests showed that, even for very good OTF and disparity maps, the tracks are fragmented, the tracks length are overestimated sometimes, and the first 15 to 20 time steps exhibit higher error values than the rest of time steps. These results suggest that the first piece of a track should be eliminated from the postprocessing if we need to reduce the noise in the data.

All the information collected were applicated to the GVK experiment, the STB results showed a slight decrease in quality compared to our tests on SWT due to the experimental problems encountered we described before. Especially the increase in particle size to limit the astigmatism problem as well as the increase in the intensity ratio between the different cameras images. Also, we showed that the use of a median filter is helpful to suppress ghost tracks, but it affects drastically the tracks length. This parameter should be used with precautions and with extended tests before deciding the best set of parameters for each run.

Finally, we made a comparison between the Trackfit version of Lavision and the Trackfit version created at LMFL. The different parameters of the software could be controlled by the user to maximize the quality of tracks as well as the spatial spectrum of velocities contrary to the black box Trackfit of Lavision. For that reason, Trackfit of Cheminet et al

2021 lead to better results in terms of temporal and spatial resolutions and it is essential to go further in the analysis of turbulence as we are able to control the filter properties.

VI.2 Perspectives

Experimental possible improvements

Due to STB dependency on image quality which are related to experimental limitations, we suggest some changes that could be made for a short, medium, and long term timeline. The main idea here is to modify the configuration to reduce the astigmatism aberrations, decrease as much as possible the particle size and moderate the intensity factor between cameras. A special attention should be made to the depth of field required (6mm) since it can be affected by changing any other setting of the cameras.

The astigmatism we observed was the biggest setback for the quality of images during the campaign in GVK, especially for cameras 2 and 3 at 22.5°. The fstop number was increased from 11 to 16 for cameras 2 and 3 in order to increase the depth of field from 5.5 mm to 11mm. Increasing the depth field results in less aberrated particle images. However, the drawback of this action was the increase in particle size to 2.9px. To minimize the astigmatism without increasing the fstop number, we could try in a first step to play on the mounting screws of the glass insert as they can introduce small bending of it as a thick gasket is compressed with these screws to ensure the sealing. The risk is to introduce water leaks or to break the glass. If the approach fails, we could try to improve our images quality without increasing the particle size by decreasing slightly the magnification by setting the cameras 200 mm further away from the glass insert (maximum allowed as there is the structure of the engines behind, see Figure V.3). This will reduce the magnification from 0.37 to 0.27, leading to particle image diffraction size similar (1.8 px compared to 1.9 px) but larger depth of focus (9.2 mm compared to 5.7 mm). By a small gain on the astigmatism problem with less glass bending couple with this solution, better images with smaller particle size can be obtained. However, the results found in Chapter III shows that a concentration of 0.05ppp will still be an optimum and we could expect about 100,000 tracks but on a larger volume. At the end, the spatial resolution will be the same or worth. Reducing the thickness of the measurement volume can improve the STB results, however as the turbulence is a 3D phenomenon, we will start to lose all the advantage of a volumetric measurement method. Putting all together, the images quality can only be improved by suppressing the astigmatism problem. If the insert mounting failed, then new inserts can be made with more thick glasses or by trying to add a cylindrical lens in front of objective lenses to compensate the aberration. This can be done by a tunable bending of a few millimeters thick plexiglass plate.

Finally, the intensity difference between cameras should be reduced as much as possible without also changing the fstop number as it increases the particle size. One solution can be to add in front of the objective lens a density plate with the good optical density.

For the medium-term timeline, there is a possibility to change the camera positions. We can set all the cameras in forward scattering and at $\pm$ 22.5° from the 6mm thick laser sheet in a top view but cameras 1 and 2 placed below the center of GVK looking to the measurement field of view by the inserts below the middle ones and cameras 3 and 4 in a symmetrical way above the center of GVK. In that way, we eliminate completely the intensity differences in cameras images. Also the lines of sight of each camera are not in the same plane in this configuration which should improve the 3D reconstruction of particle. For that, prism insert should be manufactured, and the cameras should be able to

rotate along their axis to optimize the common field of view between the four. The LMFL has recently designed and machined new Scheimpflug adaptors which have this possibility.

STB improvements

To increase the efficiency of STB, one might need to do more tests on synthetic images. There is an infinite number of parameters combination, but with the results presented in chapter IV, we can now propose quite narrow range for the optimum parameter. By making some additional tests with smaller particle image size of 1.5 and 2.5 px at seeding concentration of 0.05 ppp and 0.07ppp, one can remove the ambiguity on the optimum particle image size and concentration proposed. By making a test with a smaller magnification inside the DNS to mimic the experimental set-up, smaller displacements can be simulated to get a better view of the optimum acquisition frequency to set on STB experiments.

The usage of a median filter, which demonstrated how significantly it can impact track length, is another crucial test to be carried out with synthetic images. Finally, we should also use the smoothing method of Cheminet et al, 2021 on the reconstructed tracks to see, for the optimum test case, the real amount of signal that we can recover from the raw STB results compared to the ground truth DNS. This test can also provide a tool to estimate the cut off frequency in STB experiments. By applying flowfit interpolation on these smoothed tracks to come back to Eulerian data, we can also propose an estimation of the real spatial resolution we can expect with spatial spectrum comparisons.

At the end, 'Shake the Box' showed that it is indeed a powerful tool but to quote Spiderman *"with great powers come great responsibilities"*. Well, STB failed at a lot of its responsibilities. STB was marketed as a next gen type of algorithms that can open more research possibilities especially increasing the resolution since it doesn't rely on cross correlation methods. New upgrades have been employed recently to the new software version of Lavision, specially what is called reverse tracking. In this new version, instead of just looking forward to the next piece of a track, the algorithm is able to track back in the past direction to find some missed pieces of a track and to reduce the error to the already found pieces. This option was briefly tested at the end of this thesis work but without clear improvements, on the contrary, the results were not as good, and the computational cost is very high. For that reason, alternatives should be considered for the next research campaigns on GVK. A promising alternative is OpenLPT software that is written in C++ and was inspired from "Shake The box". The work of (Jahn et al., 2021) showed comparable results to STB black box as concluded from the thesis work of (Khojasteh et al., 2021). This team in Rennes France developed a new 4D PTV method called "*Lagrangian coherent track initialization*". It is based on local temporal and spatial coherency of neighbor trajectories. They reconstruct tracks that are consistent with the neighbor coherent motions. Their work showed a more sophisticated initialization technique, and they are able to reduce systematic errors starting from the very first detected particle of a track.

Bibliography

Adrian, R.J., 1997. Dynamic ranges of velocity and spatial resolution of particle image velocimetry. Meas. Sci. Technol. 8, 1393–1398. https://doi.org/10.1088/0957-0233/8/12/003

Adrian, R.J., 1984. Scattering particle characteristics and their effect on pulsed laser measurements of fluid flow: speckle velocimetry vs particle image velocimetry. Appl. Opt. 23, 1690. https://doi.org/10.1364/AO.23.001690

Arroyo, M.P., Greated, C.A., 1991. Stereoscopic particle image velocimetry. Meas. Sci. Technol. 2, 1181–1186. https://doi.org/10.1088/0957-0233/2/12/012

Batchelor, G.K., 1953. The theory of homogeneous turbulence. Cambridge university press. https://doi.org/10.1002/qj.49707934126

Batchelor, Townsend, 1949. The nature of turbulent motion at large wave-numbers. https://doi.org/10.1098/rspa.1949.0136

Bézier, P. (Ed.), 1986. Bibliography, in: The Mathematical Basis of the UNIURF CAD System. Butterworth-Heinemann, p. 56. https://doi.org/10.1016/B978-0-408-22175-7.50011-X

Boyle, W.S., Smith, G.E., 1970. Charge coupled semiconductor devices. Bell Syst. Tech. J. 49, 587–593. https://doi.org/10.1002/j.1538-7305.1970.tb01790.x

Champagnat, F., Cornic, P., Cheminet, A., Leclaire, B., Besnerais, G.L., Plyer, A., 2014. Tomographic PIV: particles versus blobs. Meas. Sci. Technol. 25, 084002. https://doi.org/10.1088/0957-0233/25/8/084002

Cheminet, A., Ostovan, Y., Valori, V., Cuvier, C., Daviaud, F., Debue, P., Dubrulle, B., Foucaut, J.-M., Laval, J.-P., 2021. Optimization of regularized B-spline smoothing for turbulent Lagrangian trajectories. Exp. Therm. Fluid Sci. 127, 110376. https://doi.org/10.1016/j.expthermflusci.2021.110376

Chenouard, N., Smal, I., de Chaumont, F., et al., 2014. Objective comparison of particle tracking methods. Nat. Methods 11, 281–289. https://doi.org/10.1038/nmeth.2808

Chiu, W.-C., Rib, L.N., 1956. The rate of dissipation of energy and the energy spectrum in a low-speed turbulent jet. Trans. Am. Geophys. Union 37, 13. https://doi.org/10.1029/TR037i001p00013

Cierpka, C., Lütke, B., Kähler, C.J., 2013. Higher order multi-frame particle tracking velocimetry. Exp. Fluids 54, 1533. https://doi.org/10.1007/s00348-013-1533-3

Cornic, P., Illoul, C., Cheminet, A., Le Besnerais, G., Champagnat, F., Le Sant, Y., Leclaire, B., 2016. Another look at volume self-calibration: calibration and self-calibration within a pinhole model of Scheimpflug cameras. Meas. Sci. Technol. 27, 094004. https://doi.org/10.1088/0957-0233/27/9/094004

Cowen, E.A., Monismith, S.G., Cowen, E.A., Monismith, S.G., 1997. A hybrid digital particle tracking velocimetry technique. Exp. Fluids 22, 199–211. https://doi.org/10.1007/s003480050038

David, L., Jardin, T., Braud, P., Farcy, A., 2012. Time-resolved scanning tomography PIV measurements around a flapping wing. Exp. Fluids 52, 857–864. https://doi.org/10.1007/s00348-011-1148-5

De Boor, C., 1978. A Practical Guide to Splines. Springer. https://link.springer.com/book/9780387953663

Debue, P., 2019. Experimental approach to the problem of the Navier-Stokes singularities (PhD dissertation).

Debue, P., Kuzzay, D., Saw, E.-W., Daviaud, F., Dubrulle, B., Canet, L., Rossetto, V., Wschebor, N., 2018. Experimental test of the crossover between the inertial and the dissipative range in a turbulent swirling flow. Phys. Rev. Fluids 3, 024602. https://doi.org/10.1103/PhysRevFluids.3.024602

Delafosse, A., Collignon, M.-L., Crine, M., Toye, D., 2011. Estimation of the turbulent kinetic energy dissipation rate from 2D-PIV measurements in a vessel stirred by an axial Mixel TTP impeller. Chem. Eng. Sci. 66, 1728–1737. https://doi.org/10.1016/j.ces.2011.01.011

Dracos, Th. (Ed.), 1996. Three-Dimensional Velocity and Vorticity Measuring and Image Analysis Techniques: Lecture Notes from the Short Course held in Zürich, Switzerland, 3–6 September 1996, ERCOFTAC Series. Springer Netherlands, Dordrecht. https://doi.org/10.1007/978-94-015-8727-3

Dubrulle, B., 2019. Beyond Kolmogorov cascades. J. Fluid Mech. 867, P1. https://doi.org/10.1017/jfm.2019.98

Duchon, J., Robert, R., 1999. Inertial energy dissipation for weak solutions of incompressible Euler and Navier-Stokes equations. Nonlinearity 13, 249–255. https://doi.org/10.1088/0951-7715/13/1/312

Elsinga, G.E., Scarano, F., Wieneke, B., van Oudheusden, B.W., 2006. Tomographic particle image velocimetry. Exp. Fluids 41, 933–947. https://doi.org/10.1007/s00348-006-0212-z

Faller, H., Geneste, D., Chaabo, T., Cheminet, A., Valori, V., Ostovan, Y., Cappanera, L., Cuvier, Ch., Daviaud, F., Foucaut, J.-M., Guermond, J.-L., Laval, J.-Ph., Nore, C., Padilla, V., Wiertel, C., Dubrulle, B., 2021. On the nature of intermittency in a turbulent von Kármán flow. J. Fluid Mech. 914, A2. https://doi.org/10.1017/jfm.2020.908

Foucaut, J M, Carlier, J., Stanislas, M., 2004. PIV optimization for the study of turbulent flow using spectral analysis. Meas. Sci. Technol. 15, 1046–1058. https://doi.org/10.1088/0957-0233/15/6/003

Foucaut, J.M., George, W.K., Stanislas, M., Cuvier, C., 2021. Optimization of a SPIV experiment for derivative moments assessment in a turbulent boundary layer. Exp. Fluids 62, 244. https://doi.org/10.1007/s00348-021-03339-9

Foucaut, J. M., Miliat, B., Perenne, N., Stanislas, M., 2004. Characterization of Different PIV Algorithms Using the EUROPIV Synthetic Image Generator and Real images From a Turbulent Boundary Layer, in: Stanislas, M., Westerweel, J., Kompenhans, J. (Eds.), Particle Image Velocimetry: Recent Improvements. Springer Berlin Heidelberg, Berlin, Heidelberg, pp. 163–185. https://doi.org/10.1007/978-3-642-18795-7_12

Geneste, D., Faller, H., Nguyen, F., Shukla, V., Laval, J.-P., Daviaud, F., Saw, E.-W., Dubrulle, B., 2019. About Universality and Thermodynamics of Turbulence. Entropy 21, 326. https://doi.org/10.3390/e21030326

George, W.K., 2013. Lectures in Turbulence for the 21st Century; http://www.turbulence-online.com/Publications/Lecture_Notes/Turbulence_Lille/TB_16January2013.pdf

George, W.K., 2013. Lectures in Turbulence for the 21st Century

Gouesbet, G., Grehan, G., 1999b. Generalized Lorenz-Mie theory for assemblies of spheres and aggregates. J. Opt. Pure Appl. Opt. 1, 706–712. https://doi.org/10.1088/1464-4258/1/6/309

Hadad, T., Gurka, R., 2013. Effects of particle size, concentration and surface coating on turbulent flow properties obtained using PIV/PTV. Exp. Therm. Fluid Sci. 45, 203–212. https://doi.org/10.1016/j.expthermflusci.2012.11.006

Hansen, P.C., Kilmer, M.E., Kjeldsen, R.H., 2006. Exploiting residual information in the parameter choice for discrete ill-posed problems. BIT Numer. Math. 46, 41–59. https://doi.org/10.1007/s10543-006-0042-7

Hansen, P.C., O'Leary, D.P., 1993. The Use of the L-Curve in the Regularization of Discrete Ill-Posed Problems. SIAM J Sci Comput 14, 1487–1503. https://doi.org/10.1137/0914086

Jahn, T., Schanz, D., Schröder, A., 2021. Advanced iterative particle reconstruction for Lagrangian particle tracking. Exp. Fluids 62, 179. https://doi.org/10.1007/s00348-021-03276-7

Kaga, A., Yamaguchi, A., 1997. Flow field estimation using PIV data and fluid dynamic equations. PIV-Fukui 131–136. https://cir.nii.ac.jp/crid/1570854174274953216

Kähler, C.J., Astarita, T., Vlachos, P.P., Sakakibara, J., Hain, R., Discetti, S., La Foy, R., Cierpka, C., 2016. Main results of the 4th International PIV Challenge. Exp. Fluids 57, 97. https://doi.org/10.1007/s00348-016-2173-1

Kármán, Th.V., 1921. Über laminare und turbulente Reibung. ZAMM - J. Appl. Math. Mech. Z. Für Angew. Math. Mech. 1, 233–252. https://doi.org/10.1002/zamm.19210010401

Khojasteh, A.R., Yang, Y., Heitz, D., Laizet, S., 2021. Lagrangian coherent track initialization. Phys. Fluids 33, 095113. https://doi.org/10.1063/5.0060644

Kobayashi, T., Saga, T., Sekimoto, K., 1989. Velocity measurement of three-dimensional flow around rotating parallel disks by digital image processing. SPIE Society of Photo-Optical Instrumentation Engineers, United States.

Kolmogorov, A.N., 1962. A refinement of previous hypotheses concerning the local structure of turbulence in a viscous incompressible fluid at high Reynolds number. J. Fluid Mech. 13, 82–85. https://doi.org/10.1017/S0022112062000518

Kolmogorov, A.N., 1941. On the degeneration of isotropic turbulence in an incompressible viscous fluid. Dokl Akad Nauk SSSR 31, 319–323. http://cds.cern.ch/record/739747?ln=en

Kuzzay, D., Faranda, D., Dubrulle, B., 2015b. Global vs local energy dissipation: The energy cycle of the turbulent von Kármán flow. Phys. Fluids 27, 075105. https://doi.org/10.1063/1.4923750

Maas, H.-G., 1992. Complexity analysis for the establishment of image correspondences of dense spatial target fields. International Archives of Photogrammetry and Remote Sensing, Vol. XXIX, Part B5, pp. 102-107

Maas, H.G., Gruen, A., Papantoniou, D., 1993b. Particle tracking velocimetry in three-dimensional flows: Part 1. Photogrammetric determination of particle coordinates. Exp. Fluids 15, 133–146. https://doi.org/10.1007/BF00190953

Malik, N.A., Dracos, Th., Papantoniou, D.A., 1993. Particle tracking velocimetry in three-dimensional flows. Exp. Fluids 15, 279–294. https://doi.org/10.1007/BF00223406

Mann, J., Ott, S., Andersen, J.S., 1999. Experimental study of relative, turbulent diffusion. Denmark. Forskningscenter Risoe. Risoe-R No. 1036 (EN)

Marié, L., 2003. Transport de moment cinétique et de champ magnétique par un écoulement tourbillonnaire turbulent: Influence de la Rotation. PhD dissertation. https://tel.archives-ouvertes.fr/tel-00007755

Melling, A., 1997. Tracer particles and seeding for particle image velocimetry. Meas. Sci. Technol. 8 1406. https://iopscience.iop.org/article/10.1088/0957-0233/8/12/005/meta

Nishino, K., Kasagi, N., Hirata, M., 1989. Three-Dimensional Particle Tracking Velocimetry Based on Automated Digital Image Processing. J. Fluids Eng.-Trans. Asme 111, 384–391.

Novara, M., Schanz, D., Reuther, N., Kähler, C.J., Schröder, A., 2016. Lagrangian 3D particle tracking in high-speed flows: Shake-The-Box for multi-pulse systems. Exp. Fluids 57, 128. https://doi.org/10.1007/s00348-016-2216-7

Ohmi, K., Li, H.-Y., 2000. Particle-tracking velocimetry with new algorithms. Meas. Sci. Technol. 11, 603–616. https://doi.org/10.1088/0957-0233/11/6/303

Ostovan, Y., Cuvier, C., Debue, P., Valori, V., Foucaut, J.-M., Laval, J.-P., Vincent, P., Dubrulle, B., Daviaud, F., 2019. 4D Particle Tracking Velocimetry measurements in a Von Karman turbulence experiment. 13th International Symposium on Particle Image Velocimetry. https://hal.archives-ouvertes.fr/hal-03765230

Ouellette, N.T., Xu, H., Bodenschatz, E., 2006. A quantitative study of three-dimensional Lagrangian particle tracking algorithms. Exp. Fluids 40, 301–313. https://doi.org/10.1007/s00348-005-0068-7

Parisi, G., Frisch, U., 1995. Turbulence and Predictability in Geophysical Fluid Dynamics and Climate Dynamics,. J. Geosci. Environ. Prot. 6, 84–88.

Pickering, C.J.D., Halliwell, N.A., 1984. Laser speckle photography and particle image velocimetry: photographic film noise. Appl. Opt. 23, 2961. https://doi.org/10.1364/AO.23.002961

Raffel, M., Kähler, C.J., Kompenhans, J., Scarano, F., Wereley, S.T., Willert, C.E., 2018. Particle Image Velocimetry: A Practical Guide, 3rd ed. 2018. ed. Springer International Publishing : Imprint: Springer, Cham. https://doi.org/10.1007/978-3-319-68852-7

Ravelet, F., 2005. Bifurcations globales hydrodynamiques et magnetohydrodynamiques dans un ecoulement de von Karman turbulent. PhD dissertation. https://pastel.archives-ouvertes.fr/tel-00011016

Reynolds, O., 1883. An Experimental Investigation of the Circumstances Which Determine Whether the Motion of Water Shall Be Direct or Sinuous, and of the Law of Resistance in Parallel Channels. Philos. Trans. R. Soc. Lond. 17, 935–982. http://dx.doi.org/10.1098/rstl.1883.0029

Richardson, L.F., Lynch, P., 1922. Weather Prediction by Numerical Process, Cambridge Mathematical Library. Cambridge University Press. https://doi.org/10.1017/CBO9780511618291

Rousset, B., Bonnay, P., Diribarne, P., Girard, A., Poncet, J.M., Herbert, E., Salort, J., Baudet, C., Castaing, B., Chevillard, L., Daviaud, F., Dubrulle, B., Gagne, Y., Gibert, M., Hébral, B., Lehner, Th., Roche, P.-E., Saint-Michel, B., Bon Mardion, M., 2014. Superfluid high REynolds von Kármán experiment. Rev. Sci. Instrum. 85, 103908. https://doi.org/10.1063/1.4897542

Savitzky, Abraham., Golay, M.J.E., 1964. Smoothing and Differentiation of Data by Simplified Least Squares Procedures. Anal. Chem. 36, 1627–1639. https://doi.org/10.1021/ac60214a047

Saw, E.-W., Debue, P., Kuzzay, D., Daviaud, F., Dubrulle, B., 2018. On the universality of anomalous scaling exponents of structure functions in turbulent flows. J. Fluid Mech. 837, 657–669. https://doi.org/10.1017/jfm.2017.848

Schanz, D., Gesemann, S., Schröder, A., 2016. Shake-The-Box: Lagrangian particle tracking at high particle image densities. Exp. Fluids 57, 70. https://doi.org/10.1007/s00348-016-2157-1

Schanz, D., Gesemann, S., Schröder, A., Wieneke, B., Novara, M., 2013a. Non-uniform optical transfer functions in particle imaging: calibration and application to tomographic reconstruction. Meas. Sci. Technol. 24, 024009. https://doi.org/10.1088/0957-0233/24/2/024009

Schanz, D., Schröder, A., Gesemann, S., 2014. ‘Shake The Box’ - a 4D PTV algorithm: Accurate and ghostless reconstruction of Lagrangian tracks in densely seeded flows. 17th International Symposia on Applications of Laser Techniques to Fluid Mechanics.

Schanz, D., Schröder, A., Gesemann, S., Michaelis, D., Wieneke, B., 2013b. ‘Shake The Box’: A highly efficient and accurate Tomographic Particle Tracking Velocimetry (TOMO-PTV) method using prediction of particle positions. 10th International Symposium on Particle Image Velocimetry.

Schröder, A., Schanz, D., Michaelis, D., Cierpka, C., Scharnowski, S., Kähler, C.J., 2015. Advances of PIV and 4D-PTV ”Shake-The-Box” for Turbulent Flow Analysis – the Flow over Periodic Hills. Flow Turbul. Combust. 95, 193–209. https://doi.org/10.1007/s10494-015-9616-2

Soloff, S.M., Adrian, R.J., Liu, Z.-C., 1997. Distortion compensation for generalized stereoscopic particle image velocimetry. Meas. Sci. Technol. 8, 1441–1454. https://doi.org/10.1088/0957-0233/8/12/008

Taylor, G.I., 1935. Statistical theory of turbulence III-Distribution of dissipation of energy in a pipe over its cross-section. Proc. R. Soc. Math. Phys. Eng. Sci. 151, 455–464. https://doi.org/10.1098/rspa.1935.0160

Tennekes, H., Lumley, J.L., 1972. A first course in turbulence. The MIT press, ISBN 978-0262200196.

Tikhonov, A.N., 1977. On the solution of ill-posed problems and the method of regularization. Wiley, NewYork.
http://mi.mathnet.ru/eng/dan/v151/i3/p501

Toschi, F., Bodenschatz, E., 2009. Lagrangian Properties of Particles in Turbulence. Annu. Rev. Fluid Mech. 41, 375–404.
https://doi.org/10.1146/annurev.fluid.010908.165210

Tsai, R.Y., 1986. An efficient and accurate camera calibration technique for 3d machine vision. Proc. IEEE Comput. Soc. Conf. Comput. Vis. Pattern Recognit.
https://doi.org/10.1109/JRA.1987.1087109

Ullum, U., Schmidt, J.J., Larsen, P.S., McCluskey, D.R., 1998. Statistical analysis and accuracy of PIV data. J. Vis. 1, 205–216.
https://doi.org/10.1007/BF03182514

Valori, V., Debue, P., Cheminet, A., Chaabo, T., Ostovan, Y., Cuvier, C., Foucaut, J.-M., Laval, J.-P., Wiertel, C., Padilla, V., Daviaud, F., Dubrulle, B., 2021. On Lagrangian Intermittency from 4-D Particle Tracking Velocimetry measurements of a turbulent von Karman flow. ArXiv210404222 Phys.
https://doi.org/10.48550/arXiv.2104.04222

Wieneke, B., 2013. Iterative reconstruction of volumetric particle distribution. Meas. Sci. Technol. 24, 024008.
https://doi.org/10.1088/0957-0233/24/2/024008

Wieneke, B., 2008. Volume self-calibration for 3D particle image velocimetry. Exp. Fluids 45, 549–556.
https://doi.org/10.1007/s00348-008-0521-5

Willert, C.E., 2006. Assessment of camera models for use in planar velocimetry calibration. Exp. Fluids 41, 135–143.
https://doi.org/10.1007/s00348-006-0165-2

Yeh, Y., Cummins, H.Z., 1964. localized fluid flow measurements with an He–Ne laser spectrometer. Appl. Phys. Lett. 4, 176–178.
https://doi.org/10.1063/1.1753925

Yeung, P.K., Pope, S.B., Sawford, B.L., 2006. Reynolds number dependence of Lagrangian statistics in large numerical simulations of isotropic turbulence. J. Turbul. 7, N58.
https://doi.org/10.1080/14685240600868272

Titre en français : Optimisation d'une métrologie 4D-PTV pour la caractérisation d'un écoulement turbulent à très petites échelles.

Résumé en français :

L'étude fondamentale de la turbulence revêt d'une importance significative en raison de son rôle dominant dans de nombreux domaines de la physique, des sciences de l'ingénieur, de l'astrophysique, de l'aéronautique, etc. La dissipation turbulente joue un rôle central dans l'écoulement turbulent et est donc une quantité importante dans les modèles de turbulence. Dans le but de caractériser cette dissipation, le présent travail est basé sur une technique de suivi de particules appelée "Shake-The Box" pour mesurer les champs de vitesse tridimensionnels en fonction du temps à une résolution pouvant avoisiner l'échelle dissipative. Le dispositif expérimental et le traitement de la technique Shake the Box ont été optimisés et poussés à leurs limites afin d'améliorer la résolution spatiale et la précision des trajectoires lagrangiennes mesurées. L'approche utilisée dans cette thèse est basée non seulement sur des données expérimentales mais aussi sur des images synthétiques PIV basées sur une simulation numérique directe des équations de Navier Stokes. L'investigation quantitative et qualitative nous permet de définir les paramètres optimaux pour notre application ciblée sur un écoulement de Von Karman Géant et donne les limites de la méthode.

Mots clés : Mécaniques des fluides, velocimetrie par images de particules (PIV), Turbulence, Mécaniques des fluides expérimentales.

Title in English: Optimization of a 4D-PTV metrology for the characterization of a turbulent flow at very small scales.

Abstract in English:

The fundamental study of turbulence is of significant importance due to its dominant role in many fields of physics, engineering sciences, astrophysics, aeronautics, etc. Turbulent dissipation plays a central role in turbulent flow and is therefore an important quantity in turbulence models. With the aim of characterizing this dissipation, the present work is based on a particle tracking technique called "Shake-The Box" to measure three-dimensional velocity fields as function of time at a resolution which can approach dissipative scale. The experimental setup and processing of the Shake the Box technique have been optimized and pushed to their limits in order to improve the spatial resolution and the accuracy of the measured Lagrangian trajectories. The approach used in this thesis was based not only on experimental data but also on synthetic PIV images based on direct numerical simulation of the Navier Stokes equations. The quantitative and qualitative investigation allows us to define the optimal parameters for our targeted application on a Giant Von Karman flow and gives the limits of the method.

Keywords: Fluid mechanics, Particle image velocimetry (PIV), Turbulence, Experimental fluid mechanics.